UNIVERSITÀ DEGLI STUDI DI PALERMO

Dottorato di Ricerca in

Ingegneria Chimica, Gestionale, Informatica e Meccanica

Indirizzo - Ingegneria della Produzione

COMPUTER AIDED ENGINEERING FOR THERMO-MECHANICAL-METALLURGICAL ANALYSIS OF FORGING OPERATIONS OF TITANIUM ALLOYS

IL DOTTORE
ANTONINO DUCATO

IL COORDINATORE
CH.MO PROF. SALVATORE GAGLIO

IL TUTOR
CH.MO PROF. FABRIZIO MICARI

CO-TUTOR
CH.MO PROF. LIVAN FRATINI

CICLO XXV
2012-2014

Declaration of license

TUTTI I CONTENUTI DEL REPOSITORY ISTITUZIONALE AD ACCESSO APERTO DELLE TESI DI DOTTORATO DI RICERCA DELL'UNIVERSITÀ DEGLI STUDI DI PALERMO SONO PROTETTI DAL DIRITTO D'AUTORE, IN APPLICAZIONE DELLA LEGGE 22 APRILE 1941, N. 633 E SUCCESSIVE INTEGRAZIONI E MODIFICAZIONI.

Con la presente licenza, l'Università degli Studi di Palermo richiede, a tutti coloro che immettono materiali nel Repository d'Ateneo ad accesso aperto delle tesi di Dottorato di Ricerca, le seguenti dichiarazioni e autorizzazioni.

Il/La sottoscritto/a Dott. /ssa …**Antonino Ducato**… …..……..., nato/a a …**Palermo**…, il …**22/06/1983**…, nel seguito denominato "Autore",

DICHIARA,

sotto sua esclusiva responsabilità,

- che quanto depositato il …**15/01/2015**… è la versione autentica della sua tesi di dottorato in …**Dottorato di Ricerca in Ingegneria Chimica, Gestionale, Informatica e Meccanica, Indirizzo - Ingegneria della Produzione**…, intitolata …**Computer aided engineering for thermo-mechanical-metallurgical analysis of forging operations of titanium alloys**……, che sarà presentata nella seduta del …**25/02/2015**…., unitamente ai documenti a corredo della stessa (abstract, appendici, etc.), per un totale di …**1**… documenti (files);

- che si tratta di un suo lavoro originale e non contrasta, per quanto a sua conoscenza, con il diritto d'autore di nessun altro;

- che detta tesi e i documenti a corredo della stessa non contengono dichiarazioni mendaci od offensive o altrimenti lesive dei diritti di terzi e che eventuali errori o imprecisioni nei contenuti sono riconducibili esclusivamente alla sua responsabilità;

- di essere l'unico titolare della facoltà di autorizzare la riproduzione e la comunicazione al pubblico di detti materiali per finalità non commerciali nel Repository

dell'Università di Palermo, nel seguito denominata "Università", avendo adempiuto ad eventuali obbligazioni derivanti da contratto o accordo se detta tesi è frutto di un lavoro sponsorizzato o supportato da un'agenzia o organizzazione diversa dall'Università;

- di conoscere e di avere osservato quanto disposto dall'art. 70 della Legge 22 Aprile 1941, n. 633 e successive modifiche qualora la tesi o i documenti a corredo citino, riproducano o riassumano, a scopo di critica o discussione, parti di opere protette dal diritto d'autore realizzate da terzi, ed in particolare di avere effettuato dette utilizzazioni nei limiti indicati da detto art. 70 e sempre riportando la chiara menzione del titolo dell'opera, dei nomi dell'autore, dell'editore e, se si tratti di traduzione, del traduttore, qualora tali indicazioni figurino sull'opera riprodotta;

- di avere preventivamente ottenuto le necessarie autorizzazioni dai legittimi titolari se nella tesi o nei documenti a corredo sono state riprodotte, riassunte, tradotte o altrimenti utilizzate, oltre i limiti consentiti dall'art. 70 della Legge 22 Aprile 1941, n. 633 e successive modifiche, opere o parti di opere altrui coperte dalla protezione del diritto d'autore;

- di sollevare l'Università e suoi singoli dipendenti da qualsiasi eventuale responsabilità derivante dalla violazione dei diritti morali e/o patrimoniali di terze parti per avere riprodotto, tradotto, distribuito e/o comunicato al pubblico la tesi e gli altri documenti depositati;

- di accettare che l'Università rimuova l'opera depositata dal repository qualora l'esame di dottorato avesse esito negativo;

- di accettare che l'Università, con provvedimento motivato, possa decidere di non diffondere o non comunicare al pubblico l'opera depositata, o di sospenderne la diffusione e la comunicazione, ove rilevi in essa contenuti lesivi di diritti altrui o che possano esporre l'Università e/o il personale della stessa al rischio di denunce o azioni giudiziarie, ferma restando la responsabilità esclusiva dell'Autore per le eventuali violazioni di cui al punto precedente.

CONCEDE

all'Università degli Studi di Palermo licenza irrevocabile e non esclusiva di riprodurre, comunicare al pubblico tramite la rete Internet e/o distribuire in qualsiasi formato il

materiale depositato, per finalità non commerciali di conservazione e documentazione dei risultati della ricerca scientifica, alle seguenti condizioni:

- che l'Università preservi l'integrità dell'opera astenendosi da qualsiasi intervento o manipolazione sui contenuti della stessa e limitandosi alle sole riproduzioni e modifiche di formato necessarie per assicurarne l'archiviazione nel proprio sistema informativo e l'accessibilità tecnica anche a persone con disabilità, nonché la conservazione a lungo termine;

- che l'Università cataloghi e descriva accuratamente l'opera e distribuisca e/o comunichi al pubblico, contestualmente all'opera, tutte le informazioni relative alla paternità e alla titolarità del diritto d'autore sulla stessa. In particolare, dovranno essere riportati per esteso: cognome e nome dell'autore, titolo della tesi, nome dell'Università, ciclo di dottorato, a.a., sede;

- che l'Università distribuisca e/o comunichi al pubblico, contestualmente all'opera, le informazioni sulle utilizzazioni consentite agli utenti ai sensi della Legge 22 Aprile 1941, n. 633, ovvero ai sensi di eventuali licenze unilateralmente accordate dall'Autore in aggiunta alle utilizzazioni consentite dalla Legge citata;

- che l'Università, in caso di motivata richiesta dell'Autore, da allegarsi alla presente licenza, differisca il termine della sua comunicazione e distribuzione al pubblico fino a non oltre sei mesi dopo il deposito dell'opera, ove la stessa sia gravata da vincoli contrattuali con terze parti ovvero contenga riferimenti idonei a identificare invenzioni industriali per le quali sia in corso o debba essere avviata una procedura di registrazione brevettale.

Palermo, lì **14/01/2015**

Firma _____

Università degli Studi di Palermo

SCUOLA POLITECNICA

Dottorato di Ricerca in

Ingegneria Chimica, Gestionale, Informatica e Meccanica

Indirizzo - Ingegneria della Produzione

Ciclo XXV

2012-2014

Computer aided engineering for thermo-mechanical-metallurgical analysis of forging operations of titanium alloys

Il dottore
Antonino Ducato

Il coordinatore
Chmo. Prof.
Salvatore Gaglio

Tutor
Chmo. Prof.
Fabrizio Micari

Co-tutor
Chmo. Prof.
Livan Fratini

Acknowledgments

I would like to express my sincere thanks to my adviser, Prof. Livan Fratini, for his constant support, advice, guidance, wisdom and most importantly his sense of humor, which all contributed to making this thesis possible.

I am grateful to Dr. Rajiv Shivpuri of the Ohio State University for his, advice and, most importantly, his guidance in improving my knowledge during my visiting period at ISE.

I want to show my appreciation for the coworkers of my research team Dr. Gianluca Buffa, Dr. Giuseppe Ingarao, Dr. Davide Campanella and Dr. Sergio Pellegrino who were always willing to offer more help than I could have ever expected.

I wish to thank my colleagues of the manufacturing engineering PhD course Azzurra Morreale and Anna Errore for sharing with me this three years long adventure with hard times, papers, presentations and never clarified doubts.

I also want to thank graduate students Rosario Nobile, Antonino Correnti, Salvatore Lanza and Andrea Farrugia, whose assistance proved to be critical in the completion of this document.

In the end, I would especially like to thank my family and my friends for their support and encouragement along the way.

Diventa un professionista

una persona seria

qualcuno su cui si può contare.....

Abstract

In this thesis a study on the forging processes of Ti-6Al-4V titanium alloy, with particular focus on the numerical applications and simulation design of hot forming methods, was done. The aim of this work is to collect all data concerning the material definition in terms of thermal, mechanical and microstructural properties of the selected alloy in order to filter all useful information to describe the behavior of the material under the characteristic conditions of the hot forging processes, taking into account both thermo-mechanical and metallurgical aspects involved during a such complex thermo-mechanical stage. Those information were collected and used to characterize the material properties, creating a first coupled characterization for the considered material with the aim of link both thermal-mechanical and thermal-microstructural behaviors in running numerical analysis of hot forging processes. The collected data was validated by means of comparison with a forging campaign of workpieces for aeronautical applications involved within the research project Titaform, which had the objective to study and determine a methodic design approach in set-up of precision hot forging of titanium alloys. After the first validation, all collected information were used to develop a self-consisten system based on the Johnson-Cook equation with the aim of creating a fully coupled constitive model for multiphasic titanium alloys which takes into account both thermal, mechanical and microstructural properties as function of field variables. The final objective considers the thermo-mechanical behavior of each main phase of Ti-6Al-4V alloy in order to carry out the contribution of each allotropic form during a non-isothermal deformation. Results showed a good agreement with experimental observations.

Keywords: Forging; Titanium alloys; Ti-6Al-4V; Phase transformation Self consistent; FEM.

Table of contents

1. Introduction

Titanium and titanium alloys are currently finding increasingly widespread use in many industries, such as aerospace applications, military and civil applications, and medical engineering. Their desirable combination of very good mechanical properties and low densities give very attractive strength-to-weight ratios, very low to high temperature capability, good toughness, high stiffness and excellent corrosion and erosion resistance [1]. Nowadays, the increasing demand of applications in which functionality and reliability of components are of great importance needs a strong improvement in knowledge and understanding of all processes in the manufacture of titanium components from minerals to finished parts are of great significance, in order to develope new and stronger materials and optimize the already existing processes. The most commonly used titanium alloy is the two phase Alpha+Beta alloy Ti-6Al-4V, which is able to form a variety of microstructures, due to the Alpha/Beta transformations achieved through thermo-mechanical processing, and different property combinations which permits the adaptation of properties to specific applications [1].

Titanium and its alloys are forming a continuous, stable, protective, and adherent oxide on the surface in the presence of oxygen and moisture [2]. The formation of the passive film on the surface of the titanium and titanium alloys depends on mostly the surface condition, the environment, the alloying elements in the material and the microstructure throughout the material [3]. Due to the outstanding biocompatibility of these materials, the wide variety of use in several industries and the good combination of mechanical properties.

The aim of this study was the development of a numerical tool helping process designer to properly choice the best parameters set in forging processes of Alpha-Beta titanium alloys. One critical limitation of actual numerical commercial applications for this family of forming processes is given by a non-fully coupled approach, which does not take into account the themo-mechanical properties of each phase involved during a thermo-mechanical process and their contribution in the material behavior. However, actual state of art of constitutive models and knowledge of titanium alloys allows to build the basics for a phasic self-consistent constitutive approach.

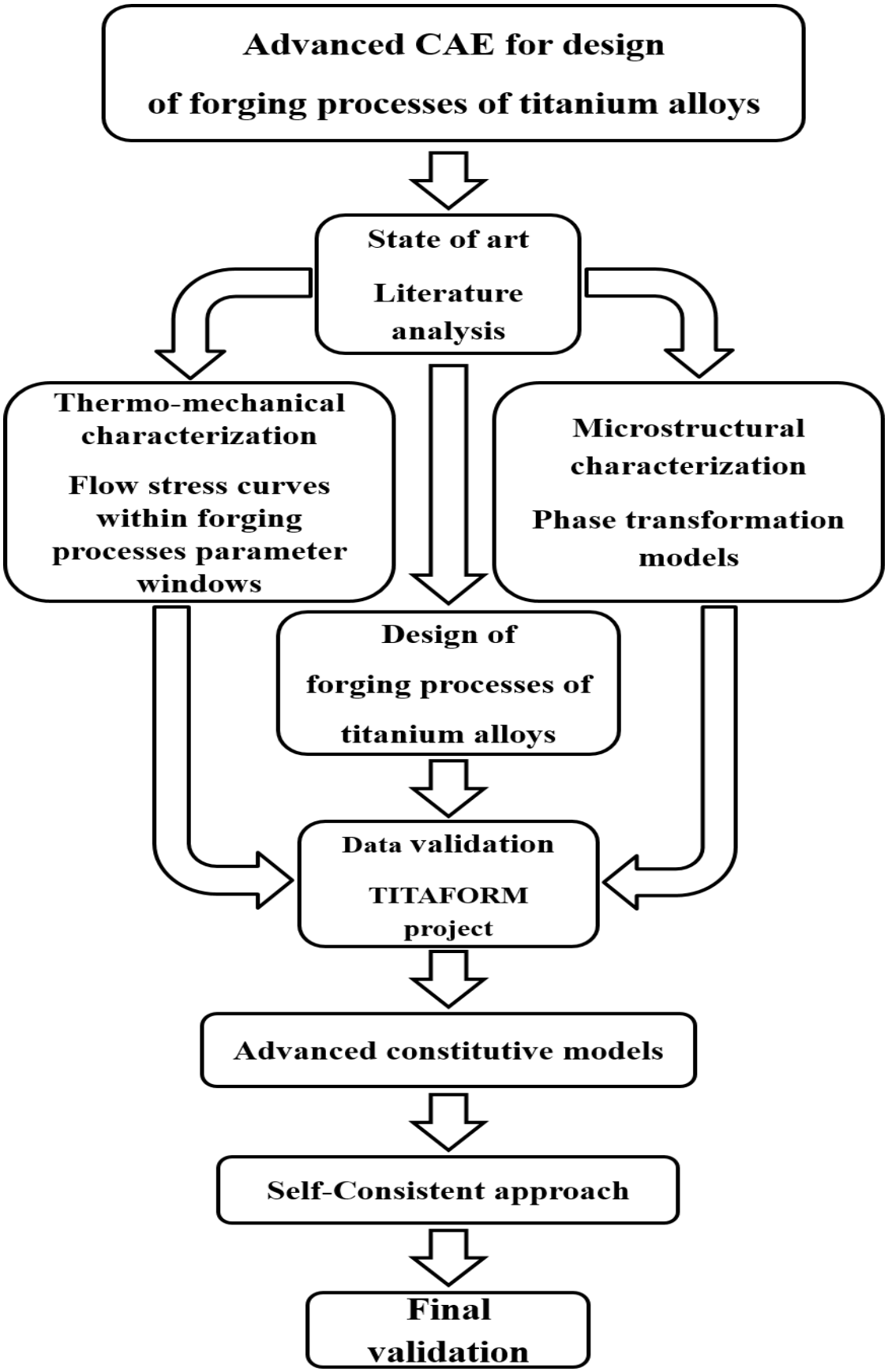
Advanced CAE for design
of forging processes of titanium alloys
State of art
Literature analysis
Thermo-mechanical characterization
Flow stress curves within forging processes parameter windows
Microstructural characterization
Phase transformation models
Design of forging processes of titanium alloys
Data validation
TITAFORM project
Advanced constitutive models
Self-Consistent approach
Final validation

2. Titanium and its alloys

Titanium is the ninth most abundant element and the fourth plentiful structural metal constituting the 0.6% of the earth's crust. It was firstly identified as a new metallic element in the mineral manaccanite by William Gregor in England in 1791 and name of Titanium was given in 1795 by the Berlin chemist Klapproth in Germany after the Titans of Greek mythology [4]. As the stable dioxide, titanium occurs in nature in different crystal modifications corresponding to the minerals rutile (93-96% TiO2) [5]; brookite and anatase (FeTiO3; 44-70% TiO2) [5] and leucoxene which is an alternation product of ilmenite [6]. The strong tendency of titanium metal to react with oxygen and nitrogen makes the production of high-purity titanium difficult and this aspect influenced its use before the last three decades. This aspect was partially solved by introduction, in the middle of 20th century, of the Kroll method which became a commercially attractive production process, which involves the reduction of titanium tetrachloride with magnesium in an inert-gas atmosphere. Its final product is a porous and spongy-like titanium that is called "titanium sponge".

Because the relatively low density of this metal (4.51 g/cm3) (about 2 times of aluminum and 60% of steels) in combination with a high yield strength (up to 400 °c), good oxidation resistance (at temperatures lower than 600 °C), excellent corrosion resistance, high specific strength, excellent bio-compatibility and its decorative appearance, it is classified as a nonferrous and light metal and its commercial interest was encouraged, in particular in the aerospace, chemical industry and medical engineering sectors. Another important aspect of titanium and its alloys is their applicability to process like forging, investment casting, powder metal technologies, joining and machining [5].

2.1. Crystal structure

Titanium atom displays an unfilled 3D shell transition metal and can crystallize in various crystal structures, which are stable within particular temperature ranges. The complete transformation from one into another crystal structure (called allotropic

transformation) takes place at transus temperature, which is called Beta-transus and is defined as the lowest equilibrium temperature at which material is 100% Beta structure. The Beta-transus point for pure titanium is at 882 °C about and, below this temperature, crystallizes as in a modified ideally hexagonal close packed (HCP), called Alpha phase (α) titanium. This structure transforms to a body-centered cubic (BCC) crystal structure, called Beta phase (β) titanium. The density of the bcc Beta phase is slightly greater than that of the closer-packed hcp α phase [1].

The lattice parameters of the hexagonal close packed crystal structure in α titanium are a = 0.295 nm and c = 0.468 nm, giving a c/a ratio of 1.587 where this is 1.633 for an ideally closed packed hexagonal lattice. The lattice parameter of bcc β titanium at 900 °C is a = 0.331 nm. Because of the interstitially dissolved atoms in the hcp lattice (e.g. C, N, or O) or the substitutional atoms with smaller atomic radii than titanium (e.g. Al) the c/a, ratio of the titanium slightly increases. Polycrystalline hexagonal Alpha titanium is extremely difficult to deform. The result of additional deformation on secondary slip systems, as well as possible mechanical twinning causes the limited ductility [1].

2.2. The alloying behavior of titanium

The chemical composition and the microstructure are the two factors, which determine the properties of titanium alloys. The alloying elements in most Ti alloys are added to control the constitution of the alloy, to alter and/or control the transformation kinetics, and to solid-solution-strengthen one or more of the microstructural constituents [7].

The alloying behavior of titanium is readily discussed in terms of the effect of different solutes on the allotropic transformation temperature of the pure metal, which is given in (Figure 1). The chemical composition of the titanium alloys determines the properties and volume fraction of the phases, Alpha and Beta. The alloying elements of titanium are classified as neutral, Alpha-stabilizers, or Beta-stabilizers depending on their influence on the Beta-transus temperature. The Beta-stabilizing elements shift the Beta phase field to lower temperatures, while the Alpha-stabilizing elements extend the Alpha phase field to higher temperatures. Neutral elements have only minor influence on the Beta-transus temperature. The alloying elements can also be divided into substitutional solutes that

their concentrations constitute the basis for commercial alloy designations and interstitial solutes. For mechanical properties point of view, Alpha is less ductile compared with the bcc Beta, due to the limited deformation capability of hcp structures. The diffusion coefficient of Alpha is more than two orders of magnitude lower than that of Beta. Therefore, the resistance to creep and oxidation increases with increasing aluminum content, while simultaneously the ductility and the deformation capability deteriorate [1, 7]. Among the Alpha-stabilizers, aluminum certainly is the most important alloying element of titanium and the interstitial elements oxygen, nitrogen, and carbon belong to this category.

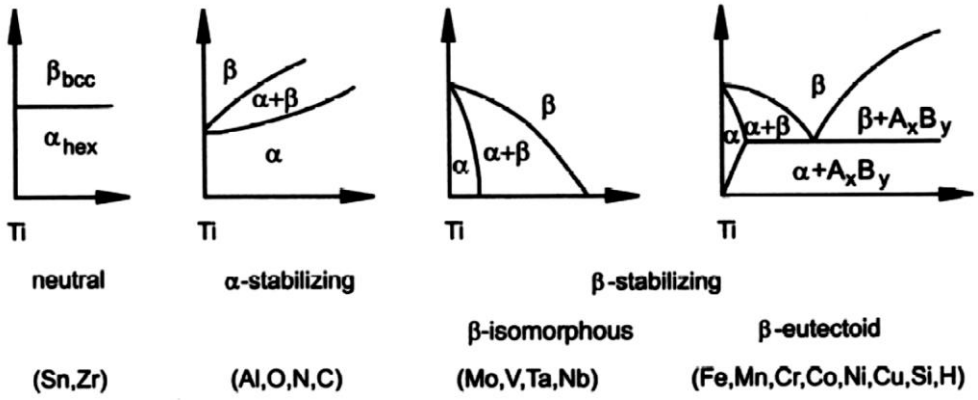

Figure 1: Influence of alloying elements on phase diagrams of Titanium alloys [1]

Oxygen is always present in Ti alloys and modern commercial practice permits good control of its concentration in order to improve the final strengthening of material. N and C are both soluble enough to be important as solid-solution strengtheners and to have significant effects on the nucleation of the Alpha phase, while B is also found as an impurity in some types of alloy. Other elements, such as Mg and Be, may dissolve as interstitials but their solubility is so limited that they are of little importance as solid solution elements. In addition, the Alpha-stabilizers develop a two-phase Alpha+Beta field at higher temperatures, while the Beta-stabilizers are subdivided into Beta-isomorphous and Beta-eutectic elements. Of these, the Beta-isomorphous elements (e.g. Mo, V, Nb and Ta) are more important due to their much higher solubility in titanium; on the other hand, even very low volume fractions of Beta-eutectic elements (e.g. Fe, Mn, Cr, Co, Ni, Cu, Si, and H) can lead to the formation of intermetallic compounds and they

decrease the transformation temperature. Si has the tendency to segregate to dislocations with the effect to prevent dislocation climb, which improves creep behavior. The solubility of H is very high in the Beta phase and relatively low in the Alpha phase because the Ti-H system forms a eutectoid and the solubility of H in the Alpha phase in equilibrium with titanium hydride is small. In addition, the noble metals (e.g. Au, Cu and Ag) as well as the heavy transition metals (e.g. Pt and Pd) tend to form eutectoid. Sn, Hf and Zr are considered as neutral elements since they have no significant influence on the Alpha/Beta phase boundary, but they are not neutral from s strength point of view since they primarily reinforce the Alpha phase. In the end, Zr tends to homogenize fine silicide precipitates [3, 6, 7].

Titanium alloys are usually classified as Alpha, Alpha+Beta and Beta alloys, with further subdivision into the near-Alpha and metastable-Beta alloys [6]. According to the three–dimensional phase diagram given in (Figure 2), the Alpha alloys comprise commercially pure titanium and alloys exclusively alloyed with Alpha-stabilizing elements and/or neutral elements. If minor fractions of Beta-stabilizing elements are added, they are referred to as near-Alpha alloys.

The Alpha+Beta alloys are the most widely used group, having a Beta phase volume fraction ranging from about 5 to 40% at room temperature.

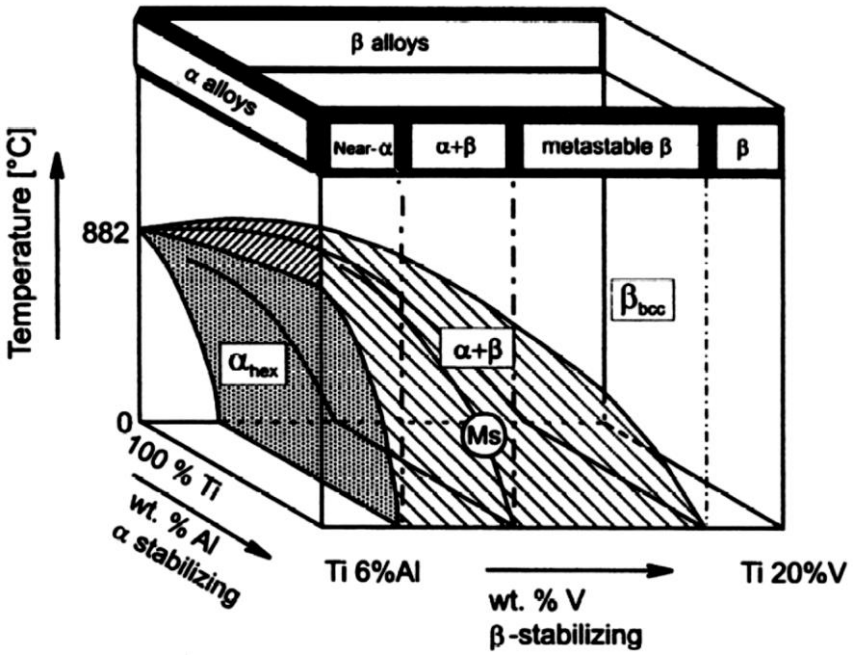

Figure 2: Three-dimensional phase diagram to classify titanium alloys [6]

If the proportion of Beta-stabilizing elements is further increased to a level where Beta phase no longer transforms to martensite upon fast quenching, the alloys are still in the two-phase field and the class of metastable Beta alloys is reached.

Metastable-Beta alloys are usually strengthened by fine omega precipitates but they are usually accompanied by falls in ductility. These alloys can still reveal an equilibrium Alpha volume fraction of more than 50%.

Finally, the single-phase Beta alloys mark the end of the alloying scale of the conventional titanium alloys [6].

2.3. Titanium alloys families

The actual known group of titanium alloys includes more than 100 titanium alloys, but only 20 to 30 have reached commercial status. Among these, the classic and most used alloy is the Ti-6Al-4V and it covers more than 50% of total amount of titanium alloys used in commercial and industrial applications.

Moreover, a good percentage of used titanium (20 to 30%) is composed by unalloyed titanium [6].

When considering unalloyed and alloyed titanium, it is common to group the materials as follows:

- Unalloyed Titanium: there are several grades of unalloyed titanium. The primary difference between grades is oxygen content. Grades of higher purity (lower interstitial content) are lower in strength, hardness and transformation temperature than those higher in interstitial content. Unalloyed titanium is selected for its excellent corrosion resistance, especially in applications where high strength is not required [8]. However, for adjusting the Alpha grain size to a desired level, thermo-mechanical treatment is performed in the Alpha phase field at 200 - 300 °C or even at room temperature [9]. The four important commercially pure titanium Grades, 1 to 4 cover a room temperature tensile strength level from 240 to 740 MPa with a decrease in formability due to the decrease in the ease of twinning. Of these, Grade 1 has the lowest strength level, excellent cold formability and corrosion resistance. It is used for deep drawing applications and as cladding alloy for steel reactors. Grade 2, with tensile strength levels between 390 and 540 MPa, is the most

popular cp titanium grade. Grade 3 is used for pressure vessel applications where higher strength and weight is a concern. Grade 4 has the highest strength of up to 740 MPa and is preferentially used for mountings and fittings [2, 3, 6, 9].

- Alpha and Near-Alpha alloys: they are primarily used in the chemical and process engineering industry due to their excellent corrosion behavior and deformability. As an interstitial alloying element, the oxygen content differs the various commercially pure titanium grades and increases strength with a simultaneous reduction in ductility. Elements like carbon and iron are impurities brought into the alloy via the manufacturing process, only oxygen is intentionally alloyed to reach the required strength levels of commercially pure (cp) titanium grades [6]. The high solubility of the interstitial element oxygen and nitrogen makes titanium unique among metals and creates such problems which are not critical in most of other metals. For example, the heating stage of titanium in air at high temperature results in inward diffusion of oxygen and nitrogen, not only in oxidation but also in solid-solution hardening of the surface, with a surface-hardened zone of "Alpha-case" (or air-contamination layer) formation. Normally, this layer is removed by machining, chemical milling or other mechanical operations prior to placing a part in service in order to avoid the decreasing in strength and ductility caused by the presence of Alpha-case [8].

Alpha alloys cannot be strengthened by heat treatment and, generally, they are annealed or recrystallized to remove residual stresses induced by cold working. They also have good weldability because their low sensitivity to heat treatment and mostly have poorer forgeability and narrower forging temperature ranges than Alpha-Beta or Beta alloys, particularly below at Beta transus [5]. The Ti-8Al-1Mo-1V was the first titanium alloy used for high temperature use but its stress corrosion problems, caused by the high Al contents, limited its applications. As consequence, all conventional titanium alloys in use today are limited in aluminum content to a maximum of 6%. The follow up alloy, Ti-6Al-2Sn-4Zr-2Mo (Ti-6-2-4-2), exhibited that addition of Si up to 0.1% improves the creep behavior because this alloying element would precipitate at high temperatures on dislocations, thus effectively hindering their climb and likewise deformation. Thanks to these studies, all new high temperature titanium alloys have been alloyed with up to 0.5% of Si [6].

Near-Alpha titanium alloys, which contain Al, Sn, and/or Zr inside, are preferred for high temperature applications as well as cryogenic applications since it combines the excellent creep behavior of Alpha alloys with the high strength of Alpha+Beta ones. Their upper operating temperature window is limited to about 500 to 550 °C [6].

If higher strength levels are required, Ti-5Al-2Sn is a good choice, especially in case of hydrogen tanks and pressure vessels [6], while the extra-low-interstitial Alpha alloys (ELI grades) retain ductility and toughness at cryogenic temperatures and, again, Ti-5Al-2.5Sn ELI has been used extensively in such applications [8].

- Alpha-Beta alloys: they contain one or more Alpha stabilizers or Alpha-soluble elements and more Beta stabilizers. After solution treatment, these alloys retain more Beta phase than near-Alpha alloys, with a specific amount depending on the quantity of Beta stabilizers present and on the heat treatment [5].

Alpha-Beta alloys can be strengthened by solution treating, which is usually done at a temperature high in the two-phase field and is followed by quenching in water, oil, or other soluble quenchant, and aging to precipitate Alpha and produce a fine mixture of Alpha and Beta phases in the retained or transformed Beta one. The specific response of Beta transformation depends on alloy composition, solution-treating temperature, cooling rate and section size [5]. Solution treating and aging can increase the strength of Alpha-Beta alloys from 30 to 50% (or more), over the annealed or over-aged condition, with a response depending on section size; alloys relatively low in Beta stabilizers [8] have poor hardenability (increasing with the content of Beta stabilizer) and must be quenched rapidly to achieve significant strengthening. The strength that can be achieved by heat treatment is also a function of the volume fraction of Beta phase present at the solution-treating temperature. All these considerations mean that, in order to produce the desired mechanical properties in the final product, alloy composition, solution temperature, and aging condition must be carefully selected. For example, Ti-6Al-4V alloy was developed with the aim of specific uses in the aerospace industry, and also used in reaction vessels, heat exchangers and gas compressors. Other Alpha+Beta alloys like Ti-6Al-6V-2Sn and Ti-4Al-4Mo-2Sn-0.5Si (IMI 550) were primarily developed for high strength. High strength and high toughness is realized with Ti-6Al-2Sn-4Zr-6Mo (Ti-6-2-4-6) [2-4, 6].

- Metastable Beta alloys: they are richer in Beta-stabilizers and leaner in Alpha stabilizers than Alpha+Beta alloys. Depending on the amount of Beta stabilizing

elements, Beta alloys can be retained in a mestable form upon cooling to room temperature at moderate to high cooling rates which means that no Alpha precipitation is taking place during cooling [4]. Processing of these alloys usually consist of a hot working operation, which is normally performed in the Alpha+Beta phase field for the leaner Beta alloys and preferentially in the Beta field for the richer Beta alloys, followed by a heat treatment consisting of a solution treatment followed by quenching and a subsequent aging treatment. Above the Beta transus temperature, a solution heat treatment causes a coarsening of the Beta grains and the temperatures below the transus leads to the precipitation of primary Alpha (αP). The heat treatment temperature controls the volume fraction of primary Alpha, while the thermo-mechanical treatment leads to a globular microstructure and, again, without any treatment a needle-like primary Alpha shape is formed. All these complex microstructural properties allow this class of alloys have excellent forgeability and can be hardened to extremely high strength levels of more than 1400 MPa and high toughness [1].

Proper selection of temperatures and deformation are the parameters, which controls the Beta grain size and size distribution. Moreover, during thermo-mechanical treatment, a film-like Alpha precipitation occurs on the grain boundaries and, by rapid cooling from the Beta phase field, the precipitation of this boundary Alpha can be prevented for small sections [1]. It is possible to avoid this film-like Alpha precipitation by obtaining a bi-modal microstructure similar in the Alpha+Beta alloys or creating a necklace type of microstructure [4].

At lower temperatures (from 400 to 600 °C), secondary Alpha precipitates finely distributed homogeneously or inhomogeneously, depending on being in lean Beta alloys or in richer alloys, respectively. The volume fraction and size of the secondary Alpha can be controlled by varying the aging temperature, time and solution treatment temperature. Also in lean alloys, precipitation of coherent ω phase can be seen at low temperatures which may cause embrittlement, while higher Beta stabilizing element forms intermetallic compounds [1].

The advantages of metastable Beta alloys in comparison with Alpha-Beta alloys are their density, lower creep strength, and lower tensile ductility in the aged condition. A good example is given by Ti-5Al-4Mo-4Zr-2Sn-2Cr (Beta-CEZ) developed in France,

Japanese alloy Ti-4.5Al-3V-2Fe-2Mo (SP 700) and Ti-10V-2Fe-3Al (TIMETAL 10-2-3) [2, 3, 6, 7, 10].

2.4. Phase transformations

Upon cooling from the Beta phase field of titanium, the most densely packed planes of the BCC Beta phase transform to the basal planes of the hexagonal Alpha phase by a nucleation and shear type process.

Martensitic transformation results in a microscopically homogeneous transformation of the BCC into the HCP crystal lattice, with a cooperative movement of atoms. It has two different crystal structures, formed by quenching of the BCC Beta phase of pure Ti and dilute Ti-alloys when the martensite start temperature (Ms) is crossed: the hexagonal martensite, which is designated α', and the orthorhombic martensite, which is designated α". Among them, the most prevalent type is α', which can occur in two limiting morphologies: massive or lath martensite (when high purity Ti and very dilute alloys, Alpha or near-Alpha alloys are used) and acicular martensite in alloys with slightly higher solute contents (lower Ms temperature), which occurs as an intimate mixture of individual Alpha plates. In the case of alloys with high Ms temperatures (Alpha or near-Alpha alloys), martensite occurs as colonies of parallel-sided platelets. The orthorhombic martensite α", which is characterized by good deformability, seems to occur mainly in Ti-alloys with Beta stabilizers of the transition metals Mo, Nb, Ta, W, Re and in Ti-alloys with Al + V. The lattice parameters of α" are strongly dependent on solute content, and the α" crystal structure is sometimes conveniently viewed as a distorted hexagonal structure. The change in morphology and internal substructure in the martensite is not dissimilar to that which occurs in ferrous alloys with increasing carbon or austenite stabilizing alloying element content. According to the martensitic transformation, strength is slightly increased compared to α titanium [4, 6, 10, 11].

In some of Alpha+Beta and Beta alloys, the occurrence of face centered orthorhombic (FCO) and FCC martensite was observe [10]. The FCO martensite seems to have the morphological characteristics of s twinned hexagonal martensite and the presence of interstitials results in the distortion from the hexagonal to the FCO structure by a similar

mechanism to the BCC to BCT (body-centered tetragonal) distortion which arises from interstitial carbon in martensite in steels. As a result of strain, martensite may be induced in the metastable Beta for alloys in which Ms is very low and Mf above room temperature [10]. On the other hand, the FCC martensite is not apparently related to the hexagonal or FCO types, but it occurs only on quenching from a temperature range low in the Beta field in Alpha+Beta alloys and it may arise from a relaxation of stresses in the metastable Beta in thin section or as a result of hydrogen contamination during electro-polishing.

In Ti-alloys with intermediate solute contents, the decomposition of the Beta phase occurs at sufficiently low cooling rates from the single β phase field into the Alpha+Beta field as a nucleation of Alpha at Beta grain boundaries and subsequent diffusion controlled growth into the retained Beta phase. The resulting microstructure is called Widmanstätten α and it consists of colonies of parallel Alpha plates having the same crystallographic orientation, which belongs to a single variant of the Burgers orientation relation with regard to the parent Beta matrix, and those are separated by plates of the retained Beta phase. Those Ti-alloys having a good amount of Beta stabilizer, which have lower transformation temperature or increased cooling rate, exhibit progressively smaller colonies, fewer platelets and appear to nucleate independently of the Beta grain boundaries. The characteristic basket-weave microstructure forms by the distribution of these smaller colonies over all possible variants of the Burgers orientation relationship [4, 12, 13]. The Widmanstätten platelets are surrounded by Beta-stabilizing elements enriched layers of the retained Beta phase, which occur as the result of rapid diffusion of these elements at or ahead of the migrating interface. The cooling rate and alloy content control the thickness and continuity of the retained Beta layers, which form a continuous network (~ 0.2 μm thick) around the Alpha platelets in the Alpha+Beta alloys. On quenching, such layers may also occur with a lesser extension and this Alpha phase transformation may be more correctly described as bainite structure [10, 13, 14].

In the case of solution treating, the alloy in the Alpha+Beta field gives a duplex structure with Beta-stabilizing alloying elements segregation and phase proportions given by the pseudo-binary equilibrium diagram. Upon cooling, the Beta phase transforms into martensite or Widmanstätten α as before or (if it is sufficiently enriched, i.e. for low solution treatment temperatures) is retained at room temperature [10].

All previous microstructural transformations have the substantial meaning of influence on the mechanical properties of the obtained material, which can be properly designed by varying and controlling the degrees of freedom of thermo-mechanical treatments, which perturb or alter the transformation mechanisms. In addition, each alloy class and type needs different controls of nature and degree of microstructure obtained [15]. For conventional titanium alloys, the size and arrangement of the two phases Alpha and Beta describes the microstructure. The two extreme cases of phase arrangements are the lamellar and the equiaxed microstructures that have a fine as well as a coarse arrangement of their two phases, with the lamellar case generated upon cooling from the Beta phase field, and equiaxed one resulting from a recrystallization process [2, 3, 6, 7, 10]. In most of the commercially important titanium alloys, the mechanism of the Beta phase during cooling dominates the development of titanium microstructure [15].

Thermo-mechanical treatments generates different microstructures as a complex sequence of solution heat treatment, deformation (by hot rolling or forging, extrusion or spinning), recrystallization, aging, and annealing for stress relief as schematically outlined in (Figure 3).

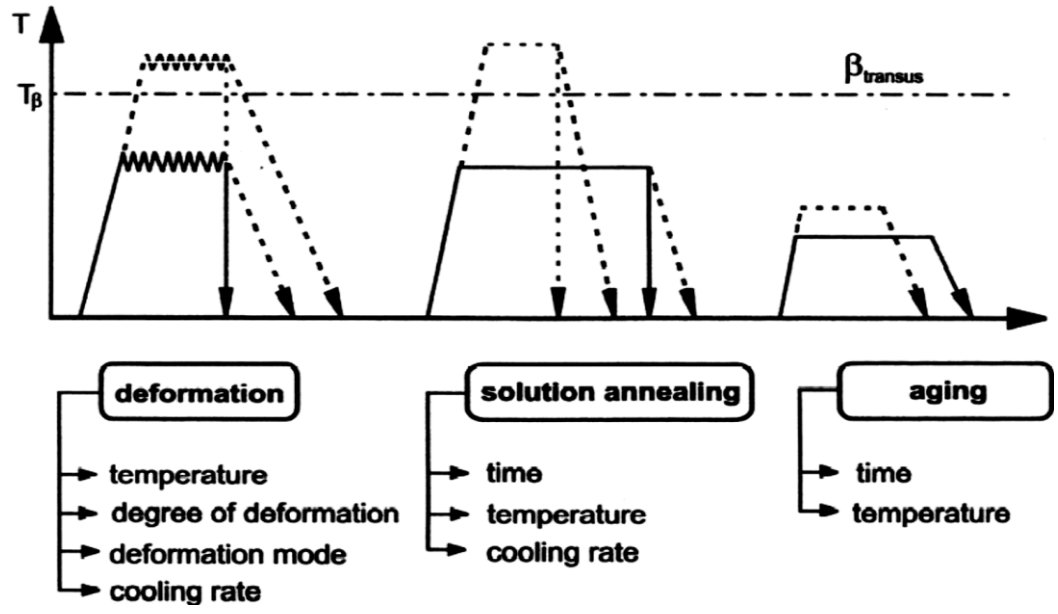

Figure 3: Thermo-mechanical treatment of titanium alloy [6]

To achieve the desired microstructure, controlling the deformation rate at any particular temperature is important because the principal effect of working is to alter the

morphology of the primary Alpha phase, which is formed by nucleation and growth in the early stages of working and by subsequent plastic deformation during subsequent working, leading to a recrystallization and globularization of Alpha. Both the amount of plastic work, strain rate and temperature are important on the modification of morphology of Alpha phase. The strain rate and temperature are critical because of a dynamic competition between in situ recovery and the plastic work storage, which will subsequently drive the recrystallization reaction. The occurrence of this recovery reaction means that there is not usually a unique combination of temperature and time to produce a given microstructure [15, 16]. By forging in the Alpha+Beta phase field, the prior Beta grain size may also be refined [10]. On the other hand, the presence of the texture in most of the hot worked products should be mentioned. The texture to be expected due to TMT is not only very sensitive to working temperature and amount of strain, but is also very sensitive to working methods [15].

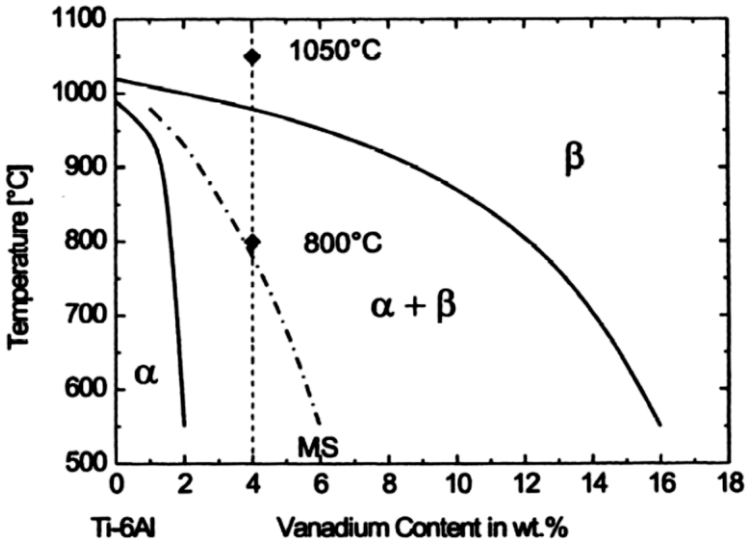

Figure 4: Schematic ternary phase diagram of Ti-6Al [6]

The slower kinetics of nucleation and growth reaction, due to higher amounts of Beta stabilizing elements, result in a competition between heterogeneous nucleation of Alpha at prior Beta grain boundaries and intragranular nucleation of Alpha.

The grain boundary Alpha, which is a general result of this competition, has a deleterious effect on properties. As previously explained, the thermo-mechanical treatment causes the acceleration of the nucleation and growth kinetics for intergranular

Alpha nucleation, while mechanical working makes the grain boundary Alpha less continuous and less deleterious to properties by breaking up and recrystallizing it [17]. Looking at the diagram (Figure 4), the Beta-transus temperature, which separates the single Beta phase field from the two phase Alpha+Beta field, is a central point for thermo-mechanical treatment [6].

It is important to understand the competition between the nucleation and growth of Alpha phase and the martensitic decomposition of the Beta phase [17].

2.5. The Ti-6Al-4V alloy

One of the most widely used titanium alloy is the Ti-6Al-4V, which has the greatest commercial importance in the various industries and applications and is being responsible for more than 50% of titanium output in the world. It is an Alpha-Beta type, with 6 wt% aluminum stabilizing the Alpha phase and 4wt% vanadium stabilizing the Beta phase, developed in 1950 in the United States at the Illinois Institute of Technology [5, 18, 19].

In Ti-6Al-4V, addition of aluminum partitions selectively to the Alpha phase and forms solid solution strengthening in the alloy. The Al concentration is usually held to 6 wt% or less in titanium to prevent secondary Alpha phase and results in decreasing of ductility, toughness and stress corrosion cracking. The V is not very soluble in the Alpha phase and is rejected from Alpha phase so that it is concentrated in small regions of the Beta phase throughout the predominantly Alpha matrix [7, 14]. In fact, it was found that Al content decreases from the center of the Alpha phase through Beta phase, while V content increases along the same direction because of a Beta-stabilizing element [14].

Because the boundary migration of these two phases requires extensive amount of diffusion, this two-phase mixture is stable with respect to coarsening. As a result, Ti-6Al-4V exhibits relatively fine microstructures and addition of Beta-stabilizing element such as V serves solid solution strengthening in the Beta phase and by refining the microstructure, overall alloy strengthening is established.

In order to produce refined martensitic or diffusionally controlled transformation products at subsequent cooling, the grain size should be as small as possible [20]. Ivasishin and Teliovich [20] compared steels and titanium alloys according to the grain

size. They explained that titanium alloys has behaved different from steels due to the formation of fine Beta microstructure. Transformation to a single-phase Beta has developed by a movement of the Alpha/Beta boundaries until the Beta phase becomes the only phase present. Unless faster heating rates were applied, the immediate grain growth would occur after the dissolution of primary Alpha phase. And also, Beta grain size could not be reduced by subsequent heat treatments if coarse Beta grain microstructure once formed. For rapid heating of the coarse-grained titanium alloys, which recovers by the end of transformation no further change in grain, size has taken place above the Beta-transus. The kinetics of grain growth depends on the particular chemistry of the high temperature phase, such that grain growth inhibiting elements content in solid solution or in the form of precipitates [21]. Again, during heating from room temperature to the Beta transus, the Beta phase in Ti-6Al-4V grew epitaxially from the pre-existing Beta phase, rather than to nucleate new Beta [22].

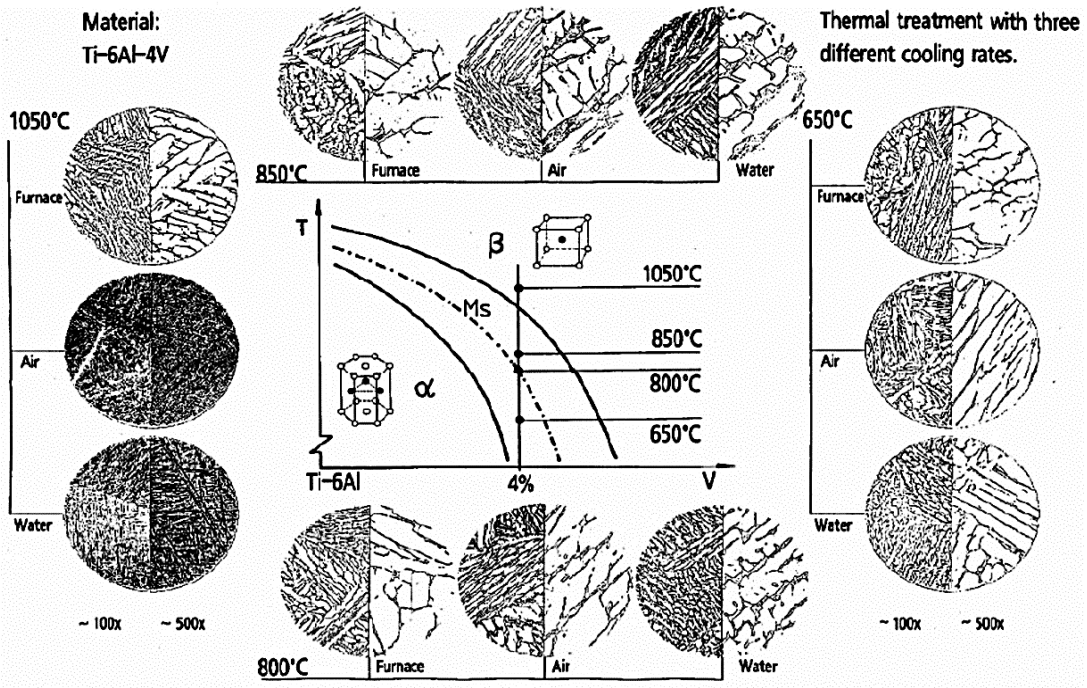

Figure 5: Influence of thermal treatment and cooling rate on the microstructure of Ti-6Al-4V alloy

Therefore, the texture formed during deformation would be modified by grain growth from pre-existing Beta orientations in the starting material during continuous heat treatment, and it also reported that the peak grain size was strongly dependent on the peak

temperature and heating rate [23]. Lower heating rates and higher peak temperatures gave rise to coarser grain sizes did the similar work under isothermal heat treatment and, found that Beta grain growth under isothermal annealing conditions was strongly affected by initial texture in materials and did not have a constant grain growth exponent and activation energy [24].

The microstructure of Ti-6Al-4V has various types and depends on the cooling rate from the Beta phase field, prior heat treatment and the chemistry [6, 14, 18] (Figure 5).

The micro constituents and microstructures are divided into grain boundary allotriomorph Alpha, globular or primary Alpha (called bi-modal microstructure when the globular Alpha is surrounded by Widmanstätten platelets), Widmanstätten, basketweave, and martensitic according to the phase transformation of Beta/Alpha [18]. Also the bi-lamellar microstructure is recently described, in which the soft, single phase Beta lamellae, lying between the Alpha platelets in a Widmanstätten structure, are hardened by fine Alpha plates [12]. At room temperature, the microstructure at equilibrium consists mainly of the Alpha phase (HCP) with some retained Beta phase (BCC) [18] and Beta phase is stabilized as a result of vanadium enrichment [11].

When Ti-6Al-4V is slowly cooled from the Beta phase region, formation of Alpha phase is seen below the Beta-transus temperature. As result of the decomposition of Beta phase by a nucleation and growth mechanism, the structure of Alpha which is formed are the grain boundary allotriomorph Alpha and Widmanstätten Alpha-plates or laths which consist of the sets of parallel plates with a crystallographic relationship to the Beta phase. These Widmanstätten plates often nucleate at the Alpha-allotromorphous and grow towards the matrix with sharp and straight surface relief, which all have a lenticular shape. When the cooling rate increases, these plates become thinner and plate size increases when the cooling rate decreases. Also, the decrease in the cooling rate results the formation of Alpha phase nucleated in the matrix by the ease of alloy element arrival to the nucleation sites in the Beta matrix. From an allotriomorph Alpha phase point of view, there is a certain decrease in size of the phase when the cooling rate increases because of a bigger diffusivity in lower cooling rates [14]. It was observed that grain boundary Alpha phase and homogeneously nucleated Alpha phase within the Beta grains in Ti-6Al-4V and Ti-6-2-4-2 alloys [25], and upon cooling from the Beta homogenization field down to 900 °C only the formation of grain boundary Alpha occurred after isothermal exposure

at that temperature. However, when the undercooling increased further, some portions of the Alpha phase nucleation and growth within the Beta grains was observed in addition to the grain boundary Alpha phase again after isothermal exposures. Also, it was observed that the retained Beta phase after slow cooling in the furnace [11] showed different precipitation temperatures of alloying elements of the Alpha phase and the different amounts of the phases during slow continuous cooling. When different annealing temperatures are used, the increase in the annealing temperature caused the Alpha plate thickness increase and lower cooling rate produced thicker Alpha plates than air cooling from the same annealing temperature [26]. Additionally, the decrease in the annealing temperature upon air cooling has caused a decrease in the volume fraction of acicular Alpha and Beta phases and an increase in the primary Alpha, whereas that was not seen in the furnace cooling condition which was full of primary Alpha. Moreover, the water quenching exhibited a higher hardness values than air cooling and furnace cooling which had the lowest value (Figure 6).

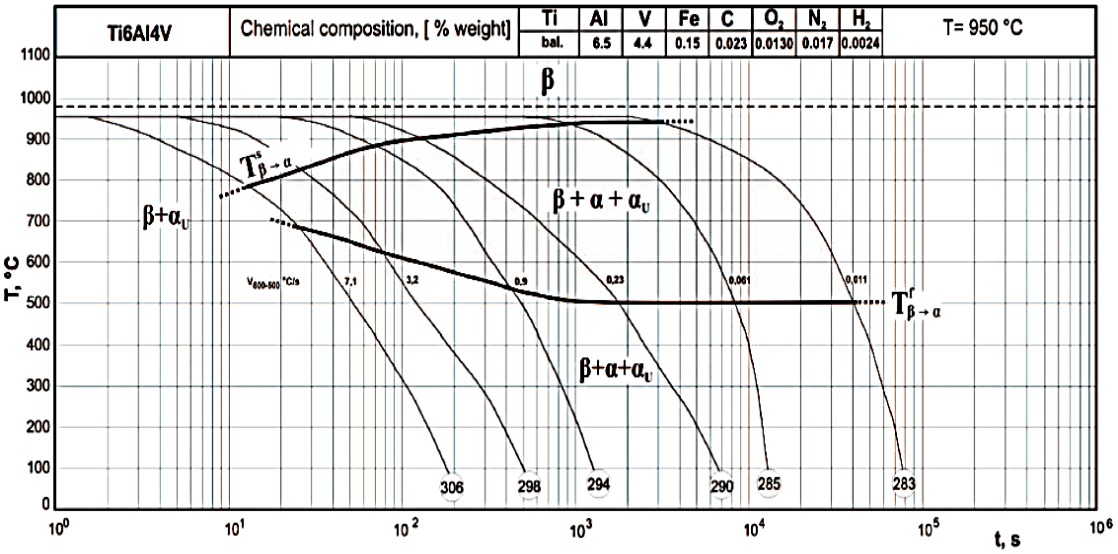

Figure 6: CCT diagram of the Ti6Al4V alloy

Lütjering [27] described the microstructural constituents of fully lamellar Alpha+ Beta titanium alloys as large equiaxed Beta grains, continuous Alpha layers at Beta grain boundaries, the Alpha colony size and the size of individual Alpha lamellae. These types of microstructures are formed according to the scheme showed below (Figure 7). After deformation either in the Alpha+Beta phase field or in the Beta phase field, a

homogenization treatment is applied in the Beta phase field. The final microstructure and the extent of Alpha-layers at Beta grain boundaries depend on the cooling rate from the homogenization temperature. There is no alloying element partitioning effect is present in the fully lamellar microstructures, so only aging treatment or stress relieving treatment is applied after step I [12, 27].

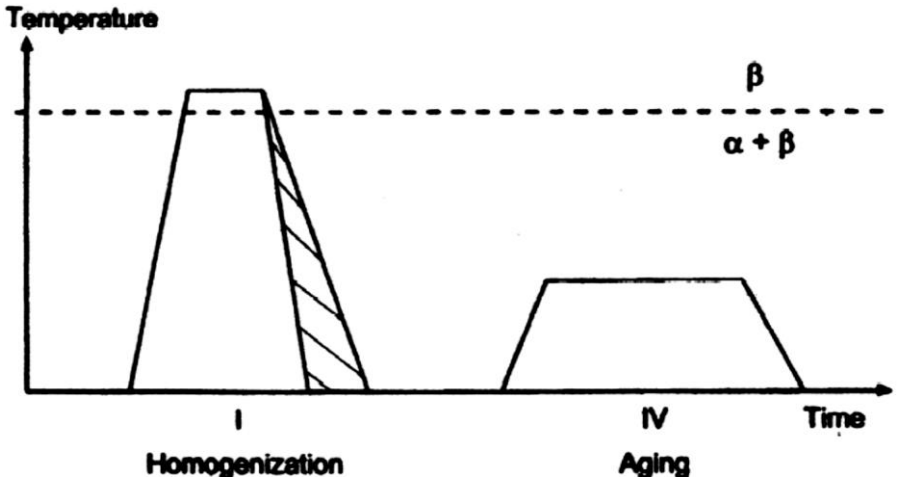

Figure 7: Processing route for fully lamellar microstructure [27]

Fujii [21] found that the Alpha phase first precipitated at the grain boundaries of the Beta matrix and by depending on the temperature drop, the growth of the side-plate Alpha phase was observed from the grain boundary Alpha phase into the Beta matrix. This side-plate Alpha nucleation has been observed in transgranular or heterogeneous form, according to the high or low degree of undercooling, respectively. In this transformation behavior, the Beta stabilizing element Vanadium has an important role by concentrating near the grain boundary Alpha phase during its formation. These results were obtained after solutionization at 1050 °C at 20 min. , rapid cooling to between 800 to 850 °C (in the Alpha+Beta region), holding there for different time intervals and helium gas quenching from those temperatures.

Ahmed and Rack [28] applied Beta solution treatment at 1050 °C for 30min. and ending the treatment with water or helium gas quenching to minimize oxidation. They obtained different microstructures at varying cooling rates. At 525 °C/s, they had hexagonal α' martensite but at 410 °C/s, a second Alpha morphology (massive Alpha) was observed for Ti-6Al-4V which had a blocky appearance and a hexagonal crystal

structure (acicular α' martensite) with a heavily dislocated internal substructure under TEM analysis. At cooling rates slower than 20 °C/s two different types of grain boundary Alpha obtained; type 1 having weaved appearance nucleated near or at the prior Beta grain boundary and type 2 conventional appearance seemed to have grown from the normal grain boundary Alpha layer, and at the lowest cooling rate (1.5 °C/s), the formation of the grain boundary Alpha was seen where the intra-granular microstructure was full of classical basketweave Widmanstätten morphology. Therefore, they suggested that for fully martensitic microstructure, higher cooling rates than 410 °C/s should be applied otherwise, a massive transformation might be observed.

Gil et. al. [29] used different temperatures, varying time intervals and cooling rates in the tubular furnace under argon atmosphere. Their results showed that the grain size increase took place when the temperature increased with time (mostly first 15 min. of the treatment) at a very fast rate to a point where grain boundary area per unit volume ratio and the interfacial energy per unit volume decreased. This means driving force for grain growth was lower. By using the solute drag theory, they explained the grain growth as a faster movement of the boundary by the diffusion of solute elements behind the boundary because of the phase transformation. The grain size effect on Beta to Alpha transformation indicated that the larger Beta grain size has produced the smaller Alpha Widmanstätten plate width, which was the result of the decrease in the starting temperature of the Beta to Alpha transformation. They gave brief explanation about the transformation and formation of Widmanstätten Alpha phase, which has been the continued transformation of nucleated Alpha phase by growth and coarsening as needles or plates within the Beta grains. They evaluated the Al and V content in the center of the plate and radially outwards at different distances by means of an analytical microscope and found that vanadium content has increased from the center through the Beta phase. And also opposite to V, Al content decreases along the same direction. These Widmanstätten plate sizes have increased due to decrease in the cooling rate because of bigger diffusivity at lower cooling rates. At low cooling rates, they found that Alpha phase nucleation occurred in the matrix while the Alpha Widmanstätten has been growing by the ease of atom movement in the matrix. If the cooling rate increased, the Widmanstätten colony size would decrease which was the reason of strength difference between the

matrix and the coarser Alpha-layer present at Beta grain boundaries causing preferential plastic deformation [14, 29].

Filip et. al. [30] studied on fractographic examinations in Ti-6Al-4V and Ti-6Al-2Mo-2Cr alloy systems. Their results showed that large grain size displays intergranular fracture faces with dimensions corresponding to the grain size and for the fine grained structure the grain boundary fracture was reduced due to the increase in the cooling rate.

Sha and Guo [31] found that at 970 °C, firstly the transformed Beta phase, which contains less vanadium than equilibrium demands, transformed to high temperature Beta phase, and whole microstructure had transformed into Beta phase when the temperature reached to 1010 °C by using differential scanning calorimetry (DSC) technique to a system which has transformed Beta phase and blocky Alpha phase. The blocky Alpha phase could not transform until the temperature high enough because of the stability of the phase gained by less Beta stabilizing element vanadium and more Alpha stabilizing element aluminum content. They concluded that transition of primary Alpha phase to Beta phase has started after the transition of transformed Beta phase to high temperature Beta phase has completed.

Stanford and Bate [22] also used phase transformation experiments on Ti-6Al-4V. However, they tried to emphasize on the variant selection of the transformed structure by using Scanning Electron Microscopy (SEM) and Electron Backscatter Diffraction (EBSD). The variant selection was explained in their study as the occurrence of the individual orientation (or variants) more frequently than the other under certain conditions. To observe the selected variants and the textures exactly which were seen in the alloy system, they used furnace cooled and slow cooled samples. They concluded that diffusional transformation exhibited strong preferred orientation. Nevertheless, if there was no relationship between the adjacent Beta grains, there could be any number of variants produced on either side of the boundary. In addition, they showed that those possible variant selections had an effect of grain boundary Alpha formation and found that grain boundary Alpha precipitation could be prolific and did not form from one growing nucleus. They explained that because of nucleation occurred just below the Beta-transus, partitioning of the vanadium ahead of the transformation front was inhibited by rapid growth of the Alpha, which prevented the retention of the Beta layer around the grain.

This result is nearly matching to the Fujii's [21] study about continuous cooling transformation of Alpha + Beta alloys for grain boundary Alpha formation point of view. Stanford and Bate [22] determined that the Widmanstätten Alpha plates chose an orientation according to the Burgers relationship during growth was initiated from the grain boundary and the c–axis of the Alpha was said to be adopted that same orientation.

The fully lamellar structure is turned into the bi-modal (duplex – globular or primary Alpha) microstructure by thermo-mechanical treatment, which is firstly deformation of lamellar structure and then recrystallization in the Alpha + Beta phase field and cooling down to room temperature as described by Lütjering studies in (1998) and (1999) [12, 27]. He figured out the formation of the microstructure by a four step process, which are homogenization in the Beta phase field (I), deformation in the Alpha + Beta phase field (II), recrystallization in the Alpha + Beta phase field (III), and aging at lower temperatures (IV), shown below (Figure 8).

For step I, the cooling rate from the homogenization temperature determines the width of the Alpha-lamellae in the lamellar structure within the Beta grains and the extent of the continuous Alpha-layer at Beta grain boundaries.

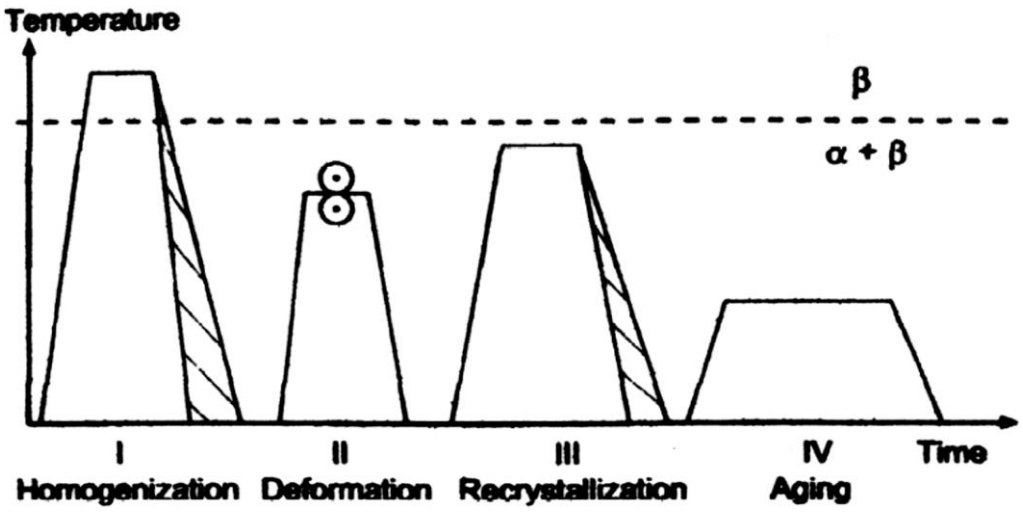

Figure 8: Processing route for bi-modal (duplex) microstructures [27]

Although the homogenization temperature is kept low, and the homogenization time as short as possible, the Beta grain size is always fairly large (≥ 500 μm). By the step II, to introduce enough dislocations, preferably high amounts of plastic deformation is

applied in the Alpha+Beta phase field for obtaining complete recrystallization of the Alpha and Beta phases during step III. Moreover, during the deformation process, crystallographic textures in the hexagonal Alpha phase and in the bcc Beta phase can develop.

The texture type depends on the deformation temperature. If the deformation temperature is low, which means high volume fraction of Alpha phase is present, an Alpha-deformation texture develops, and if the temperature is high, which means high volume fraction of Beta phase presents, a Beta-deformation texture develops. Also, there will be no significant change occurs in the textures of the hexagonal Alpha during recrystallization. For recrystallization step III, the temperature and the cooling rate from the recrystallization temperature are important parameters, which determines the volume fraction of recrystallized equiaxed Alpha located at the triple-points of the recrystallized equiaxed Beta grains and the width of the individual Alpha lamellae as well as the Alpha colony size of the lamellar structure formed during cooling within the equiaxed Beta grains, respectively. If the cooling rate from the recrystallization temperature is sufficiently low, no Alpha lamellae are formed and only the equiaxed Alpha grains will grow within the Beta grains resulting in a so-called globular structure with the equilibrium volume fraction of Beta grains located at the “triple-points of the Alpha grains. The maximum Alpha colony size is limited by the Beta grain size, which is the combination of equiaxed Alpha volume fraction and equiaxed Alpha size [12]. The effect of alloy element partitioning upon separation into equiaxed Alpha and Beta, the Alpha lamellae formed during cooling from the Beta phase have a lower concentration of elements (especially oxygen), which are promoting age-hardening by formation of coherent Ti3Al particles in aging step IV. In this step, temperature is more important that time because the occurrence of the Ti3Al particles depends on the being either below or above the Ti3Al solvus temperature [12].

Lütjering [27] explained the main differences of bi-modal microstructure and the lamellar structure as the limited Alpha colony size and the maximum length of Alpha-lamellae as well as the effective length of grain boundary Alpha-layers by small Beta grain size. The lamellar grains in the bi-modal structure are softer than the fully lamellar structure. When the cooling rate increases, which is higher than a furnace cool treatment, the Alpha colonies become progressively smaller, exhibit fewer platelets, and appear to

nucleate independently of the Beta grain boundaries. The characteristic microstructure, basketweave structure, forms by the distribution of these smaller colonies over all possible variants of the Burgers orientation relationship [9, 26].

During decomposition of Beta phase by a diffusionless process, known as martensitic transformation, α' martensite forms, which is a metastable fine plate-like, or acicular microstructure, at temperatures below. Different types of martensite may form, hexagonal α' martensite or orthorhombic α" martensite, depending upon the alloy chemistry and the quenching temperature. Some retained Beta may also be present in the structure because of the martensite end temperature, which is below room temperature. For Ti-6Al-4V, because V is a Beta stabilizer, the addition of 4% V to a Ti-6% Al alloy is sufficient to place the Mf below room temperature. Thus, upon quenching, some Beta phase may not be converted to α' or α". Because the α' martensite has a similar orientation relationship to Beta as that of Alpha, the martensitic microstructure is therefore also characterized by a very fine basket-weave structure with needle-like character due to its diffusionless nucleation process [5, 6, 14]. These results were consisted with the work of Malinov et. al. [11]. They also obtained α' martensite and no retained Beta phase during fast cooling conditions above from transus temperature in Ti-6Al-4V alloy system and quenching from 850 °C and continuing with aging between 600 and 700 °C gave them small changes in the diffraction pattern which were orthorhombic martensite (α"). Although the intensities of the α" martensite reflections were increased while increasing the treatment time at these temperatures, this microstructure were not seen at higher temperature (800, 900 and 1000 °C) treatments. Zeng and Bieler [19] reported the decomposition of α' martensite into α" during aging as decomposition of Beta phase precipitated from the decomposition of α' martensite into the α" and Beta-rich phases. The transformation of α' into α" and Beta was thermodynamically unfavorable, because of the higher principle lattice strain between α' and α" than between α' and Alpha due to the small lattice difference between α' and Alpha phases, they described the transformation as written above. In addition, after one year natural aging, they could not observe the appearance of α" and Beta phases which were all transformed into Alpha. Also, at the beginning of the experiments (quenching from 920 °C), they had no α" martensites or retained Beta phases which were found from the TEM and X-ray analysis.

Similar to the study of Malinov et. al. [11], Jovanović et. al. [26] did not observe retained Beta phase upon fast cooling conditions with an exception at 1050 °C quenching case. In this case, the presence of small amount of the Beta phase was detected in the diffractogram and this was explained due to the lower values of martensite finish temperature for this alloy. According to the X-ray analysis, a decrease in the annealing temperature caused a decrease in the intensity of α' martensite reflections indicating the decrease of the α' fraction, whereas an increase in the amount of the primary Alpha phase.

Filip et al. [32] had studies on the aging of the metastable phases which had effects on the mechanical properties. They showed that at higher ageing temperatures, the process of metastable phase decomposition became faster and the size of Alpha lamellae colonies and the thickness of Alpha-lamellae was increased and growth of equiaxial Alpha phase grains took place.

3. The forging process

Forging is a manufacturing forming process that involves applying compressive forces to a work piece to deform it, and create a desired geometric change to the material. Forging, similar to other forming processes, effects the properties of the material of the forged product. Specifically, forging can strengthen the material by eliminating cracks and empty spaces within the metal.

Forging a metal will also alter the grain structure with respect to the material flow of during its deformation. The forging process represents an optimum way to create favorable grain structure in a material greatly increasing the strength of forged parts. For these reasons, forging manufacture gives distinct advantages in the mechanical properties of work produced, over that of parts manufactured by other processes such as casting or machining.

Metalworking is one of the most important and ancient technologies, with the casting, used to make metal products. There are proofs describing the simple metalworking of gold and copper in various regions of the Middle East of Europe around 8,000 B.C.

The forming process of these materials was rudimentary due to the state of the art of refining of that period and the capabilities to remove impurities were limited. After 4,000 B.C., it was discovered that the hammering of crude metals allowed to obtain increased mechanical properties (the so-called strain hardening).

Most of metalworking methods were done by hand until the 13th century. At this time, this kind of manufacturing process was used primarily for forging bars and plates or, however, objects having a simple shapes. The hammering machines used water power to raise a lever arm that had a hammering tool at one end; it was called a tilt hammer because the arm tilted as the hammering tool was raised. After raising the hammer, the blacksmith let it fall under the force of gravity, thus generating the forging blow. This relatively simple device remained in service for a long period.

During the Industrial Revolution, the demand of metal products made with iron and steels was increased so the most of production process were revised to satisfy the customers, in particular forging equipment having a larger capacity. This aim was reached thank to the invention of the high-speed steam hammer and the hydraulic press in which

the force is supplied by hydraulic pressure. From such equipment came products ranging from firearms to locomotive parts. Similarly, the steam engine spurred developments in rolling, and in the last two centuries, a great variety of steel products rolled in major quantities.

The materials that have benefited from such developments in equipment range from low-carbon steel used in automobiles to special applications materials like aluminum, titanium, and nickel-base alloys. In the last two decades, the quality of formed products and the efficiency of production lines were increased by mean of mathematical analyses and instruments. This road was strongly supported thank of the evolution of the electronics and computer science which allowed to decrease the cost of the hardware apparatus.

3.1. Forging and forming mechanism of materials

The enforceability of the process strongly depends on the mechanical properties of the material to forge, especially the ability to undergo great deformations.

The mechanism of plastic deformation is more common in mono-crystal is the sliding movement of a block of atoms on a surface on which exceeds a critical value of shear stress (Figure 9).

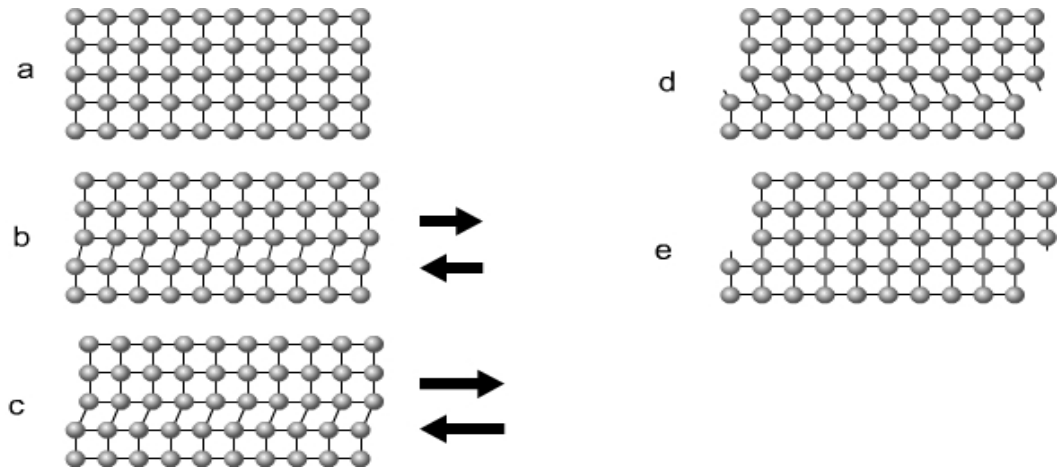

Figure 9: Atomic plane sliding movement sequence after a shear force is applied

The sliding is a multiple of the interatomic distance so that the critical stress value is directly proportional to the interatomic distance and inversely proportional to the distance between the sliding planes: therefore, scrolling occurs on plans having maximum atomic density and the direction of a maximum atomic density. The consequence is that the single crystal has an isotropic behavior. The difference between the theoretical and experimental values of forces necessary to cause plastic deformation has been explained using the theory of dislocations, which are defects in the crystal lattice structure.

In the case, for instance, of a dislocation edge (Figure 10) the sliding of one part of the lattice with respect another is caused by a shear stress less than case without defect, due to a lower number of interatomic bonds to break. At the same time, the dislocation moves along the sliding plane.

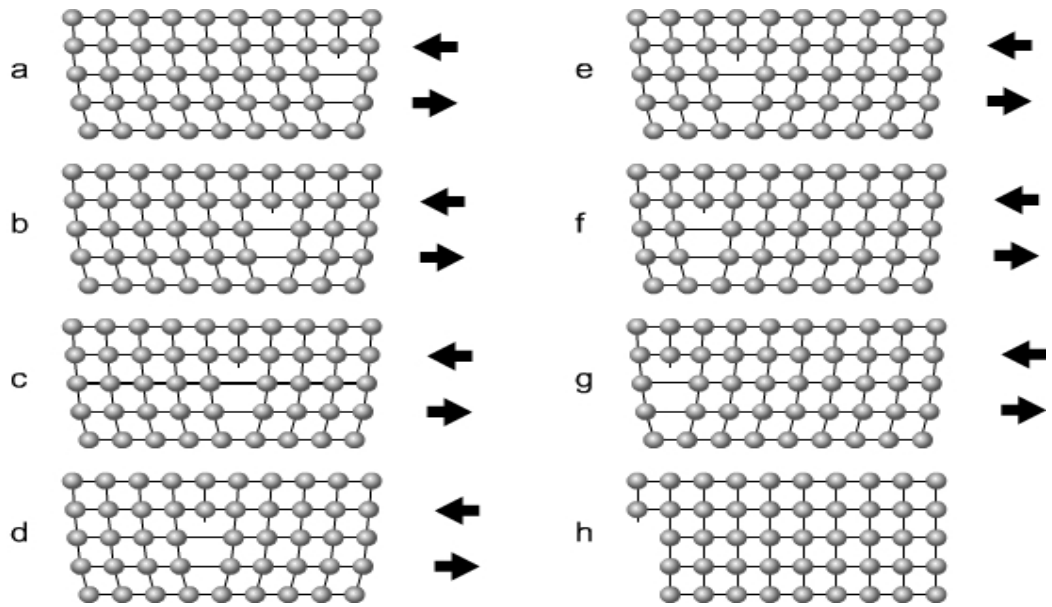

Figure 10: Sliding movement of a dislocation through a crystal grain

In the common case of poly-crystals, the movement of blocks of atoms does not take place at the same time but it starts from those crystal grains where the sliding surfaces have a favorable orientation with respect to the applied force. However, the surrounding grains limit the sliding with planes unfavorably oriented for which the reaching of the critical stress needs a greater force. The consequence is that not all of the crystalline grains undergo the same deformation.

At high temperatures, the plastic deformation takes place also for sliding on the edge of the grains. Another important aspect is that a poly-crystal, undergoing a plastic tensile or compressive deformation, shows a deformation of the grains which become elongated.

This condition makes the material anisotropic (crystallographic anisotropy). Furthermore, the impurities to the grain boundaries are aligned with the direction of the applied traction force (fibrousness).

During plastic deformation, the dislocation density strongly increases, nevertheless generating elastic tension fields such as to prevent further movement. These tensions also cause the bending of the plans involved by creep phenomena and the other adjacent planes so that, little by little, the whole mass of the crystal is distorted [33]. Therefore, with the progress of deformation, sliding can occur only on those plans requiring a greater tangent tension. This is the hardening phenomenon, which increases the tension-elongation curve in the plastic range. A further consequence is the increase of internal energy of the crystal. Other causes making difficult the propagation of dislocations in poly-crystals are the grain boundaries and the different orientation of the sliding surfaces between grains.

As explained, the consequences of a cold deformation process is an increase of the yield strength and the reduction of ductility (Figure 11). Another consequence is the microstructural change that shows an elongation of grains in the direction of the greater deformation. This transformation makes the material acquires anisotropic properties. The hardening is an important aspect of metal forming because by cold working it is possible to produce pieces having high mechanical characteristics [34].

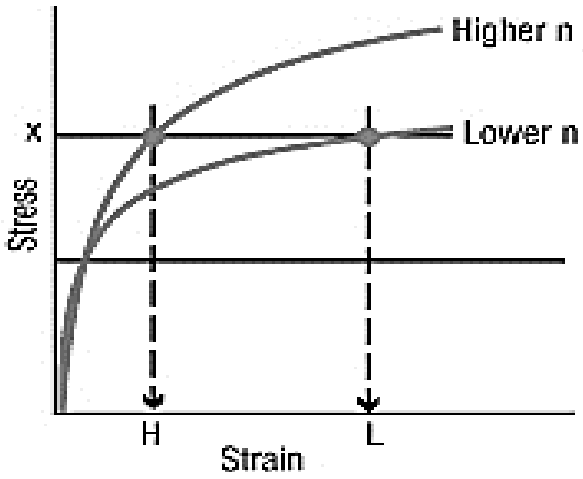

Figure 11: Effect of work hardening (higher n-value) on stress-strain curve

If the process needs a large deformation it is possible to obtain the same results by means of several forming steps, in order to prevent the increase of the needed force pressure and avoid an excessive wear on equipment, including also intermediate annealing heat treatments. When the forming process takes place above the recrystallization temperature it is defined as "hot forming process". At high temperatures the dislocations, locked in their movement due to a plastic deformation, can move easily and quickly affect other atomic planes. The formed material has a very low density of dislocations and, therefore, undergoes less strain hardening then a cold-worked, showing also a lower value of the yield strength and a greater ductility [35].

In fact, it has contemporary a softening, caused by the restoration process and propagation of dislocations, and a hardening during deformation itself. The dominant mechanism depends on the temperature, the strain rate and the crystal grain. In particular, the effect of softening dominates when the strain rate is low and the atomic diffusion are favored. The recrystallization may still occur during the later stages of the process.

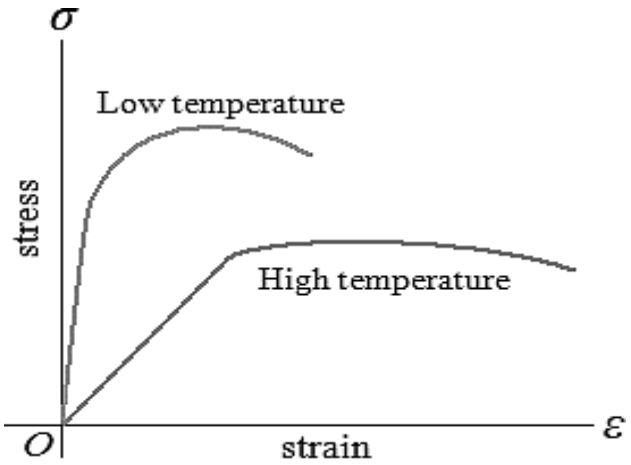

Figure 12: Effect of temperature on the stress-strain curve

3.2. Classification of bulk forming processes

Bulk deformation is a metal-forming process where the deformation is three-dimensional in nature. The primary use of the bulk deformation is to distinguish it from sheet-forming processes. In sheet-forming operations the deformation stresses are usually in the plane of the sheet metal where, as well as in bulk deformation, the deformation

stresses possess components in all three coordinate directions. Bulk deformation includes metal working processes such as forging, extrusion, rolling, and drawing.

The classification of deformation processes can be done in several ways depending on temperature, flow behavior, and stress state. The temperature of the deformation process is under direct control of the operator and has a profound effect on the viability of the process and the resulting shape and microstructure of the finished product. The flow behavior and the stress state differ from temperature in that they are a result of the actual deformation process that one chooses. The temperature classification scheme is normally divided into two primary regions, cold working and hot working. Cold working occurs at relatively low temperatures relative to the melting point of the metal. Hot working occurs at temperatures above the recrystallization one of the metal. There is a third temperature range, warm working, which is being critically examined due to energy savings and is, in some cases, used by industries.

The flow behavior of a metal or alloy during bulk deformation processes falls into one of two categories continuous flow or quasi-static. The easiest way to distinguish between these two types of flow is to imagine the deformation region during processing. If the shape of the deformation region changes during each frame of the movie, the process is a continuous-flow process. If in each frame of the movie the shape of the deformation region remains the same, even though a different material is in the region, it is a quasi-static-flow process. The bulk deformation process of forging is an example of a continuous-flow process. As the metal is formed in the forging die cavity, the deforming region, which is often the entire amount of metal, is continuously undergoing change. Processes such as rolling, wire drawing, and extrusion are examples of quasi-static flow. For example, in rolling, the formed region is pressed between two rolls and its shape does not vary, aside from initial startup and final finish, although different material flows into and out of the region. The classification based on flow is useful in determining what type of modeling scheme can be used to simulate the bulk deformation process. For a quasi-static- flow process, the deformation region can often be handled as a single region and a steady-state type of analysis can be applied while, in the case of continuous-flow process, a more complex analysis has to be used in order to simulate the process with a proper accuracy, taking into account for the continually changing shape of the deformation region.

In all bulk deformation processes, the primary deformation stress is compressive in nature. This is in contrast to sheet metal forming where tensile stresses are often used. Stress state classification consists of two categories for bulk deformation-direct compression and indirect compression. In direct compression, the tools or dies directly squeeze the workpiece. Forging, extrusion, and rolling are examples of direct compression processes [36]. In indirect compression, the deformation region of the workpiece is in a compressive stress state but the application of these compressive stresses occurs by indirect means. Wire drawing is an example of an indirect compression process, where the wire is pulled through a die. The workpiece contacts the converging surfaces of the dies, creating high forces normal to the die surface. The dies react to these forces by pushing back on the workpiece, causing a compressive stress state to exist in the deforming region of the metal. Thus although the equipment action is of a tensile (pulling) nature, the plastic deforming region is being squeezed. It should be noted that, although the stress state for bulk deformation is compressive, there are situations where tensile stress components may be present within the workpiece and fracture may occur. The metal forming engineer needs to be aware of these types of situations and to properly design the' process to avoid the potential fracturing that can occur on the workpiece due to the tensile stress components. For example, in the forging of a right circular cylinder between two flat dies in the axial direction, if friction on the top and bottom surfaces is high, the sides of the cylinder will bulge and some tensile hoop stress may occur on the outside surface of the workpiece. A more insidious example is an extrusion process where a small reduction is performed through a die with a high die angle. For this situation, the deformation region may be limited to the surface region of the workpiece, causing some internal tensile stress components along the centerline of the workpiece. If the internal tensile stress components become excessively high, they can cause an internal fracture in the workpiece. This fracture is referred to as central burst. The worst aspect of central burst is that there is no visual methods to detect it.

Forging processes can also be classified by the degree to which the flow of the material is constrained during the process. There are three major classifications in forging manufacture.

The next scheme (Figure 13) represents an exhaustive classification of the main manufacturing processes including the bulk forming processes group.

Open die forging, in which the work is compressed between two die that do not constrain the work during the process. Impression die forging, cavities within the die restrict metal flow during compression of the part, causing the material to deform into a desired geometric shape. Some material in impression die forging is not constrained by the cavities and flows outward from the die, generating the so-called flash.

In industrial forging, a subsequent trimming operation is performed to remove the flash. The third type of forging is flashless forging where the entire work piece is contained within the die in such a way that no material can flow out of the die cavity during the compression of the part, hence no flash is produced.

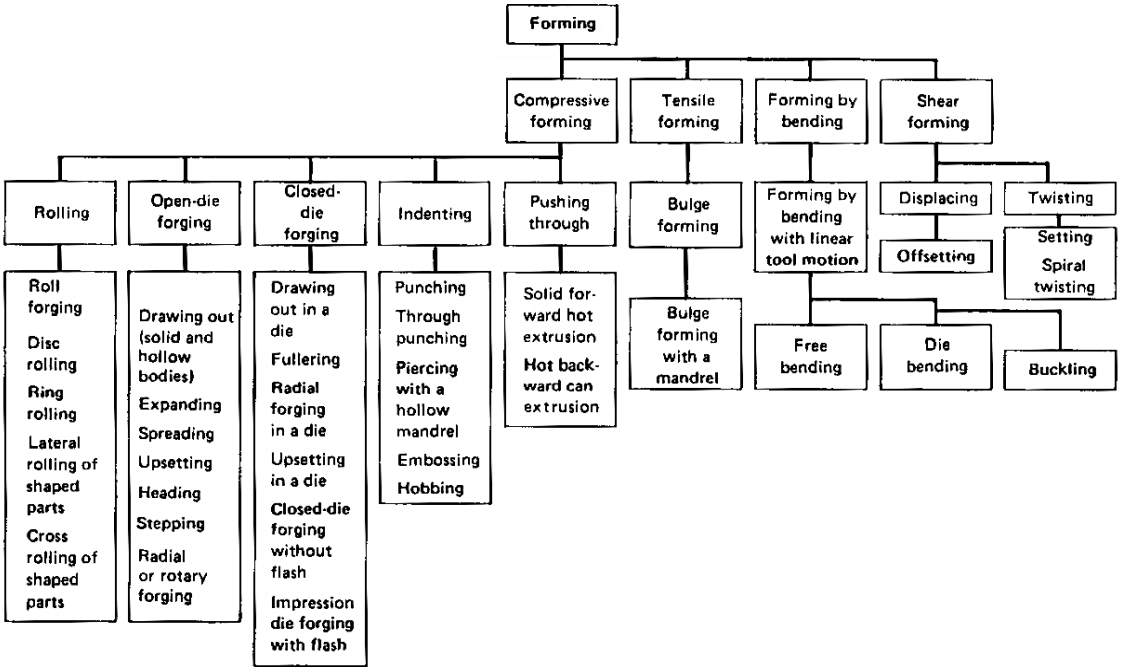

Figure 13: Scheme of forming processes [36]

3.3. Cold and hot forging

Most forging operations are carried out hot, due to the need to produce large amounts of plastic deformation in the part, and the advantage of an increased ductility and reduced strength of the work material [37].

However, this kind of manufacturing process can take place in different thermal conditions depending on the temperature reached by the material to form:

- Hot forging: it is a forging process taking place at a temperature greater than the critical temperature of recrystallization of the material. However, in practice this category includes all those processes in which the material undergoes a heating stage before the forming process. The advantages of this method are a minor request of force and power and the capability to cause large deformations in addition to get complex shapes with machines of reasonable size and capacity thanks to the higher ductility reached by the material. The disadvantages are the energy required for the heating stage and the oxidation of the surface of the material, resulting in worsening of the surface quality. Furthermore, it is difficult to predict the reachable dimensional accuracy.
- Cold forging: it is a forging process taking place at ambient temperature, although the deformation work could increase the temperature of the workpiece of a few hundred degrees. Often it is followed, after a chemical or mechanical operation of oxide removal, by a hot working operation. The advantages of this process are the great surface quality and precision. The final mechanical properties of the workpiece can be controlled using a suitable annealing treatment. In this kind of forging process, the lubrication of the interface between material and tool is much smoother than the hot case.
- Warm forging: it is a forging process performed at intermediate temperature, typically at a temperature range of 30-60% of the melting temperature of the metal on an absolute scale. The forces required to deform metal in the warm working regime are higher than during hot working. The final finish and dimensional tolerances are better than hot working but not nearly as good as a cold working process. Although warm work seems to have drawbacks, the primary driver for warm working is economic. There is significant cost in heating a metal up to hot working temperatures. If the working temperature is lowered, there could be major cost savings in the process.

3.4.Flow behavior and stress state during a forging process

The flow behavior of a metal or alloy during bulk processes can fall into one of following two categories: continuous or quasi-static flow, as consequence of deformation state. If the shape of the deformation region continuously changes, the process is a continuous-flow one; otherwise, it is a quasi-static flow system. Basing on the previous

subdivision, forging process is an example of a continuous-flow process. This classification based on flow is useful in determining what type of modeling scheme can be used to simulate the deformation process.

In all bulk deformation processes, the primary deformation stress is compressive in nature and it consists of two categories: direct compression and indirect compression. In direct compression process, such as forging, extrusion, and rolling, the tools or dies directly squeeze the workpiece. In indirect compression, the deformation region of the workpiece is in a compressive stress state but the application of these compressive stresses occurs by indirect means.

The workpiece contacts the converging surfaces of the dies, creating high forces normal to the die surface, which react to these forces by pushing back on the workpiece, causing a compressive stress state to exist in the deforming region of the metal.

It should be noted that although the general stress state for a bulk deformation is compressive but there are situations where tensile stress components may be present within the workpiece and fracture may occur. The process designers need to be aware of these types of situations and to properly design the process to avoid the potential fracturing that can occur on the workpiece due to the tensile stress components. For example, in the forging of a cylindrical component between two flat dies in the axial direction, if friction on the top and bottom surfaces is high, the sides of the cylinder will bulge and some tensile hoop stress may occur on the outside surface of the workpiece.

3.5. Open and close die forging

The manufacturing process of forging has been performed for at least 7,000 years, perhaps even 10,000 years. The most basic type of forging would have been shaping some metal by striking it with a rock. Latter the forging process, and the need for forged metal products such as swords and armor, led way to the art of blacksmithing. Blacksmithing is an open die forging process where the hammer and anvil surfaces serve as opposing flat die.

Open-die forging can produce forgings operations from a few pounds up to more than 150 tons. This process is precisely called open-die because impression dies do not confine

the metal laterally during forging (Figure 14, a) and it works the starting stock into the desired shape, most commonly between flat-faced dies. In practice, open-die forging comprises many variations of the process itself, permitting a wide range of shapes and sizes to be produced [38]. In fact, when design criteria need a structural integrity for a tricky metal component, the sheer size capability of open-die forging makes it the clear process choice over non-forging alternatives. In the case of big size values, open-die forgings are limited only by the dimension of the starting stock; namely, the largest ingot that can be cast.

Practically all forgeable ferrous and non-ferrous alloys can be open-die forged, including some exotic materials like age-hardening superalloys and corrosion-resistant refractory alloys.

Open-die shape capability is indeed wide in latitude. In addition to round, square, rectangular, hexagonal bars and other basic shapes, open-die processes can produce step shafts solid shafts (spindles or rotors) whose diameter increases or decreases (steps down) at multiple locations along the longitudinal axis.

Not unlike successive forging operations in a sequence of dies, multiple open-die forging operations can be combined to produce the required shape. At the same time, these forging methods can be tailored to attain the proper amount of total deformation and optimum grain-flow structure, thereby maximizing property enhancement and ultimate performance for a particular application [39]. Forging an integral gear [40] blank and hub, for example, may entail multiple drawing or solid forging operations, then upsetting. Similarly, blanks for rings may be prepared by upsetting an ingot, then piercing the center, prior to forging the ring.

Impression die forging manufacturing (also called cold forging process) involves compression of a workpiece by the use of a die containing cavities (Figure 14) that act to restrict the flow of metal within the die during the deformation of the work. The material will fill the space within the die cavity as it is plastically compressed into the molds.

Closing of the molds completes the deformation; hence impression forging is also referred to as closed die forging. The forged metal part will now have the geometric dimensions of the mold, provided a complete filling of the die cavity occurred during the process. As the name implies, two or more dies containing impressions of the part shape are brought together as forging stock undergoes plastic deformation. Because metal flow

is restricted by the die contours, this process can yield more complex shapes and closer tolerances than open-die forging processes. Additional flexibility in forming both symmetrical and non- symmetrical shapes comes from various preforming operations (sometimes bending) prior to forging in finisher dies.

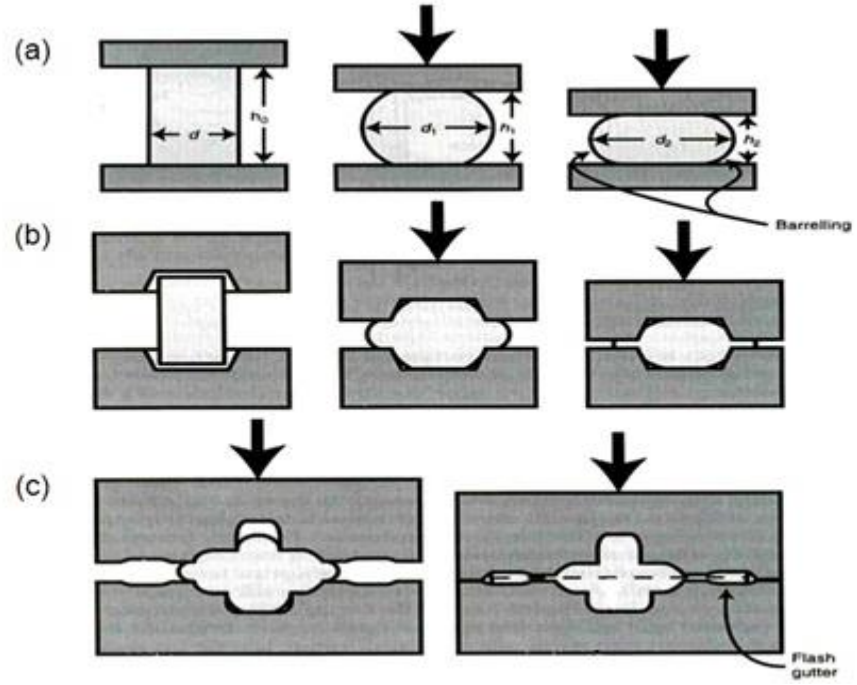

Figure 14: Open (a) and close (b, c) die forging processes

The operation of forcing metal to flow into and fill the impressions in the die will also alter the grain structure of the material. The creation of favorable grain structure through controlled material deformation should always be a consideration in the design of an impression die forging process.

One characteristic of impression die forging manufacture is the formation of flash or fin around the forged part. During the design of the forging operation, the volume of the starting work piece is made slightly higher than that of the closed die cavity. As the die close and the work, material flows into and fills the contours of the impression, some excess metal will flow out of the die into the area between the two die. This will form a thin plane of metal all around the work at the parting line, (where the two die meet when they close), of the forged product. Commonly, the impression-die forging of steel, aluminum, titanium and other alloys can produce an almost limitless variety of 3-D shapes

that range in weight from mere ounces up to more than 25 tons. This king of forging process routinely produced by mean of hydraulic presses, mechanical presses and hammers, with capacities up to 50000 tons, 20000 tons and 50000 lbs. respectively.

Part geometry's range from some of the easiest to forge simple spherical shapes, block-like rectangular solids, and disc-like configurations to the most intricate components with thin and long sections that incorporate thin webs and relatively high vertical projections like ribs and bosses. Although many parts are generally symmetrical, others incorporate all sorts of design elements (flanges, protrusions, holes, cavities, pockets, etc.) that combine to make the forging very non-symmetrical [33]. In addition, parts can be bent or curved in one or several planes, whether they are longitudinal or flat (Figure 15).

Most engineering metals and alloys can be forged via conventional impression-die processes, among them: carbon and alloy steels, tool steels, and stainless, aluminum and copper alloys, and certain titanium alloys. Strain-rate and temperature-sensitive materials (magnesium, highly alloyed nickel-based super-alloys, refractory alloys and some titanium alloys) may require more sophisticated forging processes and/or special equipment for forging in impression dies. Flash is trimmed from the forging in a latter process.

Modern technological advances in the forging process and in the design of die, have allowed for the development of a variation of the conventional forging process called precision forging. It may produce some or no flash and the forged part will be at or near its final dimensions requiring little or no finishing. The number of manufacturing operations is reduced as well as the material wasted. In addition, precision forging can produce more complex parts having thinner sections, reduced draft angles, and closer tolerances.

A sub-category of the precision forging is the flash-less forging in which the entire volume of the work material is contained within the die and no material is allowed to escape during the operation. Since no material can leave the mold as the part is forged, no flash is formed.

Like other precision forging processes, flashless forging has rigorous process control demands, particularly in the amount of material to be used in the work piece. Too little material and the die will not fill completely; too much material will cause a dangerous build up of forces.

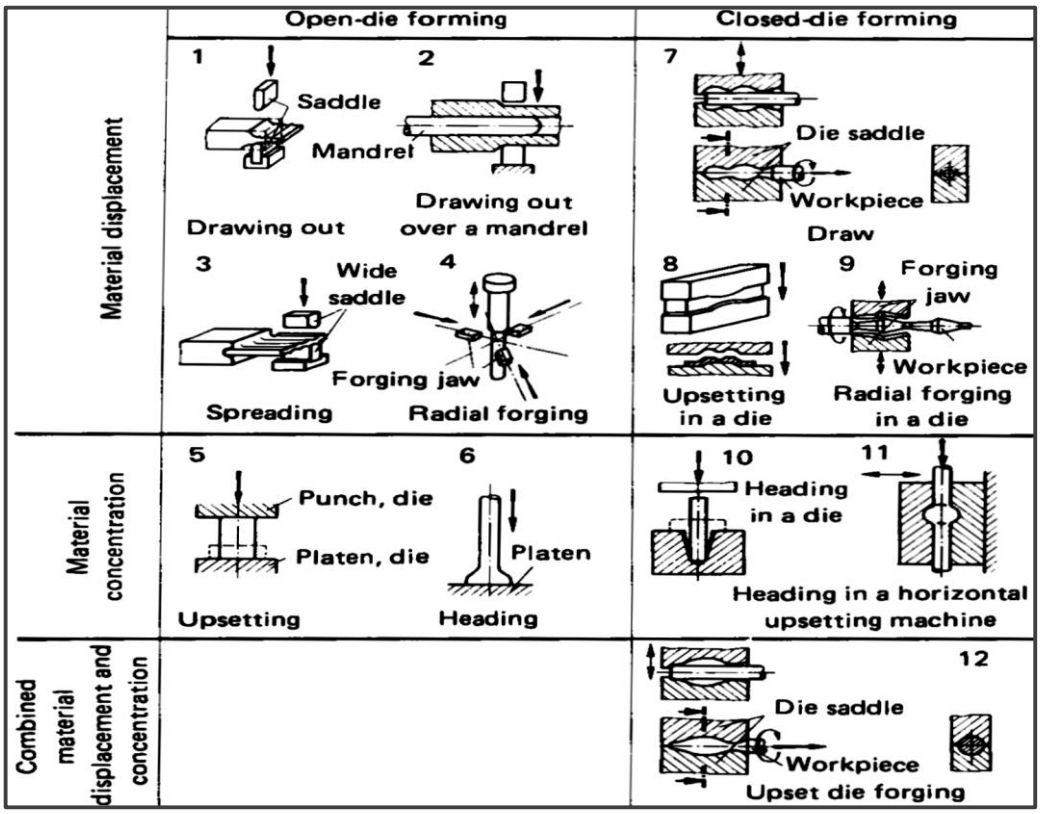

Figure 15: Forging process scheme as function of cross-section area [38]

The disadvantages of these advanced forging methods are that special machinery and die are needed, also more careful control of the process is required. In precision forging the amount of material in the work, as well as the flow of that material through the mold must be accurately determined. Other factors in the process such as the positioning of the work piece in the cavity must also be performed precisely.

3.6.Forging materials

The materials that are used most commonly in drop forging are aluminum, copper, nickel, mild steel, stainless steel, and magnesium [41].

Aluminum forgings are normally produced in high volume and these kinds of alloys are used widely in those application fields where component weight is very important due to theirs low density respect conventional steels. Consequently, aluminum alloys are used primarily in automotive and aerospace applications. The major element in aluminum

forging alloys is, of course, aluminum. Other alloying elements, for instance copper, are added to enhance the properties. The forging-alloy families using copper as the primary addition are the 2014, 2025, 2219 and 2618 series. Magnesium is sometimes added to the 2000 series alloys to enhance the strengthening of the alloy after heat treatment [42].

Magnesium is the major alloying element in the forging alloy 5083 and it provides strength to the alloy without major loss in ductility [43]. Magnesium, in combination with silicon and a small amount of copper (0.3% about), is used in the 6061 aluminum alloy also. The combination of these three alloy elements allows a good strength, especially after a heat treatment [44].

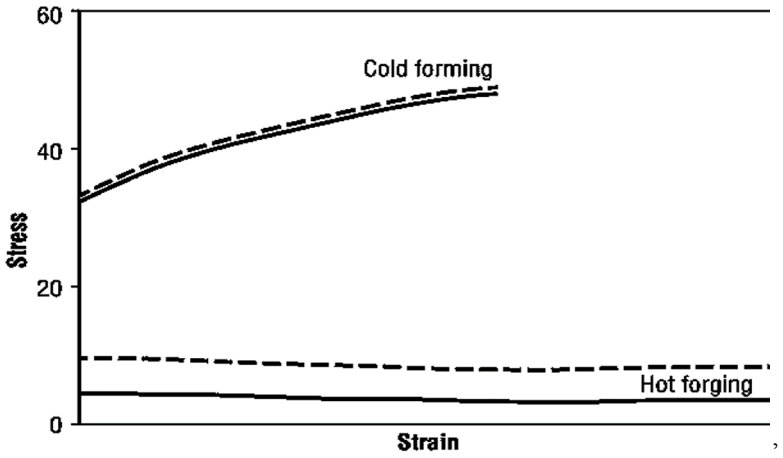

Figure 16: Flow stress thermal behavior for aluminum alloys

Due to aluminum's low flow stress and high ductility, very complex shapes can be forged from aluminum alloys relative to other metals.

The most forgeable alloy is 6061 aluminum due to its relatively low flow strength at forging temperatures (Figure 16) and can fill cavities fairly easily [45]. The series of common forgeable aluminum alloys are the ones in the 7xxx alloy series, in particular 7010, 7039, 7049, 7050, 7075 and 7079. These alloys contain zinc (5-8%) with small additions of copper and magnesium and, if properly heat-treated, they are commercial grades that can achieve the highest strength of all forged aluminum alloys.

Another important family of forgeable materials is given by copper alloys, which are strengthened by either solid solution or by precipitation hardening. For the alloys that have solid solution as the primary strengthening mechanism, copper-zinc (brasses) are

most common. The Alpha-Beta brasses are two-phase metals containing 32-40% zinc. The single-phase Alpha brasses are alloys of copper with up to 32% zinc. These alloys can also be strengthened by cold work. An unusual property of these Alpha brasses is that, in some cases, it is possible to have an alloy with additional zinc and it is both stronger and more ductile than the starting alloy.

Copper alloys having up to 10% tin (bronzes) are not usually casted and not forged. The aluminum bronzes with up to 10% aluminum and 4% iron plus small additions of other elements (excluding tin) are fairly forgeable. Forgeable cupronickels can contain up to 30% nickel [46].

An interesting family of copper forging alloys is given by the copper-beryllium alloys. These alloys contain up to 2% of beryllium and must be handled with care. They can be precipitation strengthened, reaching over 1380 MPa and are often used in electrical contacts where high strength is required.

Forged copper and brass alloys are used in several electrical applications, decorative uses, corrosion-resistant components and heat-transfer applications like pipes and sheets (Figure 17).

Thanks to their good ductility, these alloys are generally considered as easy to forge. When hot forging, the preheat temperatures are typically 730-930 °C. Figure 3 illustrates the typical hot and cold-forging ranges as well as the processing and application ranges for copper alloys.

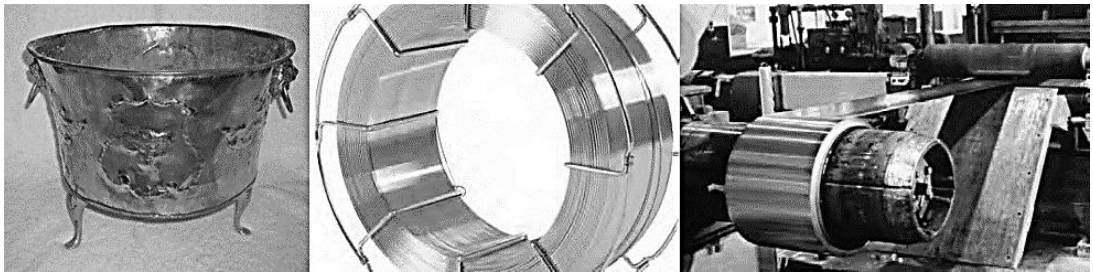

Figure 17: Typical application fields of forged copper alloys

The most forgeable (hot) copper alloy is one with 38% zinc and a small amount of lead. This alloy is a two-phase Alpha-Beta brass at room temperature, but the hot-forging temperatures take the alloy into the single-phase Beta region where deformation can

easily occur. Lubrication requirements are generally minimal because the copper oxide that forms on the surface is a natural lubricant.

As noted, copper and copper alloys can be cold forged. Cold forging is especially useful for small-sized components that can be formed to net shape with tight tolerances. Cold forging also adds cold work to the component and increases its strength, as shown in Figure 4. The caveat is that work hardening in copper alloys is more pronounced than it is in most other metals, with increasing flow stress and eventual fracture after excessive cold work [47].

When forging copper-beryllium alloys, they must be handled with care. Operators need to use appropriate safety equipment since beryllium is toxic and can cause critical problems like berylliosis or chronic beryllium disease. The beryllium coppers can be heat-treated in a fashion similar to the precipitation-hardenable aluminum alloys. They are heated to a high temperature (called solution treatment) to dissolve all the alloying elements and form a single-phase structure. Then, they are quenched to room temperature, which locks in the single-phase microstructure. In the final step, they perform another thermal treatment (lower than the solution temperature) in which a very fine second-phase solid-state precipitation occurs, leading to the increase in strength. This last heat treatment is called aging.

If the copper alloy is cold forged, its strength will be increased but its ductility may be too low for the intended application. The ductility of these alloys can be re-established by an annealing heat treatment. Be aware that ductility will increase during annealing, but the strength will decrease.

A particular consideration has to be done about the use of carbon steels [48] and stainless steels for forging operations. They are considered a special class of steels because of their high alloy content, mechanical properties, like a high strength and relatively good ductility, and their good corrosion resistance, which comes from the formation of an adherent chromium-oxide film on the surface of the metal.

Stainless steels are mostly composed of 55-90% iron, from 10-28% chromium and 0-22% of Nickel while carbon is often quite low. This characteristic often indicated using the “L” designation (especially in the case of very low content of carbon) permits them to be more easily welded.

Furthermore, because of the high cost of Nickel their price can be very high.

The stainless steels can be classified in four main types as function of their microstructure: austenitic, ferritic, martensitic and precipitation-hardening steels.

The 200- and 300-series alloys have a microstructure that is a face-centered cubic phase. Austenitic stainless steels, made adding Nickel, are both strong and ductile and their cost is high due to the one alloying element.

The 400-series can be both ferritic, with a body centered microstructure and not so high strength and ductility, and martensitic.

The 500-series denotes martensitic steels, which have the highest strength but also have the lowest toughness and ductility. Carbon in these martensitic grades can reach the 1.2% content, providing high mechanical properties. This steel series contains also precipitation-hardening stainless steels (PH grade steels) which require special post-forging heat treatments to allow the reaction of precipitation elements. Their characteristics allow a limited range of service temperatures. The ferritic and austenitic grades steels can be forged maintaining their parent microstructure because this family of stainless steels do not undergo a phase transformation during cooling. However, the martensitic grades can be forged as austenite and need to be quenched to achieve the high-strength martensitic structure. Some of the austenitic grades are metastable at room temperature so that, if they are formed at room temperature, the austenite will transform into martensite. This transformation is difficult to control but can produce a local increase of mechanical properties [49].

Because of their corrosion resistance, forged stainless steels are used in valves, bolts, shafts, kitchen equipment and food service without forgetting other important application fields like oil refining, chemical processing, mining and drilling, where stainless steel components are often used to prevent rapid part degradation. However, their service temperature has to be maintained less than 425 °C.

The conventional range of temperature for hot forging of stainless steels is 925-1260 °C, depending on the specific grade of the material and the relatively low melting temperature. Their forgeability is generally good (Figure 18) but they require relatively high forging loads and energy so that the forging equipment size can become an issue for forge shops accustomed to forging plain-carbon or low-alloy steels.

Like all steels, micro-alloyed steels are iron-based metal alloys. Normally, they are common carbon or low-alloy steel with small additions of one of three particular elements

providing higher strength and higher toughness as compared to low-alloyed steels with the same microstructure.

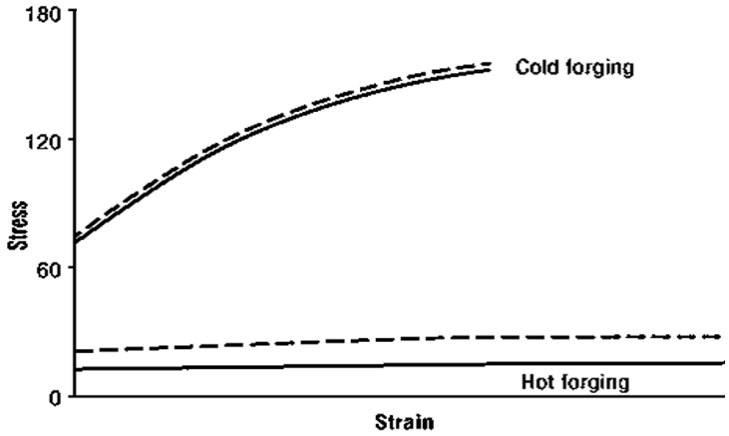

Figure 18: Flow stress thermal behavior for stainless steels

The big advantage of micro-alloyed steels is in the cost savings coming from the abolition of heat treatments, since a properly designed and forged micro-alloyed steel component does not require any subsequent heat treatment to obtain particular properties depending on the application.

Therefore, the abolition of the needed post-forging heat treatments helps offset the additional cost associated with a micro-alloyed steel (Figure 19).

It is common to see that for a low-alloy steel the subsequent hardening, tempering and stress relief after straightening requires that the part is reheated several times, increasing the total energy costs of the process while the micro-alloyed steel, if forged and cooled properly, can be used without additional heat treatments significantly reducing the energy costs. This kind of steels typically have a carbon content of 0.15-0.55%, with manganese ranging from 0.60-1.65% and silicon 0.15-0.65% and contain micro-alloy elements in small quantities, like vanadium, niobium and titanium, to form precisely micro-alloyed steels [50]. Their conventional microstructure is composed by ferrite-pearlite, but it is possible to add a small amount of molybdenum to obtain a bainitic microstructure directly after forging.

Vanadium, if added in the range of 300 to 1,000 ppm (0.03-0.10%), has a very high solubility in the austenite phase of the steel but, when the material is heated to forging temperatures, it dissolves into the austenite phase. Moreover, when the steel is forged and

subsequently cooled in a controlled manner, the vanadium can react with carbon and nitrogen to form vanadium carbonitrides, which precipitates out as fine nano-sized particles in the microstructure, increasing the mechanical properties at room temperature.

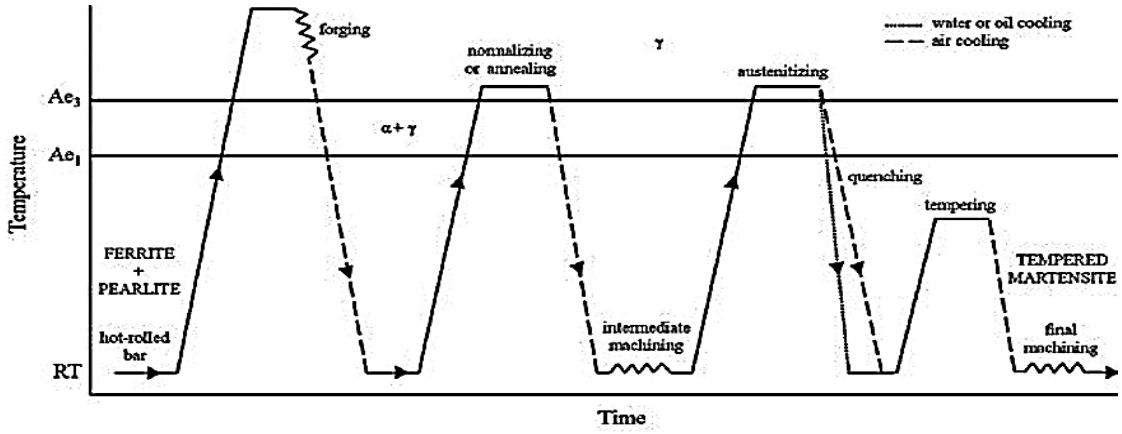

Figure 19: Time-temperature diagram of hot forged quenched and tempered micro-alloyed steels [51]

The other benefit coming from the use of vanadium as alloying element is that it can form vanadium carbonitride precipitates on MnS particles that are within the steel [34]. These MnS particles causes that the ferrite forms inside the austenite grains and maintains itself inside the final pearlite microstructure (Figure 20). The intragranular ferrite can contribute to a small increase in the toughness of the steel.

Niobium is a very common micro-alloy element in high-strength controlled-rolled plate steels. In forging steels, it is added in quantities of 200 to 1,000 ppm (0.02-0.10%). Its solubility in austenite is very temperature sensitive in fact, at high forging temperatures, most of the Nb dissolves and precipitate out when cooled similarly to vanadium. At lower forging temperatures, it cannot fully dissolve remaining as fine precipitates. It causes a grain-boundary pinning of the austenite limiting the grain growth. The size of these prior austenite grains is about 1 micron, which is indeed very fine. If fine austenite grains are present, then the transformation products (ferrite, pearlite or bainite) upon cooling will also have a very fine grain structure.

Small grains provide not only an increase in the strength of the steel; they can also increase the toughness at the same time. This grain refinement is the only known mechanism that increases strength and toughness simultaneously. We would get an increase in strength but a decrease in toughness with all the other known strengthening

mechanisms in metals. The control of these niobium-rich precipitates is much more difficult in a forge shop. The processing window for a good forging product with a niobium-micro-alloyed steel is much smaller than with vanadium. So, in spite of the lower cost of niobium as compared to vanadium, vanadium is the normal micro-alloying element for forging operations [51].

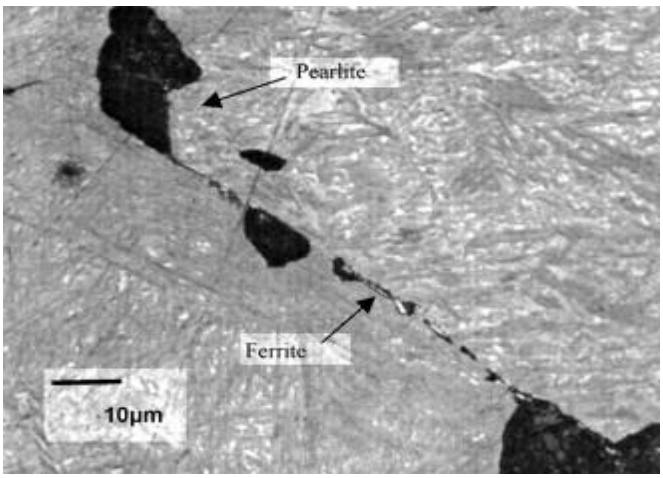

Figure 20: Ferrite grains into pearlite microstructure [34]

Another family of forged steels is given by superalloy steels. Their name comes from the high mechanical properties making them able of critical service conditions in particular applications generally require very high strengths at high temperatures frequently exceeding 600 °C and they are usually nickel-based alloys although cobalt and iron-based alloys have also been developed.

Superalloys are very complex materials and often they are composed by a wide variety of secondary phase particles in the base-metal matrix providing a good creep-rupture strength and a good oxidation resistance, so they are quite suitable for high-temperature applications. Their corrosion resistance in harsh environments makes them suitable in petrochemical components or in applications with aggressive atmospheres.

Chemistry and Grades Nickel-based superalloys are comprised of 50-78% nickel. Other major alloying elements in these complex systems include chromium from 14 to 23%, molybdenum up to 18% and tungsten up to 5%. These elements provide a solid-solution strengthening and form carbides. Additionally, iron may be added to the alloy in amount from 3 to 20% to increase the straightening, cobalt up to 5% for solid solution

strengthening and to raise the melting point and titanium up to 6% to form precipitates [52]. The most common superalloy is the Alloy 718, often called Inconel 718 or simply Inconel. This alloy appears to be a single-phase material (Figure 21).

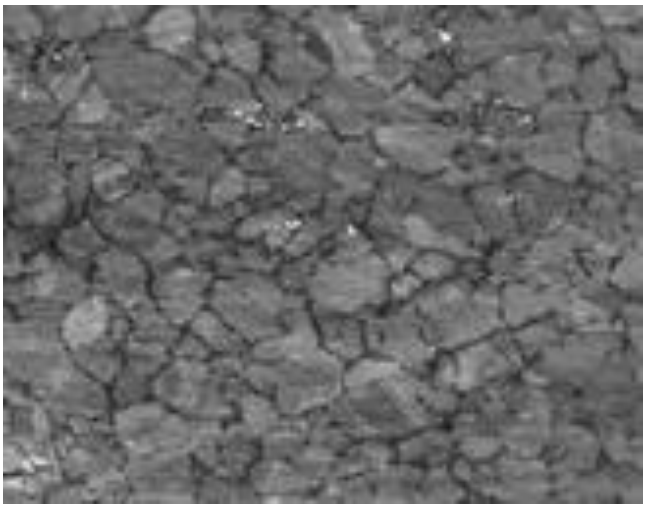

Figure 21: Optical micrographic image of IN718 alloy after heat treatment [52]

During deformation, recrystallization occurred at the prior grain boundaries, but there was not enough deformation to cause the entire component to recrystallize. This causes the duplex grain structure. Sometimes there will only be recrystallized grains outlining the prior grains. This outlined structure is called a necklace microstructure because the new small grains surrounding the larger prior grains look like a necklace. Although pretty to observe, the properties of such structures are not often useful.

The classical aim of a forging process is to obtain a piece of the selected material having the designed shape, taking advantage of the thermal treatment coming from the process itself, in order to increase the mechanical properties of the base material. Conversely, superalloys obtain strength from their base chemistry, secondary particles (controlled by heat treatment) and grain size. Fine grains are required to meet most commercial and military specifications.

Unfortunately, the grains are always growing when in a hot environment, such as pre-heating for forging or heat treatment. Consequently, temperature control during forming process is important to ensure that the proper amount of deformation is given at recrystallization temperature.

The next image (Figure 22) shows a typical flow stress diagram at various temperatures for the IN718 alloy.

These mechanical characteristic make the forging process of superalloys a strong challenge. There is usually a very narrow temperature range to forge a given alloy. Their high flow strength makes superalloys very resistant to movement.

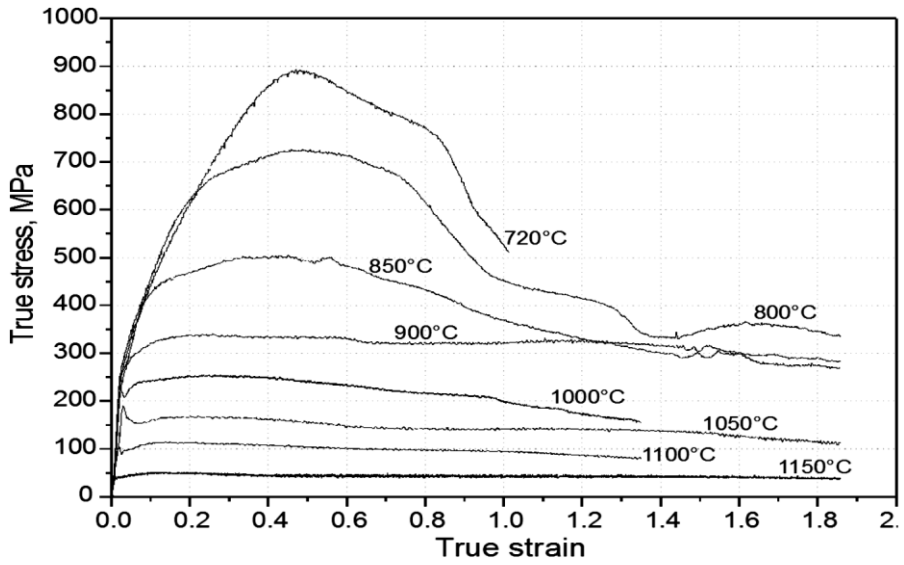

Figure 22: True stress-true strain curves for Inconel 718 [53]

Consequently, it is challenging to fill detailed die cavities in a closed die without extreme forging pressure. The sizing presses and hammers used in the production of steel parts are grossly inadequate to forge superalloys. Forging on undersized equipment can pose an insurmountable challenge. Smaller equipment results in more hits on a hammer or inadequate deformation in the final forging operation on a press. This, in turn, generally causes incomplete recrystallization and, thus, inadequate strength. Raising the temperature helps with die fill and recrystallization, but grain growth in the heating furnace can more than offset any gains.

Because of their high flow strength at high temperatures, the forger should anticipate very poor tool life when forging superalloys. Numerous examples have been reported of catastrophic die fracture after a handful of forging cycles. Even when the tooling is strong enough to avoid a low-cycle fatigue failure, tool wear is extreme relative to the forging of other metals. In many applications, superalloys are used as die material [54].

The table below (Table 1) shows the most common forging materials including their forgeability order and temperatures.

Among metals used in practical forging applications, magnesium alloys are which that have the provide the great advantage of their density as well as high specific strength and electromagnetic interference shielding capability.

Because these properties magnesium alloys are finding wide expectations and applications as light, strong materials alternative to aluminum, especially for forging processes aircraft and spacecraft parts, land transportation equipment, cargo equipment, industrial machines and tools, electronic equipment, telecommunications and optical equipment.

Table 1: Most used forging alloys with forging temperature range and forgeability order

Alloy family	Forging temperature range [°C]
Aluminum alloys	400 – 590
Magnesium alloys	250 – 350
Copper alloys	600 – 900
Carbon steels	850 – 1150
Martensitic stainless steels	1100 – 1250
Maraging steels	1100 – 1250
Austenitic stainless steels	1100 – 1250
Nickel alloys	1000 – 1150
Semi-austenitic PH stainless steels	700 – 900
Titanium alloys	1050 – 1250
Iron base superalloys	1180 – 1250
Columbium alloys	1050 – 1350
Tantalum alloys	1150 – 1350
Molyobdenum alloys	1050 – 1200
Nickel base superalloys	1050 – 1200
Tungsten alloys	1200 – 1300

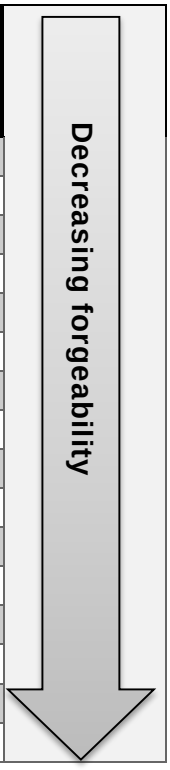

The magnesium alloys are, however, much poorer in plastic working than aluminum alloys. It is usual to find magnesium alloys provided as die-castings and their castability and mechanical properties are improved using proper alloying elements like aluminum, zinc, zirconium and manganese. Also, rare earth elements and silver may be added to provide heat resistance [44].

However, magnesium alloy castings are limited to relatively thick products due to the extreme difficulty to cast this kind of alloys into thin pieces. In addition, they can show casting defects, such as pores, and inclusions, such as oxides deteriorating the mechanical strength and the surface quality of the products.

Recently a new semi-solid forming method for magnesium alloys was proposed. It uses a temperature range in which a solid phase and a liquid phase coexist, by mean an injection technique, allowing to obtain fine crystal structures free from dendrites, common in usual castings, and also have higher density with fewer pores than die-castings. In this way, it is possible to produce magnesium alloy parts with a thickness of 1.5 mm or less.

3.7.Die materials

An important step of the sequence design of a forging process is the correct choice of the die material in order to obtain the best-required properties to forge the desired component.

This selection has to satisfy a group of characteristics as below:

- Improved physical properties respect conventional steels;
- Sufficient hardness and ability to retain this hardness at the operating temperatures;
- Good tensile strength at high temperature;
- High toughness and ductility at low and elevated temperatures;
- Sufficient hardenability and wear resistance;
- High fatigue resistance.

In fact, it is well known that the die life is strongly affected by several physical phenomena some of them influence most than others (Figure 23).

However, the correct choice of the die material requires a proper study of the forging process to be processed (Figure 24). It appears clear that all these properties require, in the case of steels, a proper use of alloying elements in order to create a family of steels to

be applied in small and medium size forging sequences, taking also into account the manufacturing processes able to obtain a uniformity of mechanical properties of the die.

It should be understood that chemistry alone does not tell the complete story of a steel's capabilities, which is why it is important to ask questions about how the steel is processed. If the steel is not melted again, it is important to stipulate the minimum forging reduction ratio and to know if a homogenizing heat treatment has been performed to get good properties from a conventionally produced grade [42].

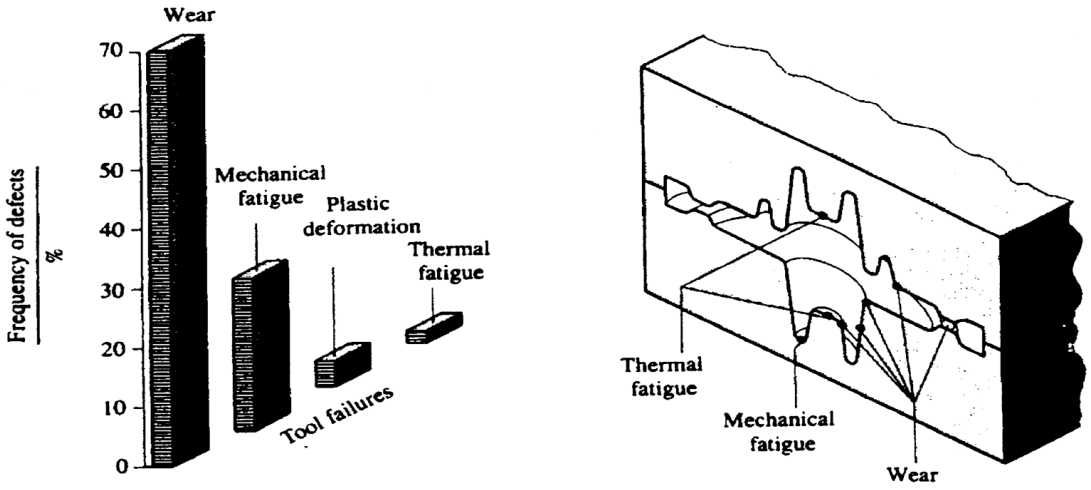

Figure 23: Physical fundamental phenomena affecting the die life [42]

Not all re-melted steels are produced using the same method. For example, grades like Uddeholm's Premium H13 (Orvar Superior), Dievar and Bohler's Premium H13 are remelted through controlled solidification in a steel bath and under a protective atmosphere, giving better homogeneity of structure and steel cleanliness than in previous ESR furnaces.

The thermal aspect is very important during the forging process so it is important to limit the thermal induced stress into the die by increasing the thermal conductivity of the material in order to reach a better distribution with a minor thermal gradient on the different zones of the die.

Always about the thermal aspect it should be considered that a good heat treatment is important to obtain the requested properties and to success the forging process [55].

The challenge is, naturally, to limit dimensional changes after heat treatment because the material provides new and improved mechanical characteristics and it could be

difficult to machine it. If the section size of forging blocks increases, the microstructure of the steel contains considerable percentages of bainite and this kind of microstructure can occur in localized deformations [56].

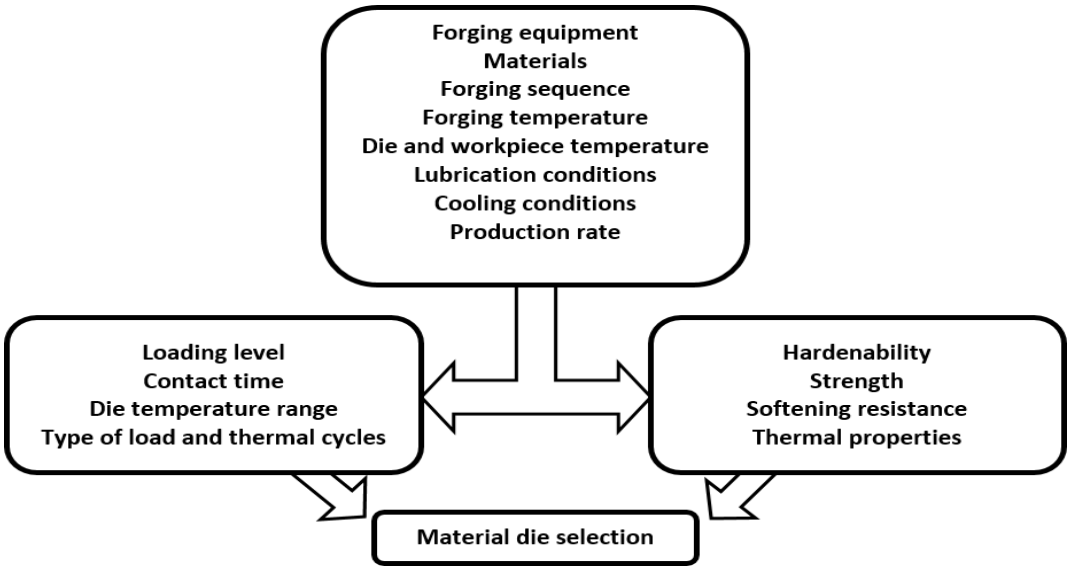

Figure 24: Forging process factors to be considered to choice the die material

Although proper heat treatment (Figure 25) can increase the properties of hot-work steels it is possible to optimize the mechanical characteristics by mean of a tempering process (once or multiple times) after the first quenching stage to provide enough toughness to better endure changes in pressures and temperatures.

Both the chemical properties and thermal treatment have to be considered concerning on the hot hardness of the selected material. In fact, during a forging process the high temperature makes the hardness of the die decreases. Therefore, it is fundamental that the initial hardness is high to compensate for the reduction due to thermal effect, especially when operating temperatures exceed the temperature at which the secondary hardness peak is achieved.

It is evident that they are considered as the best as it is high their capability to retain hardness at elevated temperature. For this purpose, new alloys have been developed with increased strength retention at elevated temperatures while taking more time to reduce their hardness during a hot-working process.

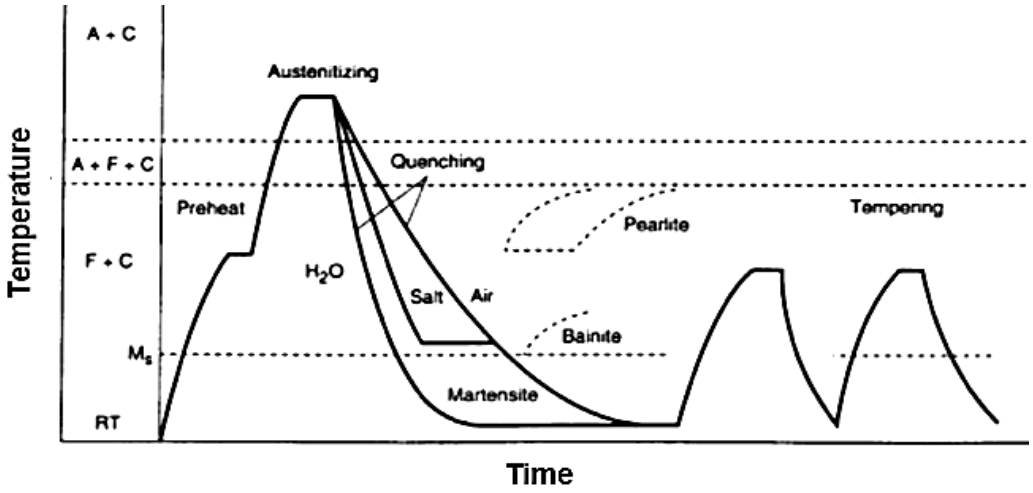

Figure 25: Hot forging die steels heat treatment cycle [42]

This property is mainly given by a good percentage of several alloying elements which makes these alloys are desirable for long contact times and higher temperatures (Figure 26). These materials contain also chromium, tungsten, and in some cases, vanadium and molybdenum. They all are alloying elements inducing deep hardening characteristics and resistance to abrasion and softening. Tungsten improves toughness and hot hardness; however, the tungsten-alloyed steels are not resistant to thermal shock and cannot be cooled intermittently with water so the water-cooling of these metals is not advisable [57].

The higher the hardenability of a material depends on its composition of the tool steel. In general, the higher the alloy content of a steel, the higher its hardenability, as measured by the hardenability factor D1 which is the diameter of an infinitely long cylinder which would just transform to a microstructure, with 50% of martensite content, at the central zone considering the heat transfer during cooling as ideal. A larger value of the D1 factor means that the steel is able to harden to a greater depth on quenching, no that it will have a higher hardness.

As previously explained the failure conditions of a die depend of other physical events and one of the most important is the wear of the material caused by corrosion, dissolution, or abrasion and removal or transportation of the wear products.

Quenched and tempered hot work tool steels, such as H11 and H13, with a tempered martensite structure, are widely used as die materials. However, reduction in hardness and strength of the surface layer, owing to tempering caused by high surface temperatures, leads to a decrease in wear resistance and limits the service life of these steels.

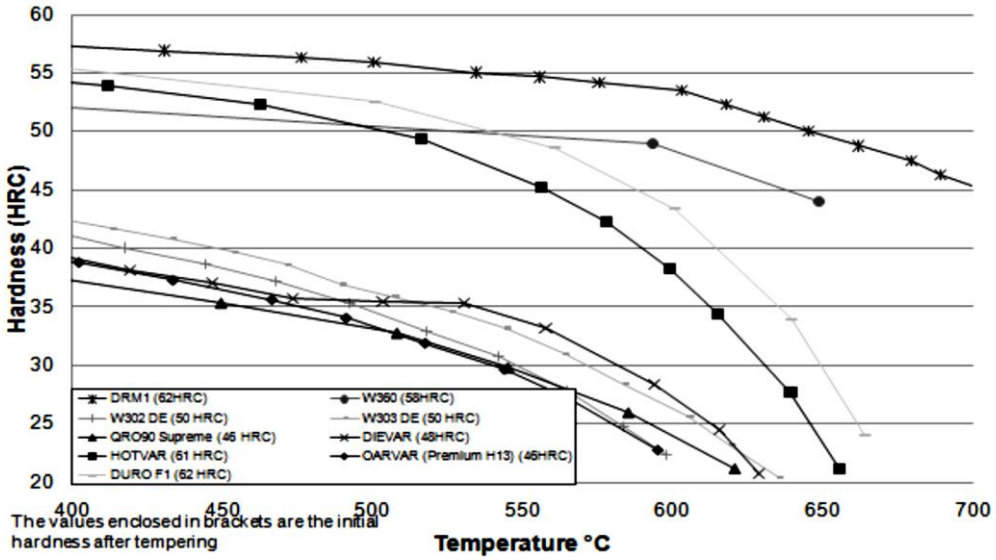

Figure 26: Hot-hardness curves for several hot-work steels [57]

Abrasion resulting from friction is the most important factor limiting the die life. The higher the strength and hardness of the steel near the surface of the die, the greater its resistance to abrasion. This is the reason making that the hot-work die steel should have a high hot hardness and should retain this hardness over extended periods of exposure to elevated temperatures [58].

Several surface engineering methods such as nitriding, CVD and PVD ceramic coating and hard-facing were used to improve the wear resistance of materials. Nitriding is widely used to improve hot-forge die life in mechanical presses and hammers; up to double the die life can be achieved. PVD and CVD methods have been successfully used for extrusion and casting dies, but not for forging; the high impact loads result in spalling of the coated layers. Under these conditions, hard-facing of dies, which produces a strong metallurgical bond with the steel substrate, is more efficient. Stellite 6 is one of the main Co based superalloys, which shows good wear resistance because of its hardness and mechanical strength at high temperatures. However, its low impact strength makes it unsuitable for hard-facing of drop forging dies.

The same important consideration has to be done about the fatigue resistance of die materials. In fact, the magnitude of the applied loads, the average die temperature, and the condition of the die surface influence the die life. Fatigue cracks usually start in those

zones having highest stress, such as at cavities with critical curvature radii, holes, keyways, and deep stamp markings used to identify die sets.

A proper die shape design, including include changes in the die impression itself or modification of the flash configuration can strongly limit the fatigue crack initiation and growth. As well as die design, the surface treatments may also reduce fatigue crack phenomena by means of nitriding treatments, mechanical polishing and shot peening. These methods are effective because they induce surface residual compressive stresses and eliminate notch effects, delaying fatigue crack initiation.

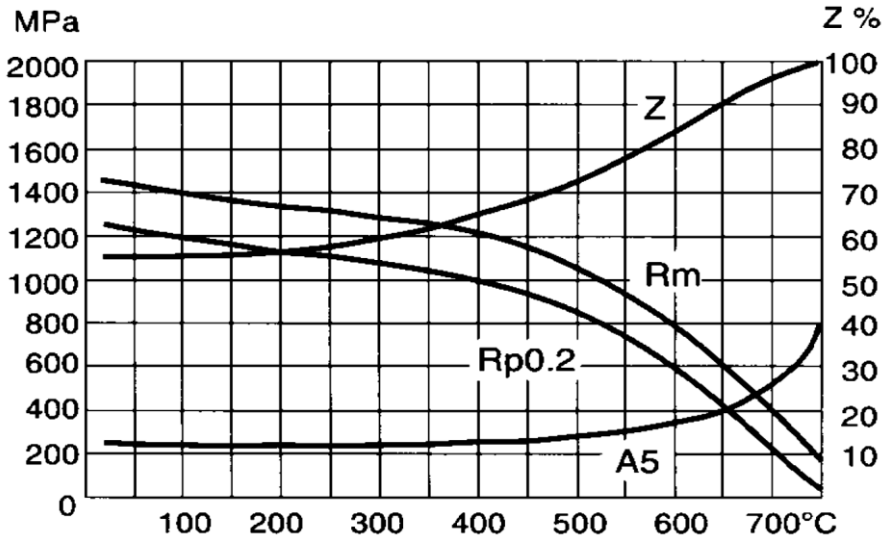

Figure 27: Yield strength and ductility vs. test temperature (A5) elongation (Z) area reduction of a H13 steel [42]

Even it is considered a minor factor with respect to the wear resistance, yield strengths of die materials has to be taken into account during the design stage. In fact, the plastic deformation resistance of materials decreases at higher temperatures. However, yield strength also depends on prior heat treatments, composition, and hardness and the higher it is, the greater the yield strength at various temperatures. In practice, the hardening process and level of a die material is determined by toughness requirements: the higher the hardness, the lower the toughness. It means that it is fundamental to harden the die block to a hardness level at which it should have enough toughness to avoid cracking processes. The image (Figure 27) shows the yield strength and ductility evolution of two common die steels as function of temperature.

Fracture toughness and resistance to load shocks are often measured using the Charpy test data of the material, or rather the absorbed energy absorbed during a fracture propagation. Unfortunately, the wear resistance and hot strength decrease with decreasing of hardness so that, in common practice, the dies are tempered to near-maximum hardness levels at which they have sufficient toughness [57, 59].

The last main physical factor influencing the die life is given by the thermal behavior of material.

Table 2: Most common commercial hot-work tool steels

Steel family	AISI designation	Wt.%					
		C	Cr	V	W	Mo	Co
Cr-Steels	H10	0.4	3.25	0.4	-	2.5	-
	H11	0.35	5	0.4	-	1.5	-
	H12	0.35	5	0.4	1.5	1.5	-
	H13	0.35	5	1	-	1.5	-
	H14	0.4	5	-	5	-	-
	H19	0.4	4.25	2	4.25	-	4.25
W-Steels	H21	0.35	3.5	-	9	-	-
	H22	0.35	2	-	11	-	-
	H23	0.3	12	-	12	-	-
	H24	0.45	3	-	15	-	-
	H25	0.25	4	-	15	-	-
	H26	0.5	4	1	18	-	-
Mo-Steels	H42	0.6	4	2	6	5	-

It is well known that a thermal gradient from the surface to the center of a die causes a non-uniform expansion, contributing to heat checking.

It means that a material having a high thermal conductivity is less influenced by these phenomena due to its capability to conduct heat rapidly away from the die surface to the core, strongly reducing temperature gradients and resulting stresses. The table below (Table 2) resumes the main commercially available hot-work tool steels.

3.8. Advantages and disadvantages of forging processes

Like all manufacturing processes, the forging process also shows both advantages and disadvantages. These aspects make it available in proper application fields as function of properties of products with respect to the production and operative conditions.

The first main aspect is the thermal control during the process resulting in improved metallurgical properties. The forging process produces directional alignment (grain flow) for important directional properties of strength, ductility, and resistance to impact and fatigue. The image below shows the grain alignment of a common piece resulting from forged compared with other manufacturing processes (Figure 28).

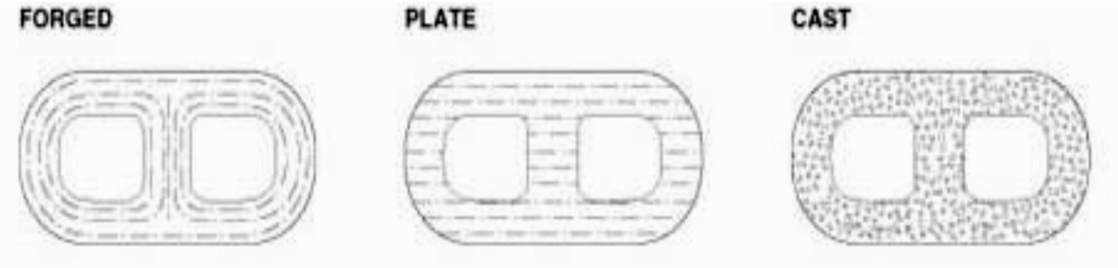

Figure 28: Grain alignment resulting from a forging operation

Through proper grain flow orientation, the forging process can develop the maximum impact strength and fatigue resistance possible in a metal.

As is well known, a forging structural reliability is excelled by no other metalworking process. In fact, there are no internal gas pockets or voids causing unexpected failure under high stress conditions. It means that more realistic safety factors based on material that will respond predictably to its environment without costly special processing to correct internal defects.

As well as the technical aspect, the economic one is important. By means of forging process, it is possible to produce pieces in a wide range of sizes and shapes with a reasonable cost. Forging's superior functional advantages of strength, fatigue resistance, reliability, and high quality combine into economic benefits. Uniform dimensional relationships result in consistent machinability and predictable response to heat treatment. This, combined with obvious strength-to-weight ratios, make forgings a top priority of the cost-conscious user. The consistency of material and dimensions from one forged part

to the next, and from separate production of forgings produced months or years apart, is extremely high. Forgings are made through a carefully controlled sequence of production steps, in contrast to a random flow of material into the desired shapes. Uniformity in composition and structure, piece to piece, insures reproducible response to heat treatment, minimum variation in machinability, and consistent property levels of finished parts. Another advantage is the higher strength-to-weight ratio that can be used to reduce section thickness in part design. Forging components have superior response to all forms of heat treatment. Due to the near absence of structural defects, forgings offer the best opportunity for strong, efficient welds. Due to the lack of internal discontinuities and surface inclusions, forgings provide a dependable machining microstructure for most metal-cutting processes. Forged parts can be readily fabricated by welding, bolting, or riveting, and are suited for most surface conditioning. A forging can also be designed to eliminate multiple assembly components.

The main disadvantages are the possibility to have scale inclusions, the high tooling cost and the general process cost, which is justifiable only in the case of large productions. Another harmful aspects to be considered is the residual stress filed coming from rapid cooling, causing strong thermal gradient within the material. It results in compressive or tensile stresses decreasing the mechanical properties of forged parts when they undergo to severe operating conditions.

3.9. Application fields of forging processes

The characteristically uniform refinement of crystalline structure in forged components assures superior response to all forms of heat treatment, maximum possible development of desired properties, and unequaled uniformity. Because forged components of weldable materials have a near absence of structural defects, material at welding surfaces offers the best possible opportunity for strong, efficient welds by any welding technique. Again, the near absence of internal discontinuities or surface inclusions in forgings provides a dependable machining base for metal-cutting processes such as turning, milling, drilling, boring, broaching, and shear spinning; and shaping processes such as electrochemical machining, chemical milling, electrical-discharge

machining, and plasma jet techniques. Forged parts are readily made by assembling processes, such as welding, bolting, or riveting. More importantly, single-piece forgings can often be designed to eliminate the need for assemblies. In many applications, forgings are ready for use without surface conditioning or machining. Forged surfaces are suited to plating, polishing, painting, or treatment with decorative or protective coatings.

High strength-to-weight ratio and structural reliability can favorably influence performance, range, and payload capabilities of aircraft. Made of various ferrous, non-ferrous and special alloy materials, forgings are widely used in commercial jets, helicopters, piston-engine planes, military aircraft and spacecraft. Some examples of where a forging's versatility of size, shape and properties make it an ideal component include bulkheads, wing roots and spars, hinges, engine mounts, brackets, beams, shafts, landing gear cylinders and struts, wheels, brake carriers and discs and arresting hooks. In jet turbine engines, iron-base, nickel-base and cobalt-base superalloys are forged into components such as discs, blades, buckets, couplings, manifolds, rings, chambers and shafts.

Strength, toughness and economy are also important in farm implements. In addition to engine and transmission components, key forgings subjected to impact and fatigue range from gears, shafts, levers and spindles to tie-rod ends, spike harrow teeth and cultivator shafts.

The characteristics of forged parts strength, reliability and economy are what makes them ideal for vital automotive and truck applications. Forged components are commonly found at points of shock and stress such as wheel spindles, kingpins, axle beams and shafts, torsion bars, ball studs, idler arms, pitman arms and steering arms. Another common application is in the powertrain, where connecting rods, transmission shafts and gears, differential gears, drive shafts, clutch hubs and universal joints are often forged. Although typically forged from carbon or alloy steel, other materials such as aluminum and micro-alloyed steels are seeing great advances in forged auto and truck applications.

One of the most important application sector for forging processes is the production of parts like dental implants and body prostheses. Up to now, the three most used metals for implants are stainless steel, like CoCr alloys and Ti alloys. Other metals used for implants include amorphous alloys and tantalum (Ta), which has excellent X-ray visibility and low magnetic susceptibility is often used for X-ray markers for stents.

Forging is typically the main manufacturing process used to obtain this kind of products and the selection of the proper parameters and the sub sequential thermo-mechanical processes depends on the mill product which is going to be produced, whether it is a billet, bar, plate or sheet. As example, during the thermo-mechanical processing of 304 stainless steels, instability bands were found when the process temperature are below 1100°C after hammer forging. As well as forming processes, there are several manufacturing methods, which can be considered as advanced processes in the manufacturing of implant materials, such as isothermal forging and isothermal forging. The first offers an improvement in the process of production as well as achieving a better quality of product while the latter reduces die chill and increases metal flow by means the higher temperature of the die.

Forgings of great size are often found in industrial equipment and machinery used by the steel, textile, paper, power generation and transmission, chemical and refinery industries to name just a few. Typical forged configurations include bars, blanks, blocks, connecting rods, cylinders, discs, elbows, rings, T's, shafts and sleeves.

Because of their superior mechanical properties and freedom from porosity, forgings are often associated with the high-pressure applications of the valve and fitting industry. Corrosion and heat-resistant materials are used for flanges, valve bodies and stems, tees, elbow reducers, saddles and other fittings. Oil field applications include rock cutter bits, drilling hardware, and high-pressure valves and fittings.

The powder forging is one of the most commonly specified powder metallurgy processes and it is used to process the same alloys families as forging and to produce components free of internal porosity. This kind of products have similar properties of conventional precision forged parts made from billets.

The P/F process is performed in three steps. During the first one, the preform is pressed as a conventional powder compaction process in which mass, density, and shape of the preform are controlled closely to ensure the requested consistency of the final forged component. Then the preform is sintered with taking care to the reduction of nonmetallic inclusions. At the end, the sintered preform is reheated, then placed in the forging die and, finally, forged to obtain the full density. In this kind of process, the tool shape is well designed to be close to the final geometry of the component, with particular attention to control the material flow in order to fill all cavities.

A complete powder forging process begins with custom-blended metal powders being fed into a die, then being compacted into a “green” shape, which is then ejected from the die. This compact workpiece, called “preform,” is different from the shape the final part will have after the process. After this step the green compact is sintered (solid-state diffused) at a temperature below the melting point of the base material in a controlled atmosphere furnace, creating metallurgical bonds between the powder particles and imparting mechanical strength to the preform.

Subsequently, the heated preform is carried out from the furnace, coated using a high-temperature lubricant and hot-forged. Forging causes plastic flow thickening the preform, strongly reducing its porosity, and reshaping it to its final form.

Powder forging allows producing parts having similar mechanical properties with respect to the base materials. The obtained workpiece can be considered as near net-shape parts requiring only minor secondary machining inasmuch they offer a greater dimensional precision and less flash than conventional precision forgings.

4. Literature review

A major disadvantage in the use of titanium alloys is the high manufacturing costs, especially when most of production processes are based on machining operations, which is at least 10 times higher than machining aluminum [60] due to different reasons. As first, it should be taken into account the high cost of raw material, which can be 3 to 10 times more than aluminum. On the other hand, the machinability of titanium and its alloys is influenced by inherent properties of these materials because of their chemical reactivity and, therefore, their tendency to weld to the cutting tool, leading to chipping and premature failures. All these aspects determine, at the end of the production cycle, a very high buy-to-fly ratio, which limits the enforceability of this manufacturing process to those applications in which the particular operative conditions of components justify their production costs. Hot forming processes, as hot forging or rolling, can help reach this objective by manufacturing of both semi-finished and finished products resulting in lower values of the buy-to-fly ratio with respect to the current practice [61].

However, titanium and its alloys are rather difficult to form into a complex shape because of their limited forging temperature range dictated by large variation of flow stress with thermo-mechanical conditions [62]. As with other common forging alloys, many titanium alloys show a strain-softening at the strain rates typically used in conventional forging processes. Each alloy has a different behavior depending on the microstructure present during the deformation above or below the Beta-transus temperature of that specific alloy. In many alloys, the Alpha case which forms on the outside of the forging has lower ductility and is subject to moderate to severe surface cracking, while Beta alloys are easier to forge than the Alpha+Beta alloys and Alpha alloys. Initial forging temperatures for ingot breakdown are higher than the intermediate forging temperatures, which are higher than the finish forging temperatures. What is referred to as conventional forging occurs at temperatures below the Beta transus, usually in Alpha+Beta region of the alloy. Beta forging occurs at temperatures above the Beta transus. The equiaxed Alpha in a Beta matrix structure, typical of forging operations below the Beta-transus point, redistributes strain and promotes dislocation movement more effectively than acicular Alpha in a transformed Beta microstructure, leading to

increased strain softening in the former. It is clear that the flow stresses describe the lower limit of resistance of titanium alloys to be formed, and present important data to set the process variables like temperature and strain rate. Because of other forging process variables, such as die temperature, lubrication, prior working history and total strain, actual forging pressures can significantly exceed the pure flow stress of any given alloy under similar deformation conditions [15].

In this scenario, a good help may come from the use of computer aided systems like finite element codes which can assist the designers to reach the best process setup by means of numerical simulations showing the process evolution in terms of material flow, cavity filling, requested equipment [63]. However, the different flow behavior of each phase [64] raises, accordingly with the phase transformation kinetics, a serious issue when a complete thermo-mechanical-microstructural characterization is needed. In fact, the most of available commercial FEM codes are able to calculate the plastic flow behavior considering a single-phase thermo-mechanical characterization without taking into account the contribution of each microstructure. Until the considered application is composed by isothermal-type processes, the prediction of flow behavior could be close enough to the real case because of the microstructural asset of the material does not undergo major changes [65, 66]. The actual state of art of constitutive models includes a wide variety of phenomenological and mechanistic laws, which are useful in the case of isothermal processes applied to materials like aluminum, nickel, steels and superalloys [67-71].

On the contrary, if the considered process includes non-isothermal stage involving phase transformations and distributions coming from the thermo-mechanical history, the previous approach may generates a wrong load prediction which, in some cases, could result 2 or 3 times different than the real one. This connection between flow behavior and microstructure evolution during a thermo-mechanical process is a fundamental aspect in following the aim of creating a model able to predict the behavior of a metal during a hot working operation. Currently, not so many models were developed and applied to multi-phasic materials, which are mostly worked in those conditions changing their microstructure, while many papers on the Ti-6Al-4V titanium alloy characterization were produced, in order to create a base for a complex prototype tri-coupled model. This choice is driven by the interest of several industries and, as consequence, a great quantity

scientific data useful to do a comparison between experimental and numerical output in order to test the validity of the numerical model.

4.1. On the flow stress properties of titanium alloys

Vanderhasten et al. [72, 73] investigated the superplastic behavior and mechanical properties such as flow stress, strain hardening and strain at rupture of Ti6Al4V alloy undergone to deformation tests conducted at a strain rate value of 5 10-4 s^{-1} and at various thermal conditions, from room temperature up to 1050°C. Results shows a classical work hardening at room temperature (Figure 29 - a) with a limited ductility. As the temperature is increasing, a gradual softening appears and the post uniform elongation increases. From 650 to 750 °C (Figure 29 - b) the ductility is larger than at the lower test temperatures and no "superplasticity" phenomena are observed. In the end, from 750 to 950 °C (Figure 29 - c) superplastic behavior is observed, with an ultimate strain greater than previous cases.

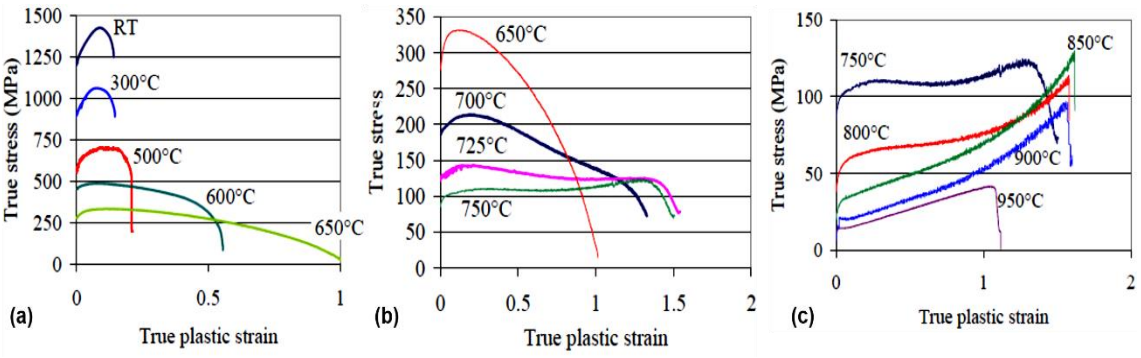

Figure 29: True stress-true plastic strain curves for Ti-6Al-4V alloy tested at 5 10-4 s^{-1} strain rate and various temperature range: from room temperature up to 650°C (a), between 650°C and 750 °C (b) and between 750 °C and 950 °C (c) [72]

Semiatin et al. [74] studied the effect of process variables on flow response hot working of Ti–6Al–4V with a colony Alpha preform microstructure, obtained by means of isothermal hot compression tests between 815 and 955 °C with a height reduction from 40 to 80 %. Two different microstructural conditions were used: microstructure "A"

having 100 mm grain size and 1 mm thick Alpha plates and microstructure B having 400 mm grain size and 1 mm thick Alpha plates.

Measured true stress–true strain curves for Ti–6Al–4V (Figure 30 – a, b, c) exhibited a peak flow stress at relatively low strains followed by moderate to extensive flow softening. The overall degree of flow softening was comparable at 815 and 900°C (Figure 30 – a, b), but slightly less at 955°C (Figure 30 – c). Furthermore, all of the flow curves tended to exhibit a noticeably lower rate of flow softening at strains of the order of 0.7. For a given temperature and strain rate, the flow curves for the A and B microstructures were almost coincident, while at the two lower test temperatures, the curves were within several percent of each other.

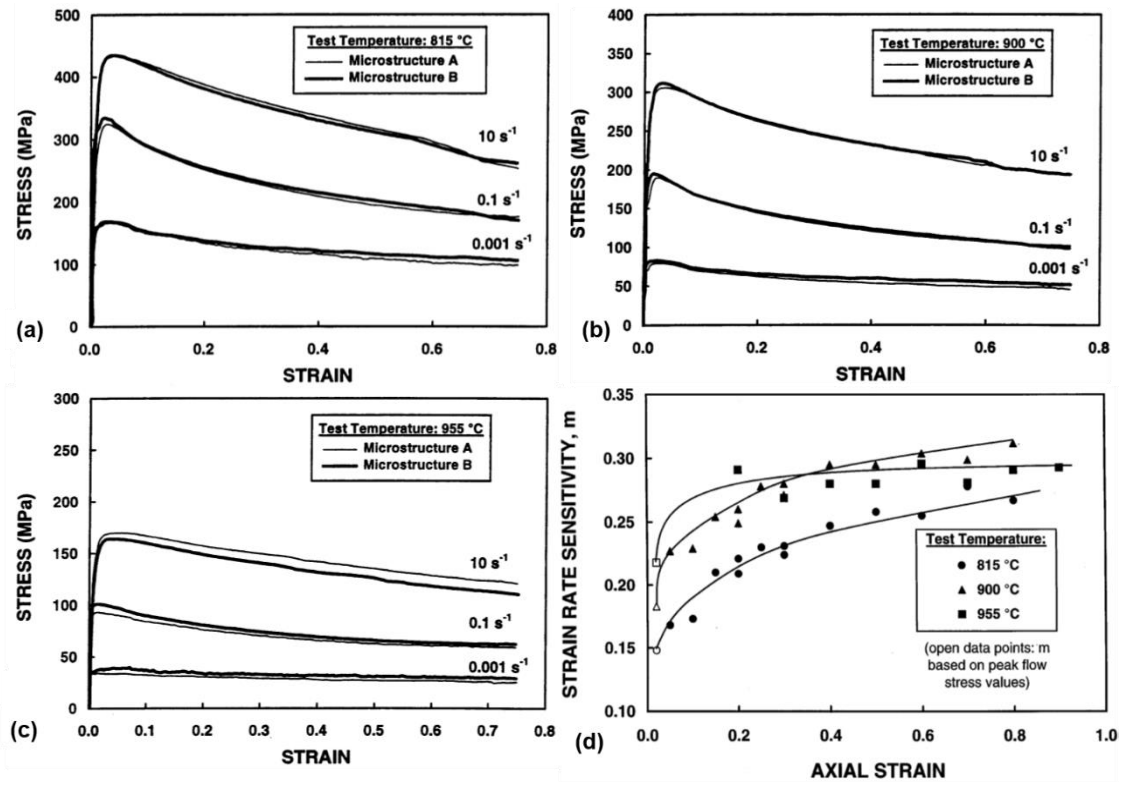

Figure 30: True stress - true strain curves for Ti–6Al–4V alloy with different microstructure at 815 °C (a), 900 °C (b), 955 °C (c) and dependence of the strain rate sensitivity as function of strain with the B microstructure [74]

The measurements of the strain-rate sensitivity (Figure 30 - d) of flow stress were essentially identical for both microstructures, with a slight increase with increasing

temperature and decreasing strain rate. The intensification was most noticeable for tests conducted at 815 and 900 °C while a similar a similar behavior was observed at 955 °C.

Seshacharyulu et al. [75, 76] studied the hot deformation behavior of extra-low interstitial (ELI) grade Ti–6Al–4V alloy with Widmanstatten microstructure in a temperature range from 750 to 1100 °C and a strain rate range from 0.001 to 100 s^{-1}. True stress–true plastic strain curves obtained at 900 °C and different strain rates (Figure 31 - a) showed a continuous flow softening behavior at lower strain rates while oscillations were observed at higher strain rates and this is representative of the material properties in the Alpha+Beta phase region.

The stress-strain curves in the Beta phase field (Figure 31 - b) revealed that the material exhibits steady-state flow at strain rates of 0.1 s^{-1} and lower. The specimens having an equiaxed Alpha-Beta microstructure showed three different evolution of stress-strain curves in the whole observed window of parameters.

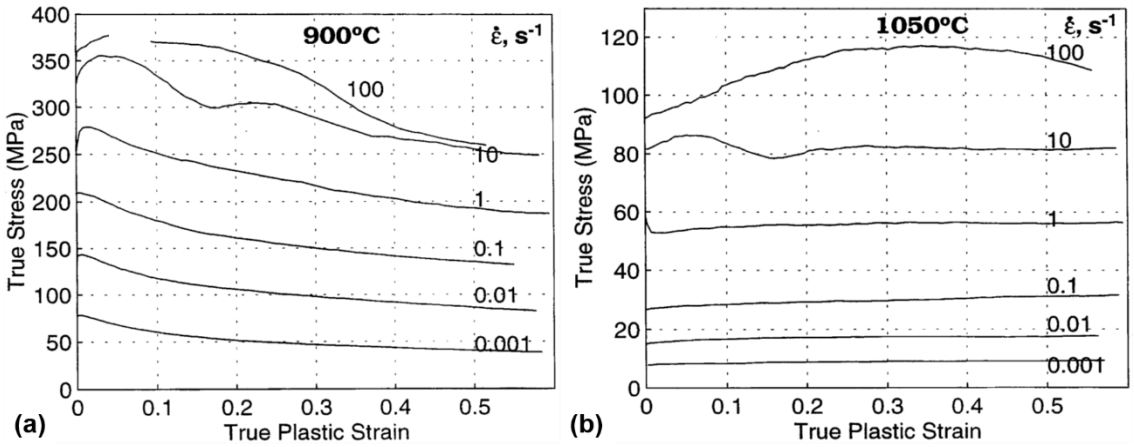

Figure 31: True stress–true plastic strain curves obtained on ELI Ti-6-4 deformed in compression at (a) 900 and (b) 1050oC and at different strain rates [75]

In fact, at strain rates slower than 0.1 s^{-1} the curves indicated a steady-state system, while at higher strain rates and temperature close to Beta field the material exhibited a continuous flow softening behavior. In the end, at high strain rate and temperature above Beta field, oscillatory flow curves were observed. The load-stroke data obtained in compression were processed to obtain true stress-true plastic strain curves using the standard method. The flow stress data obtained at different temperatures, strain rates and strains were corrected for adiabatic temperature rise (Table 3).

Table 3: Corrected flow stress values for Ti-6Al-4V with equiaxed Alpha-Beta preform microstructure as a function of temperature, strain rate and strain [75, 76]

Corrected flow stress [Mpa]									
Strain	**Strain rate [1/s]**	**Temperature [°C]**							
		750	**800**	**850**	**900**	**950**	**1000**	**1050**	**1100**
0.1	**0.0003**	109	60.9	39.5	20.1	14.1	7.3	6.2	5.4
	0.001	166.3	93.4	60.7	31.1	19.8	10.5	7.5	6.1
	0.01	273.5	182.5	125.9	75.1	36	21	15.2	12.2
	0.1	354.2	264.5	191.4	145.8	72.6	33.3	27.4	24.1
	1	446.9	353.4	280.6	196.1	106.1	47.6	46.3	37.3
	10	502	436.9	329	258.9	145.2	73.8	74.8	62
	100	523	455.4	372.7	298.4	188.6	106.7	81.1	73.3
0.2	**0.0003**	98.3	58.5	39.7	20.4	14.7	7.2	6.2	5.4
	0.001	153.4	87.6	58.2	29.9	18.9	10.1	7.7	6.4
	0.01	261	173	119.1	71.2	34.9	20.8	15.8	12.9
	0.1	342.3	249.1	180.9	137.2	70.1	33.3	28.4	25.2
	1	434.2	340	269.2	190.1	103.7	50.2	48.8	39
	10	497.1	431.1	325.8	257.2	142.1	74.9	72.9	61.6
	100	547	469.1	380.8	307.5	196.9	116.5	89.8	79.9
0.3	**0.0003**	91.9	57	38.6	20.5	14.4	7.4	6.4	5.3
	0.001	144.3	84.3	57.1	30.1	18.9	10.1	7.9	6.5
	0.01	252.1	167.1	115.3	68.9	34.3	20.6	16.1	13.3
	0.1	330.2	236.6	173.8	130	67.8	33.5	29.3	25.8
	1	416.2	323.4	255.8	182.6	101.6	52.2	50.5	40.5
	10	465.9	416.7	318.7	253	143.8	79	77.7	65.3
	100	533.2	463.9	376.9	305.3	200.3	121.8	93.2	84.2
0.4	**0.0003**	87.1	54.5	38.4	20.5	14.2	7.6	6.4	5.3
	0.001	134.8	81.6	55.9	30.6	18.9	9.8	8.1	6.7
	0.01	242.1	161.3	112.1	67.1	33.5	20.2	16.3	13.4
	0.1	321.9	227.6	168.3	125.1	65.7	32.9	29.3	26
	1	398.2	310.1	243.4	175.5	98.7	53.7	51.1	40.9
	10	454.7	403.8	309.5	244.9	139	81.1	78	67.3
	100	522.1	451.6	367.8	295.9	195.1	121.2	95.2	85.5
0.5	**0.0003**	83.8	54.5	39.2	20.8	14	7.7	6.5	5.3
	0.001	129.6	79.2	55.8	30.9	18.7	9.7	8.2	6.8
	0.01	233.7	156.2	108.6	65.6	32.7	20.1	16.3	13.4
	0.1	321.3	223.6	164.3	122.3	64.5	32.5	29.5	26.1
	1	403.1	311.9	237	169.7	95.1	54	51.7	41.2
	10	458.2	403.8	297.3	236.7	135.9	80.5	79.7	68.3
	100	513.2	436	349.1	274.3	184.2	116.9	92	83.1

Guan et al. [77] studied the formability of Ti–6Al–4V alloys related to different initial microstructures by means of hot compression tests conducted on alloys with three different initial microstructures established by combinations of several heat treatments for the first time (Figure 32).

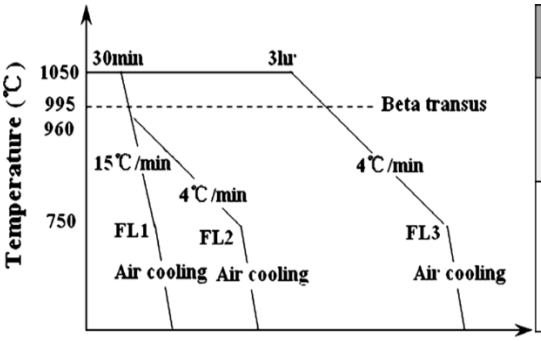

Test properties	FL1	FL2	FL3
Heat treatment	1050 °C/30 min+FC to 750 °C (15 °C/min)+AC to room temperature	1050 °C/30 min+FC to 960 °C (15 °C/min)+FC to 750 (4 °C/min)	1050 °C/3 h+FC to 750 °C (15 °C/min)+AC to room temperature
Microstructure	Small colony size, small lamellar spacing, intergranular beta	Small colony size, large lamellar + AC to the room temperature spacing, intergranular beta	Large colony size, large lamellar spacing, intergranular beta

Figure 32: Processing routes for tests and specifications on obtained microstructure [77]

Results, in terms of flow curves for Ti–6Al–4V alloy, showed peak flow stresses at relative low strains followed flow softening.

The specimen having a material with smaller a lamellar spacing shows larger flow stress than the other two materials, as shown in (Figure 33). Because the deformation mechanism is considered an interaction between dislocations slipping and a lamella counteraction, but it is not based on the function of colony structure. So the effect of colony size on flow stress is not obvious. It is observed that the flow curves for different colony sizes are almost coincident. It is important to note that, after work hardening to a peak stress level, the flow stress decreased at a steadily decreasing rate (flow softening).

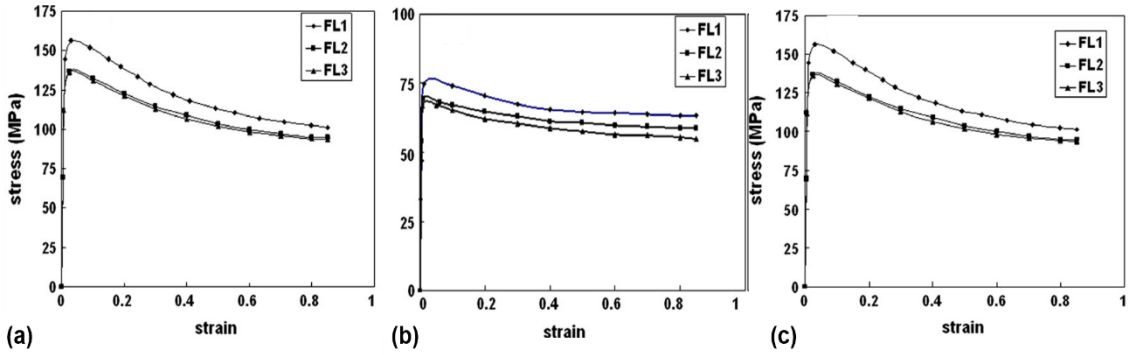

Figure 33: True stress–true strain curves obtained by compression tests for various microstructures: (a) 750 °C, $\dot{\varepsilon}$ = 0:001 s^{-1}, (b) 950 °C, $\dot{\varepsilon}$ = 0:01 s^{-1}, and (c) 850 °C, $\dot{\varepsilon}$ = 10 s^{-1} [77]

Cai et al. [78] investigated the micro-mechanical behavior of Ti–6Al–4V alloy, quenched at 950 °C, by means of micro-indentation experiments performed in a wide range of maximum loads from 200 to 4900 mN and loading speeds from 10, to 103 mN/s. In particular, the young's modulus was carried out using the following equation (Eq. 1).

$$E = (1 - \nu^2)\left(\frac{1}{E^*} - \frac{1 - \nu_i^2}{E_i}\right)^{-1} \quad \text{Eq. 1}$$

$$E^* = \sqrt{\frac{\pi}{2\beta}} \cdot \frac{S}{\sqrt{A}} \quad \text{Eq. 2}$$

Where A is the contact area coming from hardness tests, K is a constant, where E* is reduced modulus, β is a correction factor, ν is the Poisson's ratio of the specimen, E_i and ν_i are the Young's modulus and the Poisson's ratios of the indenter respectively. Results (Figure 34 – a, b) are in according with previous works [79].

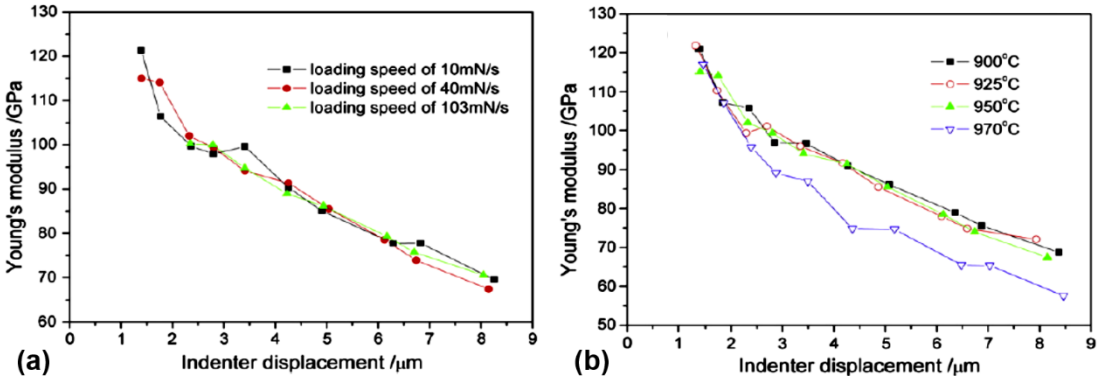

Figure 34: Influence of loading speed (a) and quenching temperature (b) on micro-hardness for Ti-6Al-4V alloy [78]

Majorell at al. [80] investigated the plastic deformation of Ti–6Al–4V alloy at within a strain rate range from 10^{-3} to 10 s^{-1} and a temperature range from 650 to 1340 K, showing that the flow stress of this alloy is strongly dependent on both temperature and deformation rate, with the temperature effect becoming negligible in the upper part of the temperature range investigated.

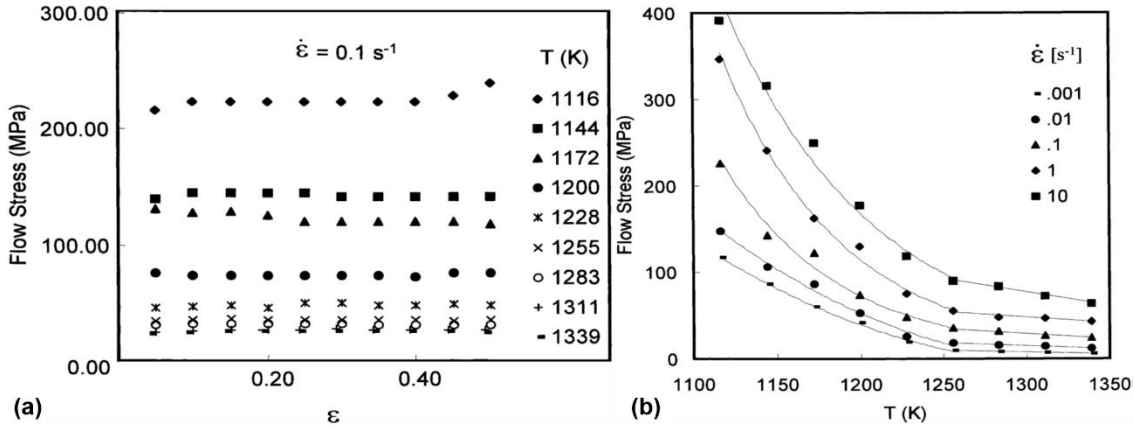

Figure 35: Stress–strain curves at strain rate of 0.1 s^{-1} and various temperatures (a) and average values of flow stress vs. temperature at different strain rates within a strain range from 0.05 to 0.5 [80]

Results, in terms of typical stress-strain curves obtained at various temperatures (Figure 35 - a) with a strain rate of 0.1 s^{-1} showed no significant yield point behavior between the elastic regime and the plateau in the stress-strain curve, as well as no serrated flow associated with dynamic strain aging at any temperature and rates investigated. Flow stress vs. temperature curves (Figure 35 - b) within 0.05 and 0.5 strain range exhibited a strain rate sensitivity is observed at all temperatures, with an essentially constant flow stress at strains larger than 0.05, while no yield point was observed at lower strains. Furthermore, the results showed a significant reduction in the flow stress with temperature up to 1255 K while the flow stresses was observed to be strain rate dependent over the whole temperature domain.

Luo et al. [81] studied the deformation behavior during isothermal compression tests of Ti–6Al–4V alloy in a temperature range from 1093 to 1303 K and strain rates from 0.001 to 10 s^{-1}. Based on the experimental results in isothermal compression of Ti–6Al–4V alloy, the effect of processing parameters on the strain rate sensitivity and the strain hardening exponents were analyzed.

The obtained results showed that the strain rate sensitivity exponent at a strain of 0.7 and strain rate of 0.001 s^{-1} firstly tends to increase with the increasing of deformation temperature until maximum value is obtained at a temperature regime close to the Beta-transus, while at higher temperatures it drops to lower values (Figure 36 – a, b). The evolution of strain in affected by both temperature and strain rate which is negative at 0.2 strain for all strain rates and most of thermal conditions and becomes positive at

temperatures above 1243 K. Basing on this analysis, the softening effect in Alpha+Beta phase field is significantly different from those in Beta phase field of Ti–6Al–4V due to the competition between thermal softening and work hardening. Therefore, predominant softening effect in Alpha+Beta phase field leads to the strain hardening exponent (Figure 36 – c, d), which is mostly negative. However, the strain hardening exponent becomes strongly dependent on the strain rate at the strains of 0.7 with a decreasing as the strain rate increase at temperatures below 1263 K.

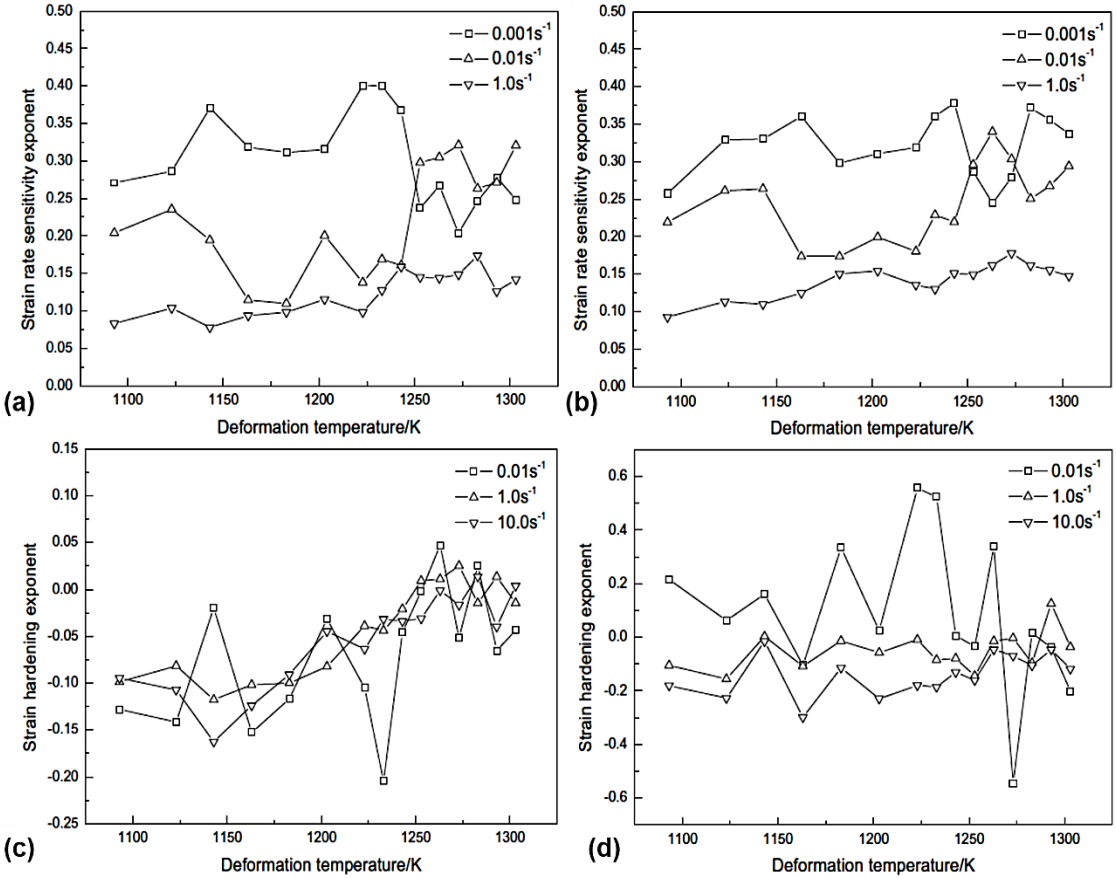

Figure 36: Strain rate sensitivity exponent as function of temperature at the strains of 0.7 (a) and 0.2 (b); strain hardening sensitivity exponent as function of temperature at the strains of 0.7 (c) and 0.2 (d) [81]

4.1.1. Developed constitutive models

Modeling of flow stress behavior for thermo-mechanical forming processes always needs to define a constitutive model for the material involved. Many models are available

in order to predict the changes in flow stress depending on the process conditions, temperature and strain rates [82]. It is possible to find in literature physically-based internal state variable models like Zerilli-Armstrong [83] or empirical models like Zener-Hollomon [84], Johnson-Cook [85], Norton-Hoff [86], Obikawa-Usui [87] and Hansel-Spittel [88], Khan–Huang–Liang [89, 90] which are used to correlate the material flow stress to strain, strain rate and temperature. The parameters identified for these laws are usually fitted to the stress–strain curves. All these models are currently applied on simulation of different manufacturing processes, from machining to hot forming.

Kim et al. [91-93] studied the high-temperature deformation mechanisms of Ti–6Al–4V alloy with a transformed microstructure, by means of inelastic-deformation theory, using load-relaxation tests conducted on samples with a lamellar structure containing different Alpha-platelet thicknesses from 715 up to 900 °C. Experimental results were used to determinate inelastic-deformation equation describing grain-matrix deformation. The constitutive relations for the plastic strain rate (Eq. 3) of both Alpha and Beta phases was formulated as kinetic equations for the mechanical activation process of the leading dislocation by the internal stress (Eq. 4).

$$\left(\frac{\sigma_f^*}{\sigma^I}\right) = exp\left(\frac{\dot{\varepsilon}_f^*}{\dot{\varepsilon}_f}\right)^p \qquad \textbf{Eq. 3}$$

$$\dot{\varepsilon}_f = \nu^I \left(\frac{\sigma_f^*}{G}\right)^{n^I} exp\left(\frac{-Q_f^I}{RT}\right) \qquad \textbf{Eq. 4}$$

Where σ^I is the internal stress due to the long-range interaction among dislocations, $\dot{\varepsilon}_{\alpha,\beta}$ is the plastic strain rate of the phase f, p and n^I are material constants, $\dot{\varepsilon}_f^*$ is the internal-strength variable and its conjugate reference strain rate, ν^I is the jump frequency, Q_f^I is the activation energy of the generic phase and G is internal modulus.

Tension tests revealed that the ductility at 0.1 s^{-1} was very low (Figure 37 - a), while at a nominal strain rate of 10^{-4} s^{-1} (Figure 37 - b), all of the specimens showed larger deformations, as expected considering the values of strain-rate sensitivity between 10^{-4} and 10^{-4} s^{-1}. All of the stress–strain curves obtained at 815 °C exhibited a peak stress at low strains and noticeable flow softening irrespective of strain rate and microstructure.

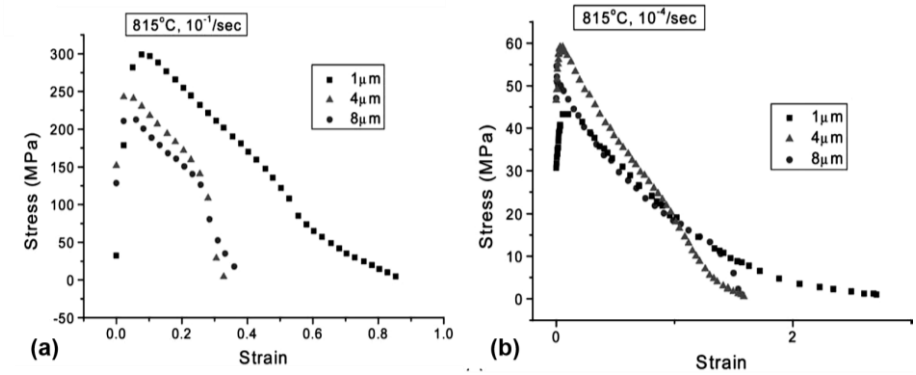

Figure 37: Stress–strain curves obtained by tensile test at 815 °C with 10^{-1} s^{-1} (a) and 10^{-4} s^{-1} (b) strain rates [91]

Giuliano [94] determined the material constants of superplastic alloys from a free forming test at constant pressure and developed a constitutive equation (Eq. 5) based on power law with hardening variables in order to fit experimental data on the flow stress of Ti-6Al-4V alloy at 1200 K.

$$\dot{\varepsilon} = \left(\frac{\sigma - R - k}{K}\right)^{\frac{1}{m}} d^{-\gamma} \qquad \textbf{Eq. 5}$$

Where c the hardening index due to grain growth, k the yield stress and R an isotropic hardening variable.

Results (Figure 38) show that the induced strain rate at p = 0.10 MPa is smaller than the strain rate values at the pressure of 0.18 MPa. On the other hand, the average grain size increases at the smaller pressure since the process time is longer.

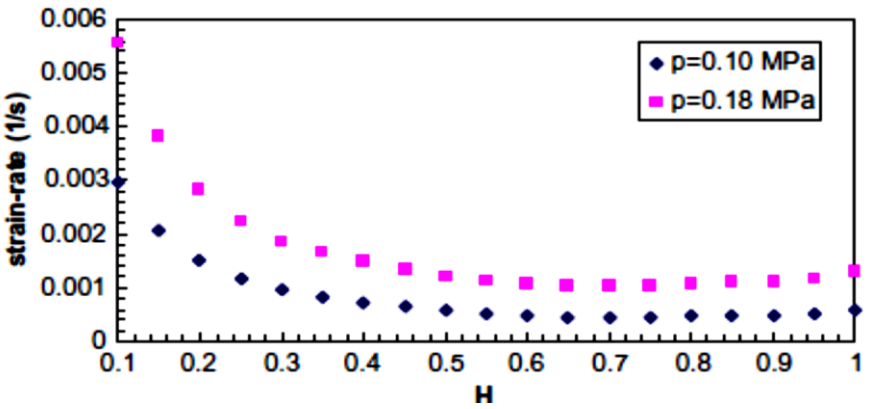

Figure 38: strain rate evolution at different pressure vs. dome height [94]

Cai et al. [95] studied the workability of Ti–6Al–4V alloy, during isothermal hot compression tests in a range of temperatures from 800 up to 1050 °C and strain rate of 0.0005 s^{-1}. In addition, developed a constitutive equation (Eq. 6, Eq. 7) for Alpha+Beta and Beta regimes was developed. The effects of temperature and strain rate on deformation behavior is represented by Zener–Holloman parameter in an exponent-type equation while the influence of strain was included by considering its effect on material constants.

$$\dot{\varepsilon} = AF(\sigma)exp\left(-\frac{Q}{RT}\right) \qquad \textbf{Eq. 6}$$

$$F(\sigma) = \begin{cases} \sigma^{n'} & \alpha\sigma < 0.8 \\ exp(\beta\sigma) & \alpha\sigma > 1.2 \\ [\sin h(\alpha\sigma)]^{n} & for\ all\ \sigma \end{cases} \qquad \textbf{Eq. 7}$$

Where $\dot{\varepsilon}$ is the strain rate , R is the universal gas constant, T is the absolute temperature, Q is the activation energy of hot deformation, A, n, n', α and β are the materials constants.

Results (Figure 39 –a, b, c), in terms of predicted flow stress, demonstrated that the constitutive equation could track the experimental data of Ti–6Al–4V alloy under most deformation conditions in Alpha+Beta and Beta phase regions. However, some deformation conditions in Alpha+Beta phase region showed a significant variation between experimental and computed flow stress data (Figure 39 –a, b).

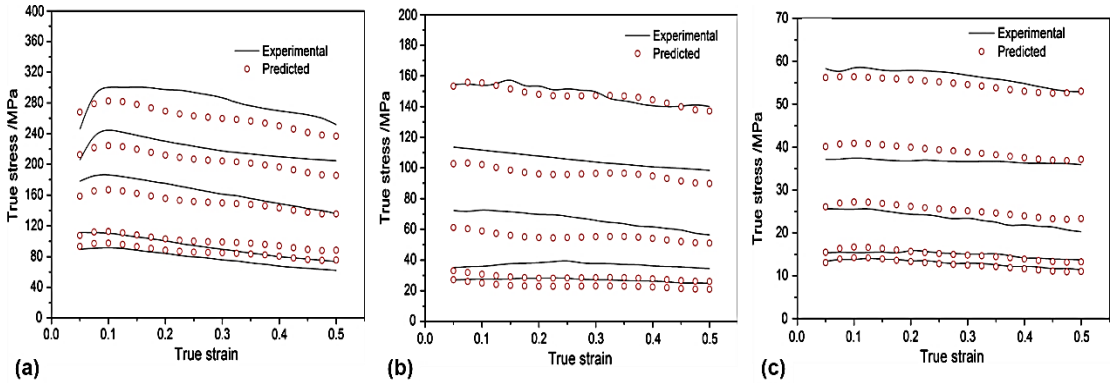

Figure 39: Comparison between experimental and predicted flow stress at 800 °C (a), 900 °C (b) and 1000 °C (c) [95]

Šlais et al. [96] studied the influence of strain rate on the mechanical behavior of the Ti-6Al-4V titanium alloy under static loading conditions in which the specimens were deformed at high strain rates using the device for the Taylor anvil test.

The results were used as a reference for the comparison of experiment and computer simulation in the LS-Dyna 3D software and determinate the parameters of Johnson-Cook [85] equation in order to obtain the best possible agreement between deformed shapes obtained by numerical simulation and by real experiment (Figure 40 - b). The best calculated parameter set is shown in (Figure 40 - a). The m exponent was determined such that the stress values for a particular temperature and medium strain rate calculated by Johnson-Cook equation correspond with the values from SHPBT test.

(a)

A [Mpa]	802
B [Mpa]	995
C	0.01
n	0.5
m	0.6

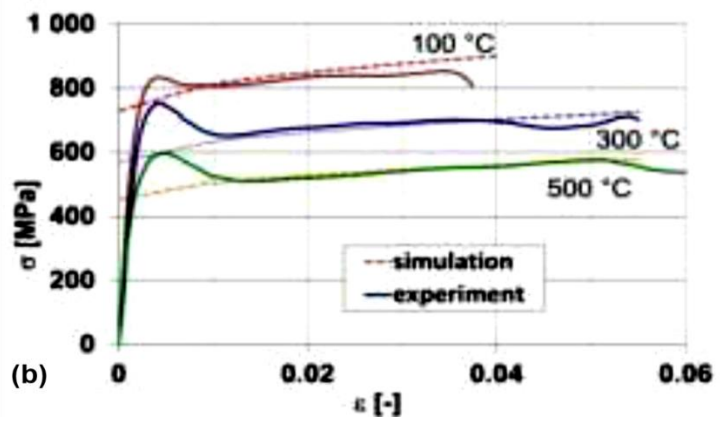

Figure 40: Comparison of stress-strain curves from Split Hopkinson pressure bar test and calculated using Johnson–Cook equation [96]

Kıranlı [97] determined the JC [85] flow stress and damage parameters of a biomedical grade Ti6Al4V alloy by means of quasi-static (from 10^{-3} up to 0.1 s^{-1}) and high strain rates tests (from 300 up to 1000 s^{-1}) within a temperature range from 25 up to 1150 °C, using both compression and tension SHPB tests. Results (Figure 41 – a, b, c) showed that the tested alloy flow stresses were found to increase with increasing strain rate for both compression and tension tests (Figure 41 – a, b) as proof of the strain rate sensitive of the considered material. High temperature test conducted at quasi-static strain rate showed that the stress values decreased greatly after about 800 °C due to Alpha-to-Beta phase change so that two different JC material models valid between 25 and 600 °C and 800 to 1150 °C were carried out (Figure 41 – c).

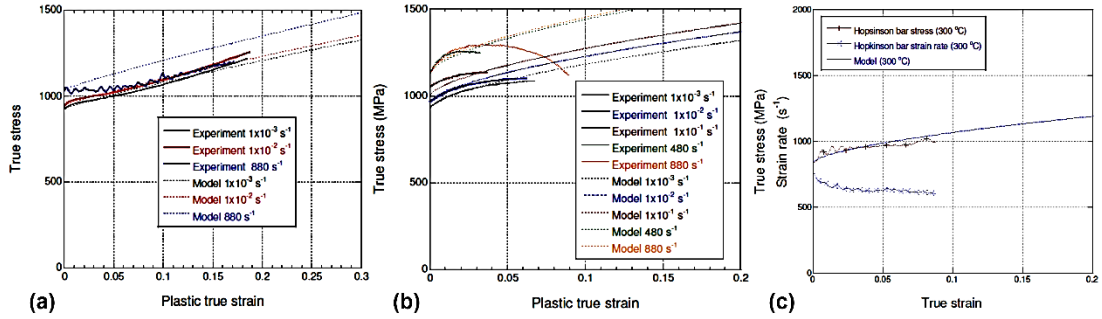

Figure 41: Comparison between experimental tests and numerical model: compression (a), tensile (b) and high temperature (c) test [97]

However, the determined JC parameters were found (Table 4) to be well agreed with the literature except the model obtained from the compression tests. The reduced strain rate sensitivity parameter of the model in compression was attribute to adiabatic heating during tests.

Table 4: JC parameters for both tensile and compression tests conducted at different temperatures [97]

Test type	A [Mpa]	B [Mpa]	c	n	$\dot{\varepsilon}_0$ [s^{-1}]	m	T_r [°C]
Compression 25 - 600 °C	**927**	**1150**	**0.0087**	**0.8674**	**10^{-3}**	**0.753**	**25**
Tensile 25 - 600 °C	**927.9**	**1062.5**	**0.0167**	**0.6214**	**10^{-3}**	**0.753**	**25**
Compression 800 - 1100°C	**30**	**50**	**0.0167**	**0.6214**	**10^{-3}**	**0.423**	**800**

Dorogoy et al. [98] carried out the Johnson-Cook [85], including the identification of the thermal softening effect in quasi static and dynamic loading as well as and the strain rate hardening effect in dynamic loading material parameters, using the shear compression specimen (SCS). The used method is of a hybrid experimental – numerical type composed by a quasi-static testing at room temperature, a quasi-static testing at a higher temperature and a dynamic testing at room temperature. An overall very good agreement is observed (Figure 42), with the exception that the current work predicts that the material is more strain rate sensitive since the value of C is almost three times the value obtained in other works [99, 100].

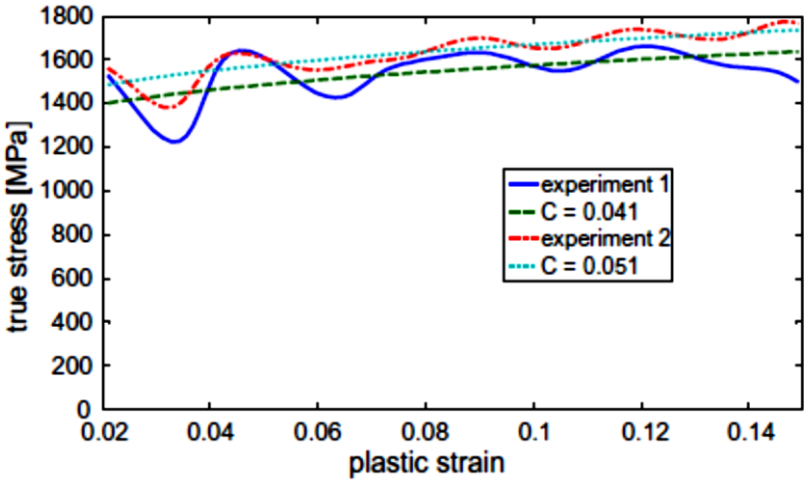

Figure 42: Stress – plastic strain curves at 3000 s^{-1} strain rate compared to the fitted JC model with C=0.041 and 0.051 [98]

Donald [101] The report describes studies of the deformation behavior of Ti-6Al-4V alloy. The obtained results at high strain rates and large strains using the split Hopkinson pressure bar method were used to evaluate the capabilities of the Johnson-Cook model to represent the deformation and failure response of Ti-6Al-4V under typical conditions of engine containment and the influence of uncontained engine debris on aircraft structures. This model was used in the LSDYNA3D finite element code and the results simulations were compared to experimental data in order to define a set of material constants for the strength component of the Johnson-Cook model for Ti-6Al-4V titanium alloy.

Guo et al. [102] developed a computer model (Eq. 8, Eq. 9, Eq. 10, Eq. 11) for the calculation of high temperature flow stress curves of titanium alloys which takes into account two competing mechanisms for deformation, either dominated by dislocation glide or dominated by dislocation climb.

$$\boldsymbol{\varepsilon = (\dot{\varepsilon}_p + \dot{\varepsilon}_s + \dot{\varepsilon}_t)t} \qquad \textbf{Eq. 8}$$

$$\boldsymbol{\dot{\varepsilon}_p = \frac{\dot{\varepsilon}_s}{K_0} ln\left[1 + \frac{\dot{\varepsilon}_i - \dot{\varepsilon}_s}{\dot{\varepsilon}_s}(1 - e^{-K_0 t})\right]} \qquad \textbf{Eq. 9}$$

$$\boldsymbol{\dot{\varepsilon}_s = AD\left(\frac{Gb}{RT}\right)\left(\frac{\sigma}{E}\right)^{n'}} \qquad \textbf{Eq. 10}$$

$$\dot{\varepsilon}_t = \left[2C_d t\left(\frac{t}{R_l}\right)^4\right]\dot{\varepsilon}_s \qquad \text{Eq. 11}$$

Where $\dot{\varepsilon}_p$ is the primary creep, $\dot{\varepsilon}_s$ is the secondary creep, $\dot{\varepsilon}_i$ is the initial creep, $\dot{\varepsilon}_t$ is the tertiary creep, K_0 and A are material constants, C_d is a material damage constant, R_l is the rupture constant, D the diffusion coefficient, b the Burgers vector, G is the shear stress, E is the Young's modulus of the matrix at the creep temperature and n' is related to the mechanism of the creep, equal to 4 for both Alpha and Beta phases in titanium alloys.

Results in terms of comparison between experimental data and model prediction (Figure 43) showed a good a good agreement in most of cases.

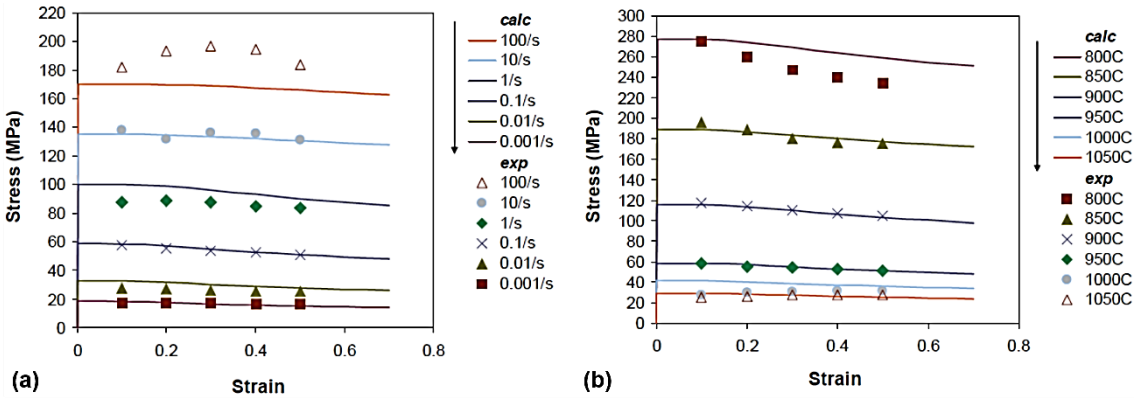

Figure 43: Comparison between experimental and calculated flow stress curves for Ti-6Al-4V alloy at 950ºC and various strain rates (a), at 0.1/s strain rate and various temperatures [102]

Babu et al. [103] investigated the plastic deformation of the Ti-6Al-4V alloy with a range of strain rates from 0.001 s^{-1} to 1 s^{-1} and temperatures between 20 and 1100 °C. Pertinent deformation. Moreover, a physically founded constitutive model based on the evolution of immobile dislocation density and excess vacancy concentration was developed. Isothermal compression tests were used to calibrate the parameters of this model which is capable of describing plastic flow of the alloy in a wide range of temperature and strain rates by including the dominant deformation mechanisms like dislocation pile-up, dislocation glide, thermally activated dislocation climb, globularization, etc. In order to compute evolution of the material state, dislocation

density and vacancy concentration were considered as internal state variables and an incompressible von Mises model for plasticity as used. The flow stress model (Eq. 12) was assumed as consisted of a stress contribution from the long-range interactions of the dislocation substructure and a friction stress needed to move dislocations through the lattice and to pass short-range obstacles.

$$\boldsymbol{\sigma_y = \left[m\alpha G b \sqrt{p_i} \right] + \sigma^*} \qquad \textbf{Eq. 12}$$

Where *m* is the Taylor orientation factor translating the effect of the resolved shear stress in different slip systems into effective stress and strain quantities; α is a proportionality factor, b is the Burger's vector; p_i is the immobile dislocation density; G is the shear factor and σ^* is the friction stress contribution.

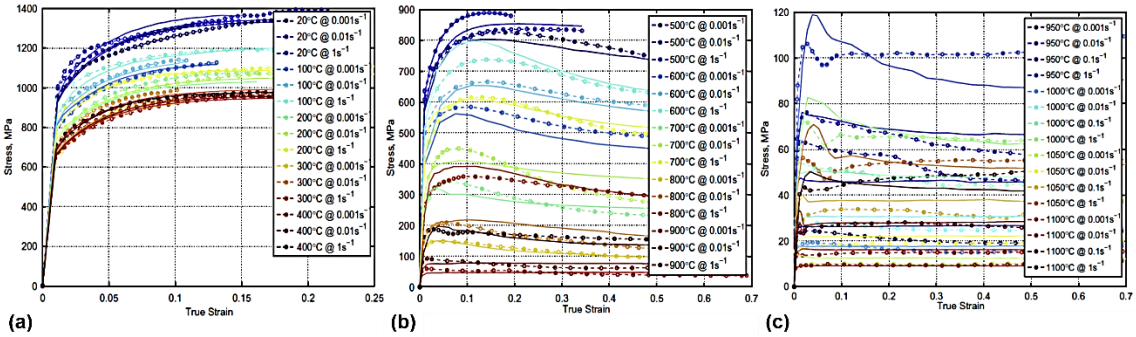

Figure 44: Comparison between experimental and calculated stress from 20 to 400 °C (a); from 500 to 900 °C (b) and from 950 to 1100 °C (c) [103]

The comparison with experimental data showed the capacity of the model to compute the flow stress of material with different thermal and strain rate conditions (Figure 44).

Nemat-Nasser et al. [104] conducted a systematic comparative study of the dynamic thermo-mechanical behavior of Ti-6Al-4V alloy with three different microstructure conditions. Experiments were performed over a wide range of strain rates from 0.001 up to 7000 s^{-1} and temperatures from 77 to 1000 K. It was proposed a physically based model (Eq. 13) divided into two parts, one due to the athermal resistance to the motion of dislocations and the other associated with the thermally activated crossing of obstacles by dislocations.

$$\tau = \tau_A^0 \gamma^0 + \tau^0 \left\{ 1 - \left[\frac{k}{G_0} T \left(ln \frac{\dot{\gamma} f(\gamma, T)}{\dot{\gamma}_0} \right) \right]^{\frac{1}{2}} \right\} \quad \text{Eq. 13}$$

$$f(\gamma, T) = 1 + a_0 \left[1 - \left(\frac{T}{T_m} \right)^2 \right] \gamma \quad \text{Eq. 14}$$

Where τ is the plastic stress, γ is the plastic strain, $\dot{\gamma}$ is the plastic strain rate, T_m is the melting temperature, a_0 is a constant depending on the initial density of dislocations, G_0 is the total energy barrier that a dislocation must overcome by its thermal activation in the absence of an applied stress, τ_A^0 is the initial dislocation density, γ^0 is the initial strain, τ^0 and k are material constants.

In the absence of dynamic strain aging the model predictions are in good accord with the experimental results (Figure 45 – a, b).

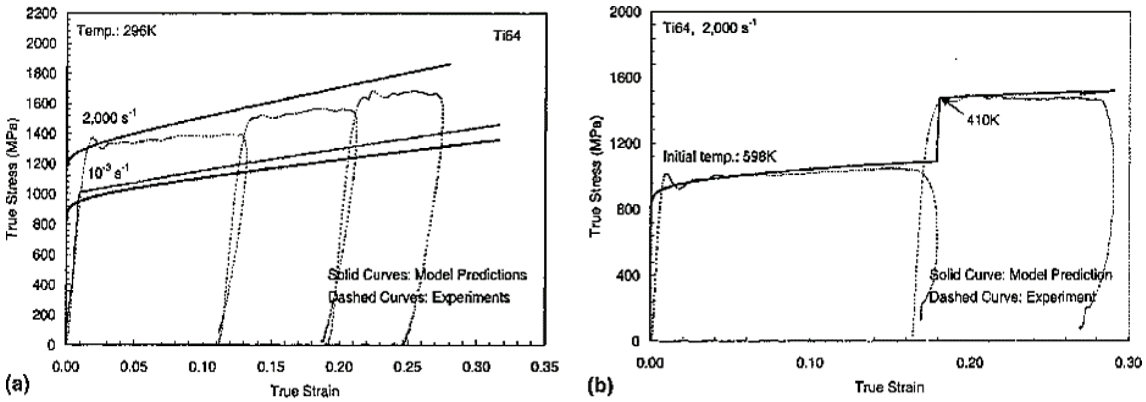

Figure 45: Comparison of models predictions with experimental results with 296 K (a) and 598 K (b) initial temperature for Ti-6Al-4V alloy [104]

Bruschi et al. [105] investigated the workability of Ti-6Al-4V titanium alloy by means of hot compression tests carried out in a temperature range from 880 to 950 °C and strain rate range from 1 to 50 s^{-1}, correlating the effect of microstructural characteristics of the deformed specimens with test temperature, total strain and strain rate. Moreover, a constitutive equation (Eq. 15) for the material behavior prediction for the considered extended strain rate range was defined considering the Zener-Hollomon parameter (Eq.

16), the inverse of strain rate sensitivity *n* (Eq. 17) and two constant, α and A, determined as functions of strain rate and stress (Eq. 18, Eq. 19).

$$\sigma = \frac{1}{\alpha} ln \left\{ \left(\frac{Z}{A}\right)^{\frac{1}{n}} + \left[\left(\frac{Z}{A}\right)^{\frac{2}{n}} + 1\right]^{\frac{1}{2}} \right\} \gamma \quad \text{Eq. 15}$$

$$Z = \dot{\varepsilon}\, exp\left(\frac{Q}{RT}\right) \quad \text{Eq. 16}$$

$$n = \frac{1}{m} = \left.\frac{\partial log\dot{\varepsilon}}{\partial log\sigma}\right|_{\dot{\varepsilon},T} \quad \text{Eq. 17}$$

$$\alpha = \left(\frac{2.303}{n}\right) \left.\frac{\partial log\dot{\varepsilon}}{\partial \sigma}\right|_{\dot{\varepsilon},T} \quad \text{Eq. 18}$$

$$A = \frac{Z}{[sinh(\alpha\sigma)]^n} \quad \text{Eq. 19}$$

Where Z is the Zener-Hollomon parameter defined as where Q is the activation energy and R the gas constant.

This model does not take into account the material behavior during non-isothermal operations.

Calamaz et al. [106] developed a new material constitutive law, based in JC generalized model, in order to analyze the chip formation and shear localization during machining operations of titanium alloys, assuming that the chip segmentation is only induced by adiabatic shear banding, without material failure in the primary shear zone. This model takes into account the influence of strain, strain rate and temperature on the flow stress and also introduces a strain softening effect, and was included through a subroutine within the commercial FE code Forge™ to run thermo-mechanical simulations. This variation of classical JC is more sensitive to temperature softening and was mostly developed for machining operations but the quality of load prediction could be improved and applied to bulk forming processes. The constitutive equation is a tanh variation of conventional JC (Eq. 20).

$$\sigma = \left[A + B\varepsilon^{n}\left(\frac{1}{e^{\varepsilon^{a}}}\right)\right]\left(1 + C ln\frac{\dot{\varepsilon}}{\dot{\varepsilon}_0}\right)\left[1 - \left(\frac{T - T_r}{T_m - T_r}\right)^{m}\right] \left\{D + (1 - D)\tanh\left[\frac{1}{(\varepsilon + S)^{c}}\right]\right\} \quad \text{Eq. 20}$$

$$D = 1 - \left(\frac{T}{T_m}\right)^{d} \quad \text{Eq. 21}$$

$$S = \left(\frac{T}{T_m}\right)^{b} \quad \text{Eq. 22}$$

Where A, B, C, n, m, T_r and T_m are the conventional JC model parameters while a, b, c and d are material constants.

Calamaz et al. [107] modified the previous model in order to obtain a better load prediction during machining processes with respect to the prior version. In this study, the JC model was modified improving the strain softening of the power law and limiting the influence of thermal effect on material flow (Eq. 23).

$$\sigma = \left[A + B\left(\frac{1}{\dot{\varepsilon}}\right)^{a}\varepsilon^{[n - 0.12(\varepsilon\dot{\varepsilon})]^{a}}\right]\left(1 + C ln\frac{\dot{\varepsilon}}{\dot{\varepsilon}_0}\right)\left[1 - \left(\frac{T - T_r}{T_m - T_r}\right)^{m}\right] \quad \text{Eq. 23}$$

This new variation of the model was able to give a good prediction of chip morphology segmentation frequency and cutting forces as well as the strain distribution into the simulated chip was in good agreement with the deformed microstructure of the chip obtained by experimental tests. Moreover, it was demonstrated that the cutting forces are not sensitive to the nature of the friction contact between the chip and the tool during the machining process. In this case, the new model is mostly intended to machining operations due to the better strain rate sensitivity with respect to those effects coming from the thermal field.

Xiao et al. [108] conducted uniaxial tests on Ti–6Al–4V alloy sheet with a temperature range from 650 to 750 °C and a strain rate range from 0.0005 to 0.05 s^{-1} up to a 25% length elongation of the specimen. After obtaining experimental data about true stress-strain curves, the Arrhenius-type equation used in modeling and charactering the

hot deformational behavior by means of four different material constants which were determined as fourth-order polynomial functions of true strain, correlating the flow stress to strain, strain rate and temperature. The comparison with experimental data showed a good precision of the constitutive model in predicting the flow stress with an overall averaged mean error of 6% about. The model calibration is referred to a temperature range in which the most of initial phase distribution is preserved and it could be considered like parent material with respect to the modifications occurring during high temperature processes.

However, very few studies were developed on the possibility to extend the same approach to those case in which the microstructure of considered metal changes during the process, influencing the flow behavior. In the case of two-phase titanium alloys, the macroscopic flow behavior is related to the characteristics of individual phases and the deformation rate and flow stress may vary from one phase to the other as well as within the individual micro-constituents. Modeling the relationship among microstructure changes, plastic deformation behavior and processing conditions, like temperature and deformation rate, is of crucial importance in controlling the forming process evolution of hot worked components. The coexistence of HCP Alpha phase and BCC Beta phase causes significant heterogeneous deformation, and complicates the microstructure development as well as the flow stress [109]. However, the knowledge in non-uniformities and inhomogeneities of local deformation, lattice rotations, cavitation, and crystallographic texture, which are the major variables controlling alloy final properties of a metal, is critical in understanding the material properties [64, 110].

Fan et al. [109] proposed an internal-state-variable based self-consistent constitutive model for predicting the flow stress during hot working of two-phase Ti-6Al-4V titanium alloy in both single-Beta region and two-phase region (Eq. 24, Eq. 25, Eq. 26). The constitutive equations of constituent phases were implemented into a viscoplastic self-consistent scheme to capture the heterogeneous deformation in the aggregate and predicting its overall response.

$$\boldsymbol{\sigma = M\tau} \qquad \textbf{Eq. 24}$$

$$\boldsymbol{\dot{\gamma} = M\dot{\varepsilon}} \qquad \textbf{Eq. 25}$$

$$\frac{\dot{\gamma}}{\dot{\gamma}_0} = \left\{ \frac{\tau}{g_0 + g_{forest} + g_{HP}} \right\}^{\frac{1}{m}} = \left\{ \frac{\tau}{\left[k\, exp\left(-\frac{T}{B}\right)\right] + \left[\chi G b \sqrt{\rho}\right] + \left[K_{HP} d^{-\frac{1}{2}}\right]} \right\}^{\frac{1}{m}} \quad \text{Eq. 26}$$

Where σ is the flow stress of a polycrystal expressed in terms of the critical resolved shear stress τ, M is the Taylor factor, $\dot{\gamma}$ is the shear rate, $\dot{\gamma}_0$ is the reference shear rate, g_0 is slip resistance related to the dislocation microstructure, g_{forest} is the working hardening due to dislocation interactions, g_{HP} is the barrier effect of grain boundaries, m is the strain rate sensitivity, T is the working temperature, k is the strength coefficient which links to the solution density of the alloying elements, B and χ are material constants, G is the shear modulus, b is the magnitude of the Burgers vector, K_{HP} is the Hall-Petch coefficient and d is the grain size.

Predictions of the model are in good agreement with experimental results of the Ti–6Al–4V alloy, following the behavior of two-phase titanium alloys undergoing to hot working processes with a correlation among flow stress, temperature, strain rate and content of alloying elements (Figure 46).

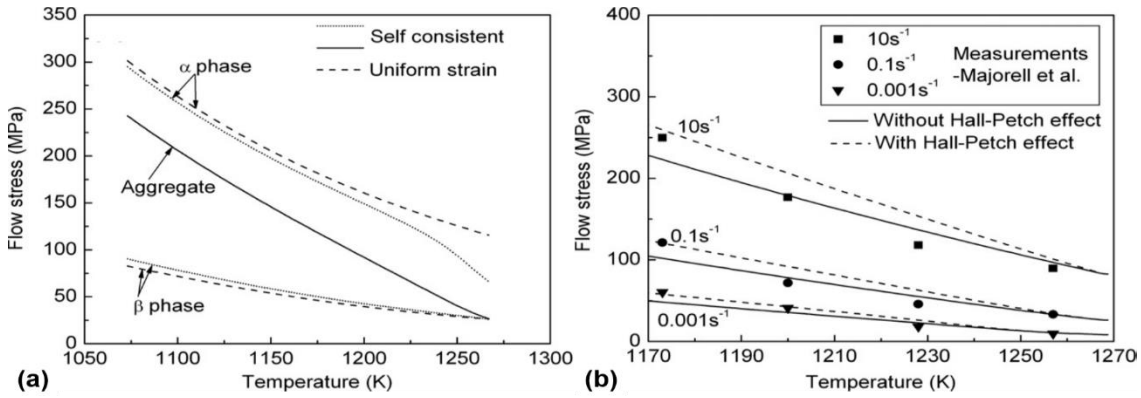

Figure 46: Predicted individual phase flow stress at a strain rate of 0.1 s^{-1} (a) and aggregate flow stress in the upper two-phase region without Hall-Petch effect (b) for Ti–6Al–4V alloy [109]

Semiatin et al. [64] developed a self-consistent model to predict the plastic flow behavior during hot working of Alpha/Beta titanium alloys having equiaxed Alpha

microstructure as function of the flow behavior and volume fractions of each phase. The proposed constitutive equation includes composition-dependent strength coefficients, which were calculated for both Alpha and Beta phases though the measurements of specific compositions and volume fractions of phases during hot working conditions. This approach was used to calculate the flow stress during hot isothermal deformation, taking into account the effect of temperature transients, high strain-rate values and volume fractions changes due to thermal conditions. The results showed a good quality of prediction under isothermal conditions but a lower value due to retention of a lower-than equilibrium volume fraction of Alpha phase during the cooling transient. However, this approach results very interesting due to the mechanical properties definition of each phase as function of alloying elements and its correlation with temperature.

The previous model was improved by Kim et al. [111] which considered high-temperature compression tests were conducted at various temperatures for the Ti-6Al-4V alloy with an equiaxed microstructure. For the linearly visco-plastic case, the constitutive relation of each of the two phases was assumed to have of the following form (Eq. 27)

$$\boldsymbol{\sigma_i = k_i^L \dot{\varepsilon}_i} \qquad \textbf{Eq. 27}$$

$$\frac{\boldsymbol{k_{\alpha+\beta}^L}}{\boldsymbol{k_\alpha^L}} = \frac{\mathbf{1}}{\mathbf{6}}\left\{\mathbf{3} - \mathbf{2}\frac{\boldsymbol{k_\beta^L}}{\boldsymbol{k_\alpha^L}} + \mathbf{5}(\mathbf{1}-\boldsymbol{f})(\boldsymbol{\rho}-\mathbf{1}) + \sqrt{[\mathbf{3}-\mathbf{2}\boldsymbol{\rho}+\mathbf{5}(\mathbf{1}-\boldsymbol{f})(\boldsymbol{\rho}-\mathbf{1})]^2 + \mathbf{24}\boldsymbol{\rho}}\right\} \qquad \textbf{Eq. 28}$$

Where σ_i and $\dot{\varepsilon}_i$ the flow stress and strain rate of the single phase, f is the volume fraction of the phase and k_i^L is the viscosity of the linear viscous phase, which is depends on the volume fraction ratio (Eq. 28). The flow behavior of the Ti-6Al-4V was calculated from the experimental results of the Ti-7Al-1.5V alloy, showing a good quality of prediction with respect to direct measurements of the various near-Beta alloys. From these results, it was demonstrated that the strength of the Alpha phase is approximately 3 (Figure 47) times higher than that the Beta phase [64] in a temperature range from 815 °C to 950 °C and the prediction is consistent with experimental results obtained from several Beta alloys.

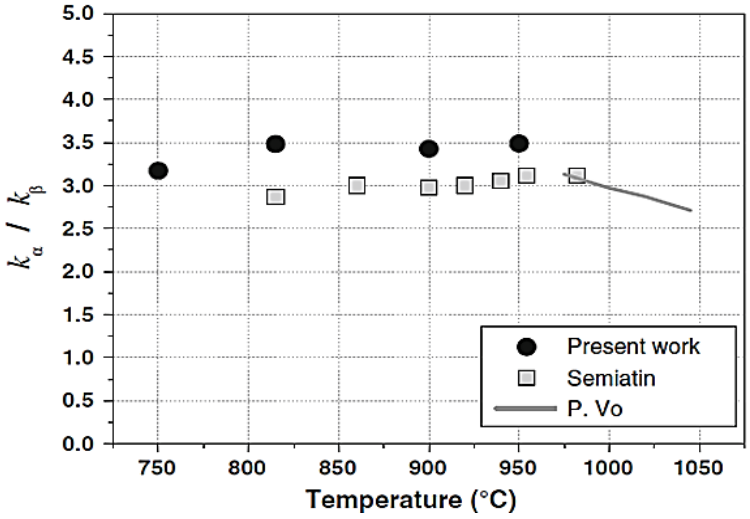

Figure 47: The ratio of the viscosity-like parameters as function of temperature [111]

Moreover, the relative strain rates observed in the Alpha and Beta phases during hot working of Ti-6Al-4V changes significantly with temperature, so that at temperature of 950 °C it results greater and the most deformation is provided by the Beta phase (Table 5).

Table 5: Predicted values for individual phase flow stress, viscosity-like parameter measured at strain rate 0.1 s^{-1} and strain rate at different temperatures [111]

Self-Consistent model parameters for Ti-6Al-4V								
Temperature [°C]	σ_α [Mpa]	$\sigma_{\alpha+\beta}$ [Mpa]	k_α	k_β	$k_{\alpha+\beta}$	$\dot{\varepsilon}_\alpha / \dot{\varepsilon}_{\alpha+\beta}$	$\dot{\varepsilon}_\beta / \dot{\varepsilon}_{\alpha+\beta}$	$\dot{\varepsilon}_\beta / \dot{\varepsilon}_\alpha$
815	309	241	427	122	344	0.727	1.9139	2.63
900	200	118	324	95	191	0.4584	1.5637	3.44
950	143	58	227	65	92	0.1537	1.3291	8.65

In the end, it was shown the dependence of the flow stress of Alpha/Beta titanium alloys in the hot working regime from temperature and volume fractions of the phases. The viscosity-like parameters were used to predict and measured the flow stress dependence on temperature at a strain rate of 0.1 s^{-1}, obtaining a reasonable agreement, except to a considerable deviation at 815 °C (Figure 48 - a). Moreover, considering the same self-consistent model at a fixed volume fraction of a Alpha phase, equal to 83 %, the difference between experimental data and numerical prediction revealed that the flow

stress decreases by 93 MPa when the temperature increases from 815 to 900 °C (Figure 48 - b).

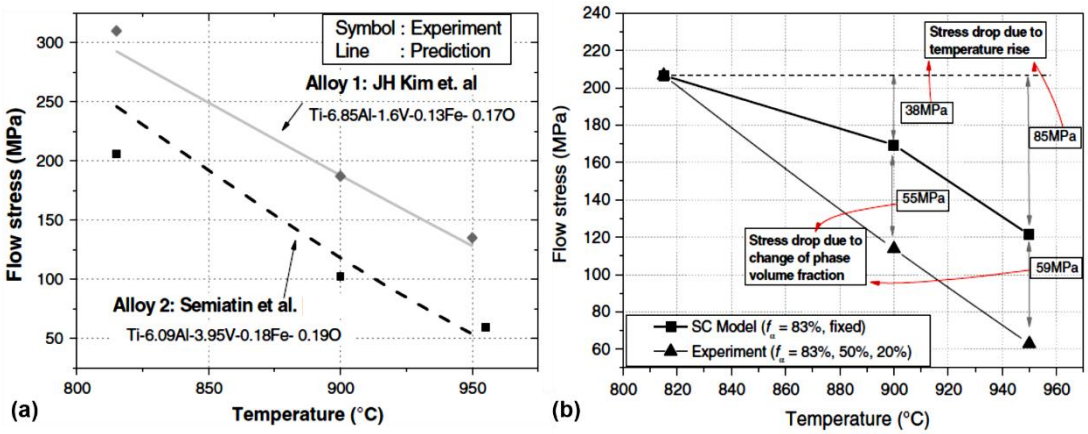

Figure 48: Comparison between experimental data and self-consistent-model for the flow stress of Ti-6Al-4V and the near-a Ti alloy at 0.1 s^{-1} (a) and assuming a phase volume fractions fixed at 83 % at a strain rate of 0.1 s–1 (b) [111]

Reddy et al. [112] studied the flow stress behavior as function of strain, strain rate and temperature during hot deformation using a neural network model, trained on both Alpha+Beta and Beta field, in order to predict the flow stress of Ti–6Al–4V alloy for any given processing conditions. The results were used to calibrate a hyperbolic sine constitutive model based on Zener-Hollomon parameter (Eq. 29).

$$\sigma|_{\varepsilon} = \frac{1}{\alpha}\left[\sinh^{-1}\left(\frac{Z}{A}\right)\right]^{\frac{1}{n}} \qquad \textbf{Eq. 29}$$

Where σ the flow stress; A and n are material constants; α the inverse of the stress associated with power-law breakdown and Z is the Zener–Hollomon parameter.

Results showed a higher accuracy of the constitutive model at different temperatures (Figure 49 - a) and strain rates (Figure 49 - b), as well as the Alpha+Beta phase regime (Figure 49 – c), while the prediction on Beta phase field at 1050 °C and strain rates equal to 1 s^{-1} and 100 s^{-1} displayed some limitation of the model (Figure 49 – d).

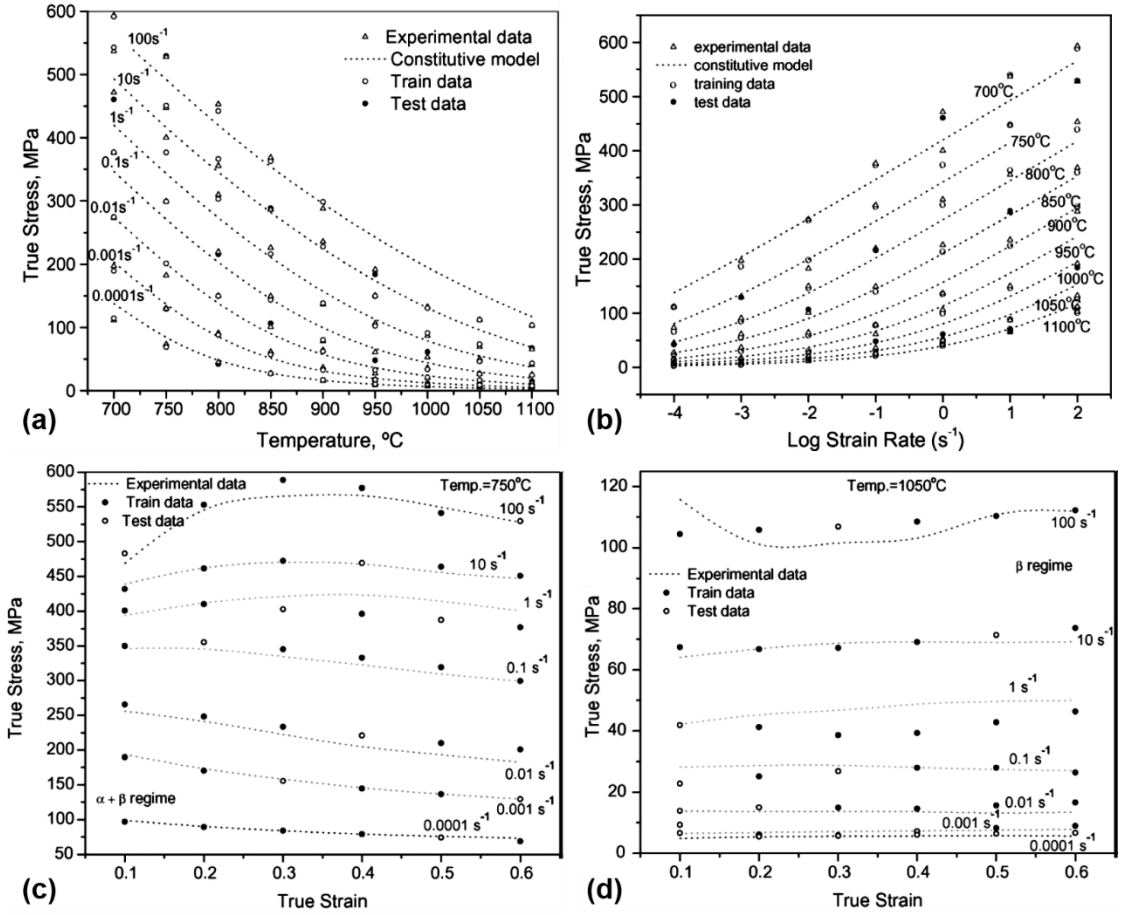

Figure 49: Comparison between experimental and predicted true stress values at 0.6 strain at different temperature (a), different strain rates (b), Alpha+Beta phase regime (c) and Beta phase regime (d) [112]

4.2. On the phase transformation and microstructural evolution

Ding et. al. [113] investigated the variation of microstructure under different hot working conditions by using strain rate, which caused a slight increase in the phase transformation and the degree of dynamic recrystallization, and temperature as the working parameters. According to their experimental results, the prior and the secondary Alpha lamellar structure was the general microstructure and the grains were fibrous, when the Ti-6Al-4V was processed in the Alpha+Beta phase field and only martensitic microstructure and elongated grains were seen, when processed in the β phase field. They grouped the lamellar morphology under five different types as the retained prior α which was the none-distorted prior Alpha platelets, the distorted Alpha which was distorted

Alpha platelets, segmented Alpha which was spheroidized prior Alpha lamella, the diffused α and the secondary Alpha (transformed Beta) lamella zones. They reported that because the mechanical deformation retarded the nucleation and the growth of the new phases, the phase transformation occurred more in the dead or unworked zone rather than in the deformation zone in the Alpha+Beta phase field which was also mentioned by Hammond and Nutting [10]. In addition to that, the dynamic recrystallization was seen only in the Beta phase field, not in the Alpha+Beta phase field.

Dabrowski [114] conducted a study on the kinetics of phase transformations during continuous cooling of the di-phase Ti-6Al-4V alloy from the diphase Alpha+Beta range at 950 °C. Experiments demonstrated that a diffusional Beta-to-Alpha transformation occurred within the whole range of applied cooling rates. Metallographic analysis (Figure 50) of the specimens showed changes in the Alpha phase morphology.

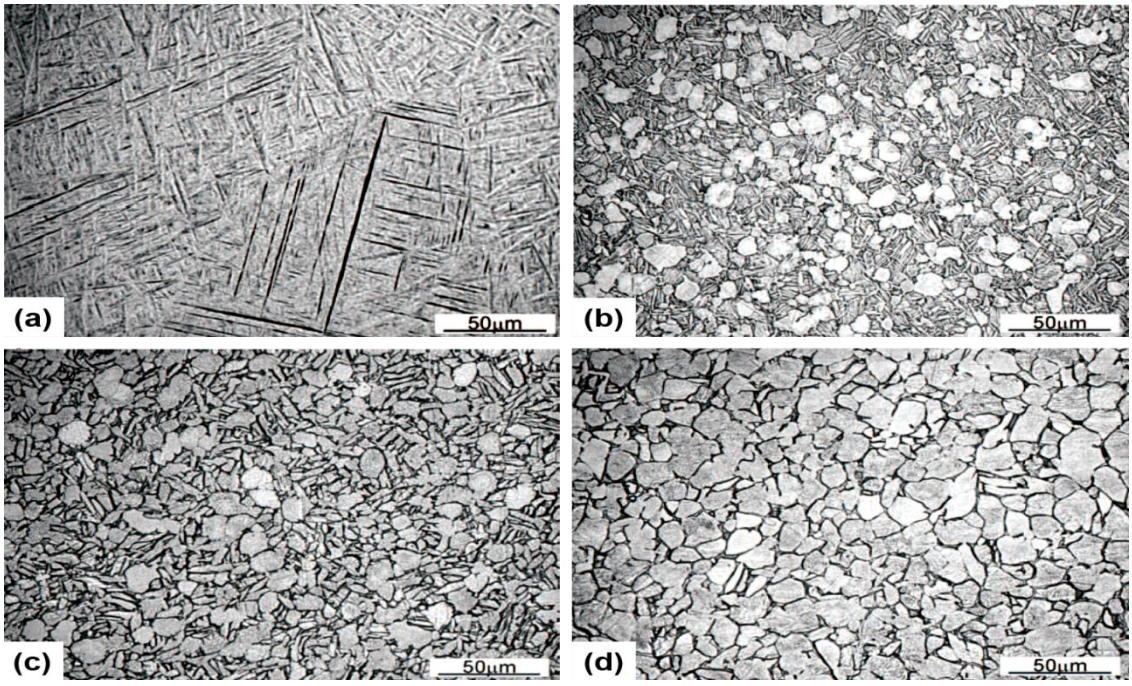

Figure 50: Microstructures of the Ti6Al4V alloy after (a) heating to 970 °C, holding for 60 minutes and cooling in water; cooled from 950 °C at (b) 3.2 °C/s, (c) 0.23 °C/s and (d) 0.011 °C/s [114]

Upon cooling at between 7.1 and 0.9 °C/s the Alpha phase precipitates show lamellar Widmannstatten microstructure, while at the slowest rates from 0.23 to 0.011 °C/s the Alpha phase precipitates in a form of grains.

Specimens rapidly cooled from Beta transus (970 °C) temperature showed a oriented, acicular precipitates of apparently α' phase, formed as a result of a Beta to Alpha diffusionless transformation. The Alpha phase precipitated at three grains contacts and prior Beta phase grain boundaries, while a decrease in the cooling rate from to 3.2 °C/s (Figure 50 - b) and subsequently to 0.9 °C/s resulted in lamellas of Alpha phase precipitate in the Widmannstatten microstructure, forming colonies oriented in the privileged directions within each Beta grain. A further decrease in the cooling rate to 0.011 °C/s (Figure 50 - d) increased the grain size- suppressing the lamellar form of Alpha phase, with residue of untransformed Beta phase.

Song et al. [115] investigated and characterized the dynamic globularization kinetics of Ti–6.5Al–1.5Zr–3.5Mo–0.3Si alloy with a colony Alpha microstructure during deformation at temperature range from 920 to 980 °C and strain rate range from 0.01 to 10 s^{-1}. The results showed that the globularization fraction and globularized grain size are sensitive to strain rate.

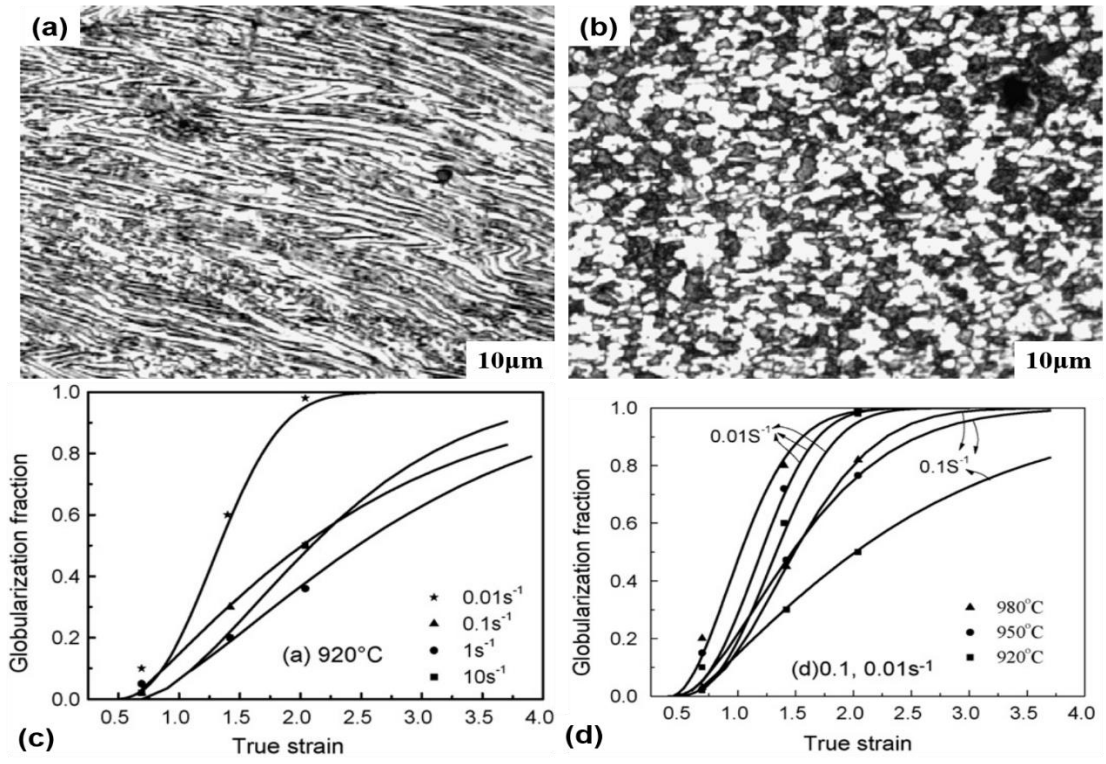

Figure 51: Optical micrographs of structure and globularization fraction as function of strain developed in specimens compressed (a, c) at temperatures of 920 °C and (b, d) strain rate of 0.1 s^{-1} and at temperature of 980 °C and strain rate 0.01 s^{-1} [115]

The specimens tested at temperature higher than 950 ◦C and strain rates higher than 0.1 s^{-1} exhibited an enhanced grain refinement and improved superplasticity characteristics. Micrographs at test temperatures of 920 °C and 980 °C at a large strain (Figure 51 - a, b) showed partially globularization with fine globularized grains at 920 °C and strain rate of 0.1 s^{-1} (Figure 51 - a), while fully globularized structure with coarser Alpha grains was found at 980 °C and 0.01 s^{-1} strain rate (Figure 51 - b).

Moreover, quantitative measurements of the fraction globularized (following an Avrami type equation) as a function of strain and globularized grain size at different strain rates and temperatures revealed that a critical strain is needed for globularization initiation and both globularization fraction and globularized Alpha grain size are very sensitive to deformation conditions (Figure 51 – c, d).

Pinke et al. [116] investigated the influence of the solution treatment at 1050, 950 and 800 °C with 1 hour water or air cooling on the Ti6Al4V alloy.

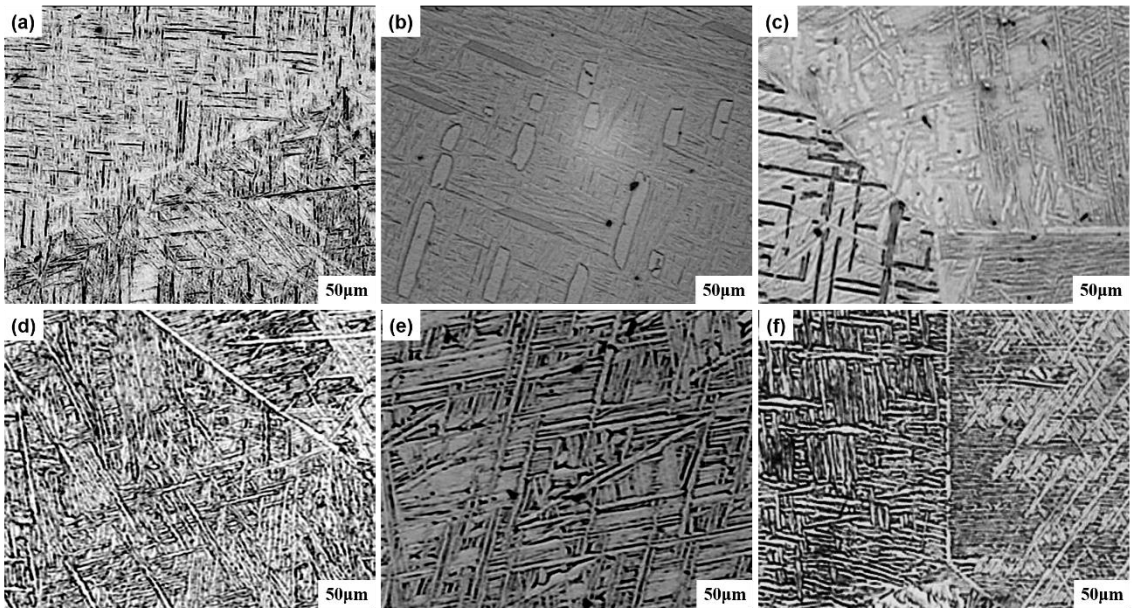

Figure 52: Ti-6Al-4V microstructure obtained after the following heat treatments: 1050 °C 1h water cooling (a), 950 °C 1h water cooling (b), 800 °C 1h water cooling (c), 1050 °C 1h air cooling (d), 950 °C 1h air cooling (e), 800 °C 1h air cooling (f) [116]

Specimens showed that the treatments from 1050 °C and 950 °C with water cooling formed a α′ martensite microstructure and primary α phase (Figure 52 – a, b), while no deposition of grain boundary α was recognized due to the fast cooling. Solution treatment

at 1050 °C by air cooling lead to the typical lamellar α + β structure with a grain boundary α on the prior β grains (Figure 52 – d), while cooling in water from 950 °C produces a microstructure which consist of acicular Alpha (Figure 52 – e), with a structure containing a lamellar mixture of α + β phases, primary α and grain boundary α. Considering the low cooling rate no α′ martensite was formed. The microstructures after the solution treatment at 800 °C showed regular lamellae of α phase (Figure 52 – c), while the air cooling case formed more coarse lamellar structure (Figure 52 – f). Moreover, no α′ martensite phase was formed after the solution treatment from 800 °C by cooling in water.

Elmer et al. [117] studied phase transformation during heating of Ti-6Al4V alloy specimens with the aim of compare experimental phase fraction calculations with thermodynamic predictions.

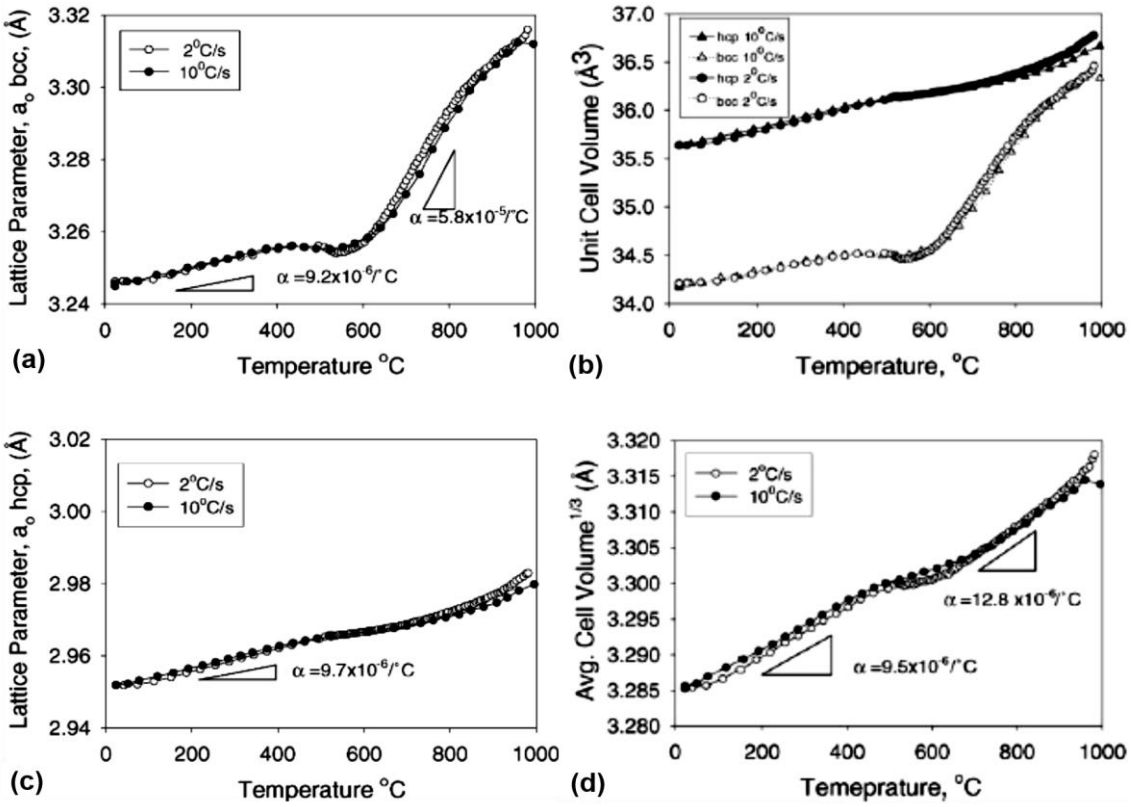

Figure 53: Measured lattice parameters as a function of temperature for both the (a) bcc and (c) hcp phases as a function of temperature during heating at two different rates; (b) measured unit cell volume for each phase at the two different heating rates plotted vs. temperature; (d) cube root of the unit cell volumes plotted vs. temperature representing the average linear expansion for the multi-phase Ti–6Al–4V alloy [117]

An interesting aspect is showed on the variations of lattice parameters of both Alpha and Beta phases during transformation due to partitioning of V content and its strong effect on the lattice parameter of the Beta phase, which displayed an unexpected contraction of the lattice parameter during heating in the temperature range between 500 and 600 °C, related to the annealing of residual stresses created by the different thermal expansion behaviors of the two phases. The effect of heating rate on the lattice parameters of the Alpha and Beta phases showed that their evolution is delayed to higher temperatures and it is also consistent with the effects of heating rate on the Beta phase fraction with temperature (Figure 53 – a, c). Differences in the thermal expansion of both Alpha and Beta phases determine internal stresses in the multiphase mixture as the alloy cools down. In addition, transformation strains may be present due to the differences in densities between both phases and this may create a lattice expansion of the multiphase mixture, which can be estimated from the lattice expansions of the two individual phases and their relative fractions in the microstructure (Figure 53 – b, d).

Pelcastre [118] investigated the microstructural evolution of Ti-6Al-4V samples deformed at room temperature up to 10% strain, using a strain rate of 0.01 s^{-1}, and annealed for 300 seconds at different temperatures between 20 ºC to 1200 ºC. Results showed that an allotropic transformation from Alpha to Beta phase occur at around 800 ºC and, when the sample is cooled down, the Beta phase transforms to a bi-phasic Alpha+Beta structure. Morphology of microstructure depends on the cooling rate and can result in a lamellar or martensitic form and, in this specific case, the author found a martensitic one (Figure 54 - f).

The resulting microstructure after the heat treatment at 300 ºC is not so different compared to the microstructure of the specimen of the original material, before heat treatments. At 500 and 600 ºC (Figure 54 – c, d) the grains have increased their grain size and in general a large amount of grains become partially equiaxed, while the samples obtained after the heat treatment at 800 ºC showed a smaller grain size in average compared to the microstructures at 500 or 600 ºC. At 900 ºC (Figure 54 - g) the microstructure was clearly elongated, it was possible to observe the allotropic transformation, with. both phases coexisting at this temperature (Alpha, the bright grey, and Beta, the dark grey).

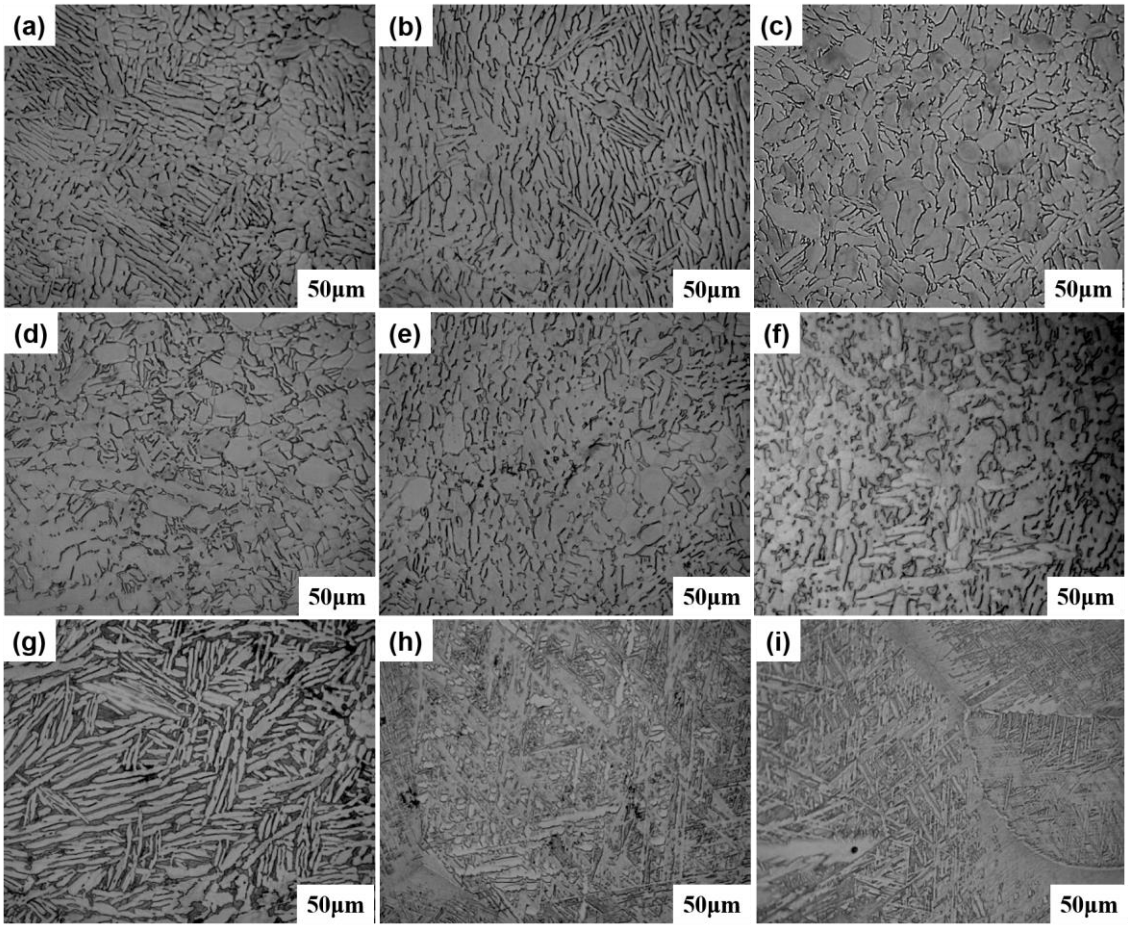

Figure 54: Microstructural evolution of Ti-6Al-4V alloy: a) without heat treatment after deformation, b) 300 ºC, c) 500 ºC, d) 600 ºC, e)700 ºC, f) 800 ºC, g) 900 ºC, h) 1000 ºC, i) 1100 ºC [118]

Pederson [18] investigated the phase transformations properties of Ti-6Al-4V alloy through a combined study of Alpha to Beta and Beta to Alpha phase change by means of continuous heating and cooling cycles.

The Alpha to Beta phase transformation analysis was carried out through heating tests at isothermal conditions of 610, 710, 800 and 900 °C and the resulting microstructures after slowly cooling down to room temperature were analyzed, revealing a microstructural coarsening affect, both of the primary Alpha and of the Widmanstätten structure, with increasing isothermal treatment temperature.

Therefore, the microstructure of the sample isothermally treated at 610 °C did not show any noticeably difference from the starting structure due to the small amount of Beta phase at that temperature, while the microstructure of the sample treated isothermally at 975 °C formed a similar morphology to the samples subjected to the continuous

heating/cooling cycle. The Beta to Alpha phase change was studied adopting a first heating to an equilibration stage at around 950°C followed by a cooling down to 610, 715, 795 or 900 °C respectively.

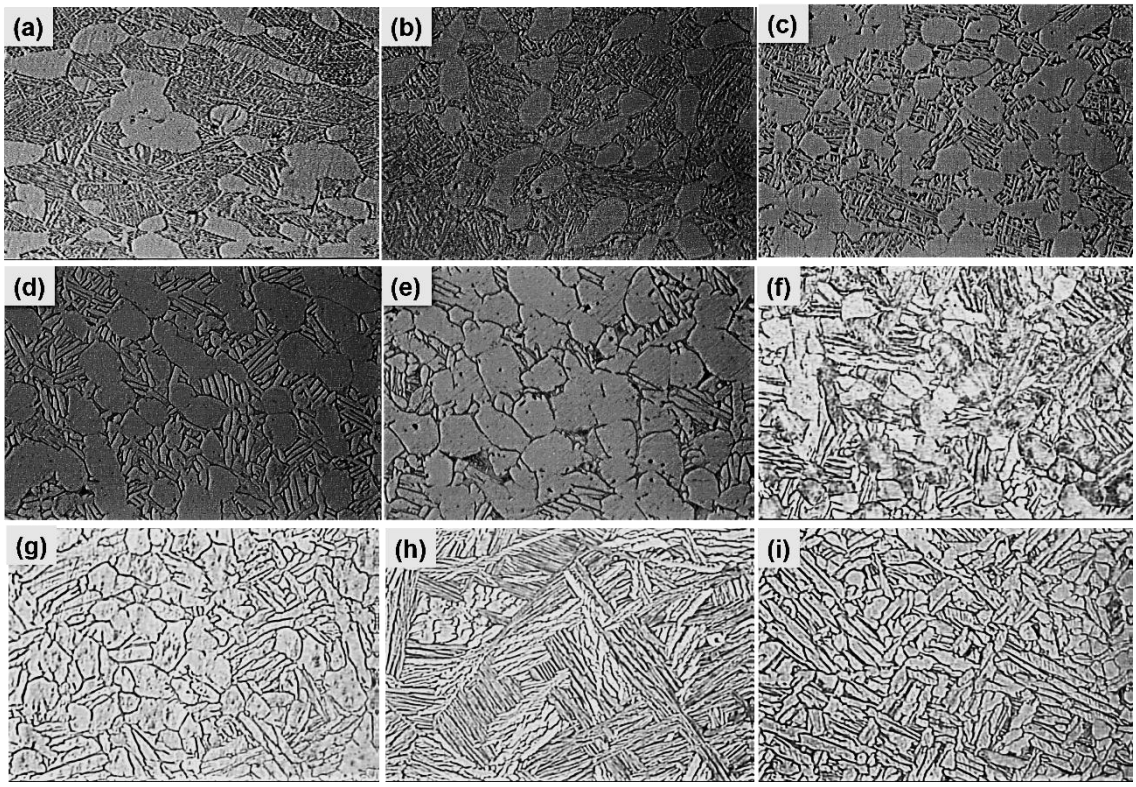

Figure 55: (a) Optical micrograph of the starting microstructure of the studied Ti-6Al-4V samples; cross-section of the heating-cooling at 610 °C (b), 710 °C (c), 800 °C (d), 900 °C (e) sample; cross-section of the isothermally held at 610 °C (f), 715 °C (g), 795 °C (h) and 900 °C (i) after equilibration at 950°C [18]

The samples showed some areas containing mainly primary Alpha grains surrounded by coarse Alpha platelets, whereas some areas displayed mainly coarse Widmanstätten Alpha platelets in prior Beta grains and surrounded by grain boundary Alpha structure. In particular, the case cooled down to 715 °C followed by isothermal hold showed large amounts of primary Alpha phase surrounded by coarse Alpha platelets, while the case cooled down to 900 °C followed by isothermal hold showed a coarse grain boundary Alpha in the prior Beta grain boundaries, while the prior Beta grains contained Widmanstätten-like Alpha platelets.

Mironov et al. [119] investigated the microstructure evolution during warm working of Ti-6Al-4V with a colony Alpha microstructure treated using a cycle comprising 955

°C/15 min + 1010 °C/15 min + furnace cool to 800 °C/soak for 20 min + controlled furnace cool at a rate of 2 °C/min to 600 °C/soak for 2 h + water quench.

Results showed that the material quenched immediately before to deformation had a classical transformed colony-Alpha microstructure consisting of: lamellar/basketweave Alpha colonies with 2 μm thick Alpha platelets, layers of Alpha at the Beta prior grain boundaries and thin Beta layers separating the Alpha lamellae (Figure 56 - a).

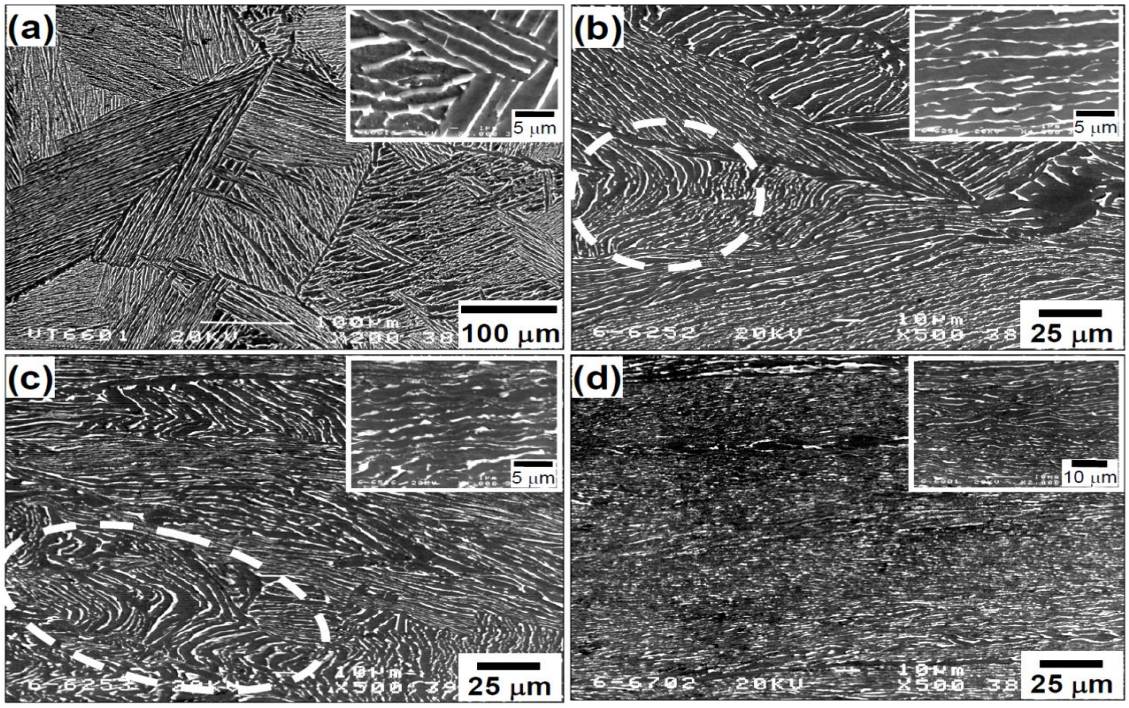

Figure 56: SEM images of Ti-6Al-4V microstructure undeformed specimens (a) and after height reductions of 25% (b), 50% (c) and 70% (d), with high magnification of the microstructure in the top right corner of each figure [119]

Microstructure evolution as a function of strain was found to be related to the orientation of specific Alpha colonies with respect to loading axis. In particular, if the angle between the Alpha lamellae and compression direction was relatively small, the Alpha laths resulted to be kinked (Figure 56 – b, c), otherwise the Alpha lamellae rotated with strain. The alignment of Alpha laths has the tendency to eliminate the morphological differences between neighboring Alpha colonies and contributes to form a homogeneous microstructure (Figure 56 – c, d). The main difference among the specimens was

displayed by the Beta layers, which generally did not break up and were continuous at large strains (Figure 56 – b, d).

Weiss et al. [120] investigated the effect of strain on lamellar Alpha phase of Ti-6AI-4V alloy under hot working with the aim of controlling morphology and final grain size. The specimens were treated by forging at 955 °C followed by annealing at 925 °C, considering different strain conditions from 6.5 to 80 % reduction and evaluating the modifications on the lamellar Alpha morphology.

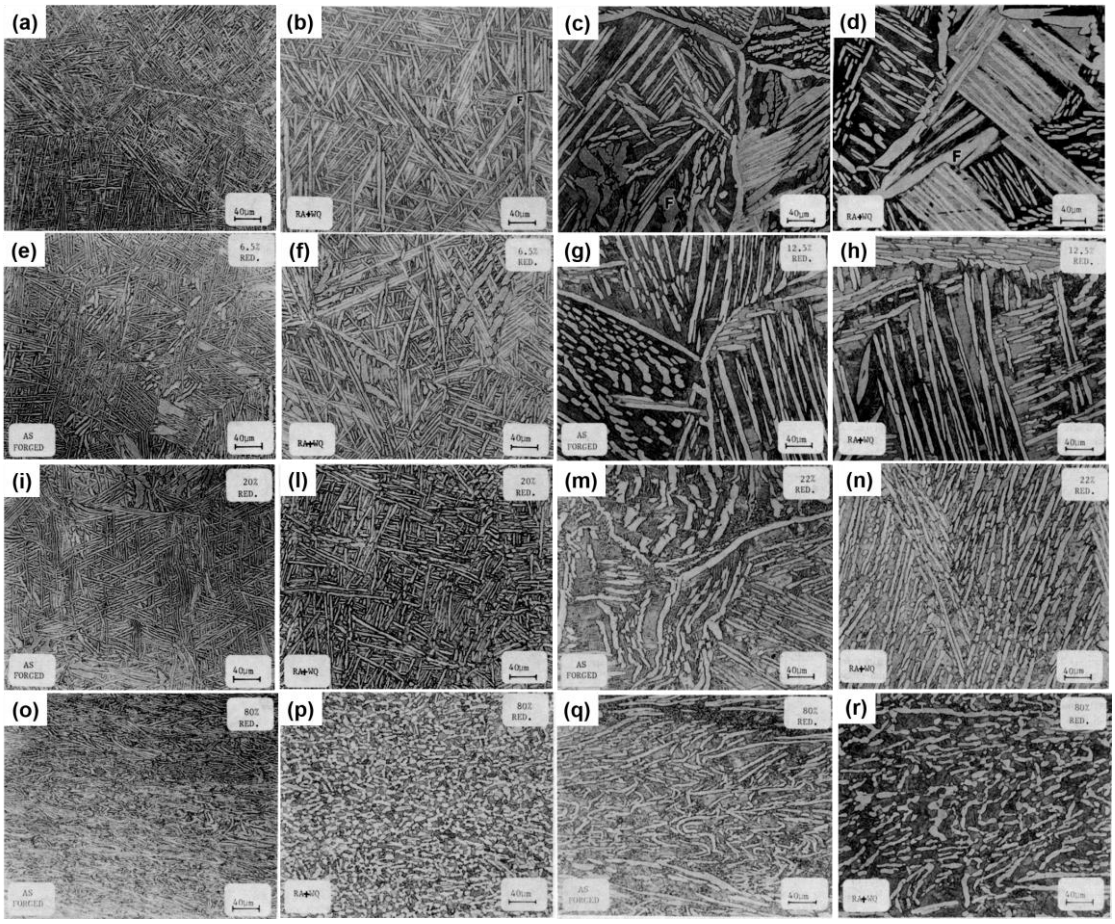

Figure 57: Undeformed thin Alpha plate material annealed at 955 °C/30min/AC (a), as in (a) + annealing at 925 °C/2h/WQ (b), undeformed thick Alpha plate material annealed at 955 °C/30min/AC (c), as in (c) + annealing at 925 °C/2h/WQ (d), thin Alpha plate material forged 6.5% reduction (e), as in (e) + annealing at 925 °C/2h/WQ (f), thin Alpha plate material forged 20% reduction (i), as in (i) + annealing at 925 °C/2h/WQ (l), thin Alpha plate material forged 80% (o), as in (o) + annealing at 925 °C/2h/WQ, thick Alpha plate material forged 12.5% reduction (g), as in (g) + annealing at 925 °C/2h/WQ (h), thick Alpha plate material forged 22% reduction (m), as in(m) + annealing at 925 °C/2h/WQ (n), thick Alpha plate material forged 80% reduction (q), as in (q) + annealing at 925 °C/2 h/WQ (r) [120]

The thermo-mechanical treatment sequences displayed some Alpha phase present along the prior Beta grain boundaries and thick Alpha plate material surrounded by Beta regions containing fine lenticular Alpha (Figure 57 - c), while the final annealing treatment at 925 °C produced thickening of the lenticular plates (Figure 57 – b, d) with unusually wide plates with the plate face orientation closely paralleling the metallographic section plane observed in the thick Alpha microstructures (Figure 57 – b). Hot deformation and subsequent 925 °C annealing produced an Alpha+Beta microstructure influenced by both the prior microstructure and the amount of applied strain, with a combination of initial thin lamellar Alpha and high strain required to produce a fine equiaxed Alpha microstructure upon annealing. Annealing following the forging at 6.5% strain produced a random orientation of lamellar Alpha (Figure 57 – e) which resulted in a high aspect ratio Alpha on annealing (Figure 57 – f), while at larger uniaxial strains (20 and 80% reduction) caused the Alpha plates to align themselves toward a direction perpendicular to the forging. Upon annealing, the lamellar Alpha morphology changed to a more compact Alpha structure (Figure 57 – l, p) with the thick Alpha plate microstructure exhibiting a similar trend of thin material. In the case of small strains with 12.5% reduction (Figure 57 – g) a homogeneous deformation was obtained, while the subsequent annealing formed a structure with lower aspect ratio Alpha phase. When high strain of 80% reduction was performed (Figure 57 – q) some equiaxed Alpha grains were observed, while the subsequent annealing lowered the Alpha aspect ratio (Figure 57 – n, r) but left some directionality in the grain orientation (Figure 57 – f).

Ahmed et al. [28] examined the phase changes of Alpha-Beta has been Ti–6Al–4V alloy at different cooling rates from 525 to 1.5 °C s^{-1} and observed the formation of both martensitic and diffusional phase transformations.

Cooling rates above 410°C s^{-1} produced a fully martensitic structure, while a massive transformation was observed between 410 and 20 °C s^{-1}, with a gradually replacing by diffusion controlled Widmanstatten formation at lower cooling rates. Continued reductions in cooling rate showed an increase in the volume fraction of this Alpha morphology, with a nucleation progressively occurring with decreasing cooling rate at prior Beta phase boundaries (Figure 58 – a, d) and at martensite plates adjacent to the prior Beta grain boundaries (Figure 58 – b, e). In the case of lowest cooling rates this transformation was observed at individual Alpha plates within the grains (c, f).

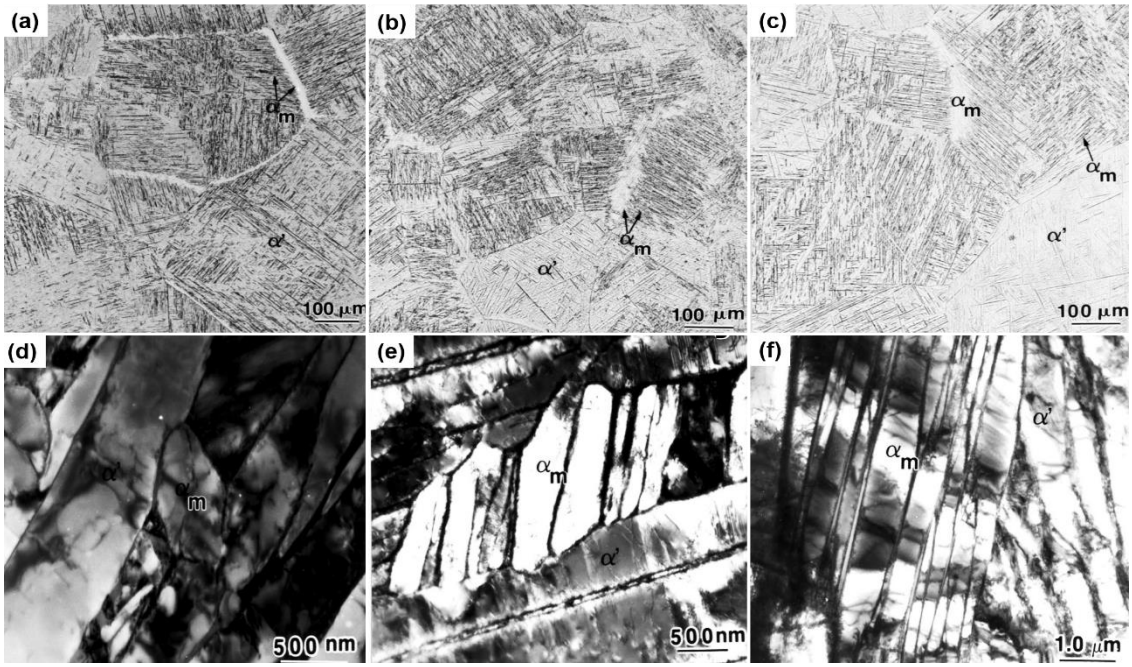

Figure 58: Ti–6Al–4V alloy microstructure after cooling at 275 °C/s^{-1} (a, d), 175 °C/s^{-1} (b, d), 20 °C/s^{-1} (c, f) [28]

Sha et al. [31] studied the Alpha to Beta phase transformation of Ti-6Al-4V under a constant rate heating process at 10 °C/min with different stop points 600, 780, 970, 1010 and 1180 °C.

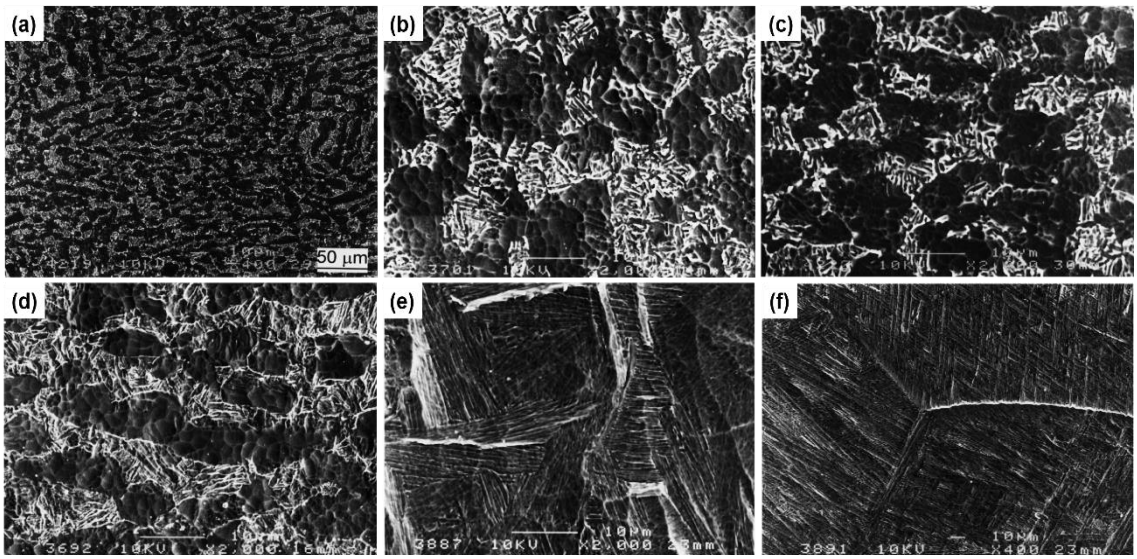

Figure 59: Microstructure of Ti-6Al-4V alloy in as-received stat (a), after cooling from continuous heating as received (b), 780 °C (c); 970 °C (d); 1010 °C (e); 1180 °C (f) [31]

The transformation upon heating of the original material started from the transformed Beta phase (Figure 59 – a, b), while no significant development was apparent in those specimens heated up to 780 °C (Figure 59 – c). Therefore, no Alpha to Beta phase transformation was observed. The specimen heated to 970 °C displayed a certain amount of phase transformation (Figure 59 – d).

4.2.1. Phase transformation kinetic models

Malinov et al. [25, 121-123] studied the kinetics of Beta to Alpha phase transformation of Ti-6Al-4V alloy by means of DSC at different continuous cooling conditions with constant cooling rates of 5, 10, 20, 30, 40 and 50 °C/min. Moreover, the DSC results were used to trace the CCT diagrams of isotransformed fraction and the kinetics of transformation were modeled using the Johnson–Mehl–Avrami JMA (Eq. 30) equation by applying the concept of additivity.

$$f = 1 - exp(-kt^n) \qquad \text{Eq. 30}$$

Where f is the product volume fraction, t is the time in seconds, k is the reaction rate constant and n is the Avrami index.

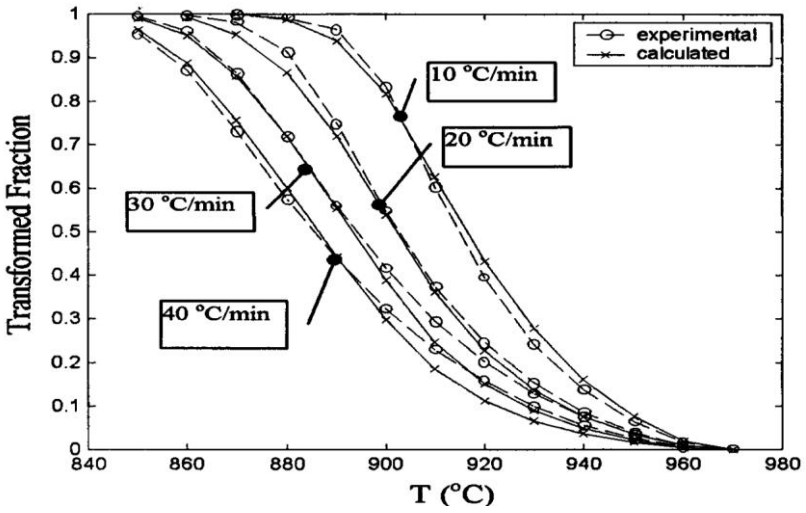

Figure 60: Experimental and predicted Beta to Alpha phase change in Ti-6Al-4V at different cooling rates [25, 121-123]

This model can be applied under specific conditions: isothermal transformation case, constant nucleation frequency and spatially random nucleation. For the calculations of Beta to Alpha phase change, it was assumed that *n* parameter does not depend on the temperature because of the temperature range involved in the transformation, while *k* was set as function of temperature. The transformed fraction of Beta phase was calculated on different cooling rates, using derived values of *n* and *k*. Good agreement with experimental measurement coming from DSC analysis were found with the exception of the case starting at 900 °C and cooled at 20 °C/min (Figure 60).

Murgau et al. [124] proposed a model to calculate the changes in microstructure of Ti–6Al–4V alloy designed to be used in a coupled thermo-metallurgical-mechanical analysis with the aim of directly affecting the mechanical properties during a manufacturing process simulation. This model is thermally driven in phase evolution calculation and a state variable approach was adopted to represent the microstructure with the objective to integrate the microstructure changes with a classical thermo-mechanical model. The calibration of coefficients was made using literature data, while the microstructure is represented by the phase fractions X_i (where subscript *i* indicates the phase considered), which are the representative state variables in the model. The model considers four different phases: the β phase and three variants of α phases. These are the grain boundary α phase (α_{gb}), Widmanstatten α phase, α_W, and martensitic α phase, α_m. The total α phase fraction, X_α, is calculated as the sum of these three state variables and it uses the Johnson-Mehl-Avrami- Kolmogorov equation [125-127] for the diffusionless formations α_{gb} (Eq. 31) and α_w (Eq. 32) while the martensite (Eq. 33) temperature-dependent diffusionless transformation was calculated using the empirical Koistinen–Marburger equation [128]

$$X_{\alpha_{gb}}^{n+1} = \left(1 - e^{-k_{gb}(t_c+\Delta t)^{N_{gb}}}\right)\left(X_{\beta}^{n} + X_{\alpha_w}^{n} + X_{\alpha_{gb}}^{n}\right)\left(X_{\alpha}^{eq\,n+1}\right) - X_{\alpha_w}^{n} \quad \text{Eq. 31}$$

$$X_{\alpha_w}^{n+1} = \left(1 - e^{-k_{w}(t_c+\Delta t)^{N_{w}}}\right)\left(X_{\beta}^{n} + X_{\alpha_w}^{n} + X_{\alpha_{gb}}^{n}\right)\left(X_{\alpha}^{eq\,n+1}\right) - X_{\alpha_{gb}}^{n} \quad \text{Eq. 32}$$

$$X_{\alpha_m} = \left(1 - e^{-b_{KM}(T_{ms}-T)}\right)X_{\beta} \quad \text{Eq. 33}$$

Where the superscript *n* denotes the beginning of the current time step, *n + 1* denotes the end of the current increment; *eq* denotes the equilibrium fraction of phase; the parameters k and N are the JMAK transformation kinetic parameters of each specific phase.

The authors calibrated the model using different combinations of parameter sets coming from the literature data [25, 121] for JMHK equation coefficients, in order to get the best model set-up. Results (Figure 61) showed good agreements with respect to experimental data.

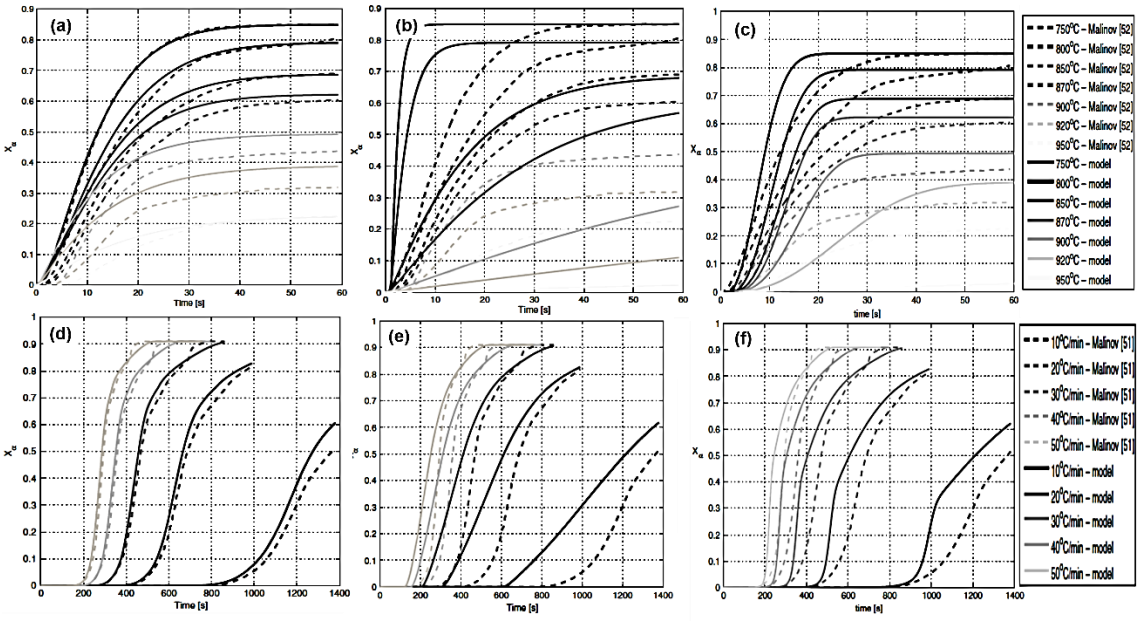

Figure 61: Comparison between experimental data coming from literature and JMHK model predictions of Alpha phase amount with different calibrations of coefficients at different temperatures (a, b, c) and different cooling rates (d, e, f) [124]

Neelakantan et al. [129] used the Ghosh and Olson's theory [130] to develop a thermodynamics based model to predict the compositional dependence of the martensite start temperature Ms valid for Ti binary alloys. This equation (Eq. 34) has been obtained by considering 150% of the solute fraction dependence, ignoring the ternary and higher order interactions and grain size dependence. The predictions were compared with an empirically estimated Molybdenum equivalence (Eq. 35).

$$M_s = 1156 - 150Fe_{wt\%} - 96Cr_{wt\%} - 49Mo_{wt\%} - 37V_{wt\%} - 17Nb_{wt\%} - 7Zr_{wt\%} + 15Al_{wt\%} \quad \text{Eq. 34}$$

$$Mo_{eq} = 1.00Mo + 0.28Nb + 0.22Ta + 0.67V + 1.6Cr + 2.9Fe - 1.00Al \quad \text{Eq. 35}$$

The results were validated by means of a comparison between the Ms temperature of a number of commercial martensitic alloys and the equivalent Mo.

An approximately linear correspondence between both criteria was observed and it was found that Ms values reaching room temperature are indeed achieved by alloys displaying a Mo eq. approaching the experimentally observed range of 9.5 to 11.5 for most of the existing metastable Beta alloys (Figure 62).

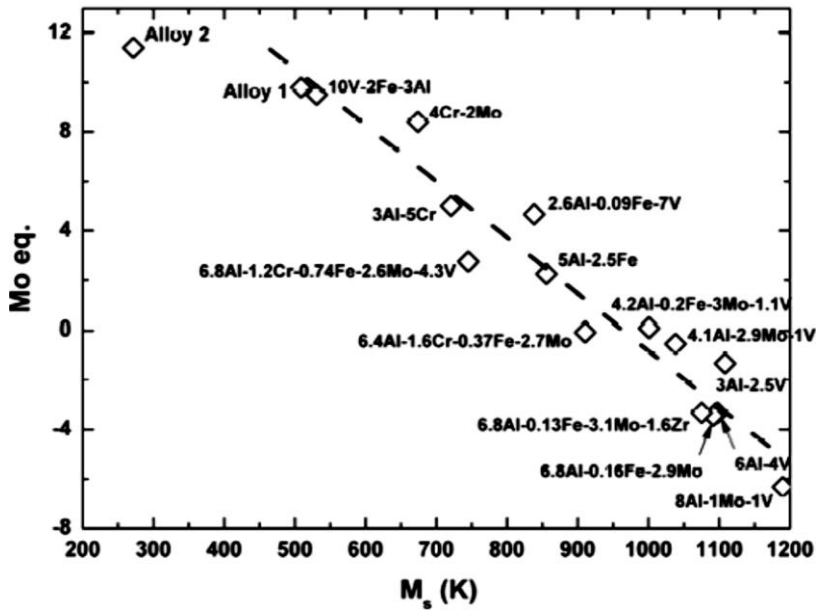

Figure 62: Comparison of calculated Ms temperature equivalent Mo criterion for various Ti alloys undergoing martensitic transformation [129]

Shah et al. [131] studied the activation energy for the Alpha+Beta to Beta transformation of Ti-6Al-4V alloy using a non-isothermal dilatometric technique based on the JMA equation, which was originally derived for homogeneous isothermal reactions by introducing a time differential such that it is valid for an infinitesimal time. This method involved the determination of the inflection point Ti (where Ti is the temperature

in K) of the maximum transformation rate and the activation energy Q is related to Ti and heating rate (H) by means of the next equation (Eq. 36).

$$ln\frac{T_i^2}{H} = ln\frac{Q}{Rk_o} + \frac{Q}{RT_i} \qquad \textbf{Eq. 36}$$

Where *k* and *R* are the pre-exponential factor of the JMA equation and the gas constant respectively.

Results (Figure 63) showed that the effect of such second activation energy term is not apparent, while the present activation energy is much larger in magnitude than that for diffusion of aluminum in α-Ti (75-100 kJ/mol) or in β- Ti (160-190 kJ/mol) [132] or for diffusion of vanadium in α-Ti (120-160 kJ/mol) [133].

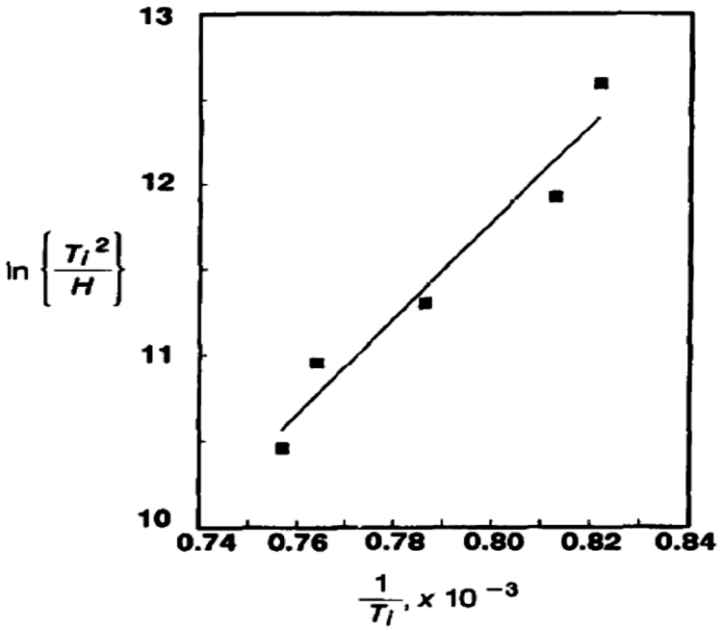

Figure 63: Activation energy for Beta phase formation in Ti-6AI-4V alloy [131]

Semiation et al. [134] developed a mathematical model (Eq. 37) based on diffusion-controlled growth for the prediction and control of microstructure evolution (Figure 64) during heat treatment of wrought Alpha/Beta titanium alloys in the two-phase field with the aim of controlling the induction heating trials on Ti-6Al-4V, consisted of heating to and soaking at a peak temperature of 955 °C and controlled cooling at a fixed rate of 11,

42, or 194 °C/min to a variety of temperatures and final water quenching. This model was also used to establish a criterion for describing the initiation and growth of secondary Alpha as a function of supersaturation, diffusivity, and cooling rate.

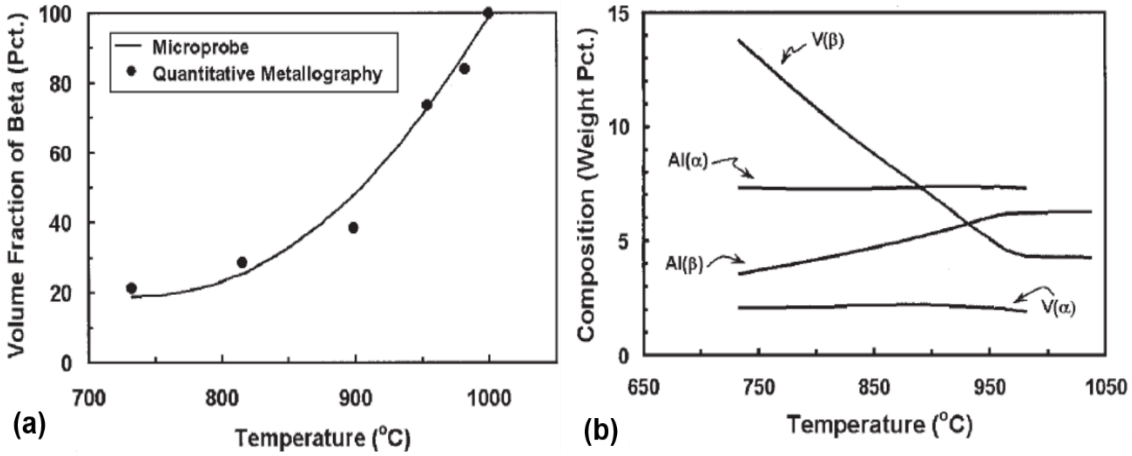

Figure 64: Phase equilibria data for Ti-6Al-4V alloy with Beta-approach curve (a) and phase compositions (b) [134]

$$f_\alpha = f_{\alpha_0}\left(\frac{R}{R_0}\right)^3 \qquad \textbf{Eq. 37}$$

$$R(t) = (2\Omega D t)^{\frac{1}{2}} \qquad \textbf{Eq. 38}$$

$$\Omega = \frac{(C_M - C_I)}{(C_p - C_I)} \qquad \textbf{Eq. 39}$$

$$C_M = \frac{(C_0 - f_\alpha C_\alpha)}{(1 - f_\alpha)} \qquad \textbf{Eq. 40}$$

Where, f_α is the Alpha phase volume fraction, f_0 is the initial Alpha phase volume fraction, R_o is the particle radius, D is the diffusion coefficient, Ω (Eq. 39)is the supersaturation, C_M (Eq. 40) is the composition of the matrix far from the matrix-particle interface, C_I is the composition of the matrix at the matrix-particle interface, C_P is the composition at the matrix-particle interface, C_I is the equilibrium matrix composition, C_P is the particle composition, C_o is the overall alloy composition and C_α is the Alpha phase particles composition.

Results (Figure 65 - c) showed a good quality in phase amount prediction as function of temperature and alloying elements diffusion phenomena (Figure 65 – a, b).

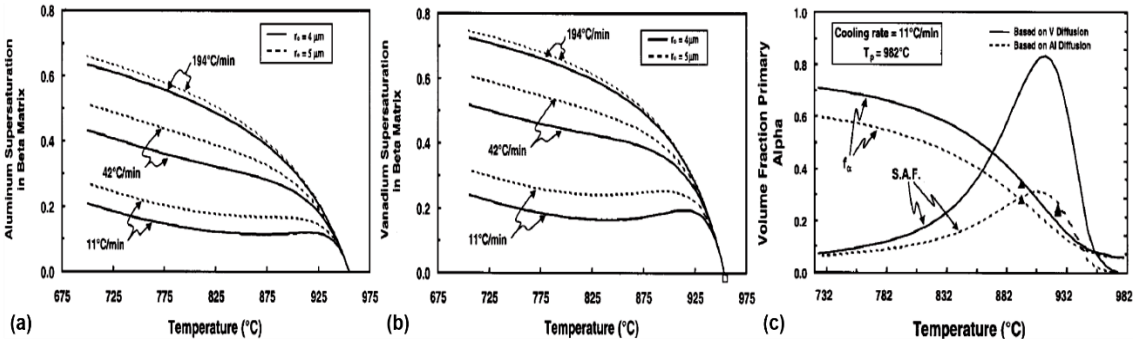

Figure 65: Model predictions of the aluminum (a) or vanadium (b) supersaturation as a function of cooling rate for a peak temperature of 955 °C and initial Alpha-particle size of 4 and 5 μm and model predictions of temperature dependence of the volume fraction of primary Alpha phase based on aluminum or vanadium diffusion/supersaturation assuming a peak temperature of 982 °C, a cooling rate of 11 °C/min and an initial Alpha-particle size of 3.5 μm [134]

Crespo et al. [135] presented a model for phase transformations Ti-6Al-4V alloy based on solid-state phase change kinetics equation, following the thermal cycles showed below (Figure 66).

In this model, the amounts of the Alpha f_α and Beta f_β phases depend on the temperature as given by the following equations (Eq. 41, Eq. 42):

$$f_\alpha(T) = 1 - f_\beta(T) \qquad \text{Eq. 41}$$

$$f_\beta(T) = \begin{cases} 0.075 + 0.92e^{[-0.0085(980-T)]} & T < 980\ °C \\ 1 & 980\ °C \leq T \leq T_{melt} \end{cases} \qquad \text{Eq. 42}$$

It is well known that, during the solidification, the microstructure consists of Beta phase only and may transform into two different phases, depending on the cooling rate (Figure 67). If the cooling rate is lower than 410 ºC/s, a diffusion-controlled transformation will take place and the Beta phase will progressively transform to Alpha phase as it cools from 980 ºC (Beta transus point) to room temperature.

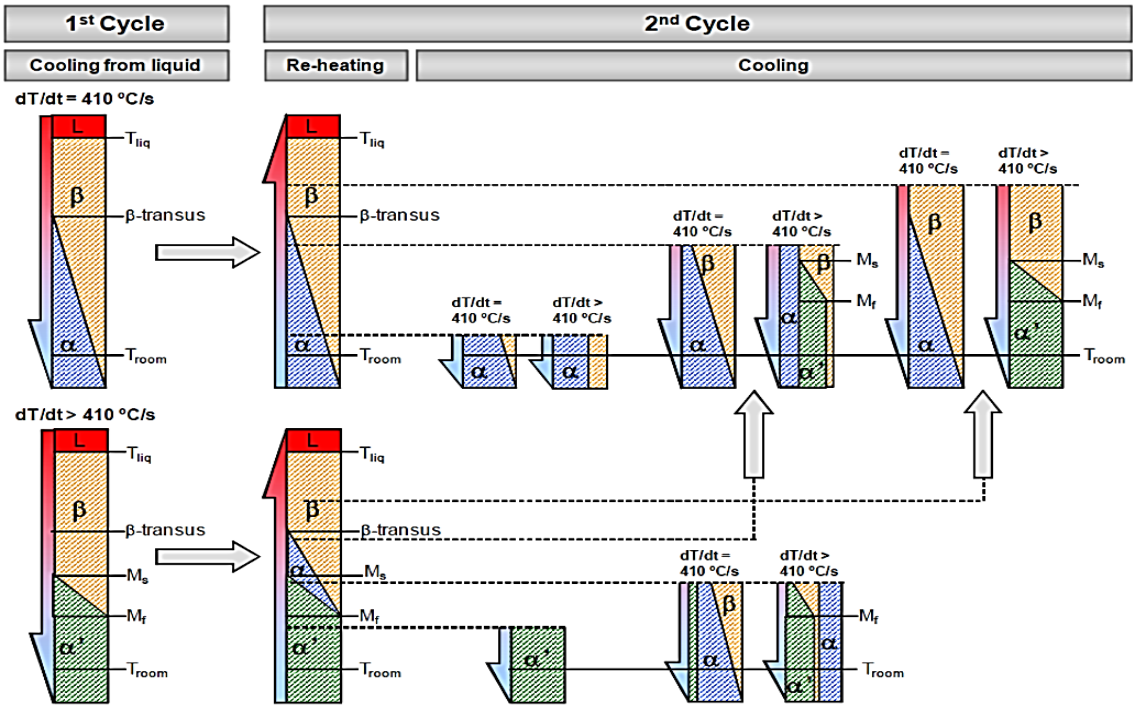

Figure 66: Thermal cycles used by authors during the model calibration [135]

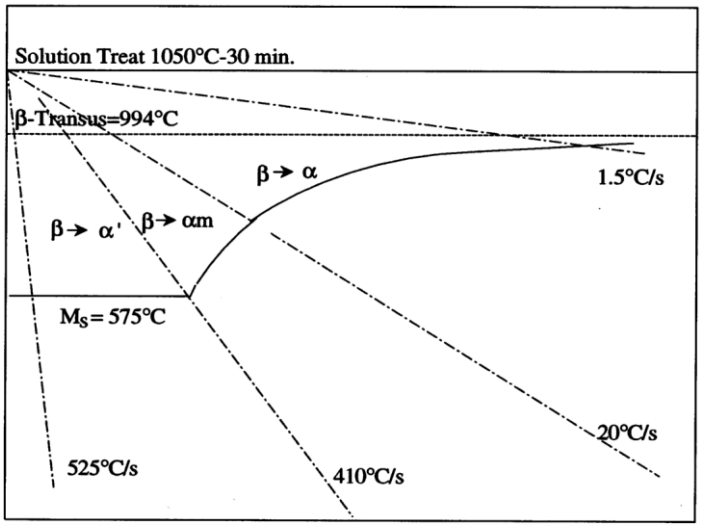

Figure 67: Schematic continuous cooling diagram for Ti–6Al–4V Beta-solution treated at 1050°C for 30 min [28]

In isothermal condition, the kinetics of this transformation is described by the Johnson-Mehl-Avrami equation (Eq. 43):

$$f(t) = 1 - e^{-(kt)^n} \quad \text{Eq. 43}$$

Where *f(t)* is the transformed phase fraction, *k* is the reaction rate and *n* is the Avrami exponent, determined using literature data [123].

It should be noted that the Johnson-Mehl-Avrami equation strictly applies to isothermal transformations, but it can be generalized to an isothermal condition by the additivity rule [121, 136].

In the case of cooling rates higher than 410 °C/s the Beta to Alpha transformation is suppressed and Beta phase transforms to α' martensite by a martensitic evolution and its amount is given by the following equation (Eq. 44):

$$f_{\alpha'} = 1 - exp[\gamma(M_s - T)] \quad \text{Eq. 44}$$

Where M_s is the martensite start temperature equal to 650 °C, M_f is the martensite finish temperature equal to 400 °C and γ is a coefficient equal to 0.015 [137].

Results showed that, if the microstructure resulting from the first thermal cycle consisted of Alpha+Beta phase, reheating causes the diffusional transformation (which is the reverse of the transformation that occurred during cooling at rates lower than 410 °C/s) of Alpha into Beta, with a kinetics described by the JMA equation (Eq. 43), while a heating up the martensite leads to its decomposition into the equilibrium proportions of Alpha and Beta phases. In the end, when the decomposition of martensite is incomplete, tempering results in a three-phase microstructure consisting of α' + Alpha + Beta.

Further results showed that, during the second thermal cycle, the cooling of martensite continues to decompose into Alpha and Beta and, in the case of cooling rates higher than 410 °C/s, the Beta phase may undergo a martensitic transformation or be retained at room temperature depending on the volume fraction of this phase present in the alloy. The kinetics of this transformation is explained by the following equation (Eq. 45):

$$f_{\alpha'}(T) = f_{\alpha'}(T_0) + \left[f_{\beta}(T_0) - f_r\right]\{1 - exp[\gamma(M_s - T)]\} \quad \text{Eq. 45}$$

Where $f_{\alpha'}(T_0)$ is the volume fraction of α' before quenching.

If the cooling rate results lower than 410 ºC/s, the Beta phase transforms into Alpha by a diffusional kinetic.

4.2.2. Transformation plasticity phenomena

The phenomenon of transformation plasticity consists of an irreversible transient mechanical weakness of a material subjected to an applied stress while it is undergoing a phase transformation in the solid state [138]. This phenomena was first observed in steels and many industrial metals alloys undergoing allotropic phase transformations where thermal, mechanical and metallurgical behavior are intrinsically linked among themselves (Figure 68).

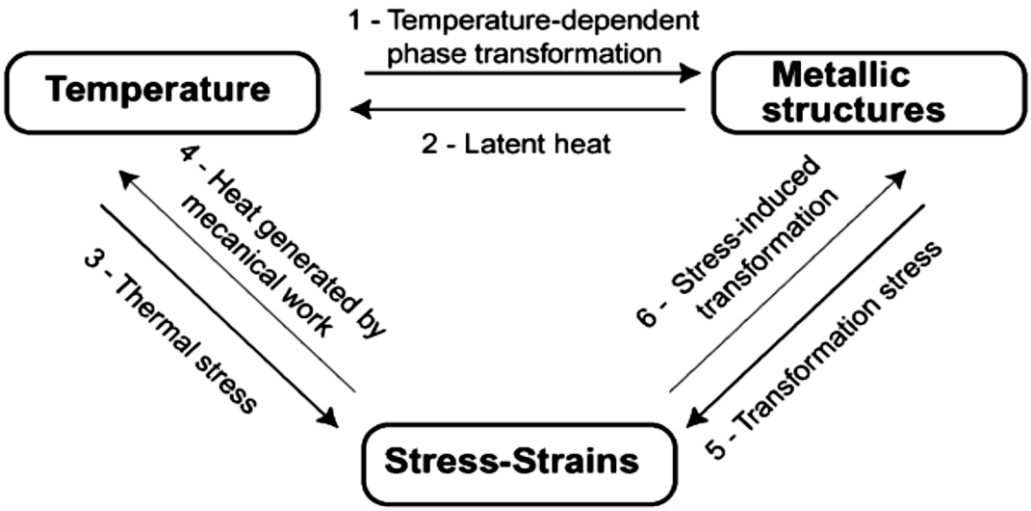

Figure 68: Illustration of the various coupling among mechanics, thermics and metallurgy [139, 140]

These transformations generate thermal, metallurgical and mechanical phenomena in the material, which can be observed under form of: thermo-mechanical characteristics generally depend on the metallurgical structure; recovery phenomenon occurring during phase transformation, so that the transmission of the strain hardening from the parent phase to the product phase can be total or partial; metallurgical phase changes (without applied stress) generating an isotropic specific volume change due to the compactness difference between parent and son phases, which produce a transformation strain; transformation plasticity (tp) phenomena.

Magee's [141] study demonstrated that transformation plasticity is caused by an orientation of the newly formed phase by the applied stress. Such a mechanism is strongly related to martensitic phase transformation, which develops in the form of plates, which generate high shearing in the austenitic phase. When no external load is applied, the plates orientation is generally random and no microscopic stresses are observed, while in the case of applied load, internal stresses are generated and a particular direction for the formation of martensitic plates is displayed.

Greenwood and Johnson's [142] observed that transformation plasticity is caused by the compactness difference between parent and son phases. If micro-stresses are applied, they are associated to the transformation, which generate micro-plastic strains in the weaker phase (due to the lower yield stress). Without applied stress, the average micro-plasticity is generally negligible and only global variation of the volume is observed. When deviatoric stress is applied, micro-plasticity is guided in the same direction of the applied stress, which generates transformation plasticity.

If diffusional transformations take place, only the Greenwood-Johnson model explains transformation plasticity and the volume variation, especially in the case of martensitic transformation [143].

Taleb et al. [144] proposed a study and comparison on the transformation plasticity strain rate prediction basing on the existing major models [145-148]. These phenomena can be modellized (Eq. 30, Eq. 47, Eq. 48, Eq. 49, Eq. 50) by using an equation composed by three different terms, which are functions of the relative characteristics of parent and product phases, the transformation progress and the applied stress conditions respectively.

$$\underline{\dot{\varepsilon}}^{tp} = \left(\boldsymbol{f_1}\left(\frac{\Delta \boldsymbol{V}}{\boldsymbol{V}}; \boldsymbol{\sigma_1^y}\right), \boldsymbol{f_2(Z)\dot{Z}}, \boldsymbol{f_3}\left(\boldsymbol{S};\ \boldsymbol{\sigma_y(Z)}\right)\right) \qquad \textbf{Eq. 46}$$

Where $\frac{\Delta V}{V}$ is the relative difference of volume between parent and product phases σ_1^y is the yield stress of the weaker phase, Z is the volume proportion of the product phase; S is the deviatoric stress tensor and σ_y is the yield stress of the mixture.

$$\dot{\boldsymbol{\varepsilon}}^{\boldsymbol{tp}} = -\frac{\boldsymbol{2\Delta\varepsilon_{12}}}{\boldsymbol{\sigma_1^y\left(\varepsilon_1^{eff}\right)}}\boldsymbol{ln(Z)\dot{Z}\sigma} \qquad \textbf{Eq. 47}$$

$$\dot{\varepsilon}_1^{eff} = -2\Delta\varepsilon_{12}\frac{ln(Z)\dot{Z}}{1-Z} \quad \text{Eq. 48}$$

$$\Delta\varepsilon_{12} = (\alpha_1 - \alpha_2)\Delta T - \Delta\varepsilon_{12}^{RT} \quad \text{Eq. 49}$$

$$\sigma_1^y\left(\varepsilon_1^{eff}\right) = \sigma_1^y(T) + h\varepsilon_1^{eff} \quad \text{Eq. 50}$$

Where σ_1^y is the yield stress of the weaker phase, Z is the volume proportion of the product phase, $\Delta\varepsilon_{12}$ is the difference of thermal strains, ε_1^{eff} is the cumulative plastic strain due to phase transformations, α_1 and α_2 are the thermal expansion coefficients of parent and product phases and h is the hardening modulus of the product phase.

This model was applied to a 16MND5 steel and showed a good quality of prediction with it slightly underestimates such a kinetic at the beginning of the transformation.

Neelakantan et al. [149] investigations into the possibility of improving the strength-ductility relation in the metastable Beta-titanium alloy Ti-10V-2Fe-3Al by means of plasticity induced transformation (PiTTi) phenomena. The specimens were subjected to different thermal conditions in both Beta and Alpha+Beta fields in order to study the influence of temperature evolution on both the microstructure, which controls the PiTTi effect.

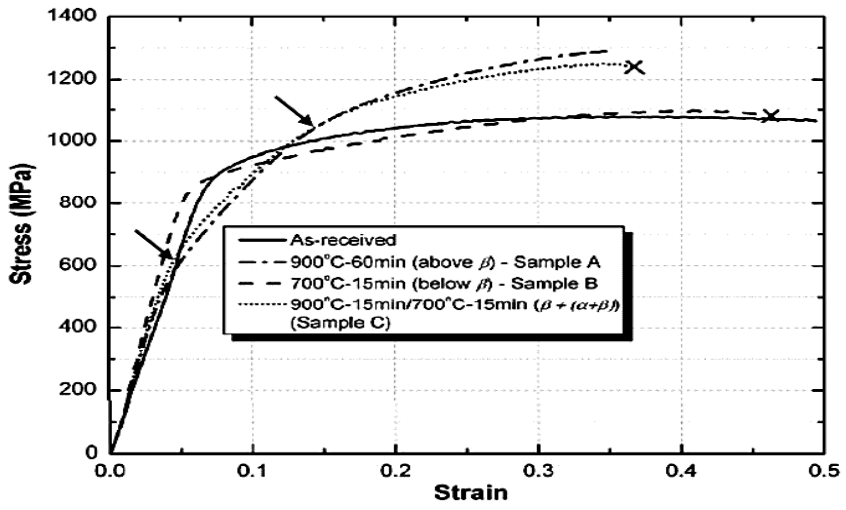

Figure 69: Compressive Stress-Strain curves with a double yield point behaviour associated to stress-induced martensitic phase transformation [149]

The studies indicate that plasticity induced martensitic transformation in Ti-1023 alloy can be successfully controlled to achieve improved mechanical properties and the stress-induced martensite formation influences the microstructural evolution. The stress-strain curves exhibiting stress-induced martensite showed about 20% increase in strength, while retaining a reasonable ductility level (Figure 69). The formation of stress-induced martensite was accompanied with double yield point under compression testing, observed in both Beta and Alpha+Beta fields. The ability to undergo such hardening via inducing the formation of seems to be related to the control of the heat treatment temperature and time, and the Beta phase amount.

More recently, the effect of stress induced martensite has been observed in Beta titanium alloys [129, 150-153], where a fundamental parameter to control such effect is the microstructure of the alloy, in particular the stability of the β phase, which can be expressed in terms of parameters such as the martensite start temperature (Ms) [129, 151-153]. It means that the material composition and grain size could be subjected and controlled via a proper selection of heat treatments [129, 150, 154, 155].

4.3. Numerical applications in forging processes design of titanium alloys

As the previous arguments are much more fundamental in understanding the material behavior in the prospective to define a good characterization, the use of methods in forging parameters optimization by means of numerical tools may be extremely useful in correct set-up of forging sequences [156, 157]. In fact, in the case of complex shapes made out of expensive materials (like titanium alloys) in which the geometrical aspects arise in a large initial amount of material, it can be important to identify those geometrical parameters mostly influencing the cavity filling. Similar considerations can be made for the residual stresses calculations, which induce a different shape than the planned one.

In this scenario, the numerical simulation of forging processes with FEM based codes can assist the forging engineer in establishing and optimizing process variables and die design (Figure 70), obtaining process development efforts and costs reduction [158, 159].

This tool can be used to perform analysis of the die design parameters, and to get the accurate results without damaging any physical structure. Moreover, the structure can easily be modeled in CAD package and then can be transferred to FEA package where the various analysis can be done. The product optimization can be reached by change material properties or the geometry in CAD model.

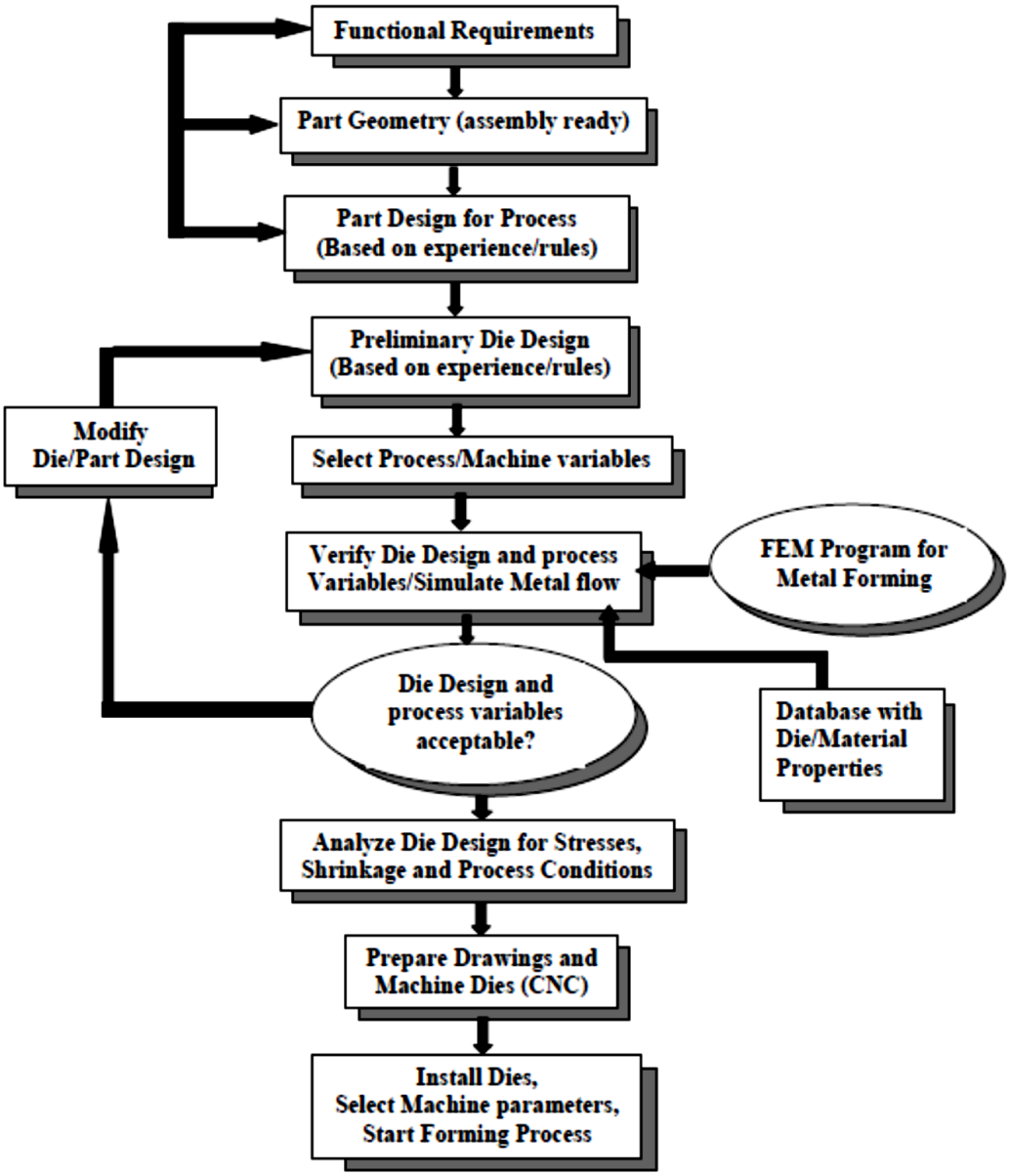

Figure 70: Flow chart illustrating forging process design [160]

Castro et al. [161] presented an evolutionary genetic algorithm to calculate the optimal work-piece shape geometry and work-piece temperature. The design problem was

formulated as an inverse problem incorporating FE thermal analysis and an optimization technique conducted based on an evolutionary strategy, adopting a rigid viscoplastic flow-type formulation, valid for both hot and cold processes.

The two numerical examples of an inverse problem were efficiently solved in order to obtain the minimizing of barreling effect when upsetting a cylinder and fitting a prescribed polynomial free boundary shape. The final shapes resulted very close to the intended ones under energy-minimizing constraints. Moreover, the developed genetic algorithm displayed being no-sensitivity-dependent, runs well even for discontinuous derivative fields, discrete design variables and did not introduce iteration-dependent numerical errors.

Kim et al. [162] have summarized the results of industrially relevant work in progress research with the DEFORM™ software, by means of a study on a new tool design for cross groove inner race for a constant velocity joint, the flashless forging of an aluminum connecting rod, design of cold forgings and forming sequences, die wear in warm forging extrusion.

Kim et al. [163] have given several examples of cold forged parts collected from literature and cold forging industry. For the example parts, forming process sequences, including the dimensions of the workpiece at each forming station, are given. They have been verified forming sequences generated by FORMEX with FE simulation program such as DEFORM.

Song at al. [164] studied the process design for closed-die forging of a bevel gear used for a component of automobile transmission made out using a 3D FE simulations. Process variables of the closed-die forging of the bevel gear were selected to be the pressing type, punch location, and billet diameter and, on the base of FE simulation results, an appropriate process design avoiding under-filling and folding defect was carried out. In addition, cold forging of the bevel gear was experimentally tested in order to estimate effectiveness of the designed process, the design process for the closed die forging of the bevel gear for the numerical analysis. The experimental results showed that bevel gear with complete formation of the teeth, obtained without making any forming defects, while flash in a forged product and punch fracture was occurred due to a slight difference in the punch stroke during formation. Through numerical/experimental comparison, it was

found that die clamping device increased the die clamping force was needed to improve the die safety.

Duggirala et al. [165] have developed three design schemes using different die shapes by means of finite element simulations of cold forging process of the spur gear with two-dimensional axial-symmetric model. The post processing data was used to investigate the strain distributions and velocity distributions, which are important pointers to be evaluated. Three-dimensional simulation for the relatively better scheme was performed considering the complicated geometric nature of gear and the results showed that the corner filling was improved and well-shaped gear was forged. Moreover, an experimental specimen was created in order to support and validating the numerical simulation and theoretical investigation.

Im et al. [166] developed a computer aided process design technique, based on a forging simulator and commercial CAD software, which have been used together with its related design system for the cold-former forging of ball joints. The forging sequence design was assisted by knowledge-based rules and some basic laws. The detail designs for a design candidate of the selected forging sequence were carried out in an automatic or interactive manner by considering design constraints and experience-based laws. From the detail designs, all of the forging simulation information was extracted automatically and the whole forging process was simulated without any user interface. The forging sequence design and its detail designs were generated through user/computer interaction using templates, design databases, knowledge-based rules and some basic laws.

Kim et al. [167] proposed a technique to determine the initial billet geometry for the forged products using a function approximation by means of a three-layer neural network and a back-propagation algorithm was implemented to train the network. The neural network were applied to find the optimal initial billet size for a plane-strain rib/web product in cold forging and for an axisymmetric rib/web product in hot forging. Finally, the billet geometry was determined by applying the ability of the function approximation of neural networks to determine an optimal billet, which satisfies the forming limitations; minimizes incomplete filling in the die cavity, load, and energy and secures a more uniform distribution of effective strain. Thanks to this approach, the number FEM simulation in process planning was significantly reduced.

Hsu et al. [168] proposed a cold forging process design method based on the induction of analytical knowledge, using a finite-element-based software to analyze various multi-stage cold forging processes based on pre-defined process condition parameters and tooling geometry. Two industrial cases have been studied to demonstrate how to use the analytical knowledge for process design, accomplished with two different approaches: one is the forward manner seeks what the product will be, based on the pre-defined process conditions; and the other is the backward manner, which optimizes the process condition parameters based on the required product information. According to the simulation results, a knowledge-acquisition procedure was instituted and a neural network model, in which the multi-layer network and the back-propagation algorithm are utilized to learn the training examples from the simulation results, was developed. Moreover, an industrial case study for the multi-stage cold forging process design of a low-carbon steel speaker tip was studied and the optimal process condition parameters, such as the preform punch geometry and the preform punch stroke were found, based on the requirement of homogeneous plastic deformation of the cold-forged product. This method resulted useful to decide the cold forging process parameters for producing a part within the required minimum quantity of the die set.

Altan et al. [169] investigated real applications of forged parts with particular focus on suck-in type extrusion defects, forging of bevel gears, stress analysis of forging tooling, design of multi-stage cold-forging operations, design of a net-shape cold-forging operation for pipe fittings and development of a new test to evaluate lubrication in cold forging.

Badawy et al. [170] described a computer-aided system called “FORMING” for designing the forming sequence for multistage forging of round parts. This CAE software can handle only solid round parts without protrusions and can be expanded to design forming steps for hollow parts and parts with internal protrusions that are forged without flash in upsetters, automatic forging machines, and vertical presses.

Di Lorenzo et al. [171] studied the finishing forging in order to obtain the desired product without shape defects such as underfilling or folding and with a minimum material loss into the flash in closed die forging. It was applied an inverse approach to the preform shape optimization problem using a response function which links the set of parameters defining the preform shape with the fulfillment of the product design

specifications. This approach was applied to a closed die forging process aimed to the production of a C-shape component, and has allowed to determine the optimal preform geometry which ensures the complete filling of die cavity .

Tomov et al. [172] provided a description of some die forging operations selected as representative steps for the near-net-shape forging of spur gears. The main results are obtained on the basis of quasi-static model material experiments that have been applied to collect data needed for statistical processing or to verify some analytical solution and computer simulations. A combined approach of using model material experiments and statistical processing of the data collected together with some analytical solutions and FEM simulations has been applied to cover certain consecutive steps of the near-net-shape forging of cylindrical spur gears. Simple regression equations were derived for calculating both the shape changes and the force conditions for some preparatory open-die forging operations and an improved pre-forging shape for preform design in the closed-die forging of H-shaped parts was proposed. These results could be helpful in engineering practice for simple calculations in process planning design.

Liou at al. [173] presented a study on the optimization of forged parts by means a robust design methodology and FE analysis to identify the controlling process parameters which have great effects on the formation of residual stresses in the radial forging process.

The experimental plan, in which frictional coefficient, length of die land, reduction percentage, inlet angle and corner fillet were taken into account, was performed by using the orthogonal array and concept of the signal-tonoise ratio. The ANOVA analysis showed that the inlet angle, friction coefficient and length of die land have the most significant effects on the optimum residual stresses.

Either, parametric FE simulations were carried out in order to optimize the design parameters of the manufactured products and the manufacturing processes.

The selected controlling process parameters of the forging operation influencing the residual stress distribution in products were: length of die land (L); inlet angle (a); friction coefficient (F); reduction percentage of cross-section (R); corner fillet (C).

Results (Figure 71) showed that the inlet angle (a) was the dominant process parameter in deciding the residual stresses in the forged products. The smaller the inlet angle, the smaller the residual stresses. The comer fillet (C) showed a negligible effect on the forged residual stresses, while the longer die land (L) had a better surface finish, but from the

robust analysis, it resulted that the longer die land produced a higher residual stresses causing higher deformation. In addition, the longer die land might required higher punch loads during the forging operation due to the higher interfacial friction between the workpiece and the die. Hence, the smaller the friction, the smaller the residual stress.

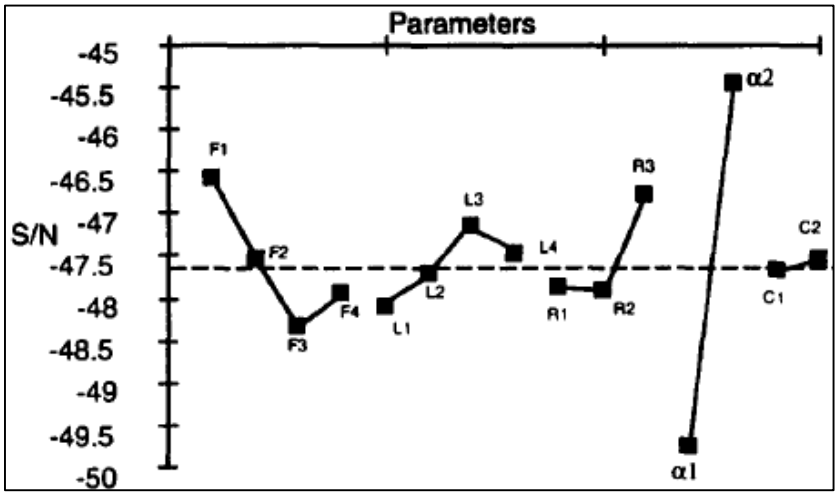

Figure 71: The response graph of forged residual stress of each parameter [173]

Banaszek et al. [174] studied the influence of main parameters of forging process and shape of tools on the homogenization of local strain values in whole cross section by means of a theoretical analysis verified through laboratory tests. The analysis was focused to determine the shape and geometry of tools giving a uniform distribution of strain intensities in the forgings during the forging process. The results indicated that it is possible to exert a substantial effect on the kinematics of material flow during the process of forming a forging by the appropriate selection of the shape of anvils.

Hu et al. [175] described and compared the effects of temperature and strain rate on the forming characteristics of 6Al-4V Ti alloy and the intermetallic alloys, TiAl and Ti3Al. Process conditions for forging 6Al-4V alloys were examined in detail to establish material and boundary condition data for accurate simulation of forging processes by finite element methods and the hot-die forging process was taken into account as a possible economic method for the production of blade forms near to net-shape. A comparison of the forging characteristics of 6Al-4V, super a2 and y titanium alloys has been obtained, while the determination of the boundary conditions during hot-die forging of titanium alloy has established the fundamentals step for the net-shape forging of

aerofoil blades. The results (Figure 72) demonstrated that the numerical techniques can predict process and product characteristics close to experimental values.

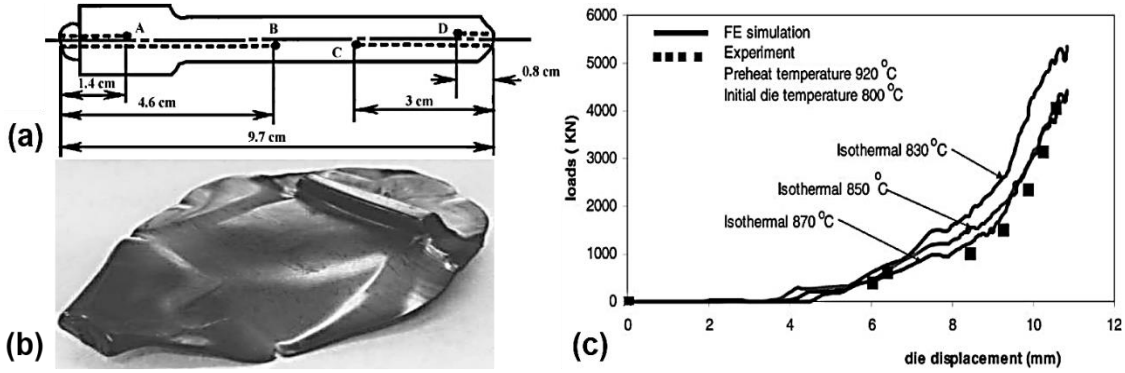

Figure 72: Forged blade design (a) and experimental test (b); numerical/experimental comparison of forging load [175]

Shaeffer et al. [156] studied the forging process of a component with axial symmetry, carried out using three different forging stages on an initial billet of 7 kg made out of l6MnCr5 steel. The study was pursued using both cold and hot (1200 °C) processes, performed by means of a 40 MN mechanical press. Moreover, the commercial software QForm 3D was used to carry out a comparative numerical campaign.

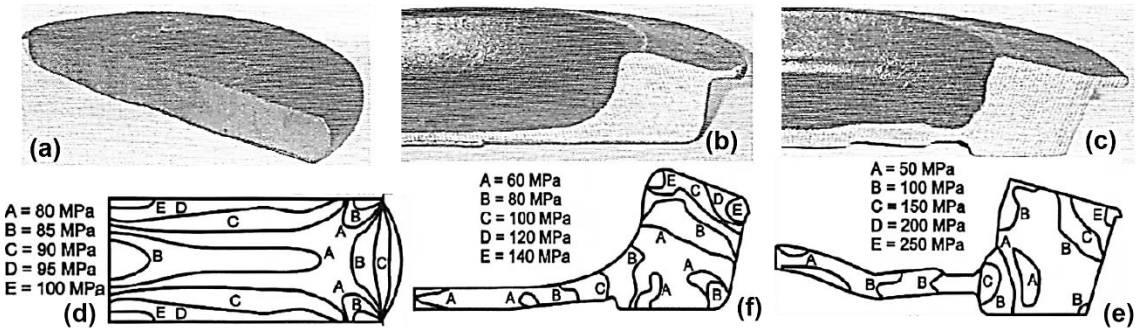

Figure 73: Experimental and numerical forging steps: (a) upsetting and (d) calculated effective stress , (b) preform and (f) calculated effective stress; (c) final shape and (e) calculated effective stress [156]

In both processes analyzed, the results of simulations showed an excellent correlation with the real experiments. In particular, the hot forging simulation demonstrated that it is possible to forge the component without flash, without a significant increase in the forging load as well as the die stress. The material saved in the flashless process was

about 0.33 kg per workpiece, which (depending on the production volume) may be a very significant saving.

The cold forging simulation reproduced the location of the lap found in practice. It also showed that the stress peak in the lower punch was 2350 MPa, which is higher than the flow stress of the AISI M2 (2100 MPa) steel.

Hu et al. [176] continued the study on the hot die forging of titanium alloy aerofoil sections, by means of both experimental and numerical tests. A two-dimensional thermal–plastic coupled finite-element model was used to analyze the mechanical and thermal interactions between the forging dies and the workpiece, and a particular attention has been paid to deformation, temperature, stress and strain inside the blade. All these parameters were used in combination with an internal state variable to determine the evolution of the Beta microstructure of the blade during hot forging (), in which the initial Beta phase amount and grain size was modelled using simple Arrhenius relationships for the temperature range of interest.

The comparison between theoretical with experimental results showed that the developed model may be used to accurately predict microstructural parameters. Moreover, it resulted that the flow behaviour of Ti–6Al–4V is predominately a function of Beta phase grain size and volume fraction.

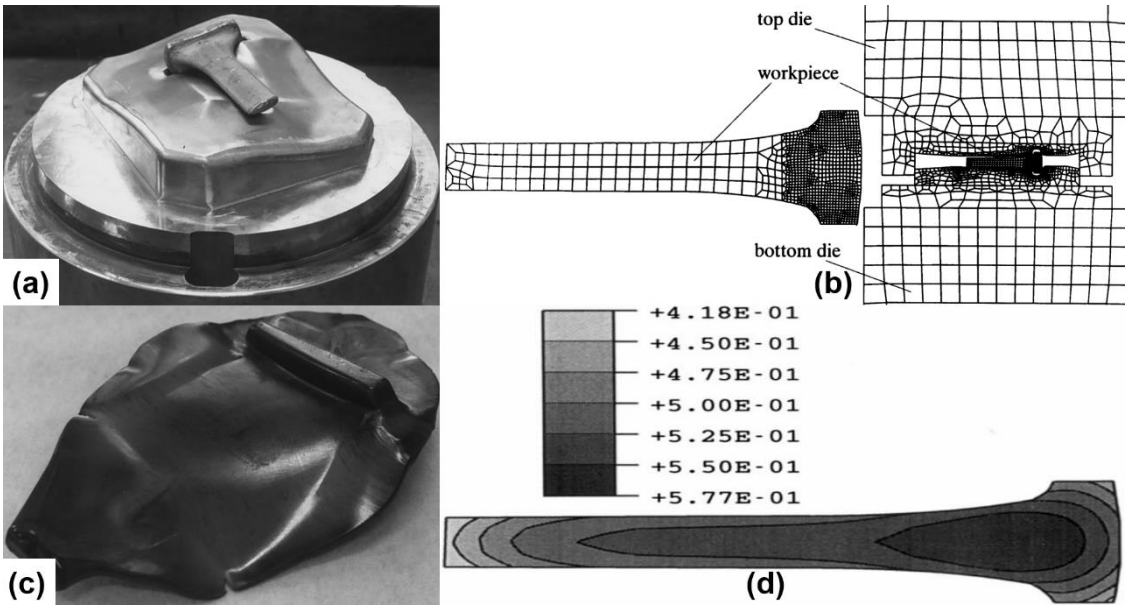

Figure 74: (a) blade preform, (b) FE longitudinal section, (c) blade bottom die and (d) Beta phase volume fraction (x100%) [176]

Parikh et al. [177] optimized the forging process and reduced the required force to forge a complex provided by Queen City Forging Company by means of a simulation campaign developed design the forging sequence able to product the workpiece using a press of 800 ton of forging load capacity. Solid Edge™ software was used to model the dies while MSC-SuperForge™ was used to simulate and analyze the forging process by adopting different solutions in order to obtain a final product forged in two stages with a maximum load of less than 750 ton. Results demonstrated that the force requirement for a part was very high for a single set of dies, while an appropriate selection of preform shape significantly reduced the required load.

Srivastava [82] investigated the process parameters such as billet temperature, die speed and friction coefficient in a hot closed die forging of automotive. A generic Artificial Neural Network (ANN) model was developed with the help of training data obtained from finite element simulations. The inputs were simultaneously fed to two different networks, which predicted three final forging load and evaluated the maximum equivalent strain rate. This study displayed the capabilities of ANN models in calculating correlations between various processes parameters of a manufacturing process calculated by means of FEM simulations. Moreover, the influence of die speed, fiction coefficient and initial billet temperature on the final forging load and maximum equivalent strain rate were studied with the aim of using this data in training ANN under parallel prediction scheme. The results from these models can assist in achieving energy and material saving, quality improvement and in the development of sound automotive pistons. As this approach is generic in nature, other complex industrial processes can be similarly modelled.

Gohil [178] studied the variation of various parameters such as stress, strain, temperature and force during a closed die hot forging process of AISI 1016 using a computer modeling approach to transform the theoretical aspects in to a computer algorithm which would be used to simulate and analyze the closed die hot forging process. The whole process was appropriately divided in to finite number of steps and then the output values were computed at each deformation step with the aim to significantly improve the productivity and reduce the energy consumption of the overall process for the components which are manufactured by the closed die forging process and contribute towards the efforts in reducing the global warming. The results of the simulation

campaign were showed that the selection of material parameters from the material property database and the friction coefficient are strongly related to a correct selection of input data and number of trials.

5. Numerical characterization of Ti-6Al-4V alloy

5.1. Themo physical properties

The first step of numerical characterization of the Ti-6Al-4V alloy was to collect all needed thermal and physical properties of the material in order to obtain a good response with respect to the temperature conditions of hot forging processes. It is possible to find a huge amount of literature data on thermo-physical behavior of Ti-6Al-4V but the last results obtained by Boivineau [179] showed a sensible improvement in characterization. Moreover, the use of JMatPro [180] database resulted to be very exhaustive in both thermal and mechanical aspects of the considered alloy.

The specific heat capacity at constant pressure C_p has been considered within a wide temperature range up to 1400 K (Figure 75). The peak observed at 1220 K corresponds to the Beta-transus point. Prior studies showed some difference in property evolution with temperature [181] pulse-heating experiments, in particular from 800 to 1100 K.

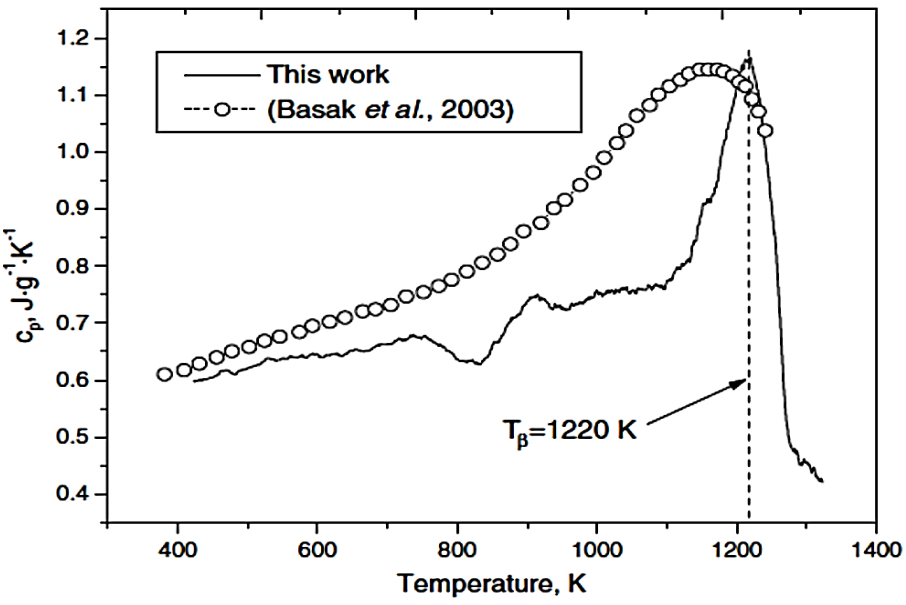

Figure 75: Specific heat capacity of solid Ti-6Al-4V [179, 181]

Again, the thermal conductivity (Figure 76) was included in material definition in order to take into account the thermal evolution during a thermo-mechanical stage.

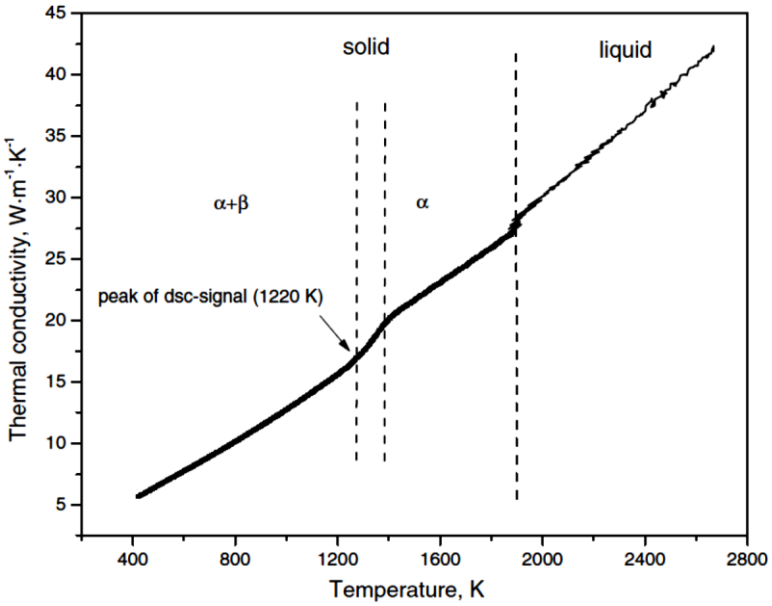

Figure 76: Thermal conductivity of solid and liquid Ti-6Al-4V versus temperature [179]

The specific volume variation calculated by considering the radial expansion measurements has been also taken into account in material characterization (Figure 77).

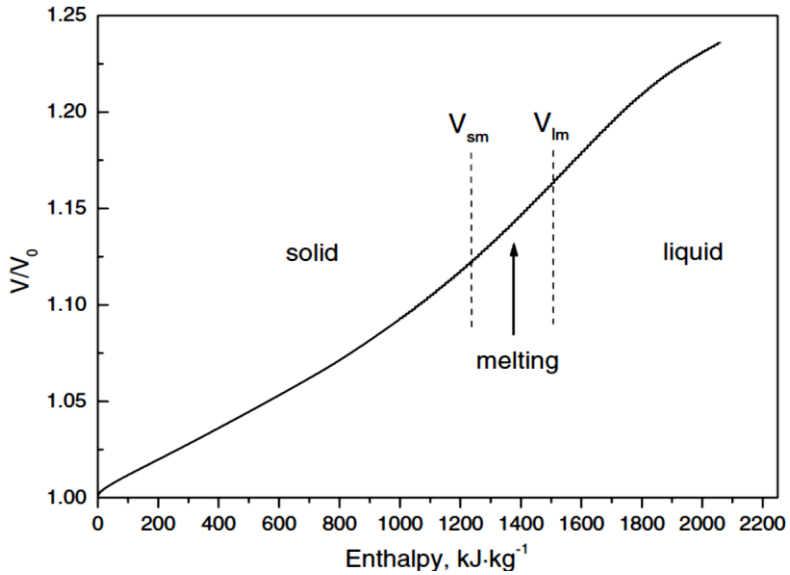

Figure 77: Specific volume of solid and liquid versus enthalpy for Ti-6Al-4V alloy [179]

It should be noted that the physical properties undergo to a discontinuity at the Beta-transus temperature, highlighting that the multiphasic nature of the material and the differences between the allotropic forms constituting the base alloy.

5.2. Elastic behavior

The elastic mechanical properties of the considered alloy were carried out by considering the data included in the JMatPro database [180] both Young's modulus (Figure 78 - a) and Poisson's ratio (Figure 78 - b). The Young's modulus of Ti-6A1-4V alloy exhibits a minimum at about 800°C, which correspond to the temperature of transition from retained Beta to α' or α" martensite.

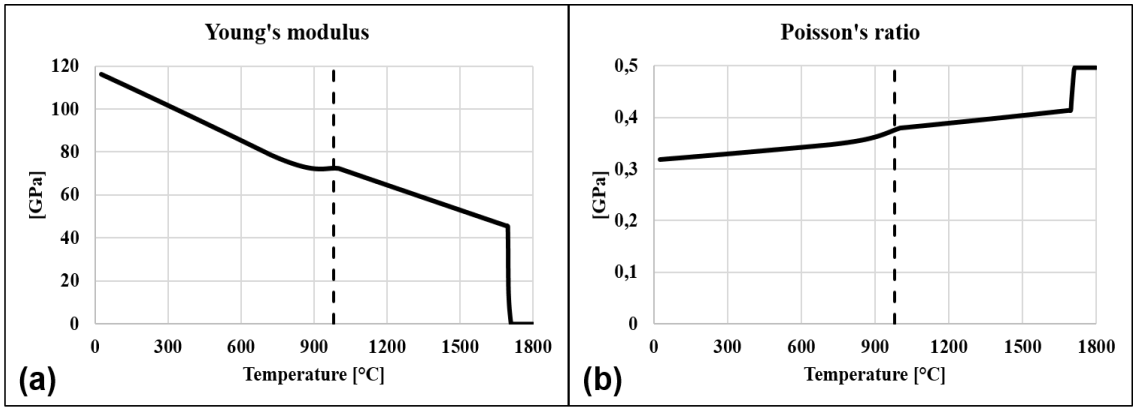

Figure 78: Young's modulus (a) and Poisson's ratio (b) versus temperature for Ti-6Al-4V alloy with Beta-transus point (vertical dashed line) [180]

At the same time, thermal expansion was considered in definition of elastic behavior of the material.

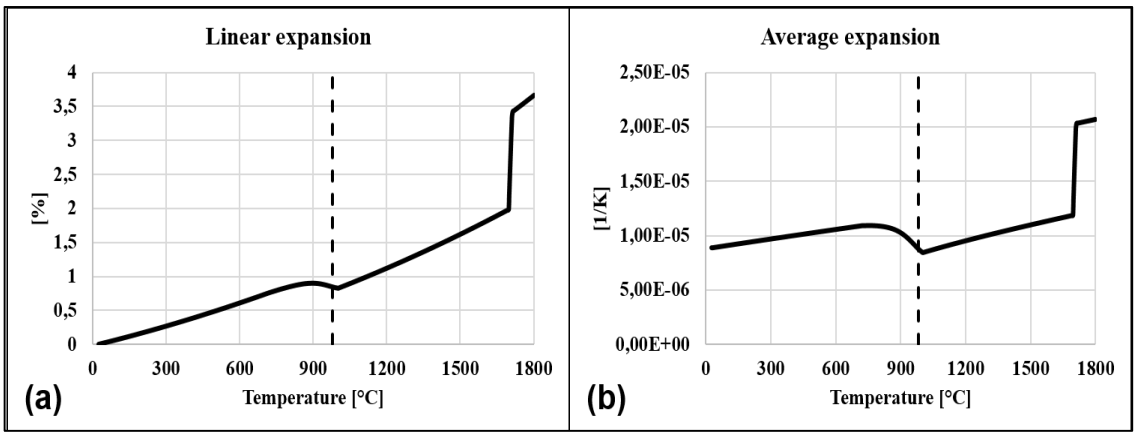

Figure 79: Linear (a) and average (b) expansion of Ti-6Al-4V alloy with Beta-transus point (vertical dashed line) [180]

This behavior displays that a correlation between single-phase properties and phase chance is involved within the whole base material.

5.3.Plastic behavior

The Ti-6Al-4V phase titanium alloy is often hot deformed, mainly by open die or close-die forging., and the desired mechanical properties can be achieved alloys by development of proper microstructure in plastic working and heat treatment processes [16, 32, 182].

A great amount of plastic flow stress conditions was considered in order to run coherent numerical analysis of complex thermo-mechanical behavior of Ti64 alloy in a proper strain rate range.

Using both the data collected during the literature research (see Cap. 4.1) and JMatPro [180] database a wide set of 119 plastic flow stress curves in a strain rate range from 0.001 to 1000 s^{-1} and a temperature range from room temperature to 1500 °C was included in material definition (Table 6).

Table 6: Plastic flow stress curve set selected for Ti-6Al-4V characterization

Strain rate [1/s]	Temperature [°C]																
0.001	25	50	100	200	300	400	500	600	700	800	900	1000	1100	1200	1300	1400	1500
0,01	25	50	100	200	300	400	500	600	700	800	900	1000	1100	1200	1300	1400	1500
0.1	25	50	100	200	300	400	500	600	700	800	900	1000	1100	1200	1300	1400	1500
1	25	50	100	200	300	400	500	600	700	800	900	1000	1100	1200	1300	1400	1500
10	25	50	100	200	300	400	500	600	700	800	900	1000	1100	1200	1300	1400	1500
100	25	50	100	200	300	400	500	600	700	800	900	1000	1100	1200	1300	1400	1500
1000	25	50	100	200	300	400	500	600	700	800	900	1000	1100	1200	1300	1400	1500

Most of curves are extended to strain values greater than 100% in order to consider the tensile phenomena involved in forging processes, in particular the direction the surface curvatures [183]. An example of stress-strain curve set is given by the following image (Figure 80).

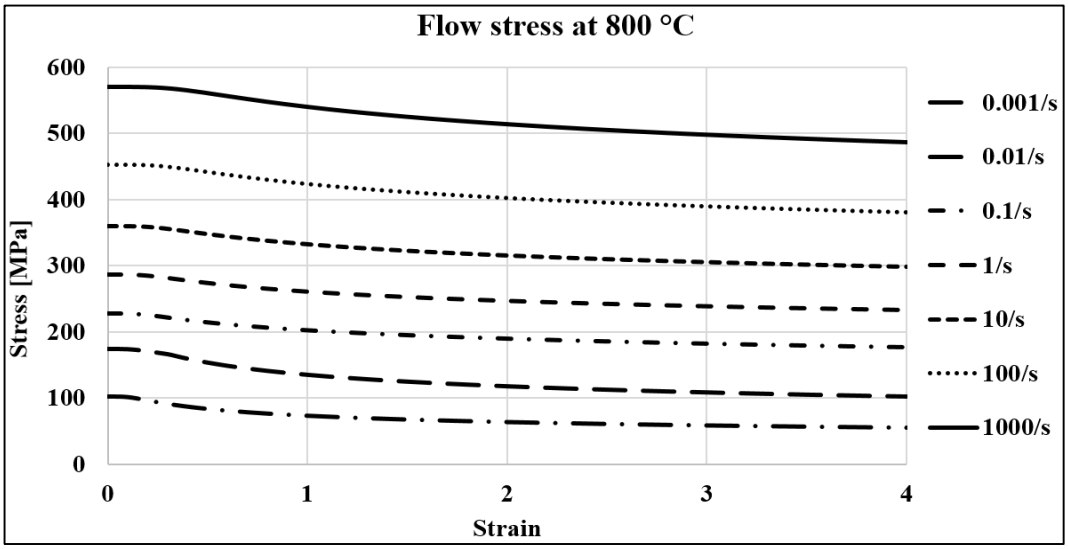

Figure 80: Stress-strain curves at 800 °C for Ti-6Al-4V alloy [180]

5.4. Phase transformation behavior

Another important step for the model tuning was the implementation of data describing the phase transformation phenomena, namely the transformation from the Alpha phase to the Beta phase during heating up and the transformation from the Beta phase to the Alpha+Beta phase during cooling down.

The first transformation was modeled by means of the simplified form of the Avrami [125] model (Eq. 51) already embedded within the code:

$$f_{\alpha\rightarrow\beta} = 1 - exp\left[a\left(\frac{T - T_S}{T_E - T_S}\right)^d\right] \qquad \text{Eq. 51}$$

Where $f_{\alpha\rightarrow\beta}$ represents the amount of phase change;T represents the instantaneous temperature; Ts is the transformation starting temperature set to 600 °C; Te is the end of

transformation temperature set 980 °C; a and d are coefficients calculated by performing a minimization of the standard deviation with the experimental curve at 1°C/s of the phase transformation and the numerical model curve and their value is -1.892 and 5.1 respectively. This approach does not take into account the influence of thermal energy rate in kinetics of phase transformation. The approximation of the curve fitting at 1 °C/s (Figure 81) was done with the aim to have sufficient approximation with a conventional heating cycle. In those cases in which a heating stage is given by plastic work on the material, with rapid heating coming from fast deformations, the quality of the model rapidly decreases. However, the error is acceptable due both to the average temperature of forging processes of titanium alloys and the low amount of residual Alpha prior phase involved in that kind of transformation.

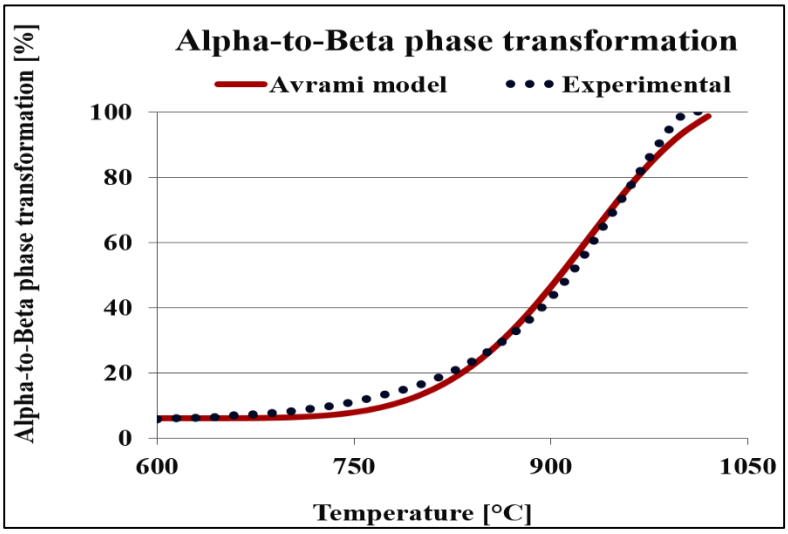

Figure 81: Curve fitting of generalize Avrami model [125] with respect to experimental data [180] for Alpha to Beta phase transformation at 1 °C/s for Ti-6Al-4V alloy

The Alpha+Beta phase change was implemented using the generalized Avrami equation [125] (Eq. 52) and the TTT start curve for Ti-6Al-4V (Figure 82).

$$f_{\beta\rightarrow\alpha+\beta} = 1 - exp(-kt^n) \qquad \text{Eq. 52}$$

Where $f_{\beta\rightarrow\alpha+\beta}$ represents the amount of Beta phase transformend into Alpha+Beta phase during a cooling stage; k is a coefficient calculated by means of TTT start curve

(Figure 82) and *n* is the Avrami number and it was set equal to 1.32 basing on experimental results coming from literature [123]. It is known that the Avrami model can be applied under the specific conditions of isothermal transformation, but it is possible to solve this issue by considering that the simulation code solves the calculation of a non-isothermal process with a series of step-by-step iteration having an isothermal stage.

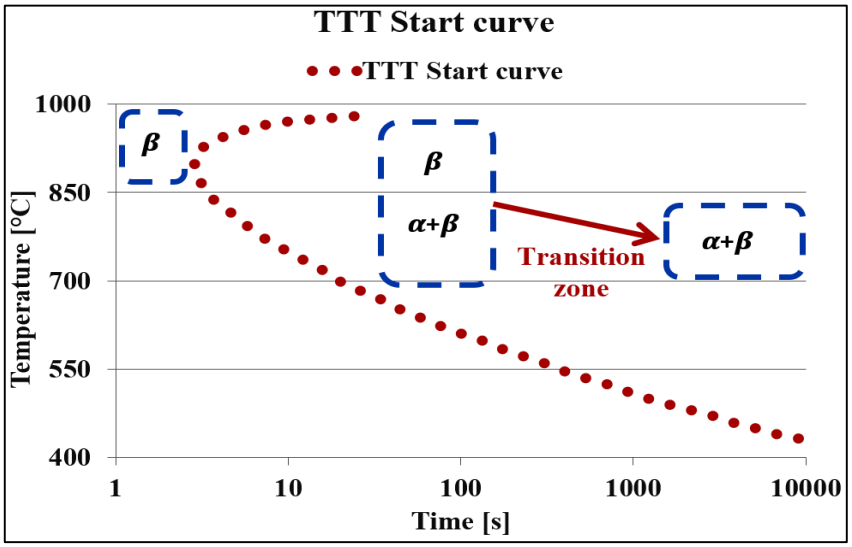

Figure 82: TTT start curve for Ti-6Al-4V alloy with transition zones

In the end, the Beta to martensitic Alpha phase change was included into the characterization in order to cover those cases in which a part of forging is rapidly cooled due to its geometry and boundary thermal conditions. In fact, in this case it is possible to obtain a cooling stage with temperature rates from 20 to 410 °C/s (Figure 67), which results in martensitic Alpha phase formation.

The transformation kinetic associated to this phase evolution was modeled again using the Avrami model (Eq. 53), taking into account the studies of Crespo [135].

$$f_{\alpha'} = 1 - exp[\gamma(M_s - T)] \qquad \text{Eq. 53}$$

Where M_s is the martensite start temperature equal to 650 °C, M_f is the martensite finish temperature equal to 400 °C and γ is a coefficient equal to 0.015 [137].

6. Data validation

6.1. The TitaForm project

TitaForm (Project code: PON01_00538) is the acronym of a research project proposed to a national call defined PON (Piano Operativo Nazionale), Linea 1. Such call required the set-up of proper consortia made of SME, public and private research centers and Universities. The final goal of the project is the identification of the process parameters to realize mock-ups of aerospace components made of titanium alloys having a geometry very close to the actual one, minimizing machining operations in order to obtain a decreasing of buy/fly ratio.

The main objective was to introduce innovative forging processes, by completely revising the currently standardized process methods. In fact, instead of using the precision hot forging in closed dies (unusual technology in Italy) from ingots, leading to the above listed buy/fly ratios close to 20, the goal was to study the development of ingots derived from a low cost powder compaction in metallic billets having a geometry close to that of the final mock-up. The conditions of the forging process were investigated aiming to complete the forging process at a temperature higher than the Beta-transus, in order to grant an adequate plasticity of the material, allowing production of complex shapes with limited amount of edge trim removal and machining rework after forging. The investigation focused three workpieces: two of them having weight less than 1 kg and another one higher than that, both identified among the representative ones of the aerospace industry.

The project included a tuning and testing stage of effective commercial numerical models based on the finite element method and the most effective deformation tool were adopted with the aim to carry out effective numerical analyses on the basis of rheological models and libraries for the considered titanium alloy at the varying of strain, strain rate and temperature. In addition, the libraries of implemented elements, the robustness of the remeshing models, the contact algorithms and specific metallurgical models were considered.

At the end of the testing period, the DEFORM™ software was chosen and, using the material characterization previously explained, a series of comparisons with compression tests of billets and specimens was carried out to properly complete with the material behavior in the different considered case studies. The numerical models were validated through basic experiments including fundamental variables ad the forging loads [184].

6.2. Flow stress data validation

Before applying the numerical modelization of Ti6Al-4V to simulate the forming processes involved within the Titaform project, all collected data was tested by means of a comparison with in-house isothermal hot compression tests (Table 7) conducted at the University of Naples (involved within the Titaform project) in order to evaluate the quality of themo-mechanical characterization.

Table 7: Isothermal hot compression tests campaign scheme

Strain rate [s^{-1}]	Temperature [°C]			
	800	900	1000	1100
0.1	X	X	X	X
0.5			X	
0.7	X	X		X

The simulation campaign used a cylindrical billet workpiece having both diameter and height equal to 10 mm (Figure 83), while the process was carried out using very low friction conditions among dies and billet.

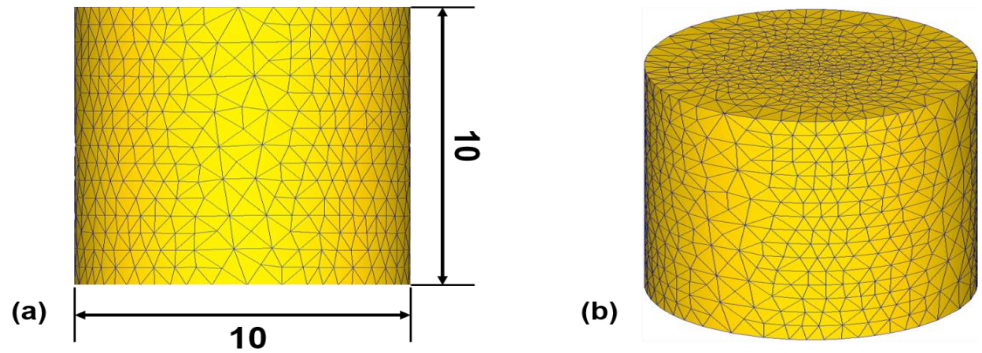

Figure 83: (a) Dimensions in mm and 3D view (b) of the billet used in isothermal hot compression tests

The numerical campaign displayed a good agreement with experimental data at varying of temperature and strain rate within the classical range of hot forging processes of Ti-64 alloy. Looking at the graph (Figure 84) it is possible to observe that the numerical prediction shows a minor estimation at lower deformation while the load calculation becomes higher at larger strains.

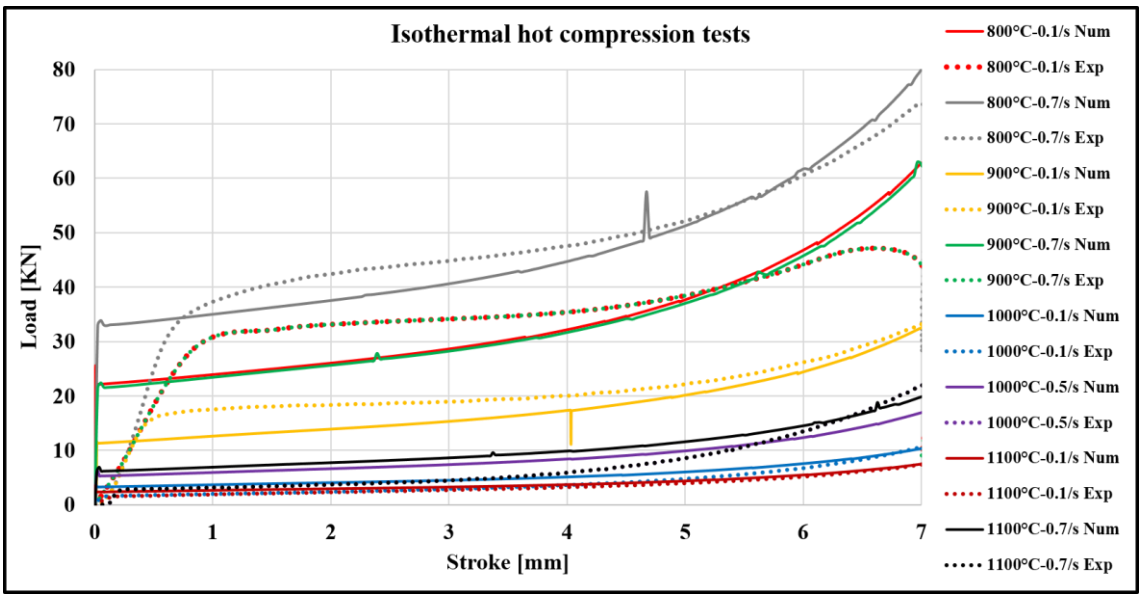

Figure 84: Comparison between experimental and numerical load/stroke data for isothermal hot compression of Ti-6Al-4V cylindrical billets

Basing on these first results, the flow stress characterization of the used alloys was considered acceptable to satisfy the requirements of the research project in terms of numerical campaign applied to the simulations of forging processes workpieces included within the proposal.

6.3.Numerical experiments on the transformation plasticity

The poor literature data focused on the transformation-plasticity modelling of titanium alloys did not allow to modellize these phenomena and insert proper parameters into the numerical characterization of the used alloy. The absence of specific coefficients prompted the set-up of a numerical campaign of isothermal hot compression tests based

on the one used to evaluate the flow stress characterization (Table 7, Figure 83) with the aim to test the influence of the transformation plasticity equation already included within the numerical code in both phase distribution within the billet and load prediction.

The DEFORM™ software includes a transformation plasticity equation in which only a single coefficient (*k*) needs to be defined (Eq. 54).

$$\dot{\varepsilon}_{ij}^{tp} = \frac{3}{2} k_{ij} h(\varepsilon_j) \dot{\varepsilon}_j s_{ij} \qquad \textbf{Eq. 54}$$

Where $\dot{\varepsilon}_{ij}^{tp}$ is the induced strain tensor, k_{ij} is the coeffcient for transformation from i to j phases, $\dot{\varepsilon}_J$ is the phase transformation rate, $h(\varepsilon_J)$ is the transformed phase, s_{ij} is the deviatoric stress tensor.

Each case was simulated considering the isothermal hot compression numerical campaign (Table 7) used in flow stress data validation. Moreover, 5 different values of *k* coefficient of the transformation plasticity equation of the Alpha+Beta and Beta to Alpha+Beta phase changes were used: 10^{-4}, 10^{-3}, 10^{-2}, 10^{-1} and 0, where the last value corresponds to the case with disabled transformation plasticity calculation. The choice of transformation coefficient *k* value was done taking into account that, when transformation plasticity of austenitic steels is considered, the coefficient value is very low.

The numerical output considered the load/stroke curves, compared to the experimental ones, and the final phase volume fraction distribution along the middle section of the billet (Figure 85).

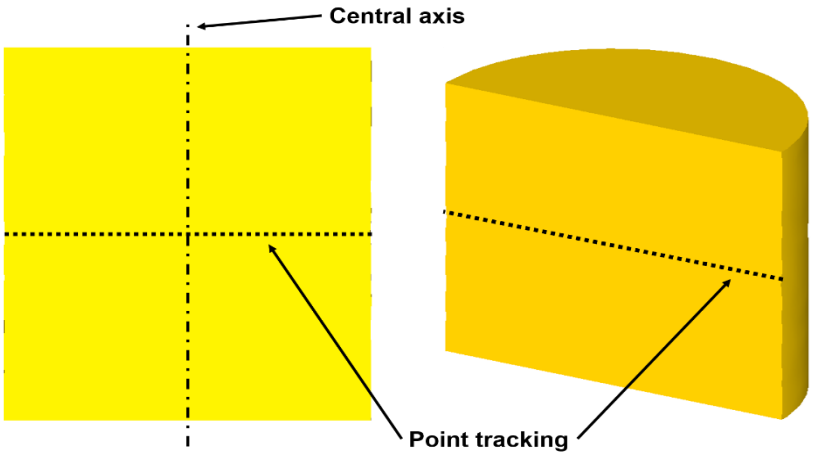

Figure 85: Point tracking distribution along the middle section of the billet

At the end of this test campaign, no significant influence on the strain rate and compression loads was found. The output displayed that increasing in *k* value does not produce any substantial variation in load prediction with respect to the case without transformation plasticity calculation. An example of load/stroke plotting of TP simulation campaign is shown below; with focus on 800 °C cases (Figure 86 - a, b).

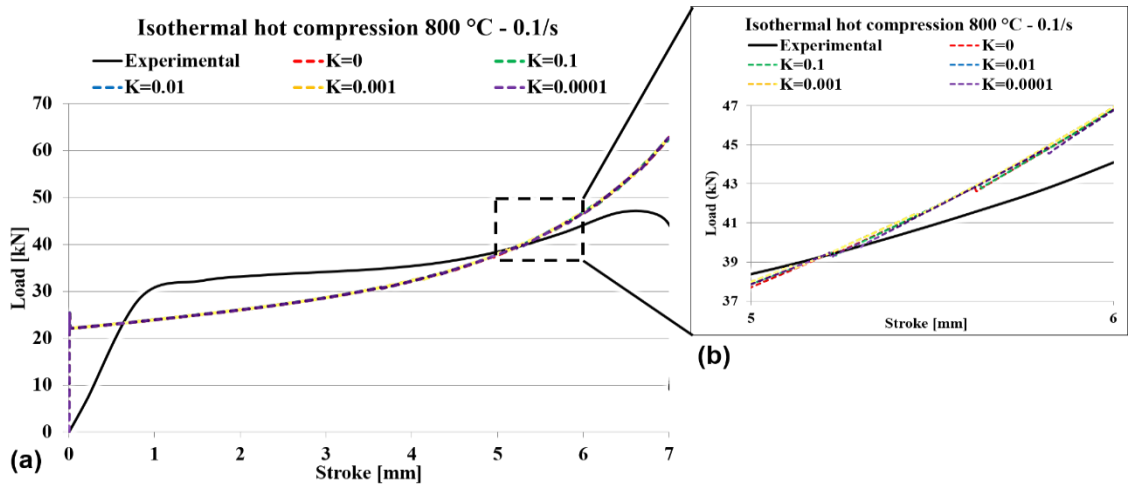

Figure 86: (a) Load/stroke numerical prediction at different values of transformation plasticity coefficient for isothermal hot compression at 800 °C and 0.1/s strain rate and (b) magnification of graph area

The case at 800 °C and 0.7/s strain rate displayed some peak distributed along the graph with significant variations, which can be associated to remeshing stage of the numerical code (Figure 87 - a, b).

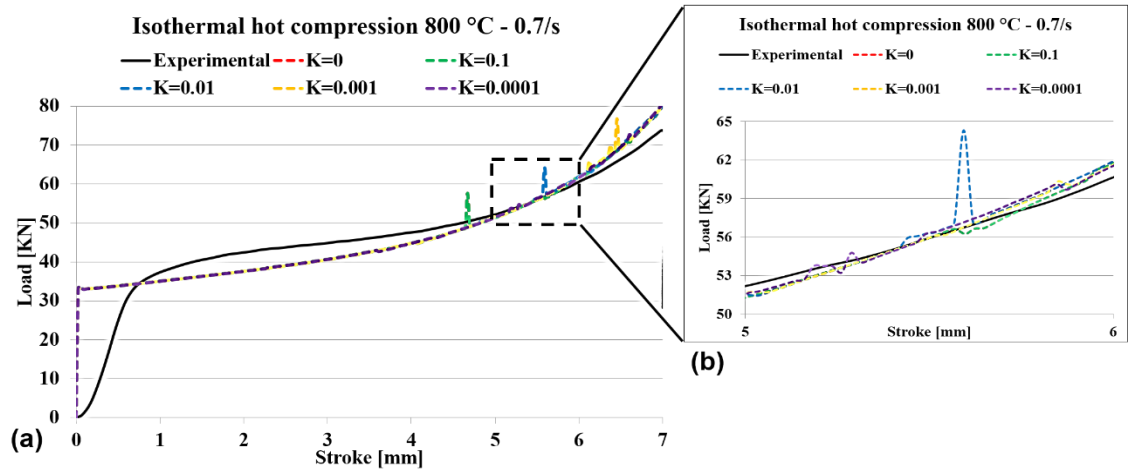

Figure 87: (a) Load/stroke numerical prediction at different values of transformation plasticity coefficient for isothermal hot compression at 800 °C and 0.7/s strain rate and (b) magnification of graph area

The results displayed a negligible effect on the phase distribution with very negligible variation along the middle section of the specimen from 0.02 to 0.4 % of phase amount (Figure 88, Figure 89, Figure 90). Since transformation plasticity adds a strain rate component, the deformation work undergoes to differences, which can result in variation of aliquot of mechanical work converted to thermal energy. It means that a different thermal cycle with different phase transformations could be applied to the material. The consequence is a different phase distribution into the specimen at the end of thermo-mechanical cycle. In order to evaluate this influence, final phase volume fraction point tracking was checked, following the same numerical campaign used in evaluation of differences in load/stroke predictions.

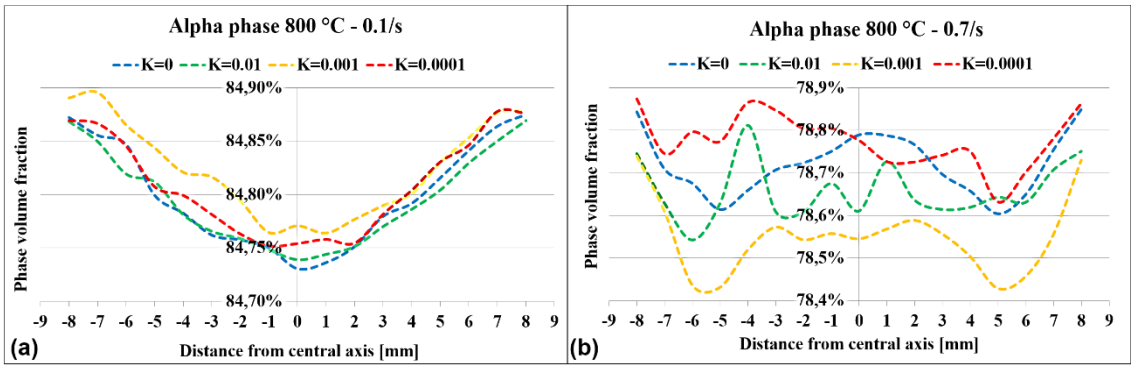

Figure 88: Alpha phase volume fraction variation at varying of transformation plasticity coefficient along the middle section of the cylindrical billets undergone to isothermal hot compression at 800 °C and (a) 0.1/s strain rate with final air cooling, and (b) 800 °C and 0.7/s strain rate with final air cooling

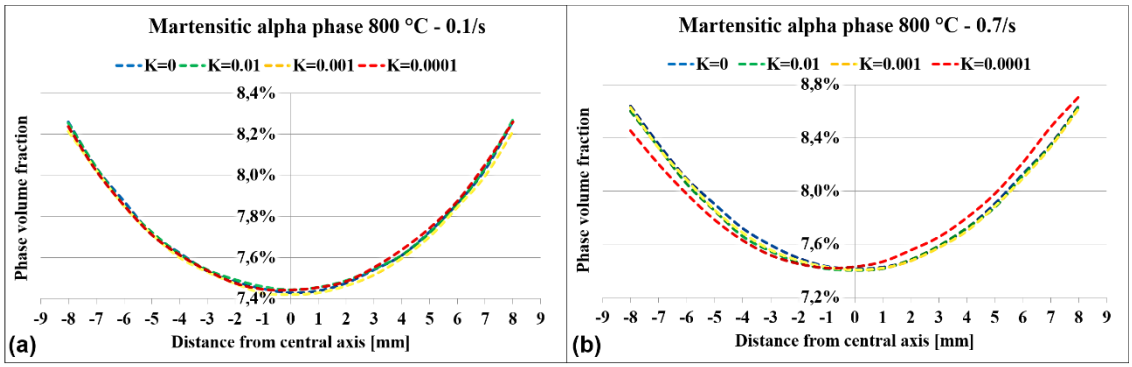

Figure 89: Martensitic Alpha phase volume fraction variation at varying of transformation plasticity coefficient along the middle section of the cylindrical billets undergone to isothermal hot compression at 800 °C and (a) 0.1/s strain rate with final air cooling, and (b) 800 °C and 0.7/s strain rate with final air cooling

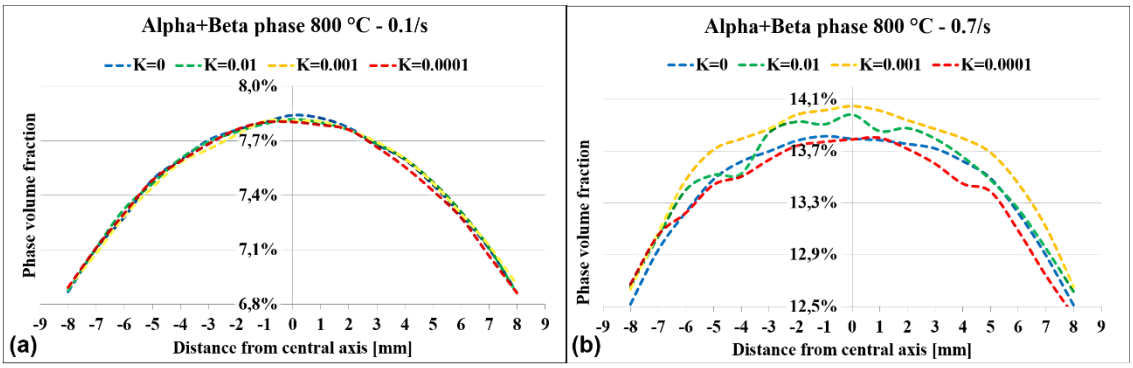

Figure 90: Alpha+Beta phase volume fraction variation at varying of transformation plasticity coefficient along the middle section of the cylindrical billets undergone to isothermal hot compression at 800 °C and (a) 0.1/s strain rate with final air cooling, and (b) 800 °C and 0.7/s strain rate with final air cooling

Each case was simulated considering both the heating at specific temperature, compression at specific strain rate and air cooling stages in order to consider the Alpha-to-Beta, Beta-to-martensitic Alpha and Beta-to-Alpha+Beta phase formations. In the end, the already used *k* values were considered.

Considering the output of this preliminary simulation campaign, no transformation plasticity phenome was taken into account in the main numerical analyses included within the research project.

6.4.Project forging work package

The Titaform project was based on the optimization of hot forming of 4 different components made of Ti-6Al-4V alloy, which require, in the case of pure machining production, a high buy-to-fly ratio.

The final aim is to reduce the buy-to-fly ratio with respect to the pure machining production of the same geometries, by means of a single-step forging sequence of a cylindrical billet, followed by a soft machining.

The geometry of this part displays some thin parts with a high rib/web ratio which may require more than one forging step to obtain a near net shape part (Figure 92).

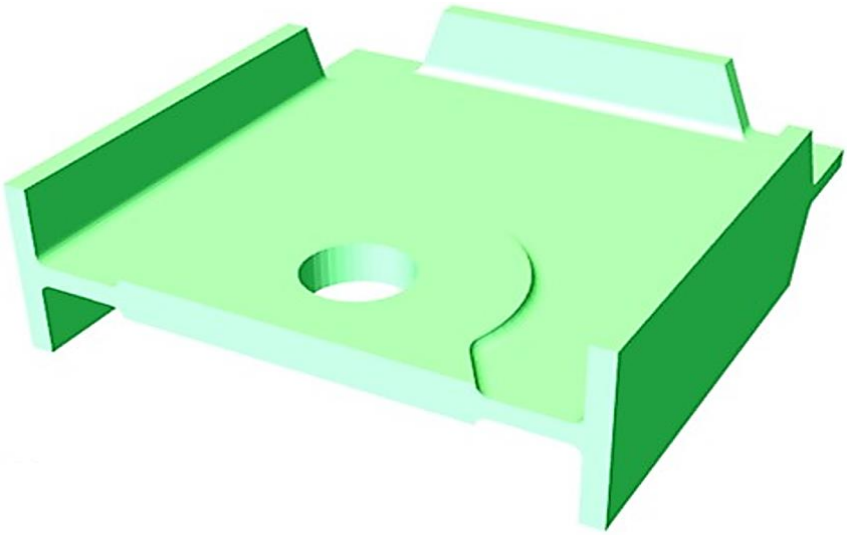

Figure 91: Small S2S machined workpiece 3D view

The smallest workpiece is called S2S (Small Part, 2-Sided, Symmetric) and has a weight of 160 g about (Figure 91).

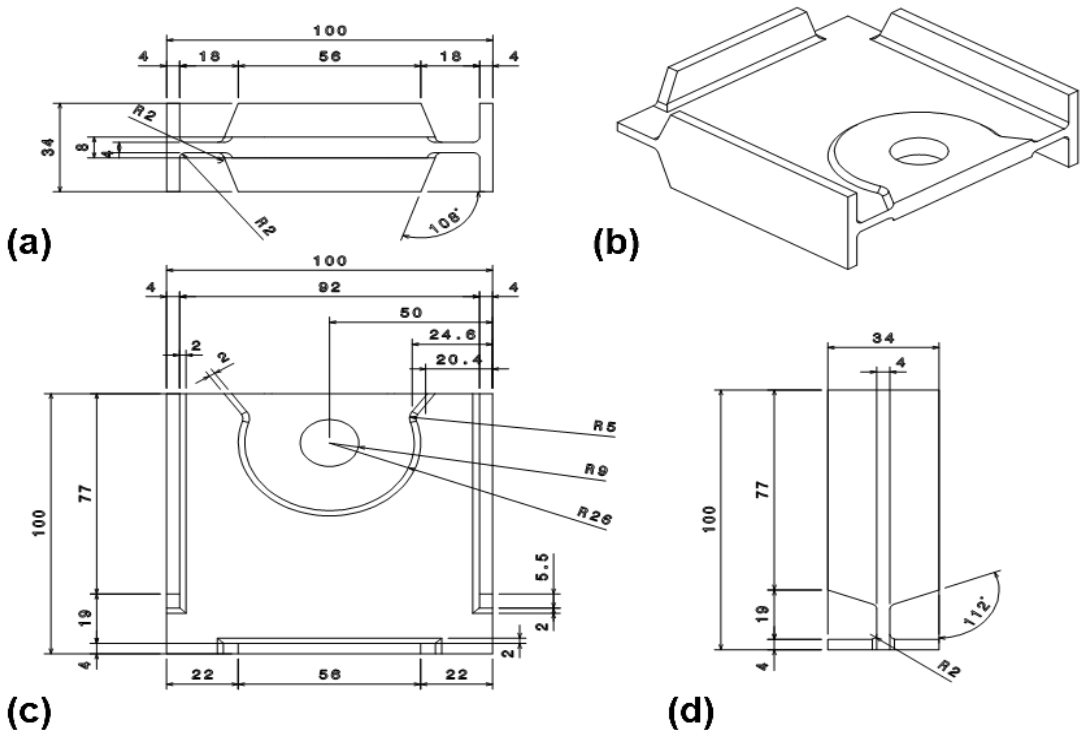

Figure 92: Small S2S machined workpiece measures: (a) front view, (b) 3D view, (c) top view and (d) side view

The second workpiece is called M2S (Medium Part, 2-Sided, Symmetric) and has a weight of 820 g about (Figure 93).

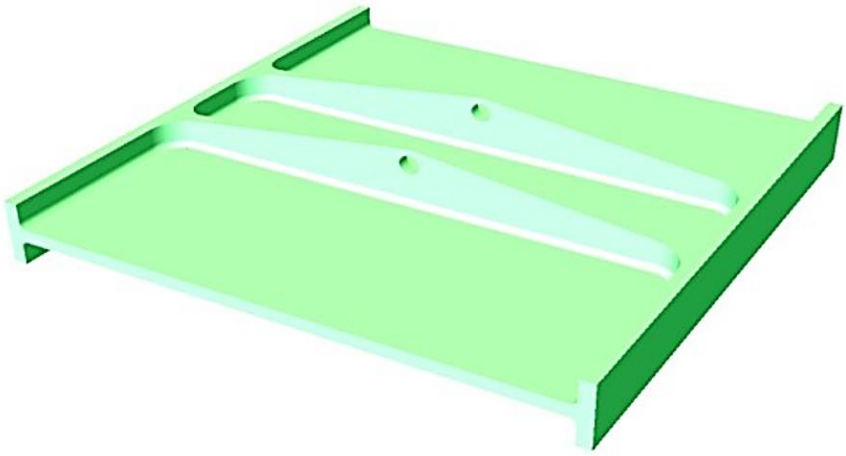

Figure 93: Medium M2S machined workpiece 3D view

Even this part displayed some thin parts with a high rib/web ratio and a symmetric central structure (Figure 94).

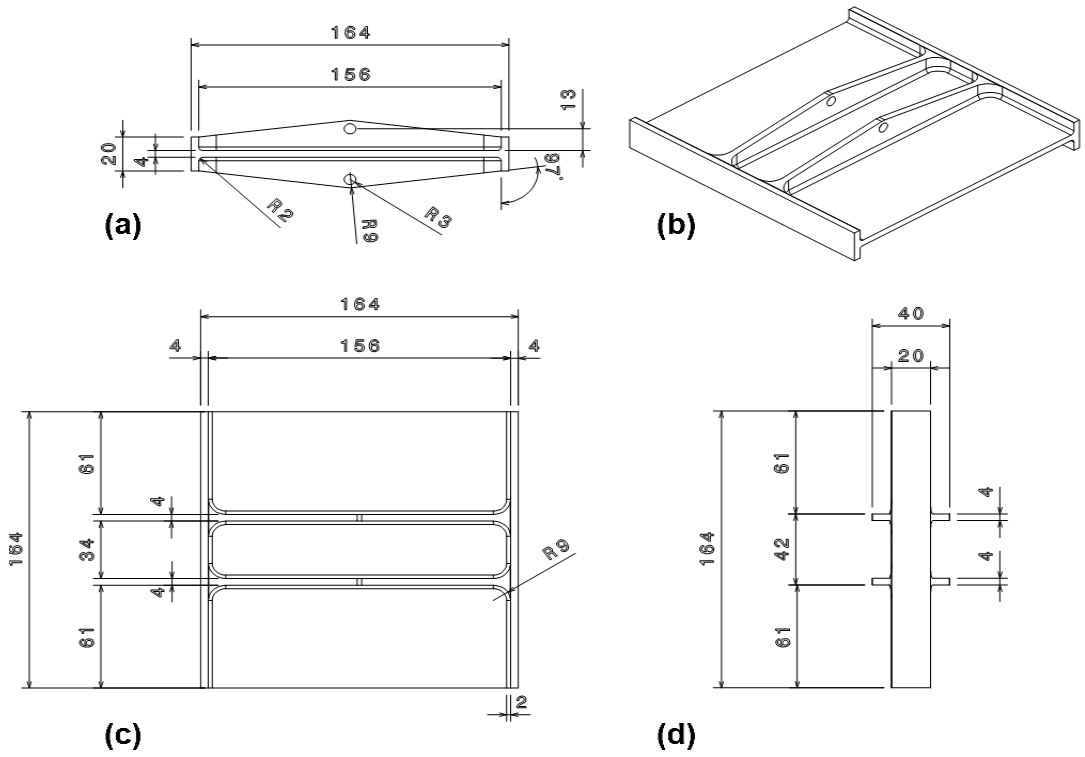

Figure 94: Medium M2S machined workpiece measures: (a) front view, (b) 3D view, (c) top view and (d) side view

The third workpiece is called L2S (Large Part, 2-Sided, Symmetric) and had a weight of 1200 g about (Figure 95).

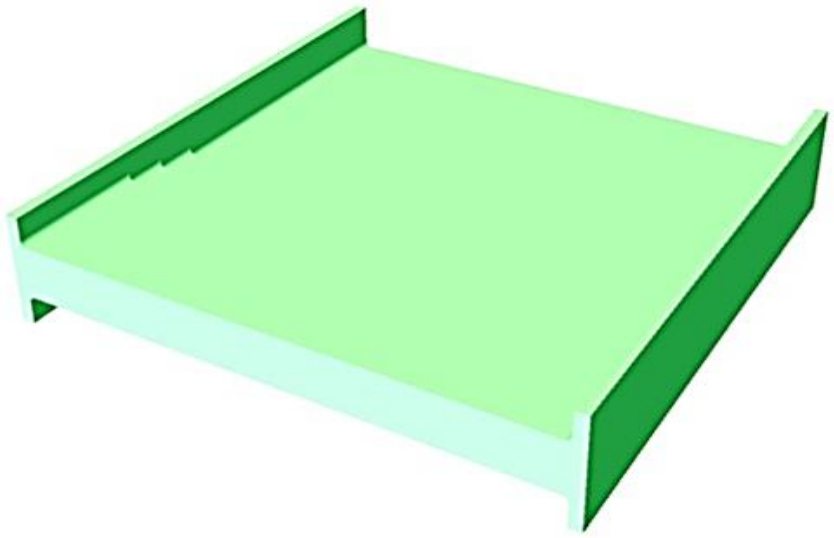

Figure 95: Large L2S machined workpiece 3D view

This workpiece showed less critical geometrical ratios, which allow an easier process and die design (Figure 96).

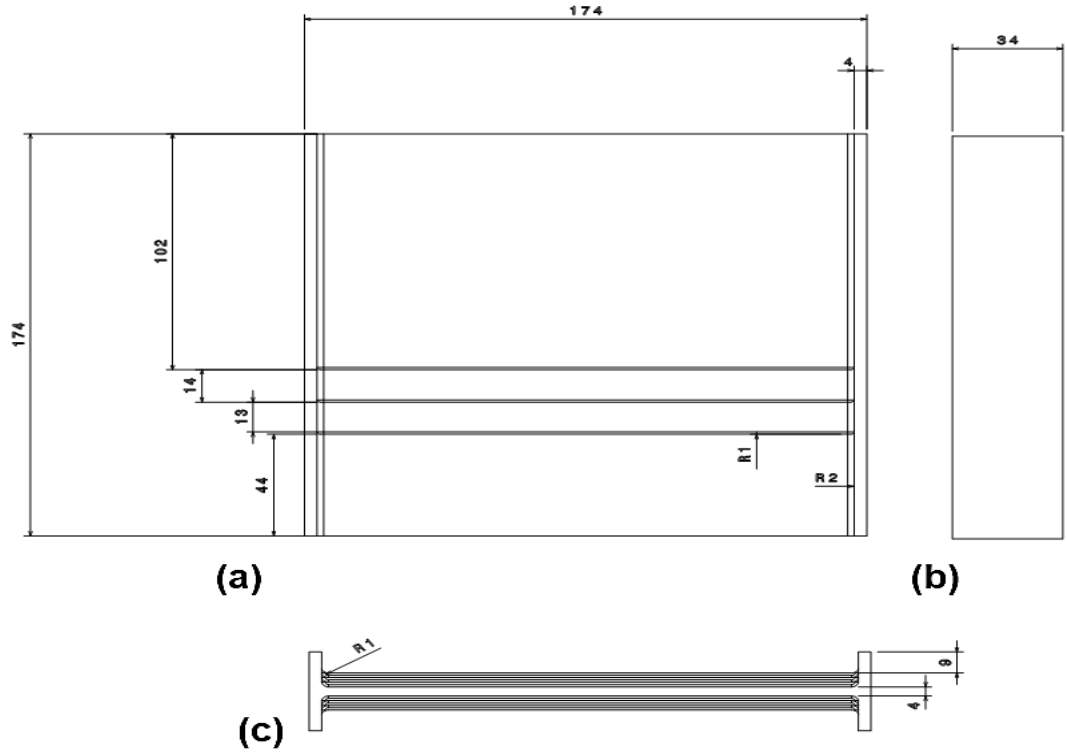

Figure 96: Large L2S machined workpiece measures: (a) top view, (b) side view and (c) front view

The last workpiece is a round carter (Figure 97) which showed the most simplified case among those included into the project (Figure 98).

Figure 97: "Flangia – 20718" machined workpiece 3D view

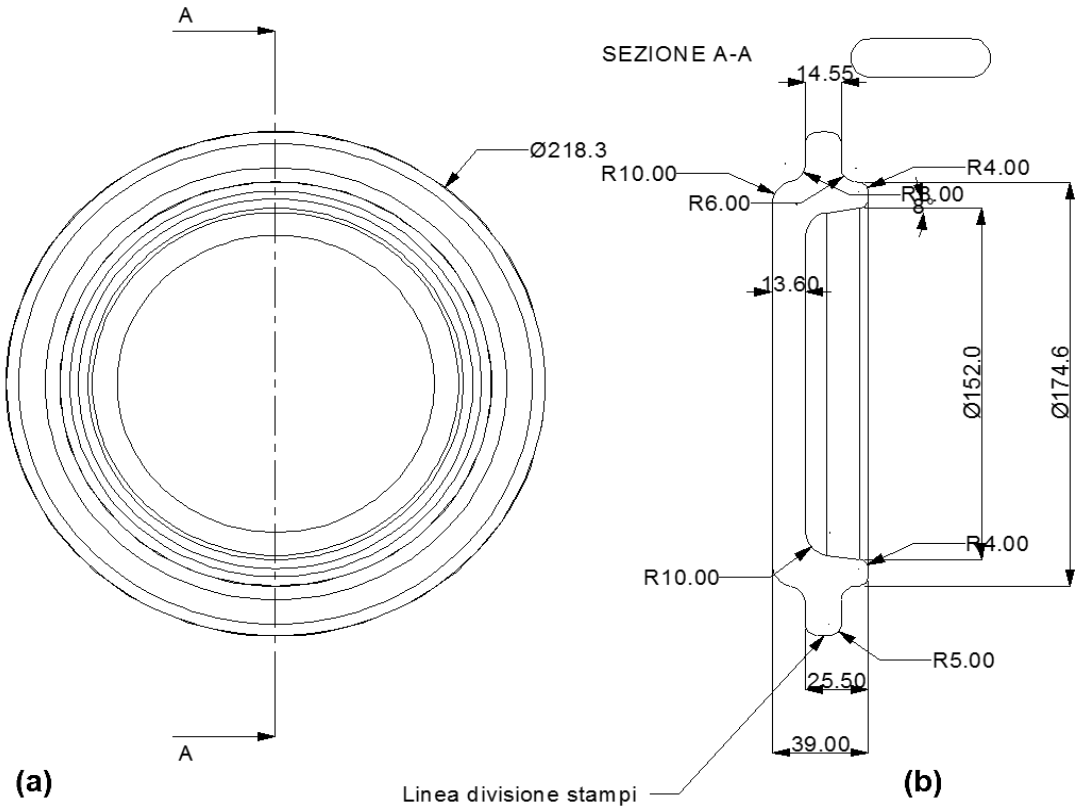

Figure 98: "Flangia – 20718" machined workpiece (a) top view and (b) middle section view

6.5. Die geometry determination

Considering the machined geometries and their geometrical ratio, an optimization plan based of numerical experiments was used with the aim of minimizing the initial amount of material to form the pre-machined part.

In fact, if pure machining process is considered starting with a rolled rectangular pancake or a cylindrical billet, all parts needed a high value of buy-to-fly ratio to reach the final geometry. In example, the weight of the initial amount of Ti64 needed by the S2S workpiece is about 19 times greater than the weight of the machined part. It means that, considering the cost of raw material, the economic aspect in obtaining this kind of component could represent a critical barrier in perspective of industrial production. In this scenario, the use of a proper forging sequence to reach the near-net-shape may significantly reduce the material requirement and cost of the machining operation. The use of FE codes can help to reach a good process setup in order to evaluate the feasibility of forging these parts in the case in which the rib/web ratio changes to critical values. In each case study, the forging geometry was designed using the classical rules for die design recommended for forging processes [33, 185, 186].

The reaching of the near-net-shape in only two forging steps, maintaining a low buy-to-fly ratio, requested particular arrangements in the use die design rules to find the optimum shape for both preform and finisher dies. This objective was obtained by means of a DOE in which the most significant variables in die filling were selected among all those participating to the forging process. After a training simulation campaign, it was found that the most important parameters influencing the correct cavity filling were the billet radius and the fillet radius for both preform and finisher dies. A range of values was selected for normalization and, at the end, an experimental plan based on latin hypercube [187] was used to calculate the values for each selected parameters to be used in the simulation campaign. The die filling value, obtained after each simulation, was used as target function in order to estimate the quality of solution (Table 8). In this case, the workpiece geometry was deprived of its flash by means of a virtual trimming operation in order to compare the flash-less volume with the die cavities, obtaining a filling percentage.

Table 8: DOE for forging process optimization for the S2S case

DOE for process optimization				
Run	**R billet [mm]**	**R corner [mm]**	**R corner [mm]**	**Die filling [%]**
1	35.5	4.43	14.58	87.25
2	33.5	3.43	13.78	90.73
3	34.4	4.23	14.08	62.31
4	32.8	3.73	13.08	93.99
5	34.2	3.93	14.58	68.48
6	33.8	5.23	14.28	98.88
7	35.0	5.03	15.08	99.04
8	35.7	4.73	13.58	95.58

Once the best solution (run 7) was found, a cylindrical billet having a radius 35 mm dimensions was chosen, while the optimum geometries for preform and finisher dies were built by considering the results of optimization procedure (Figure 99).

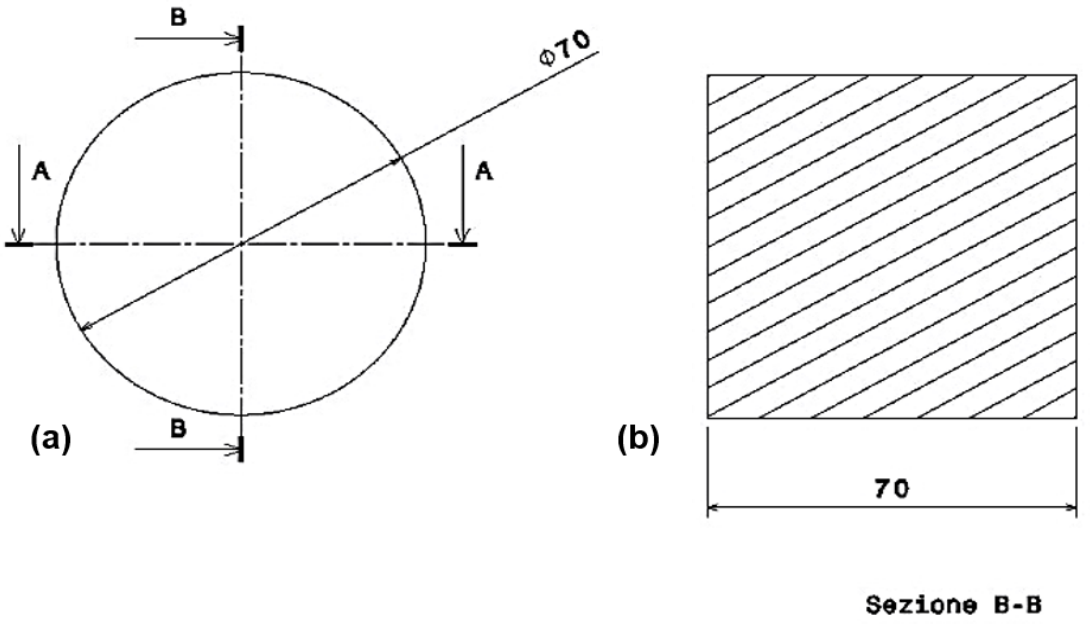

Figure 99: Small S2S billet measures: (a) top view and (b) B section view

By means of this solution, a buy-to-fly ratio of 3.67 was achieved in forging instead of the original amount achieved by using the pure machining process. The final die design (Figure 100, Figure 101) was carried out at the "CSM - Centro sviluppo materiali" (involved within the Titaform project) in Rome.

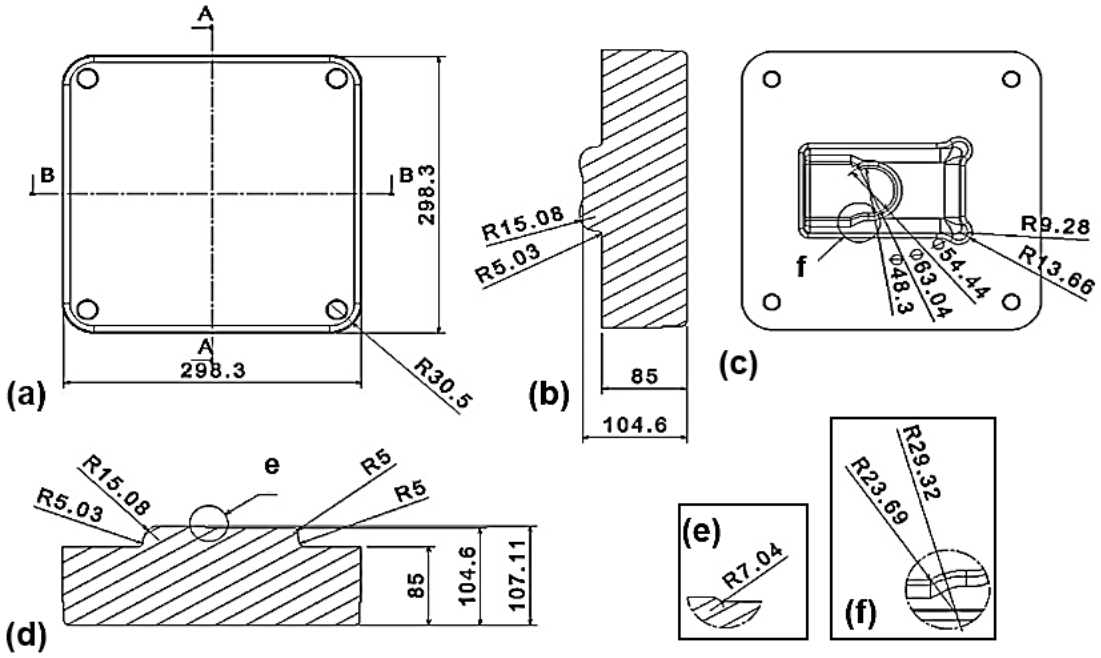

Figure 100: Small S2S top die measures: (a) top view, (b) A section view, (c) bottom view, (d) B section view and (e, f) details magnifications

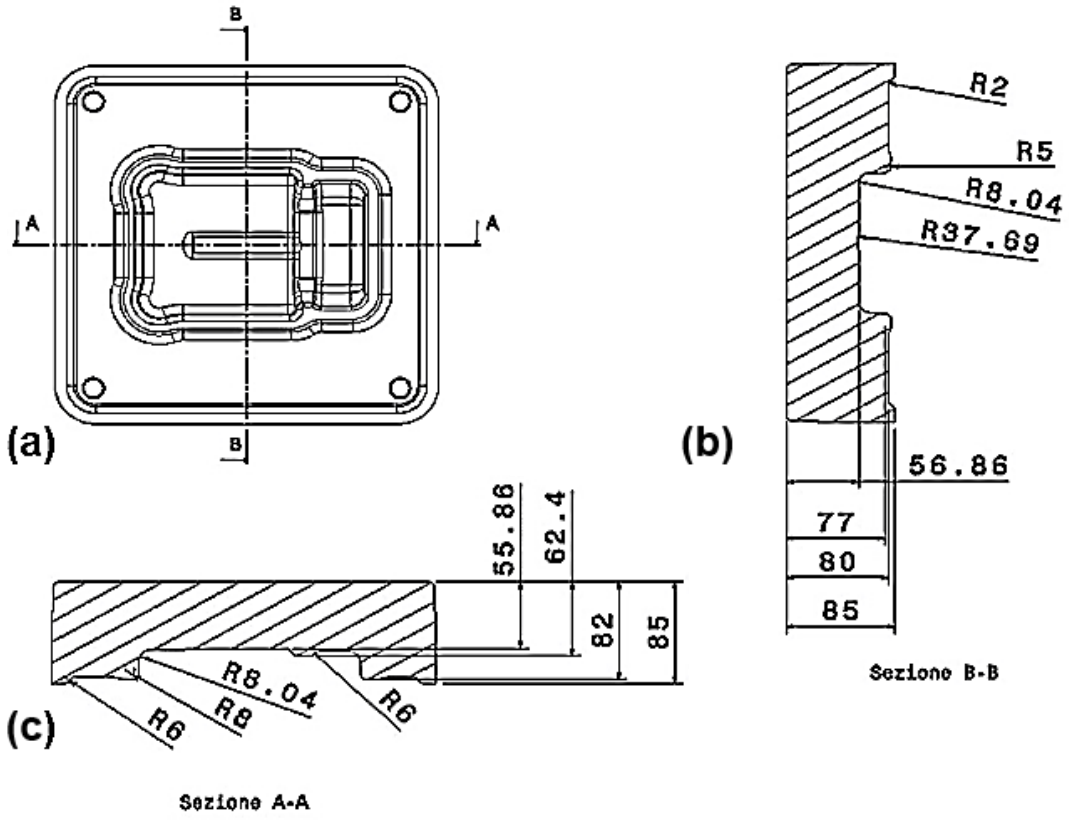

Figure 101: Small S2S bottom die measures: (a) top view, (b) B section view and (c) A section view

Using the same approach, the geometries of dies of the others cases were designed and simulated (Figure 102, Figure 104, Figure 105).

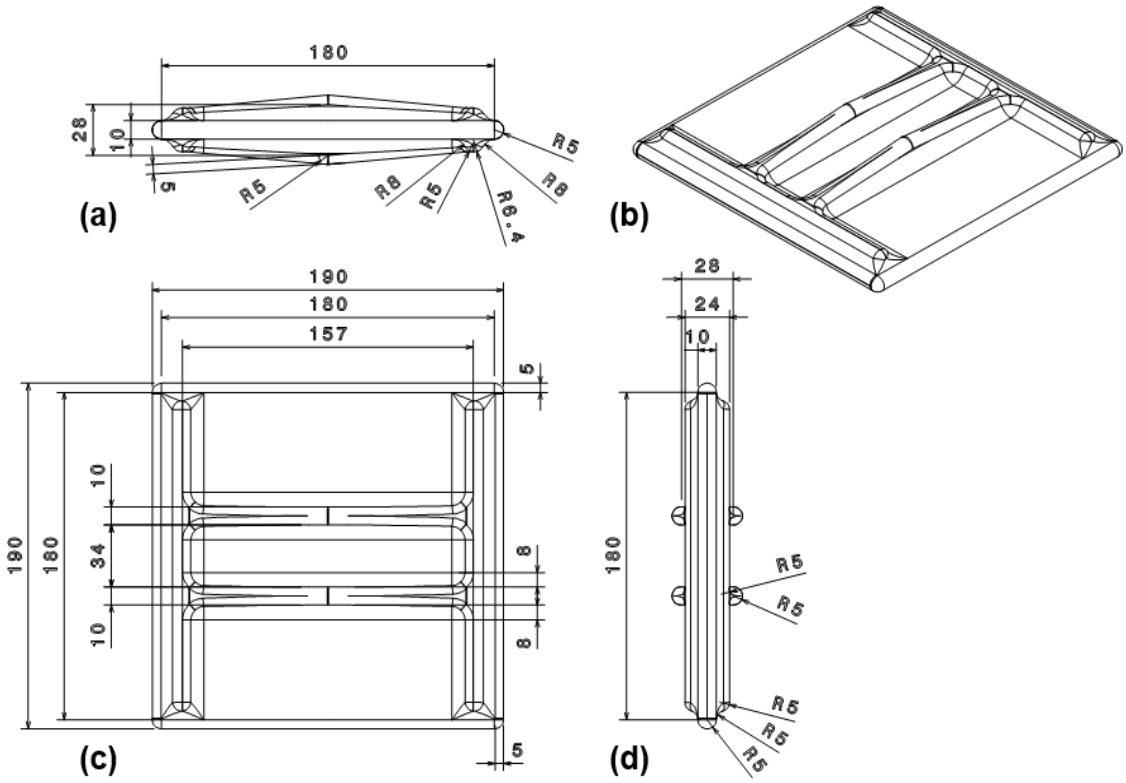

Figure 102: Medium M2S forged measures: (a) front view, (b) 3D view, (c) top view and (d) side view

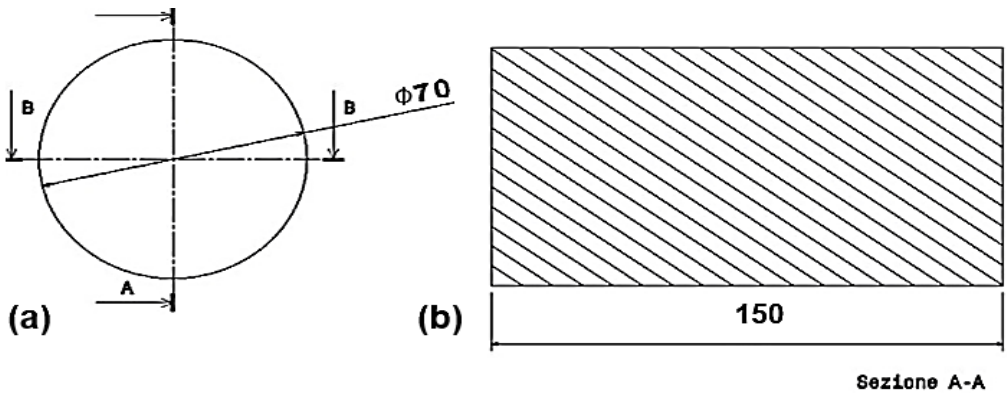

Figure 103: medium M2S billet measures: (a) top view and (b) A section view

Moreover, in order to optimize the practical application during the forging of real parts a billet with fixed diameter of 70 mm and variable length as function of the initial amount of material was chosen (Figure 106).

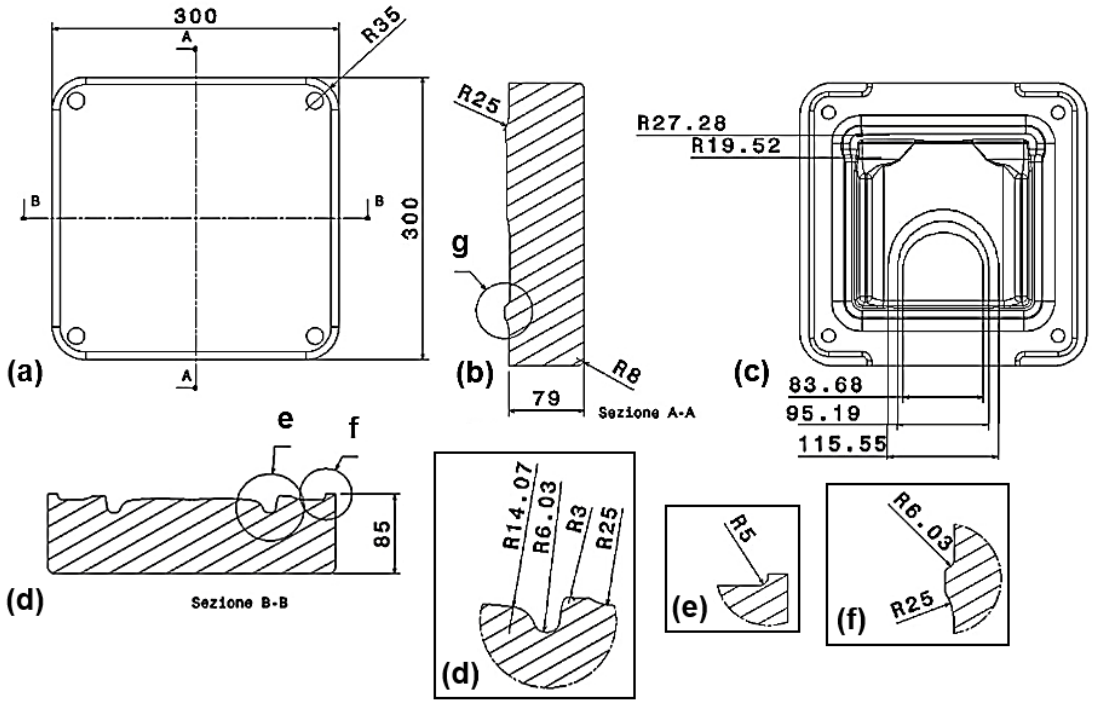

Figure 104: Large L2S top die measures: (a) top view, (b) A section view, (c) bottom view, (d) B section view and (e, f, g) details magnifications

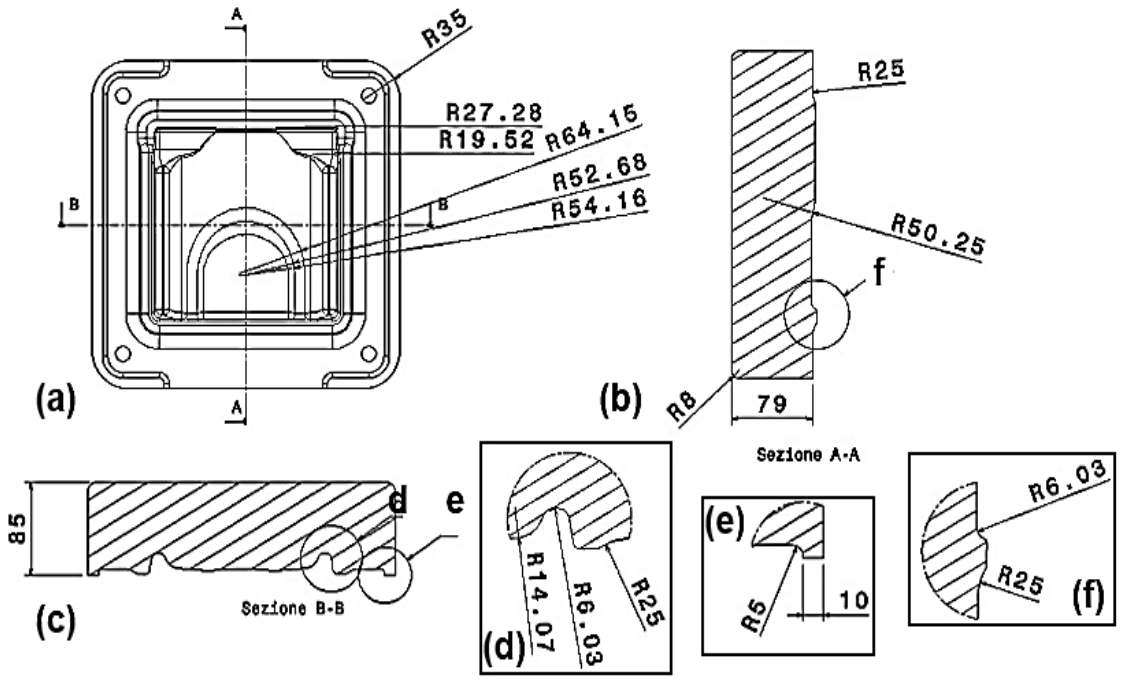

Figure 105: Large L2S bottom die measures: (a) top view, (b) left side view, (c) right side view and (d, e, f) details magnifications

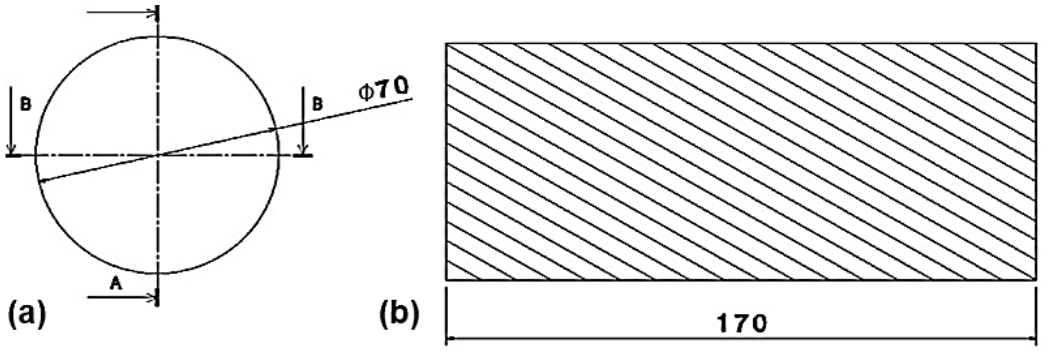

Figure 106: Large L2S billet measures: (a) top view and (b) A section view

The carter case was developed considering the same approach in die design (Figure 107, Figure 108) but a different billet was used (Figure 109).

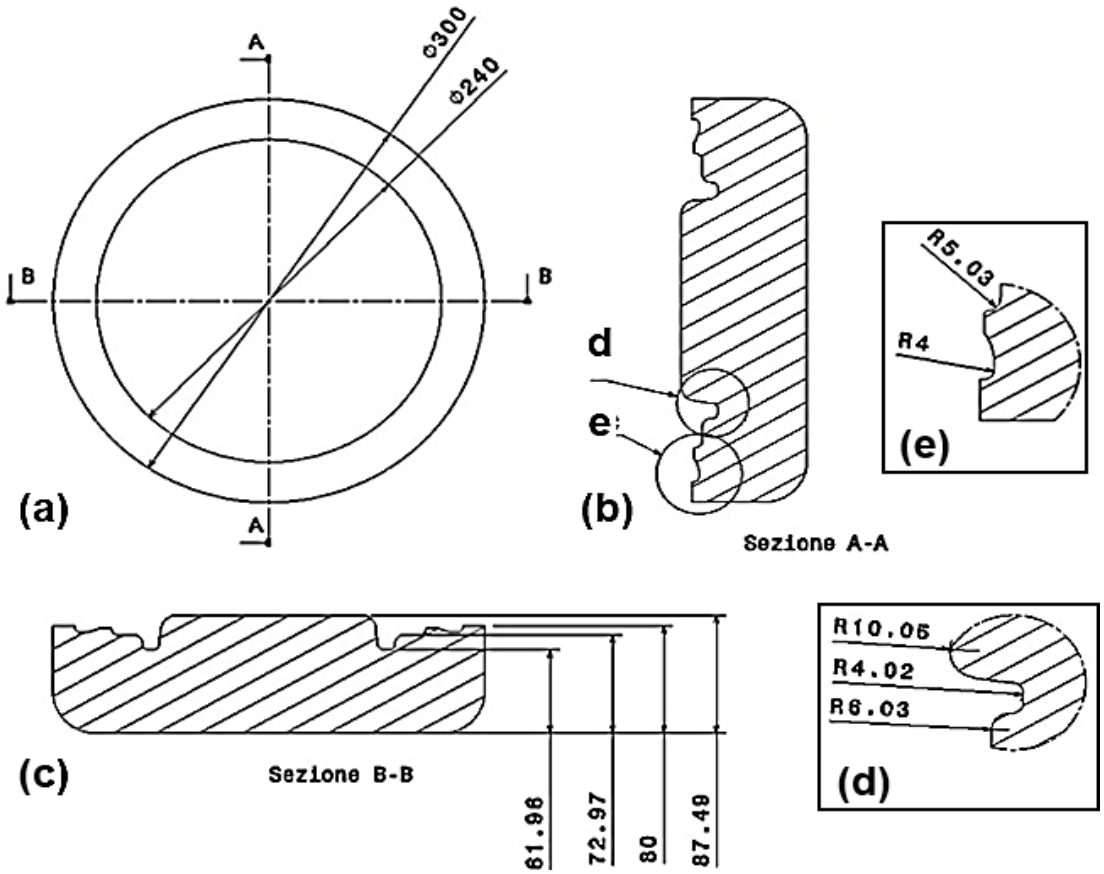

Figure 107: "Flangia – 20718" top die measures: (a) bottom view, (b) A section view, (c) B section view and (d, e, f) details magnification

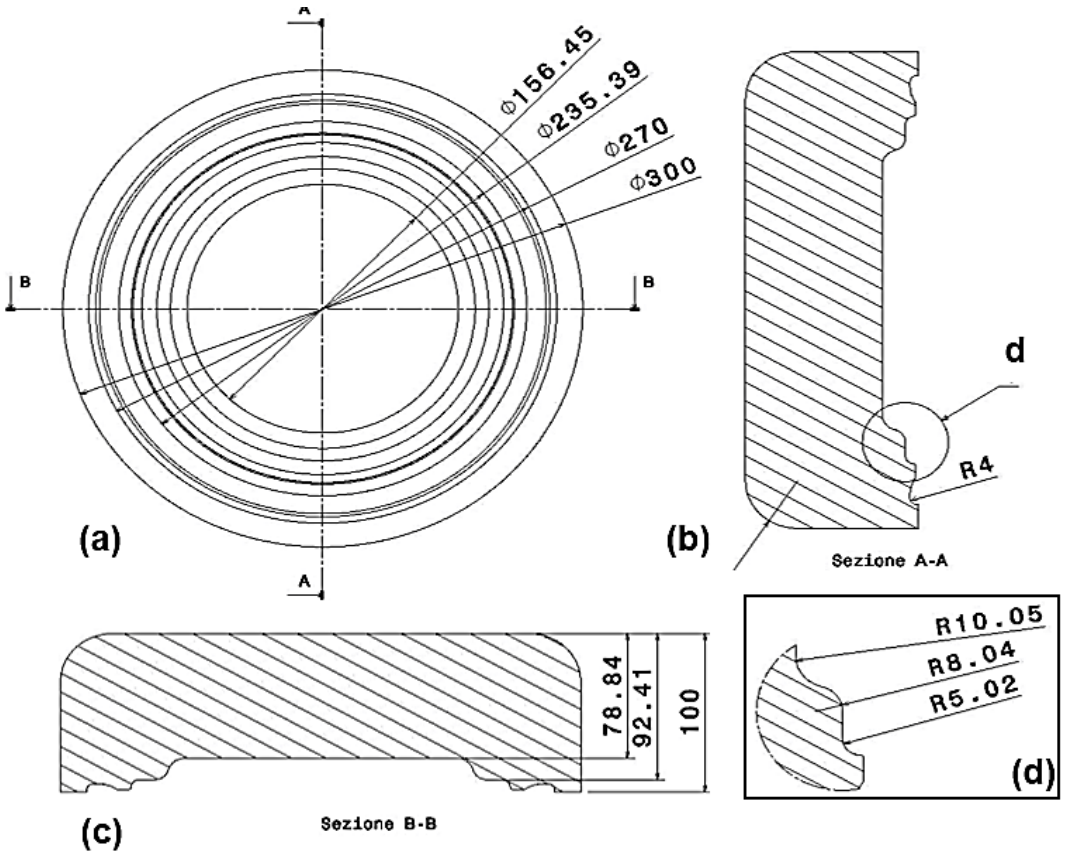

Figure 108: "Flangia – 20718" bottom die measures: (a) top view, (b) A section view, (c) B section view and (d) details magnification

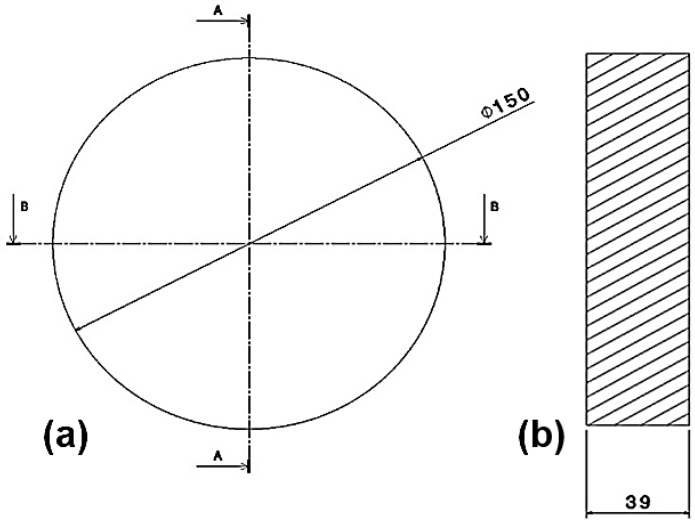

Figure 109: "Flangia – 20718" billet measures: (a) top view and (b) B section view

The configured campaign produced a good reduction in the theoretical amount of material compared to the pure machining procedure. An example of advantages in terms

of buy-to-fly ratios is shown in the table below (Table 9) in which buy/fly value for both hard machining and forged approach is displayed. The reduction in initial amount of material is ranged between 28.1 % of S2S case to 50.1 % of M2S case, which is most complex workpiece among those proposed.

Table 9: Workpieces volume and buy-to-fly reduction

Part	Machined part volume [mm^3]	Hard machining billet [mm^3]	Forging billet [mm^3]	Hard machining buy/fly	Forged buy/fly	Buy/fly lowering
Small	73369	374544	269392	5.10	3.67	28.1%
Medium	154174	1157352	577267	7.51	3.74	50.1%
Large	293870	1115136	654236	3.79	2.23	41.3%
Carter	682442	1572744	689187	2.28	1.01	55.7%

The forging campaign was configured using two different temperature levels in order to study the material behavior when both Alpha-Beta and Beta field are considered for the initial thermal conditions.

The billets were pre-heated at 950 °C and 1050 °C for Alpha-Beta and Beta field forging respectively, while the initial die temperature was selected at 400 °C in all cases.

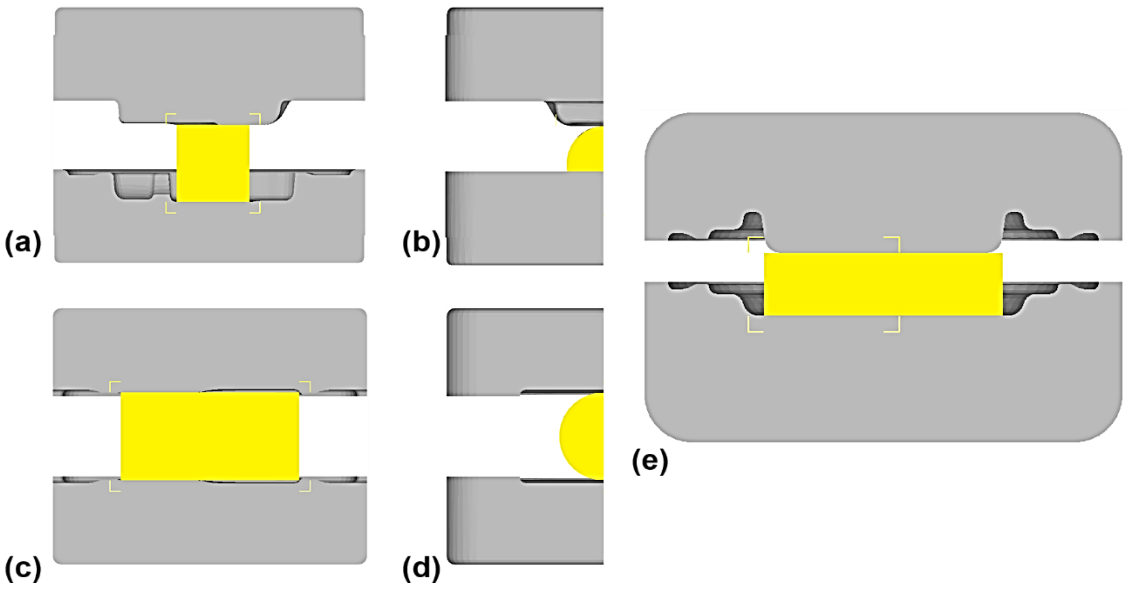

Figure 110: Billet positioning with respect to the dies: (a) S2S case axial symmetry plane, (b) S2S side view, (c) L2S case axial symmetry plane, (d) L2S side view and (e) Carter case

The forming stage was performed by means of a hammer press die speed in order to prevent critical cooling of billets, which may produce incorrect material flow with bad cavity filling and incorrect final shape coming from rapid cooling of layers at contact with dies. Moreover, dry lubrication conditions were used to carry out all forgings.

In the end, a short trial and error campaign was used to establish the correct position of billets of the S2S and L2S cases along their axial directions. The previous image (Figure 110) shows the initial position of billets with respect to the dies.

6.6. Simulation campaign output

After designing the process set-up, a simulation campaign was carried out in order to compare numerical output and experimental results, with the aim to evaluate the quality of prediction of numerical analysis, using the material characterization previously explained. In particular, the correct cavity filling and final volume fraction of phases was focused. Different significant points were selected for each workpiece in order to extract data concerning the major field variable. The image below (Figure 111) shows the position of point tracking on the middle section of each simulated part. The Medium M2S workpiece was not taken into account in the experimental campaign.

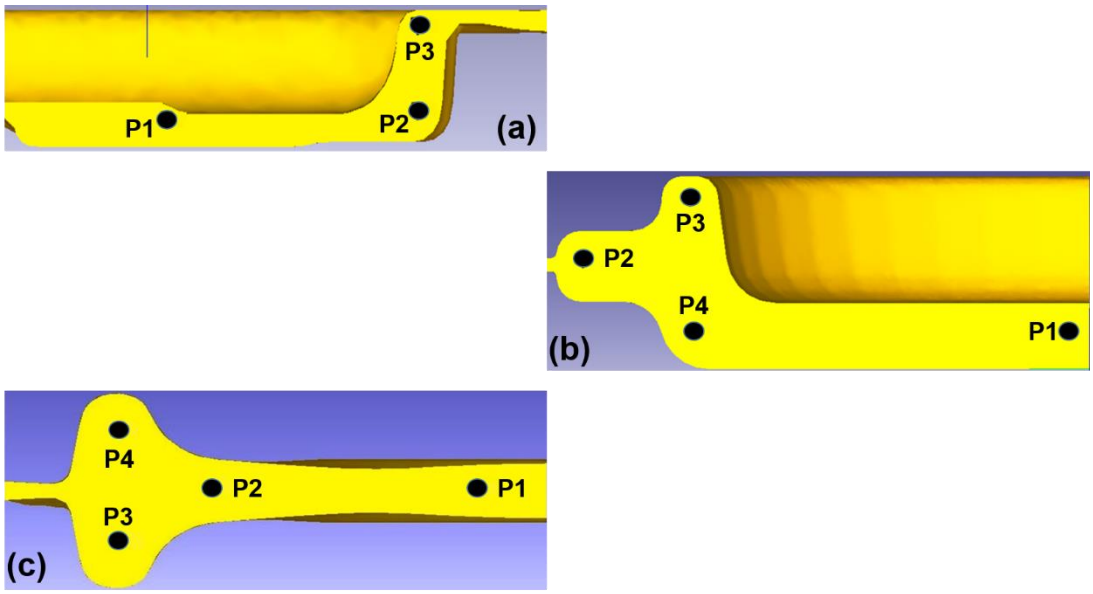

Figure 111: Point tracking positions for data extraction of (a) S2S, (b) Carter and (c) L2S workpieces

6.6.1. Forging load prediction

As first, after the flow stress data validation previously explained, the first numerical output focused on forging load for each examined case in order to quantify the magnitude order of tonnage and allow the forging partner to correctly select the forging machine and equipment.

The S2S case (Figure 112) showed variation of 100 tons about for the forging load at varying of billet temperature, with the 950 °C case needing a higher tonnage up to 600 tons to completely fill the die cavities while the 1050 °C case was slightly above 500 tons. Looking at the load curve evolution, it is displayed a significant increase of value during the last part of die stroke which denotes a strong influence of friction conditions between die and workpiece. The same observation could be given to the low difference between the two forging loads: the variation in flow stress at higher temperature and its advantage in terms of tonnage is contrasted by the shape of cavities, which produce a higher friction increasing the required load.

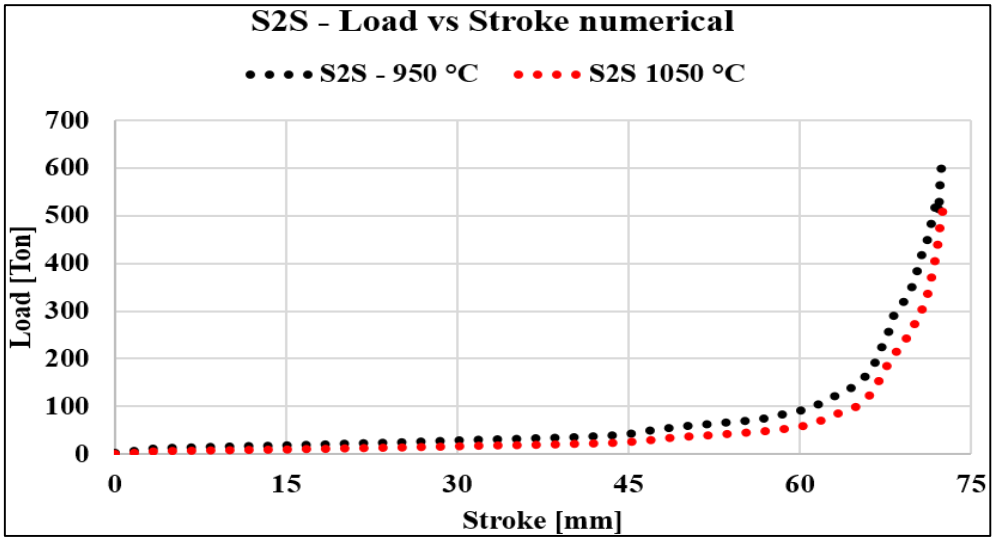

Figure 112: Forging load prediction for the S2S workpiece

The L2S case (Figure 113) showed a similar behavior observed in S2S case analysis with a forging load close to 700 tons for the 950 °C while the 1050 °C case needed a lower forging load (450 tons about) than the S2S 1050 °C case. These results can be justified by means of differences in shape complexity between the two cases. In fact, the

S2S showed more critical geometrical ratios in cavity die filling with a strong influence of friction actions while, even the L2S case has bigger dimensions, it is not affected by the same inconveniences.

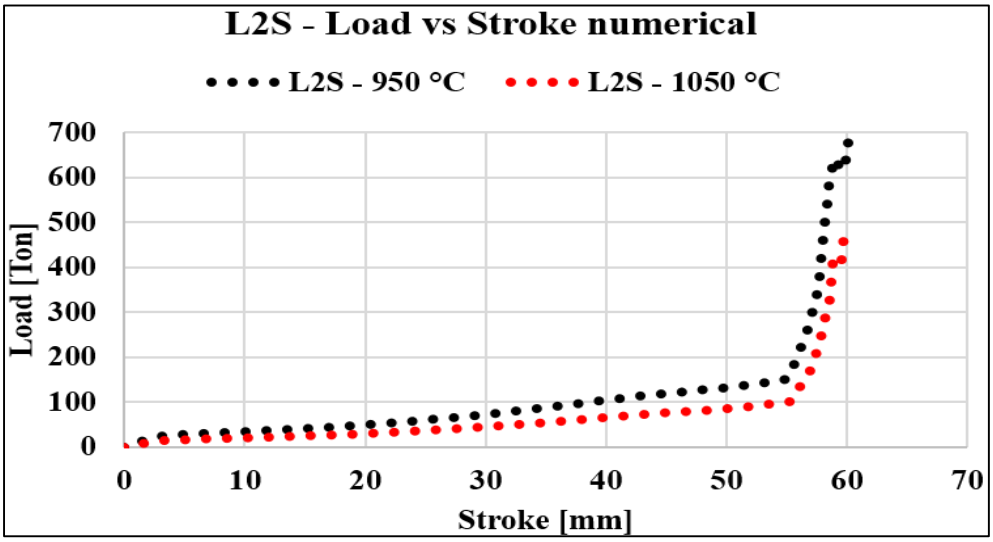

Figure 113: Forging load prediction for the L2S workpiece

In the end, the Carter case (Figure 114) needed the lowest forging load in both cases, 280 tons about for the 950 °C case against 270 tons about for the 1050 °C case. In this case, a low influence of friction actions affected the material flow and a double step curve was obtained because of double cavity on the die.

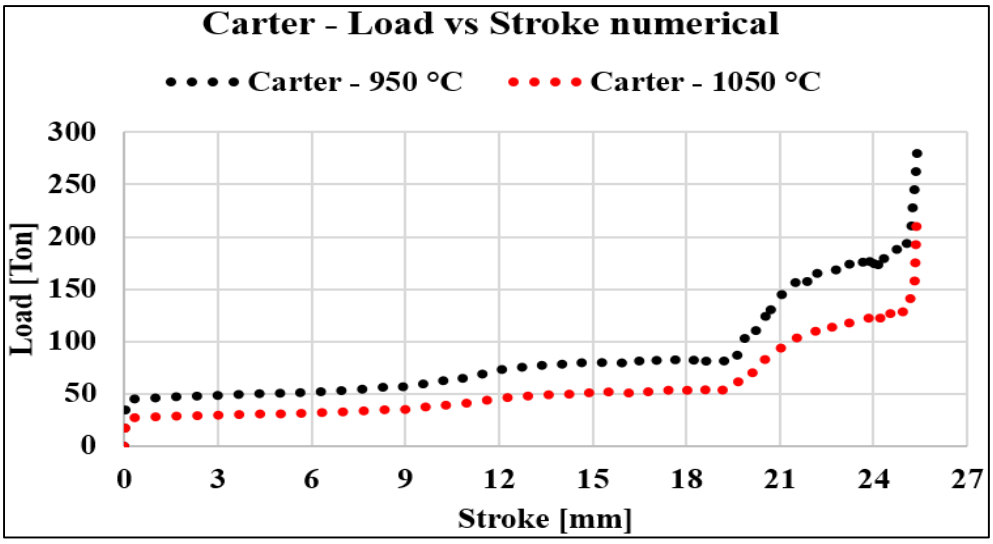

Figure 114: Forging load prediction for the Carter workpiece

6.6.2. Temperature prediction

As well as the forging load prediction, also temperature prediction was carried out in order to observe the thermal evolution of the significant points (Figure 111). Both forging and cooling in air stages were considered in temperature calculation.

The S2S temperature calculation (Figure 115) showed a similar evolution for all selected significant points with a temperature variation within the typical cooling speeds avoiding the martensitic Alpha phase formation. However, during the forging stage, the rapid deformation work causes a heating of the workpiece which reaches in some zone 1010 °C about (Figure 115 - b) in the 950 °C case and 1075 °C about (Figure 115 - d) in the 1050 °C case. It means that the initial amount of Alpha phase coming from heating stage could decrease due to a further Alpha-to-Beta phase transformation during forging.

If the thermal colormap of the middle section at the end of forging stage (Figure 116) is observed, it appears that the workpieces undergo to a slight cooling in the central zone because of the thermal exchange with the dies, while the peripheral points increase their temperature due to high deformation work.

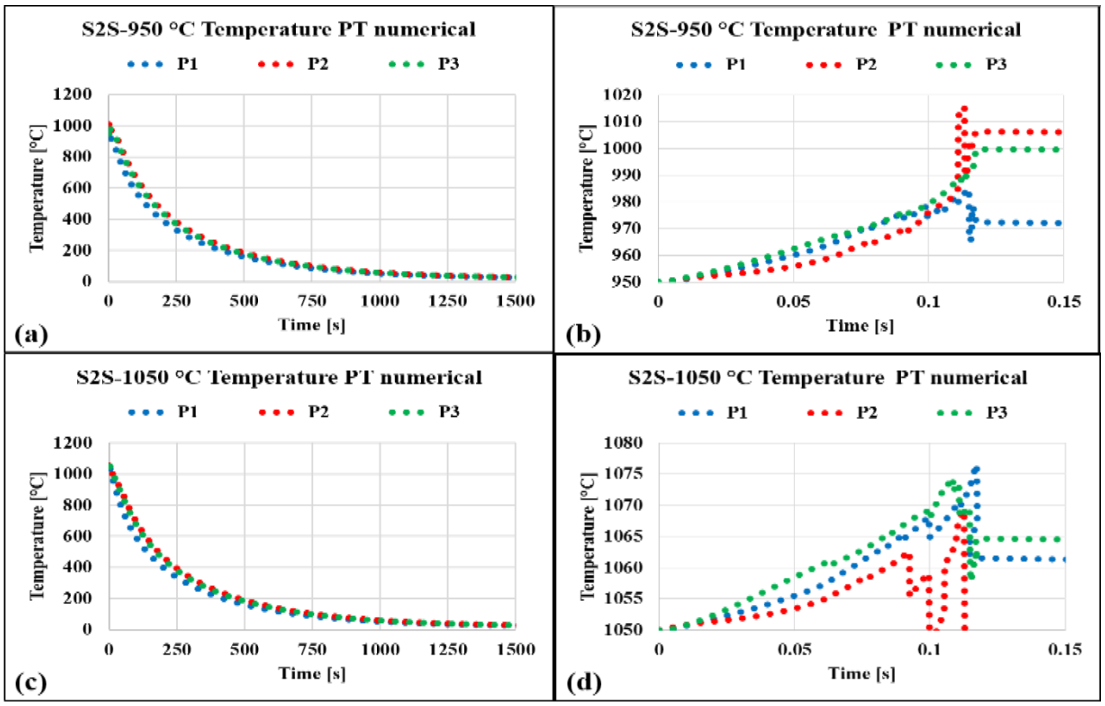

Figure 115: Temperature prediction point tracking for the S2S case forged at (a) 950 °C with (b) magnification at forging stage and (c) 1050 °C billet temperature with (d) magnification at forging stage

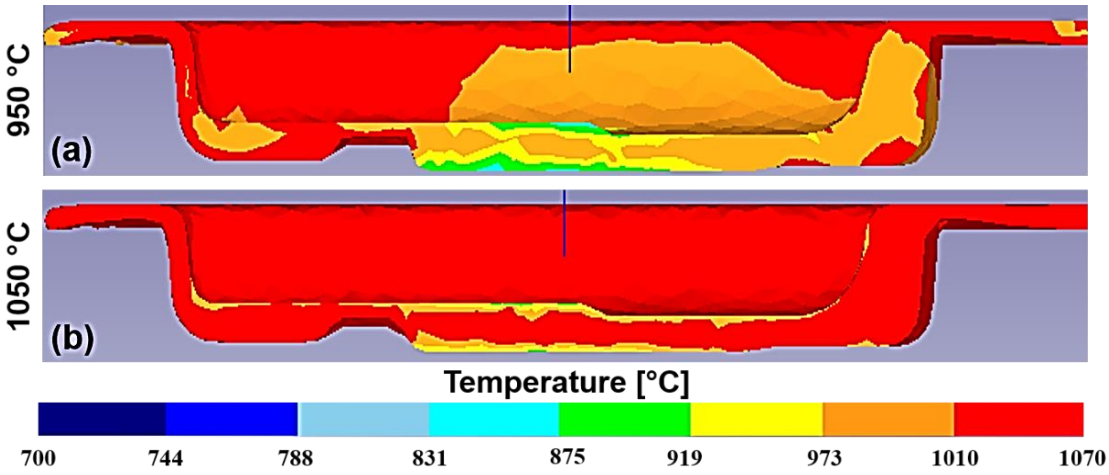

Figure 116: Temperature colormap of the middle section at the end of forging stage for the S2S case forged at (a) 950 °C and (b) 1050 °C billet temperature

Similar considerations can be used in the L2S cases (Figure 117, Figure 118).

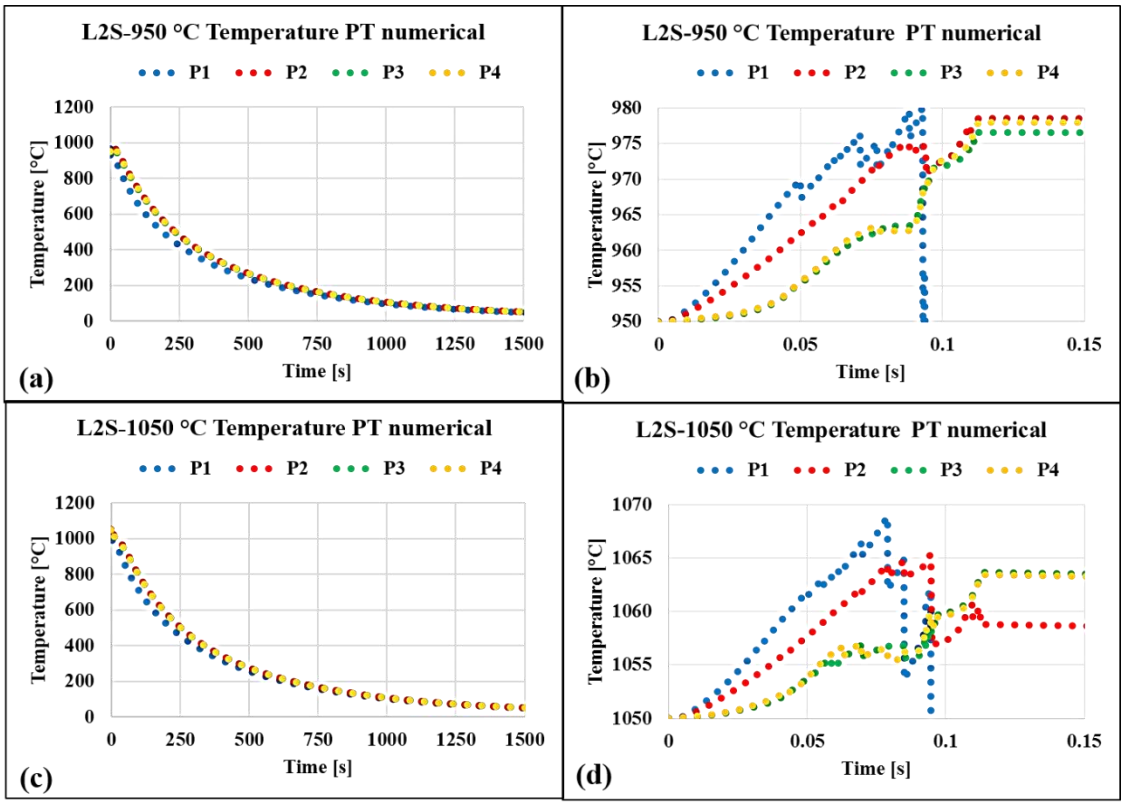

Figure 117: Temperature prediction point tracking for the L2S case forged at (a) 950 °C with (b) magnification at forging stage and (c) 1050 °C billet temperature with (d) magnification at forging stage

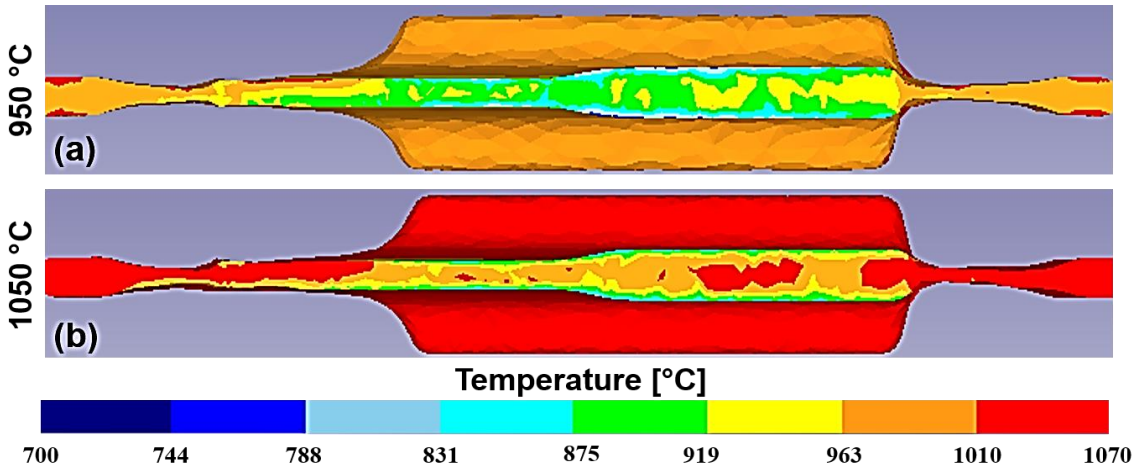

Figure 118: Temperature colormap of the middle section at the end of forging stage for the L2S case forged at (a) 950 °C and (b) 1050 °C billet temperature

The Carter case displayed similar evolutions in temperature of selected points with the exception of slower cooling due to a more bulk shape.

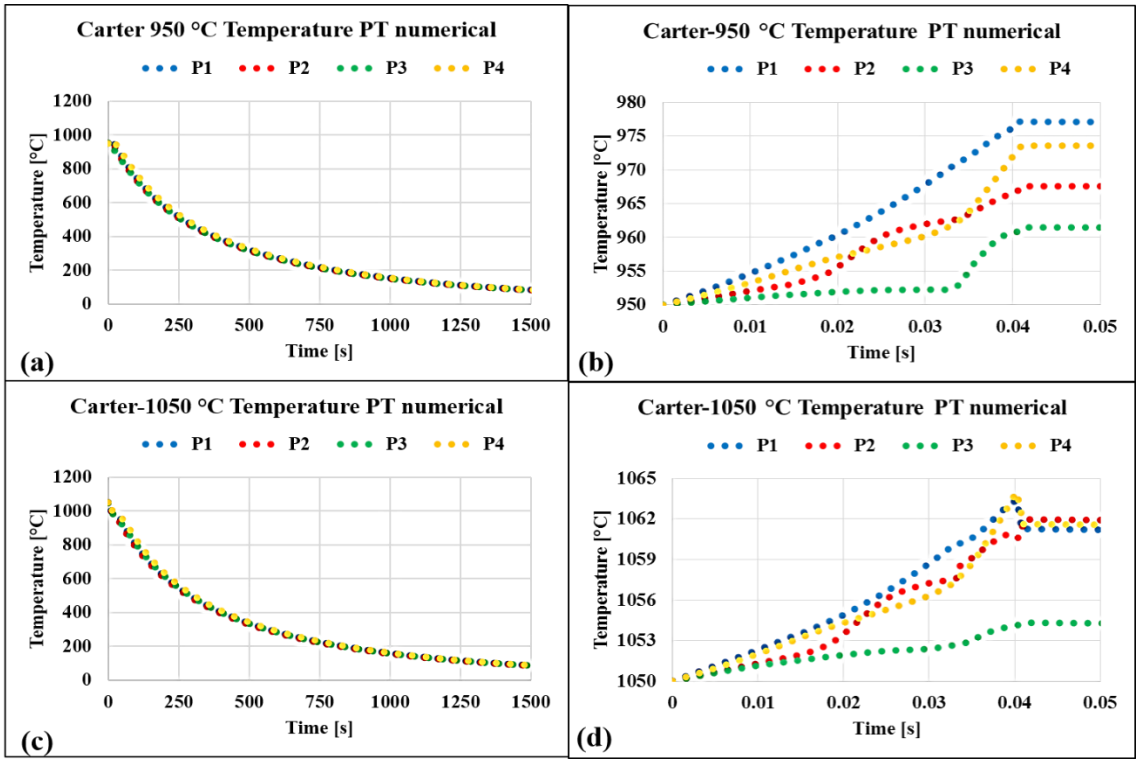

Figure 119: Temperature prediction point tracking for the Carter case forged at (a) 950 °C with (b) magnification at forging stage and (c) 1050 °C billet temperature with (d) magnification at forging stage

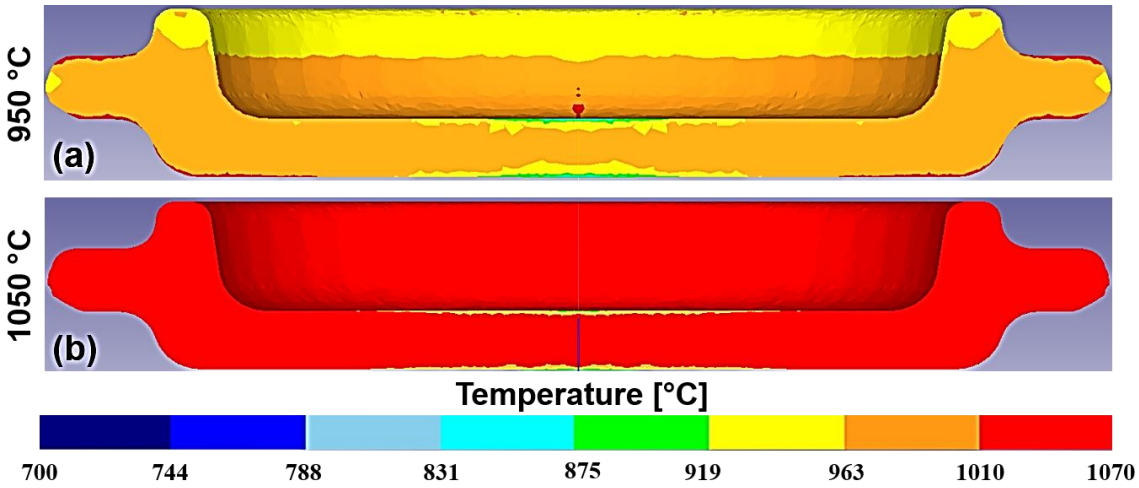

Figure 120: Temperature colormap of the middle section at the end of forging stage for the Carter case forged at (a) 950 °C and (b) 1050 °C billet temperature

However, the short forging time and lesser deformation work with respect to the previous cases produced a lower increasing in temperature during the forging stage, with the 950 °C case reaching 975 °C about and the 1050 °C reaching 1060 °C about (Figure 119 – b, c; Figure 120).

6.6.3. Effective strain prediction

Effective strain of selected points (Figure 111) was carried out in order to predict the deformation of most significant zones of each workpiece and estimate the material flow of the used alloys at varying of geometries and temperature.

The S2S case showed the greatest effective strain during the forging stage, with all tracked points similarly evolving up to 3 about (Figure 121) and almost identical behavior for both 950 °C and 1050 °C billet temperature. Looking at the colormap (Figure 122), it is possible to observe some zones affected by higher values than the point tracking measures with a couple of areas where the effective strain exceeds 4.38.

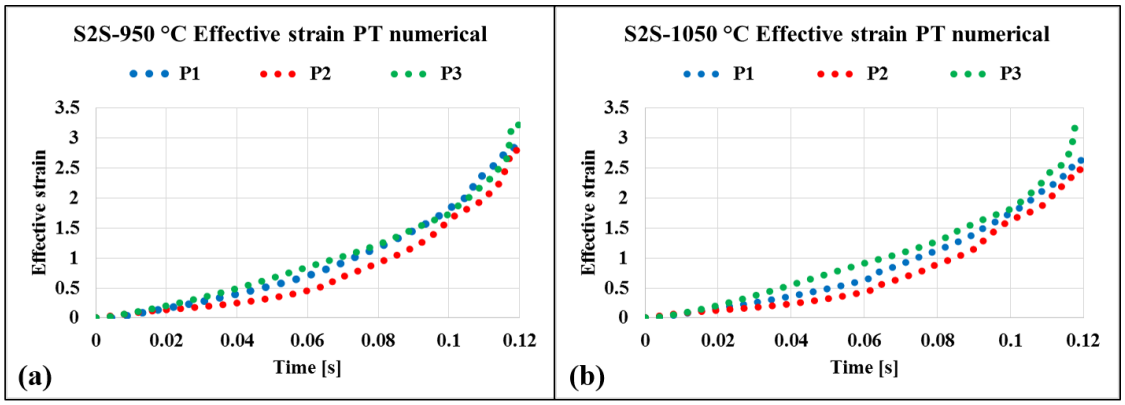

Figure 121: Effective strain prediction point tracking for the S2S case forged at (a) 950 °C and (b) 1050 °C billet temperature

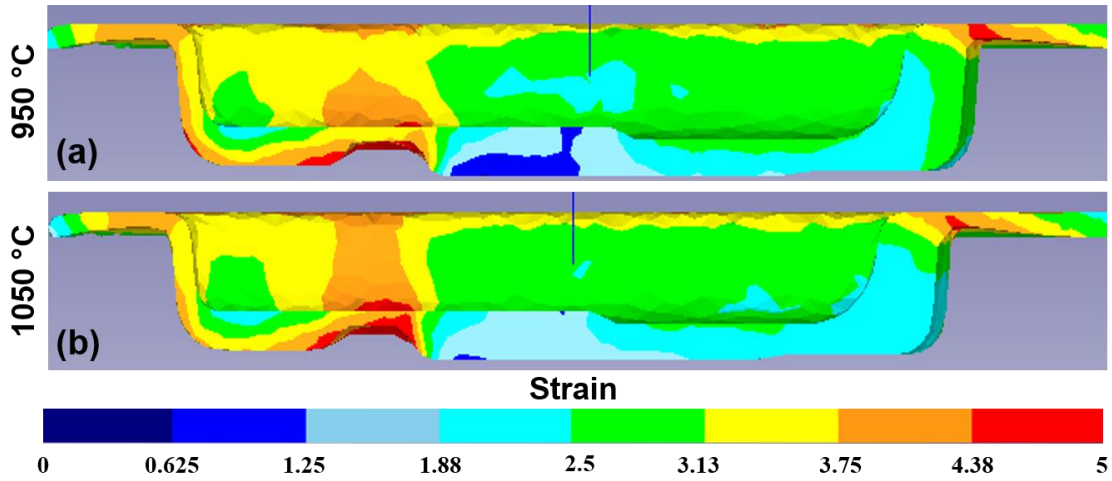

Figure 122: Effective strain colormap of the middle section at the end of forging stage for the S2S case forged at (a) 950 °C and (b) 1050 °C billet temperature

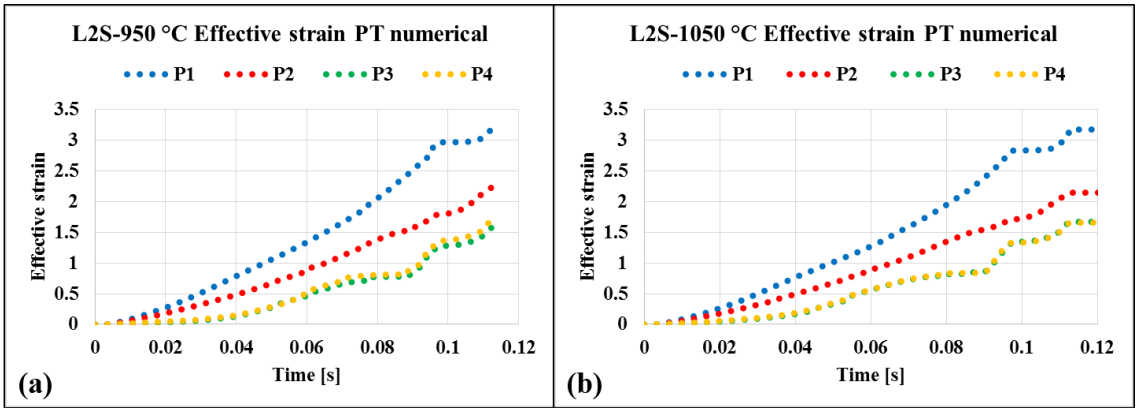

Figure 123: Effective strain prediction point tracking for the L2S case forged at (a) 950 °C and (b) 1050 °C billet temperature

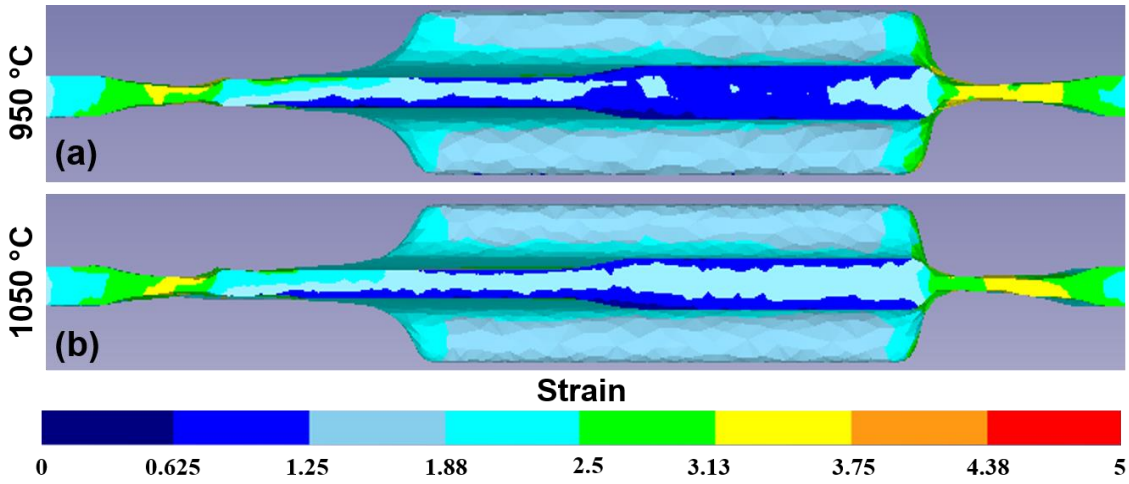

Figure 124: Effective strain colormap of the middle section at the end of forging stage for the L2S case forged at (a) 950 °C and (b) 1050 °C billet temperature

Same behavior was found for L2S case at both billet temperatures (Figure 123), with P3 and P4 points having the same evolution during the forging stage and P1 point exhibiting the greater deformation. However, even the values are very similar to the S2S case, if previous colormap (Figure 124) is considered; the workpiece shows lesser effective strain than the Small case (Figure 122).

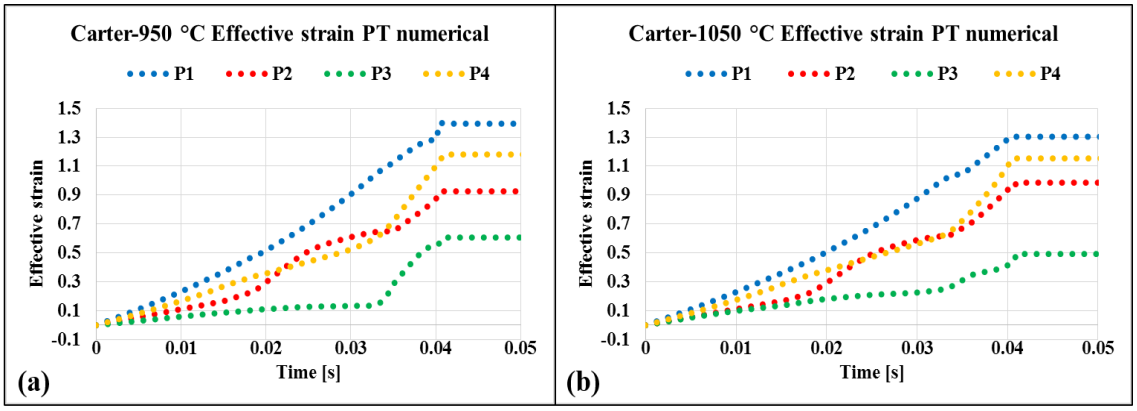

Figure 125: Effective strain prediction point tracking for the Carter case forged at (a) 950 °C and (b) 1050 °C billet temperature

The Carter workpiece displayed the lowest deformation among all forged parts, with an effective strain point tracking growing up to 1.3 about (Figure 125) and a double step evolution which can be related to the load/stroke graph (Figure 114) previously explained.

If effective strain colormap is considered (Figure 126), the workpiece shows a layered trend with the upper zone affected by a low strain and a central ring exhibiting the greatest deformation.

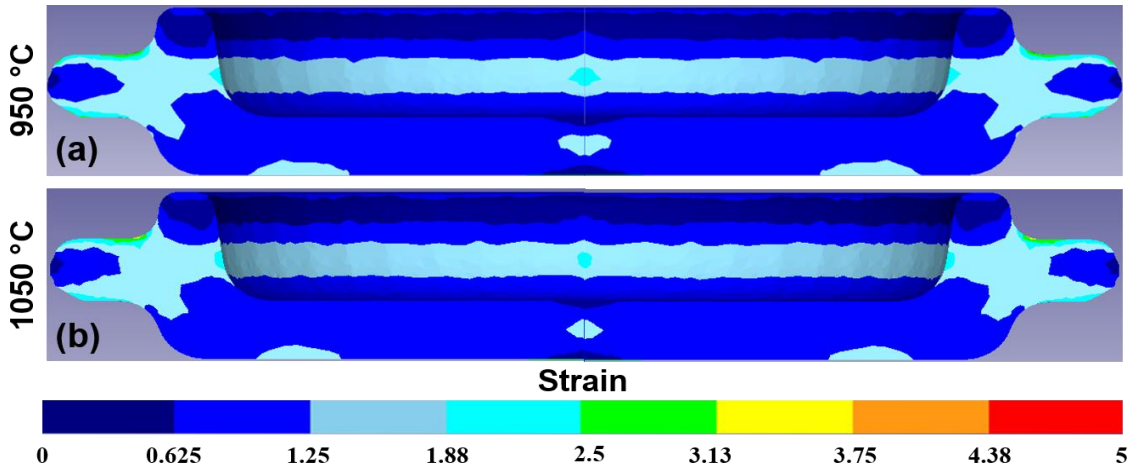

Figure 126: Effective strain colormap of the middle section at the end of forging stage for the Carter case forged at (a) 950 °C and (b) 1050 °C billet temperature

6.6.4. Effective strain rate prediction

As well as effective strain, the effective strain rate of selected points (Figure 111) was carried out in order to predict the deformation rate of most significant zones of each workpiece and evaluate the forgeability by means of comparison with workability maps found in literature [76].

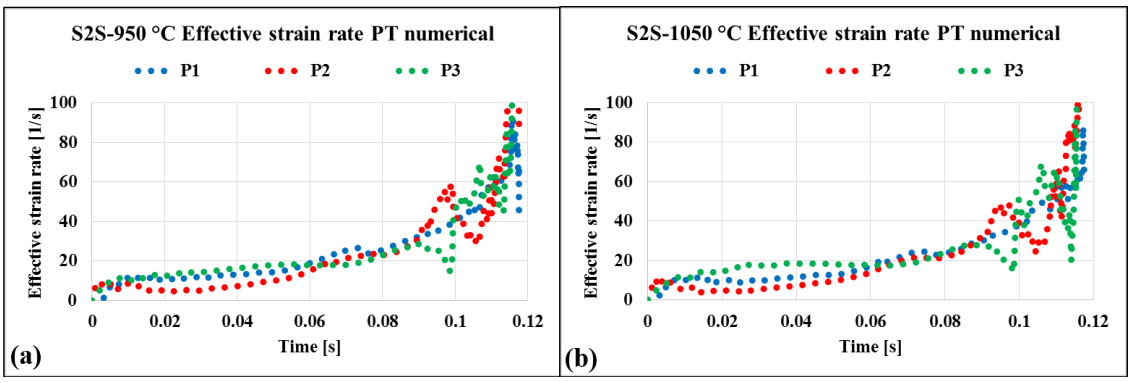

Figure 127: Effective strain rate prediction point tracking for the S2S case forged at (a) 950 °C and (b) 1050 °C billet temperature

As it was observed in effective strain output, point tracking of S2S and L2S workpieces showed comparable evolutions with very similar peak values between the 950 °C and 1050 °C cases. The S2S part point tracking displayed very close strain rate curves for all selected points during the forging stage (Figure 127) and lower values at the central zone of the workpiece (Figure 128).

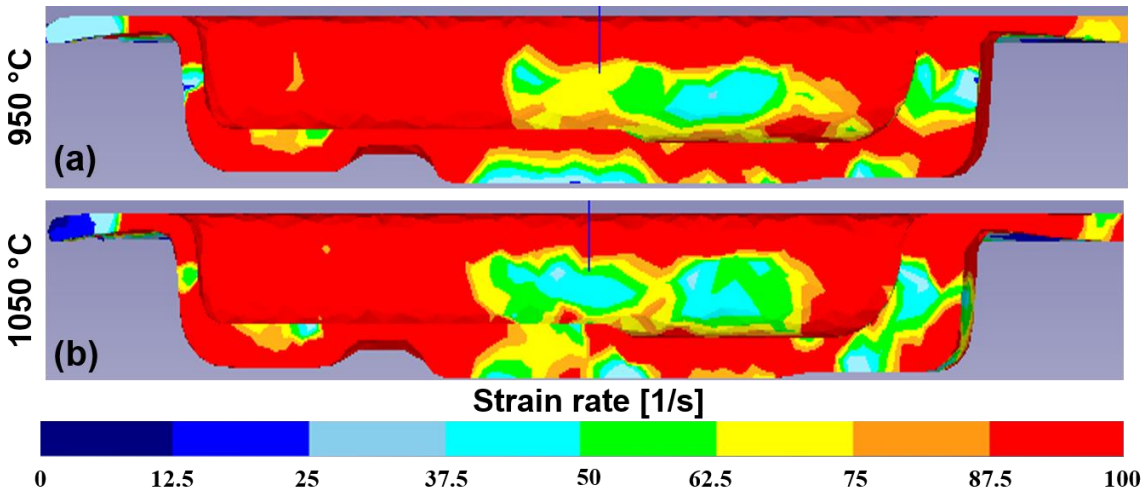

Figure 128: Effective strain rate colormap of the middle section at the end of forging stage for the S2S case forged at (a) 950 °C and (b) 1050 °C billet temperature

The L2S workpiece strain rate resulted in similar behavior of S2S part (Figure 129, Figure 130), while the Carter workpiece showed lower values (Figure 131, Figure 132).

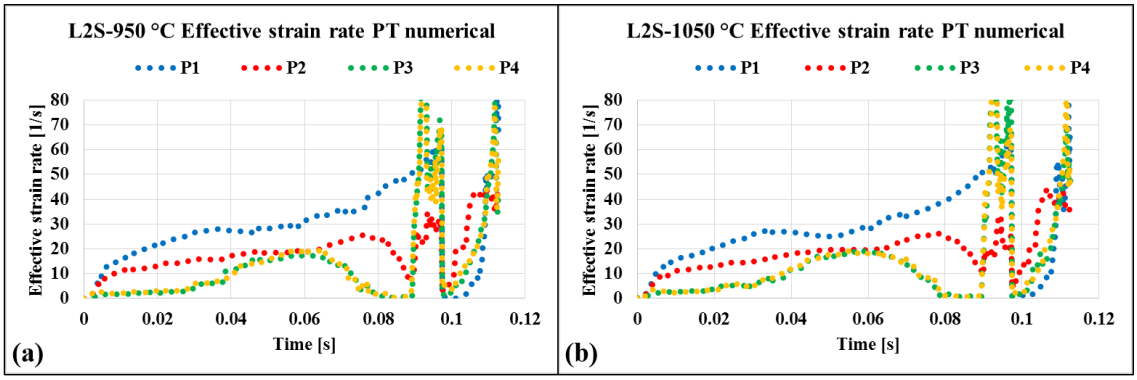

Figure 129: Effective strain rate prediction point tracking for the L2S case forged at (a) 950 °C and (b) 1050 °C billet temperature

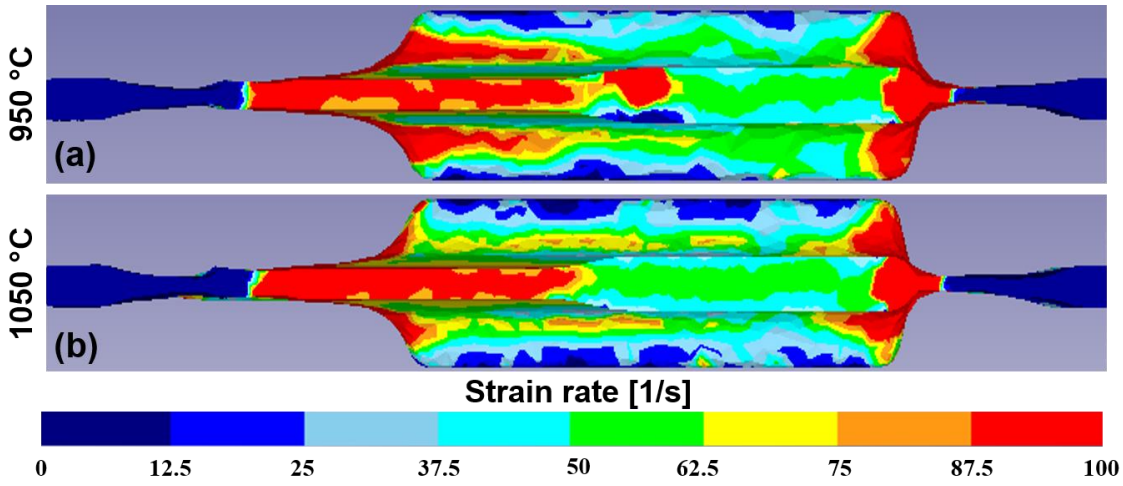

Figure 130: Effective strain rate colormap of the middle section at the end of forging stage for the L2S case forged at (a) 950 °C and (b) 1050 °C billet temperature

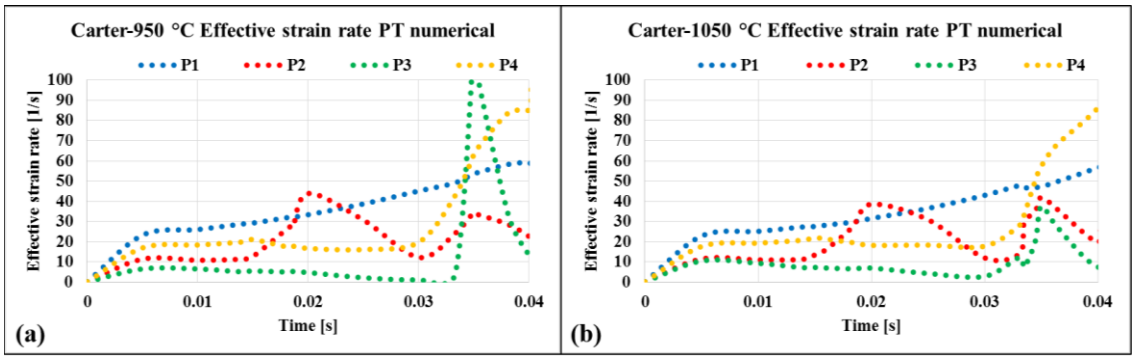

Figure 131: Effective strain rate prediction point tracking for the Carter case forged at (a) 950 °C and (b) 1050 °C billet temperature

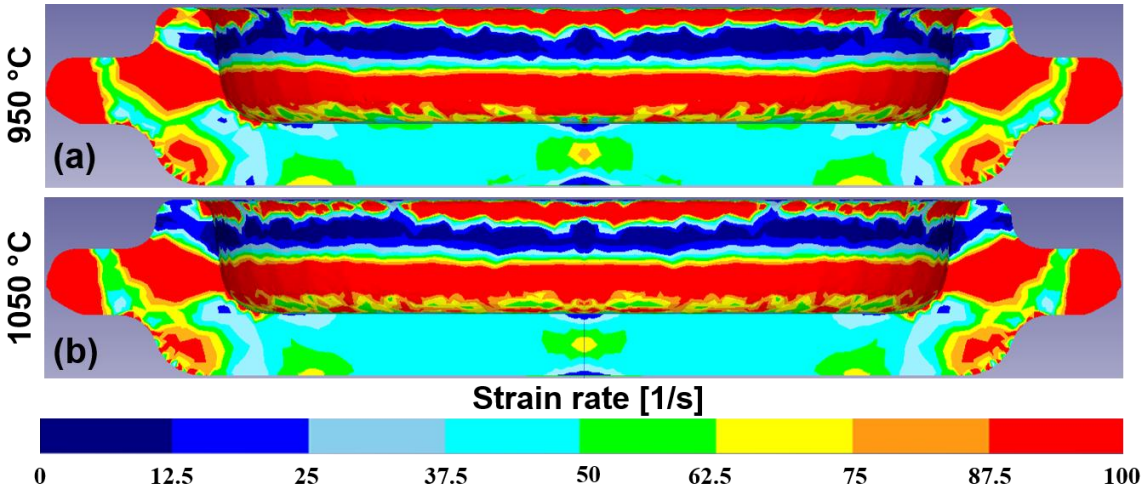

Figure 132: Effective strain rate colormap of the middle section at the end of forging stage for the Carter case forged at (a) 950 °C and (b) 1050 °C billet temperature

6.6.5. Phase transformation prediction

The last field variable carried out at the end of the simulation campaign was the phase evolution of the selected points during the whole process and the phase distribution along the middle section of each workpiece at the end of both forging and cooling stages.

The S2S case forged at 950 °C showed a residual Alpha phase content of 20 % about for the P1 point, coming from the heating stage below the Beta transus point, and 10 % about for the other selected points, due to the overheating during the forging stage. This determine a constant amount of Alpha phase during the cooling stage (Figure 133), while the complementary amount of Beta phase at the beginning of the forging stage was subjected to a transformation to Alpha+Beta phase due to the cooling phenomena. Different phase change behaviors were found on the selected points. In fact, the complete phase transformation of P2 and P3 points requires about 35 sec, while the P1 point required 17 sec about for a complete Beta-to-Alpha+Beta phase transformation. However, all points were subjected to a cooling speed slightly above the martensitic phase formation conditions. If the post-forging colormap (Figure 134) is observed, the point tracking results (Figure 133) are confirmed with a residual Alpha phase at the central zone of the workpiece, while the other zones transformed another fraction of Alpha phase due to the heating coming from deformation work.

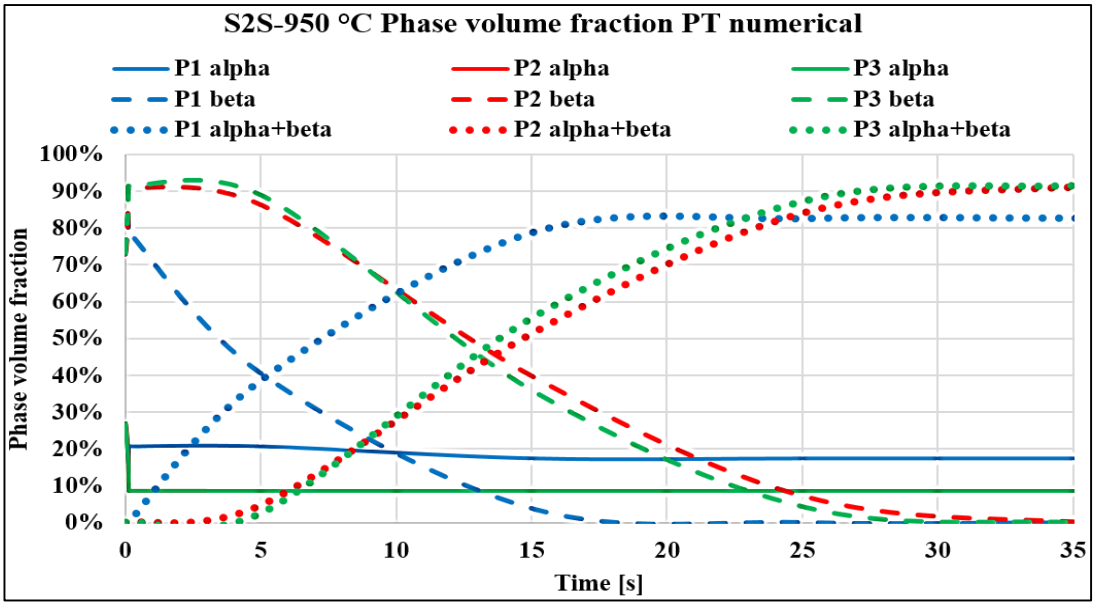

Figure 133: Point tracking of phase volume fraction evolution for the S2S case forged at 950 °C

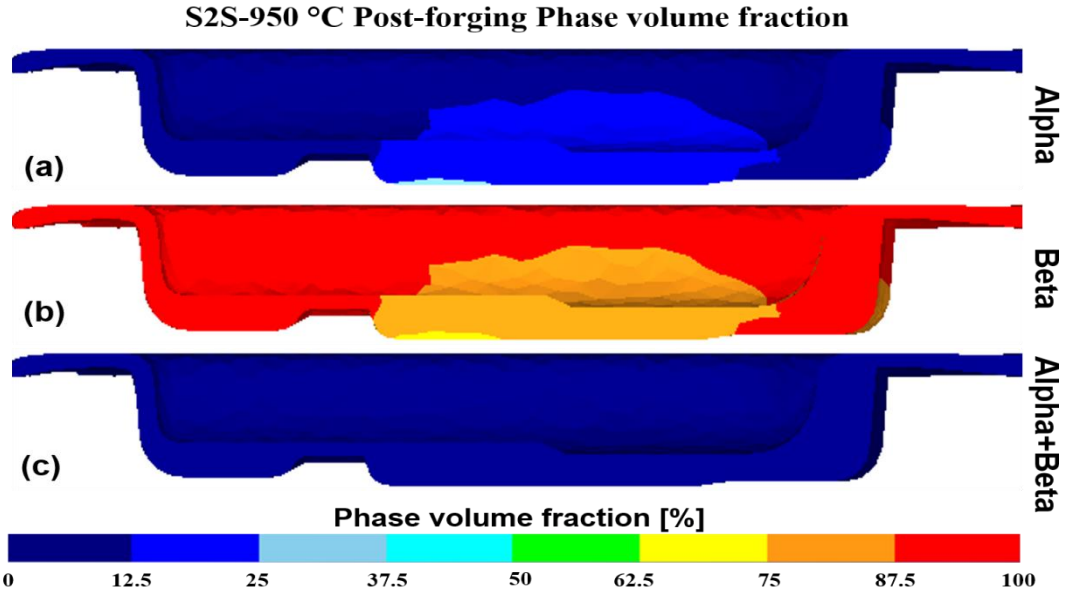

Figure 134: (a) Alpha, (b) Beta and (c) Alpha+Beta phase volume fraction colormap at the end of forging stage for the S2S case forged at 950 °C

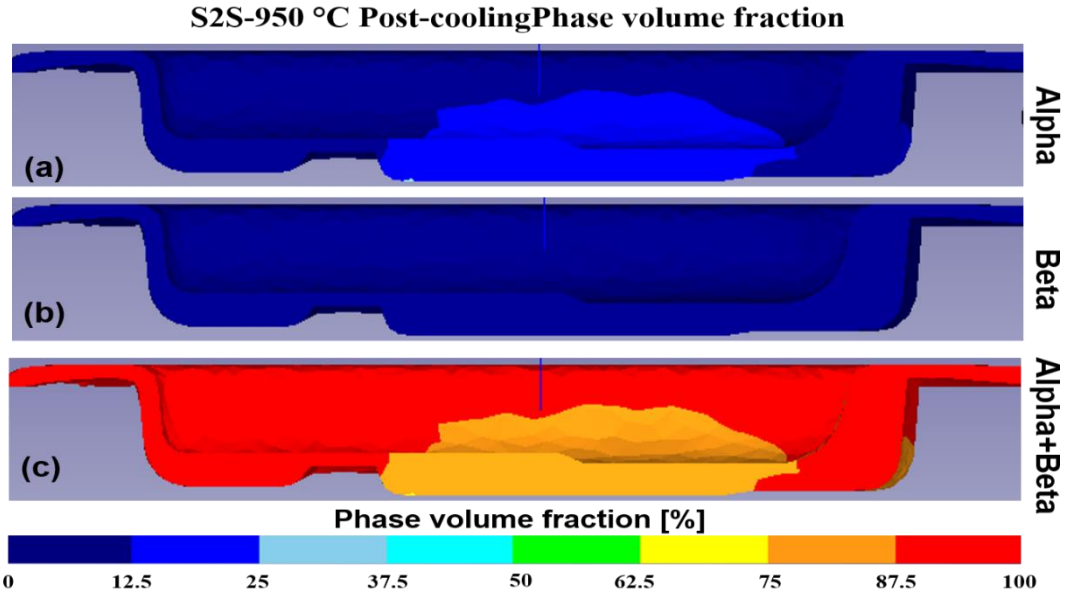

Figure 135: (a) Alpha, (b) Beta and (c) Alpha+Beta phase volume fraction colormap at the end of cooling stage for the S2S case forged at 950 °C

If the post-cooling colormap (Figure 135) is observed, the same residual Alpha phase amount distribution already seen on the post-forging colormap (Figure 134) is showed while the Beta phase totally transformed to Alpha+Beta phase. It is different the S2S case forged at 1050 °C (Figure 136) billet temperature, in which no residual Alpha phase

appears at the beginning of forging step due to the heating stage over Beta transus temperature.

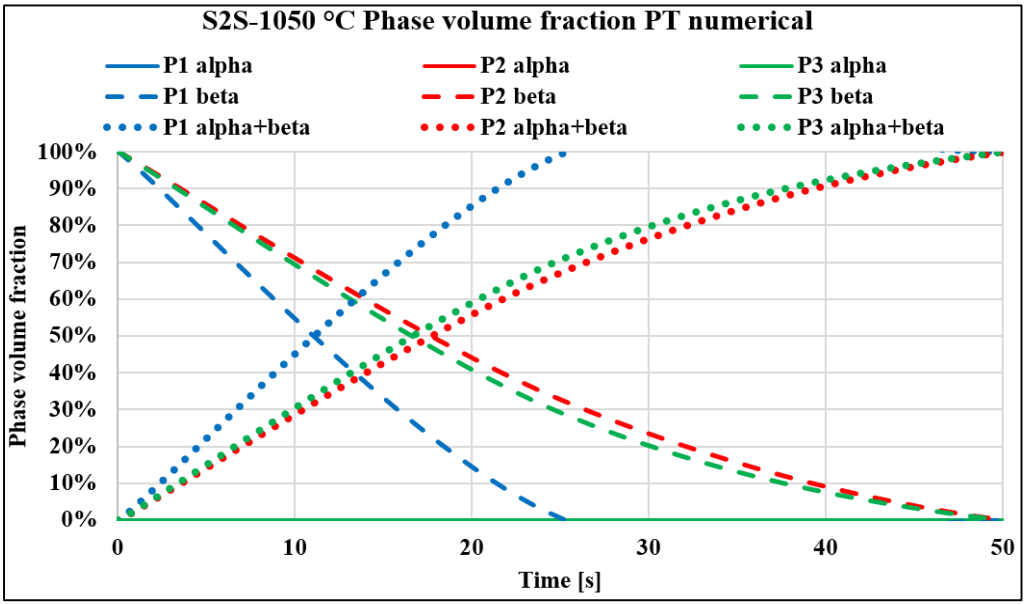

Figure 136: Point tracking of phase volume fraction evolution for the S2S case forged at 1050 °C

The total amount of initial phase after deformation is Beta (Figure 137) and a complete conversion to Alpha+Beta phase within 50 sec was found.

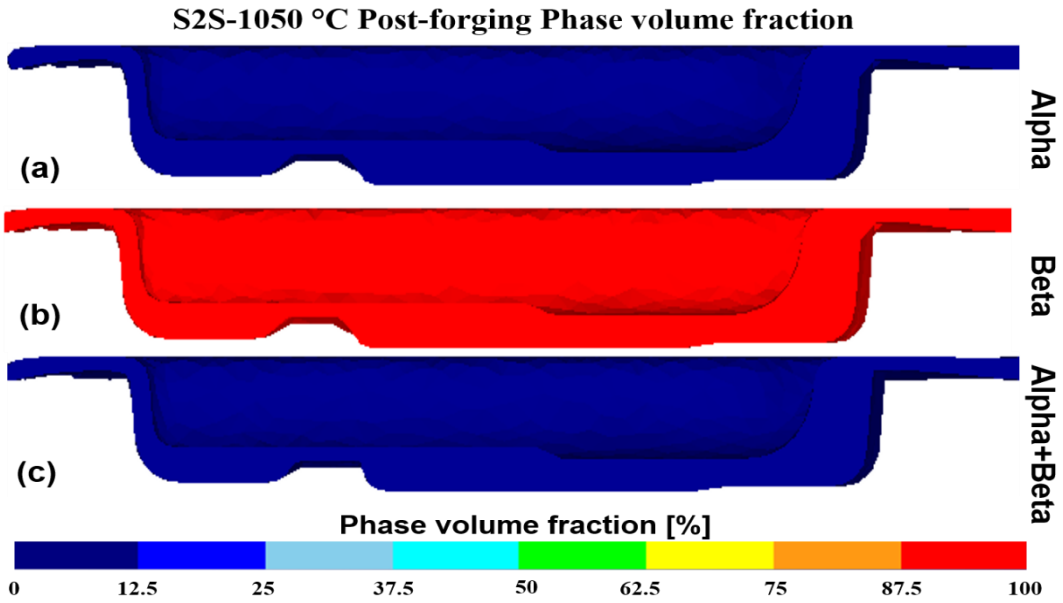

Figure 137: (a) Alpha, (b) Beta and (c) Alpha+Beta phase volume fraction colormap at the end of forging stage for the S2S case forged at 1050 °C

The post-cooling colormap (Figure 138) displayed a workpiece with a total amount of Alpha+Beta phase only coming from the conversion of Beta phase after the forging stage.

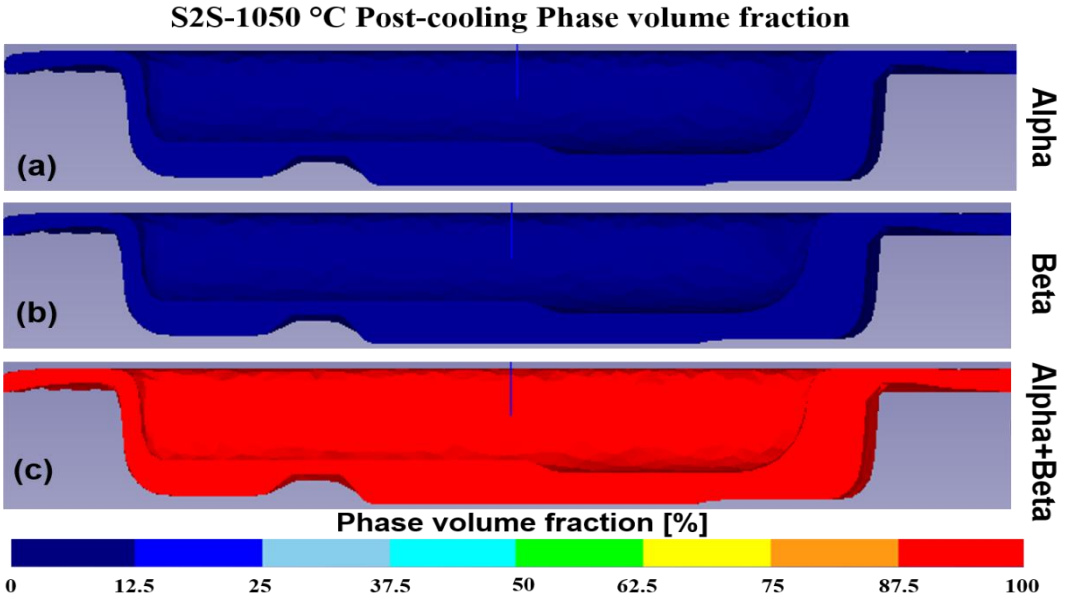

Figure 138: (a) Alpha, (b) Beta and (c) Alpha+Beta phase volume fraction colormap at the end of cooling stage for the S2S case forged at 1050 °C

Same considerations can be done for the L2S case (Figure 139) where the residual Alpha phase at the beginning of the forging stage was partially transformed to Beta phase.

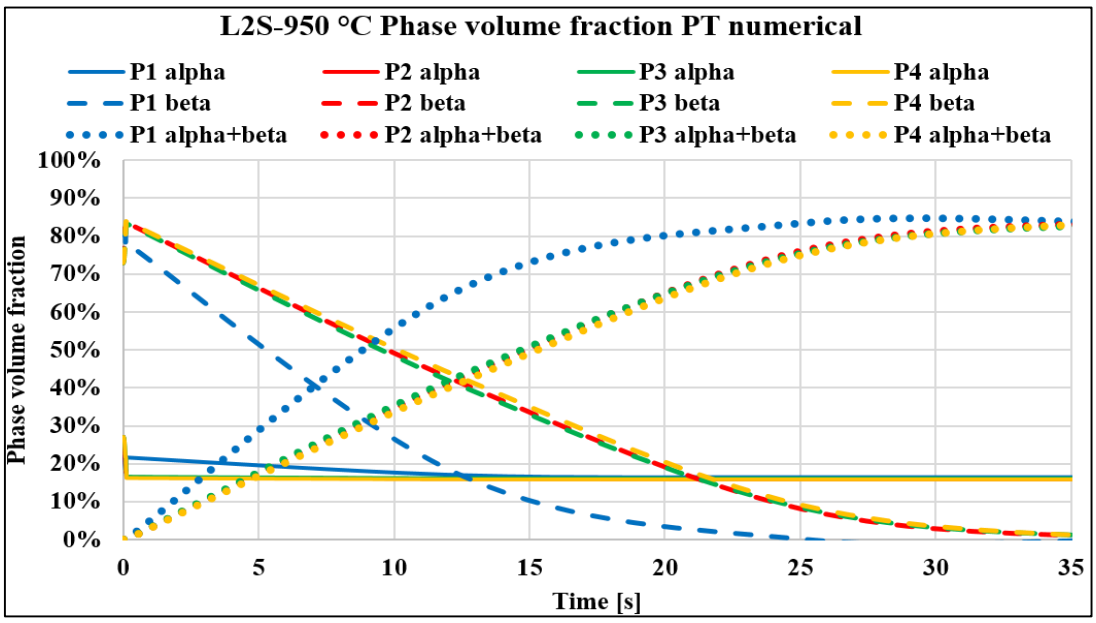

Figure 139: Point tracking of phase volume fraction evolution for the L2S case forged at 950 °C

It is caused by the heating coming from deformation work (Figure 140) and subsequential Beta-to-Alpha+Beta transformation was completed within 35 sec.

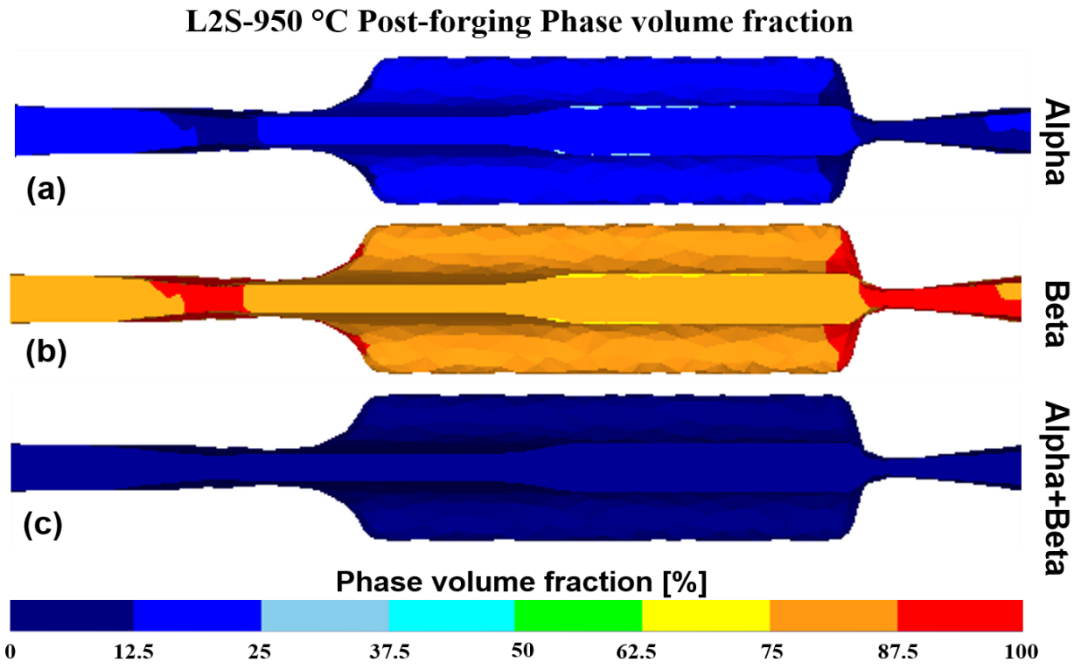

Figure 140: (a) Alpha, (b) Beta and (c) Alpha+Beta phase volume fraction colormap at the end of forging stage for the L2S case forged at 950 °C

From the end of forging stage to the final cooling at room temperature, the same behavior observed in the S2S case was found (Figure 141), while the 1050 °C case exhibited an identical behavior (Figure 142, Figure 143, Figure 144) of S2S case.

The Carter workpiece showed the same kind of phase transformation behavior (Figure 145).

The residual Alpha phase at beginning of forging stage which undergoes to a partial transformation due to the overheating coming from deformation work and generates a greater amount of Beta phase (Figure 146) which transforms to Alpha+Beta during the subsequential cooling stage (Figure 147).

In the end, the Carter case forged at 1050 °C billet temperature (Figure 148) exhibited a complete Alpha-to-Beta phase transformation before the forming stage (Figure 149) with a total amount of Alpha+Beta phase at the end of cooling stage (Figure 150).

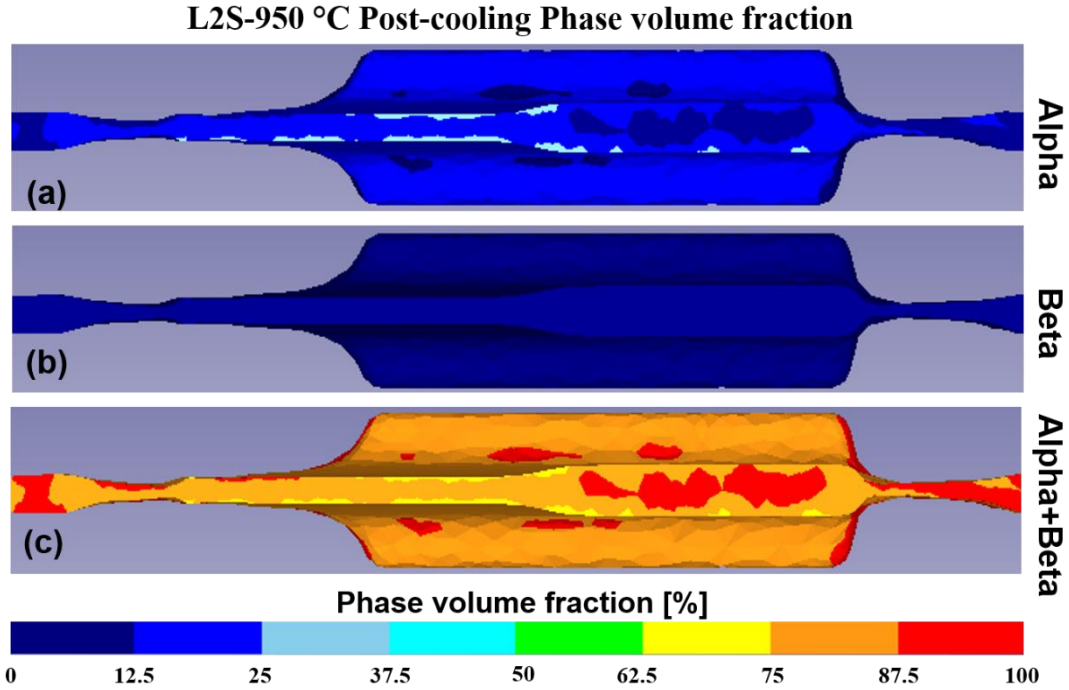

Figure 141: (a) Alpha, (b) Beta and (c) Alpha+Beta phase volume fraction colormap at the end of cooling stage for the L2S case forged at 950 °C

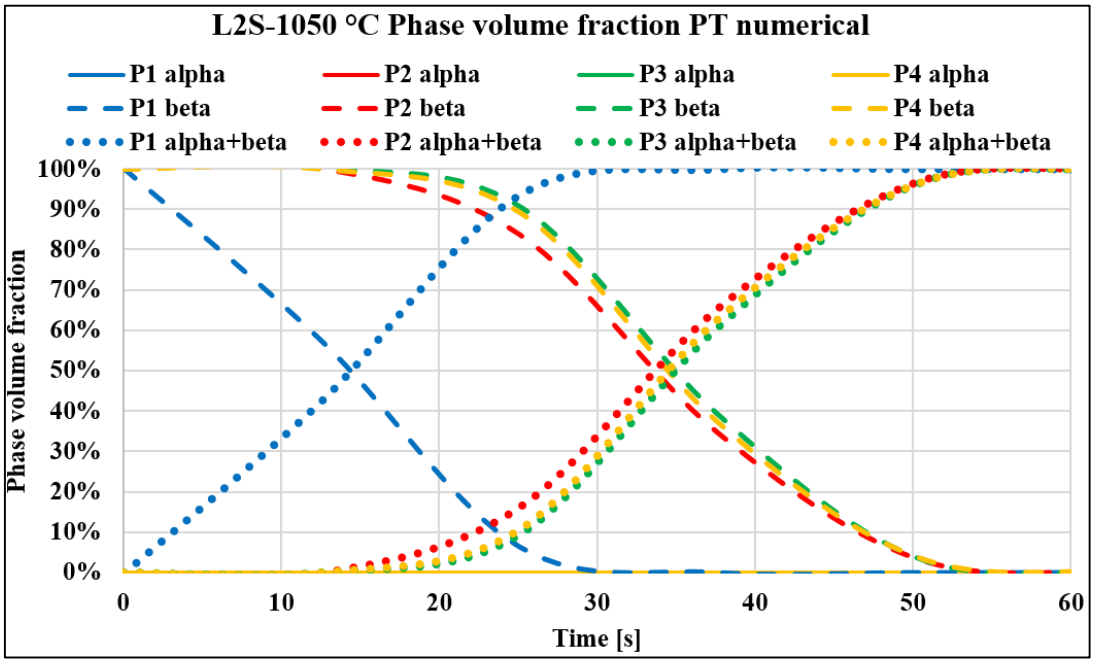

Figure 142: Point tracking of phase volume fraction evolution for the L2S case forged at 1050 °C

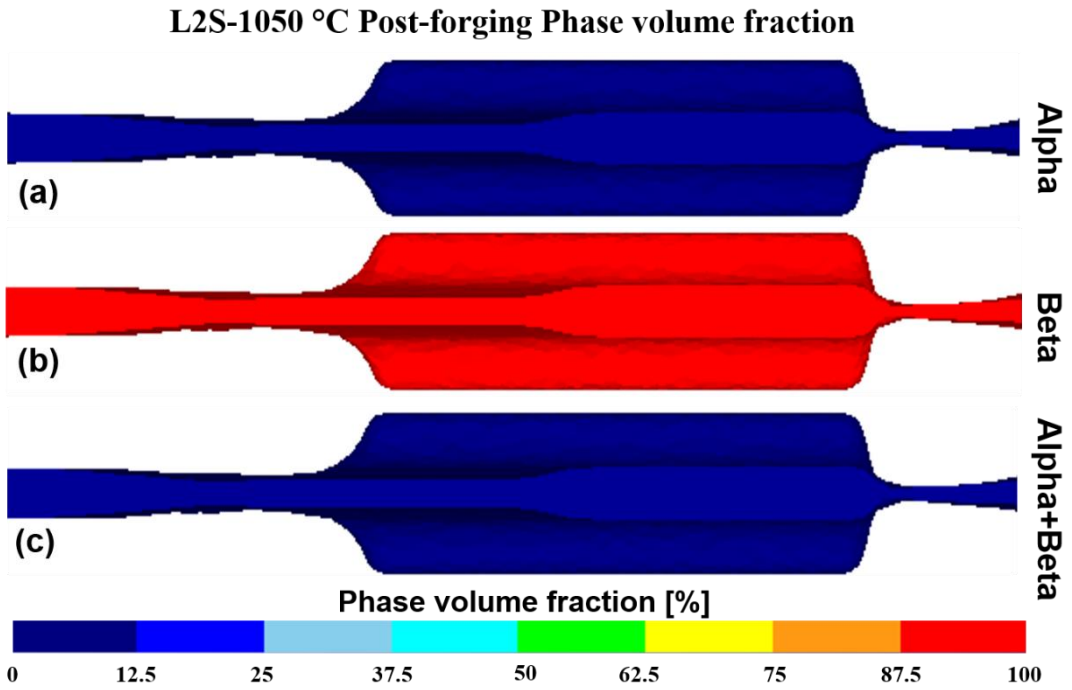

Figure 143: (a) Alpha, (b) Beta and (c) Alpha+Beta phase volume fraction colormap at the end of forging stage for the L2S case forged at 1050 °C

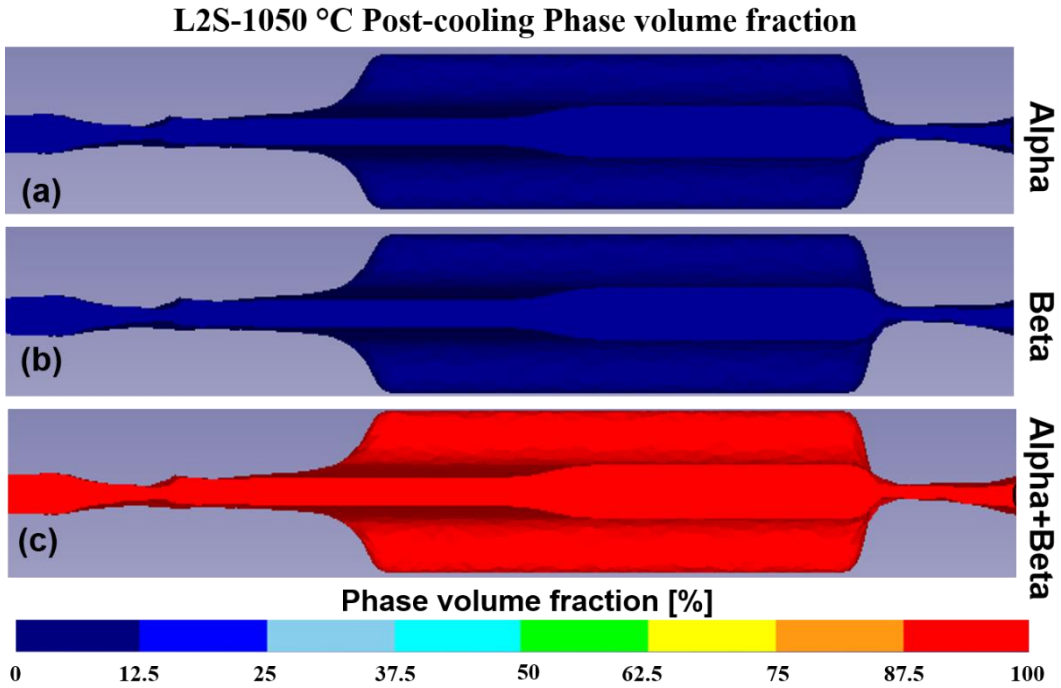

Figure 144: (a) Alpha, (b) Beta and (c) Alpha+Beta phase volume fraction colormap at the end of cooling stage for the L2S case forged at 1050 °C

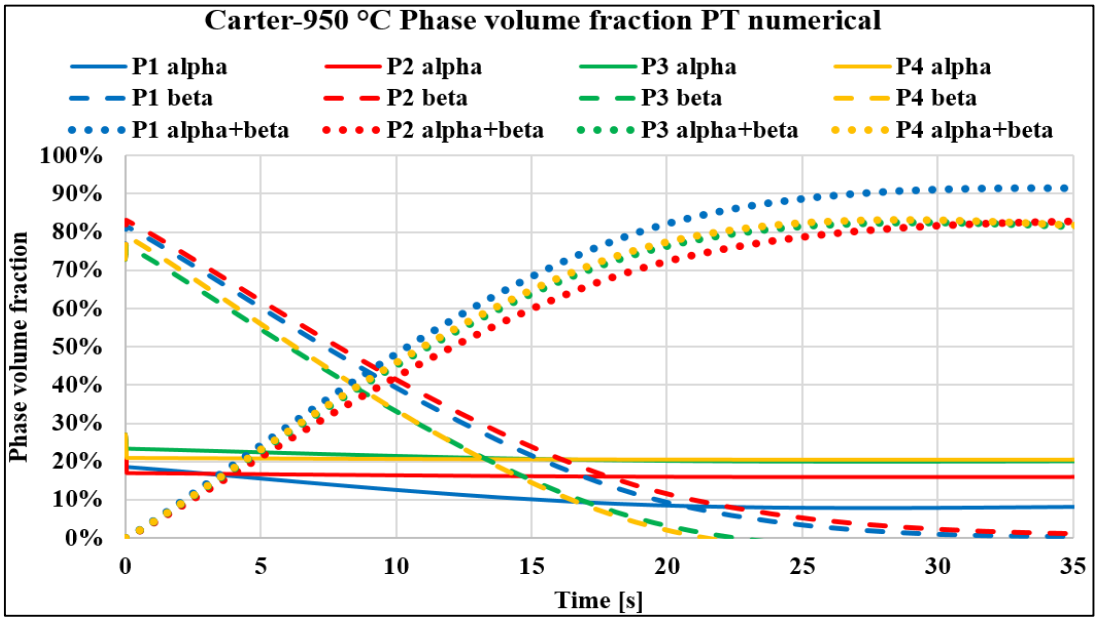

Figure 145: Point tracking of phase volume fraction evolution for the Carter case forged at 950 °C

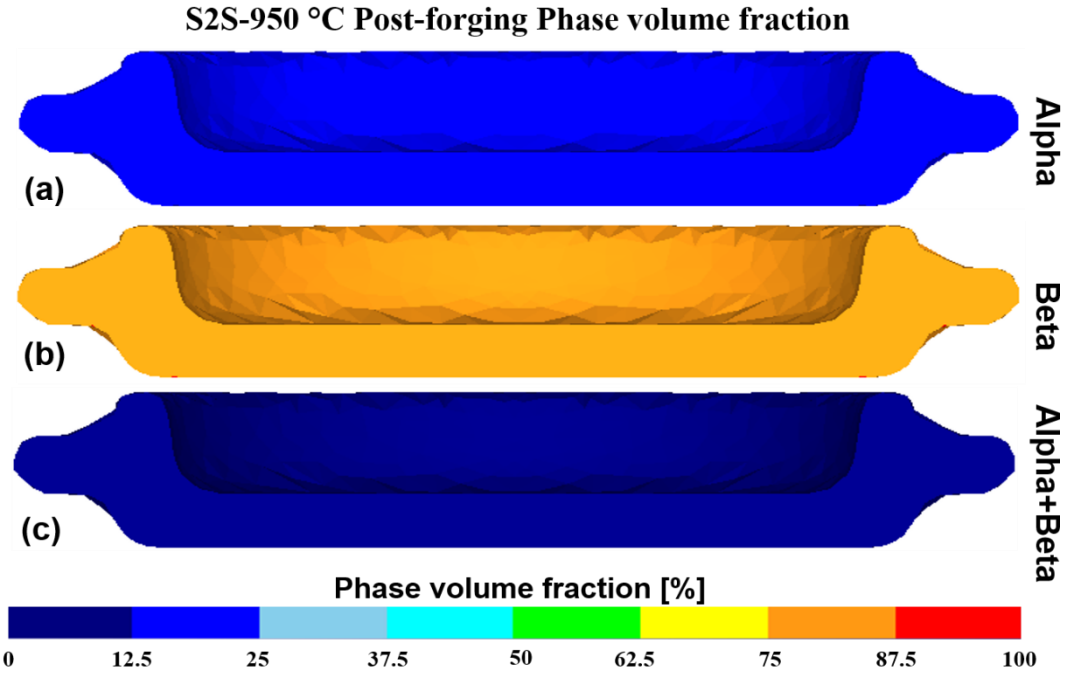

Figure 146: (a) Alpha, (b) Beta and (c) Alpha+Beta phase volume fraction colormap at the end of forging stage for the Carter case forged at 950 °C

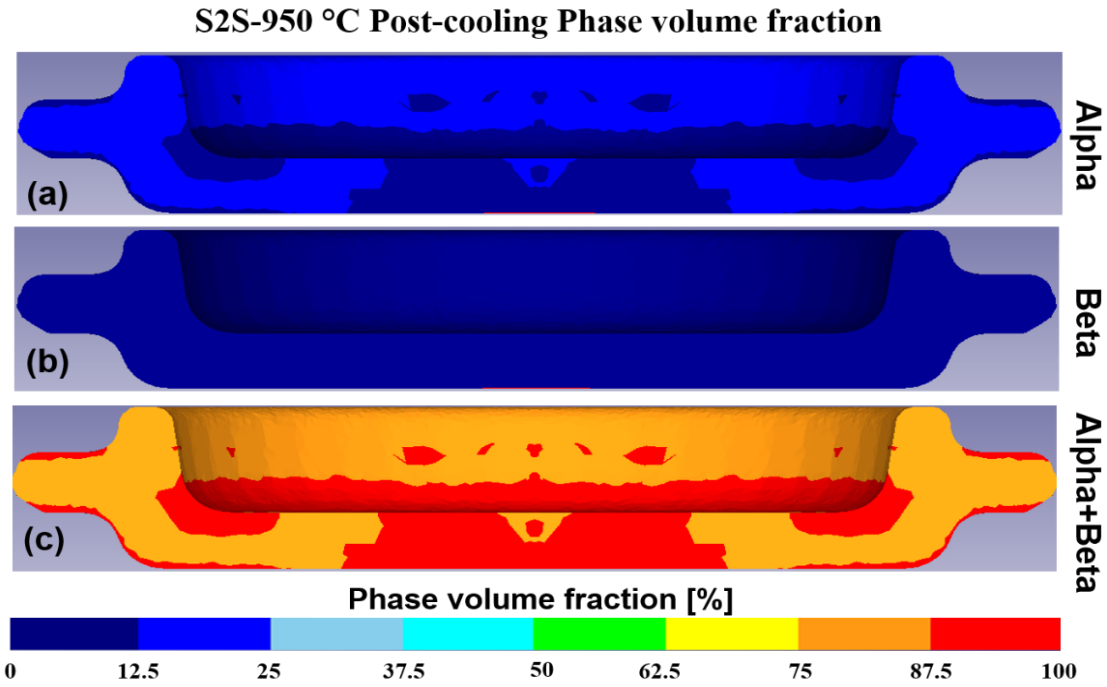

Figure 147: (a) Alpha, (b) Beta and (c) Alpha+Beta phase volume fraction colormap at the end of cooling stage for the Carter case forged at 950 °C

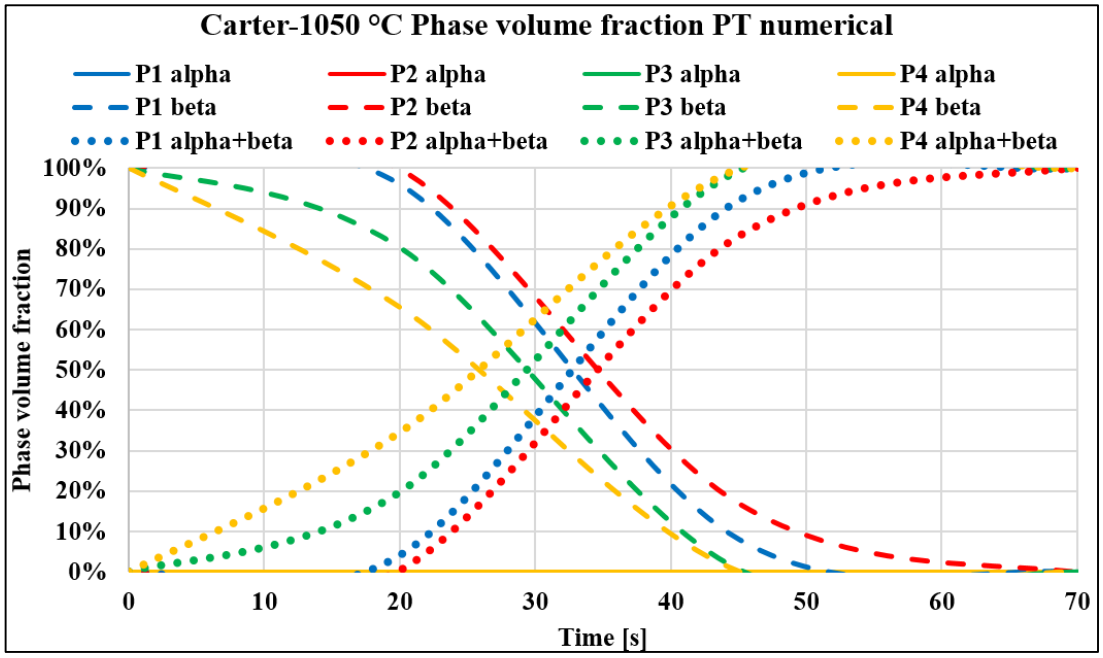

Figure 148: Point tracking of phase volume fraction evolution for the Carter case forged at 1050 °C

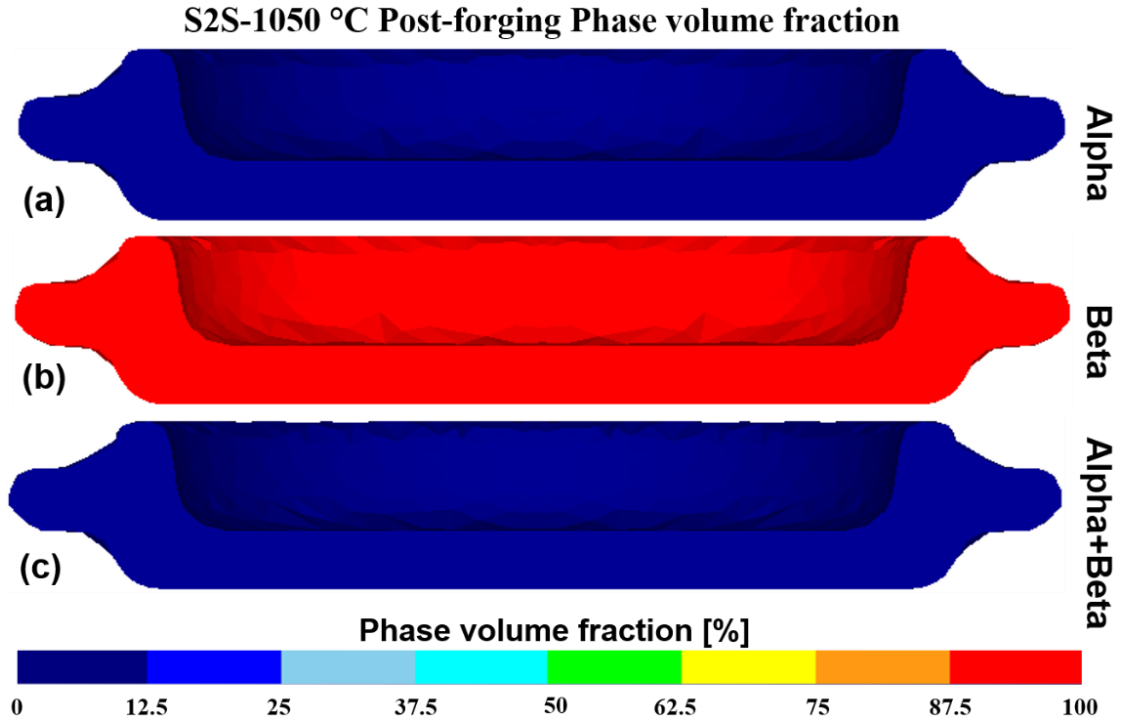

Figure 149: (a) Alpha, (b) Beta and (c) Alpha+Beta phase volume fraction colormap at the end of forging stage for the Carter case forged at 1050 °C

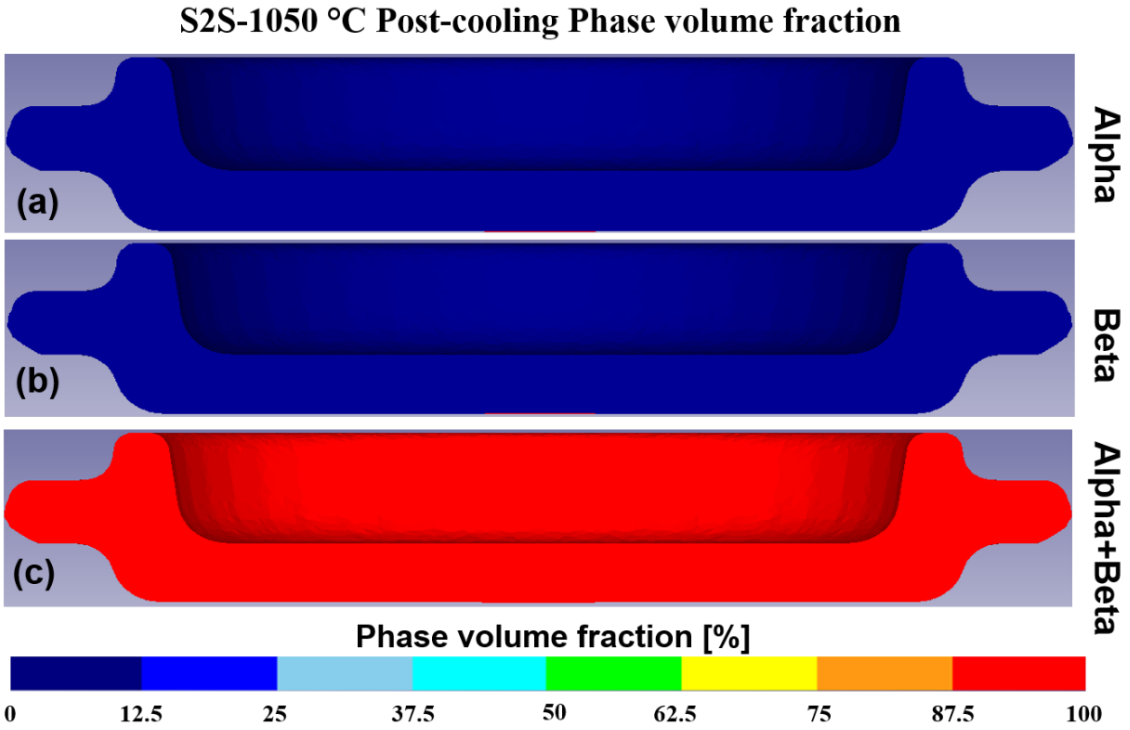

Figure 150: (a) Alpha, (b) Beta and (c) Alpha+Beta phase volume fraction colormap at the end of cooling stage for the Carter case forged at 1050 °C

6.7. Comparison with experimental data

6.7.1. Flow instability and forging defects analysis

Numerical data carried out for strain rate and temperature of the selected points was used to analyze the evolution in a temperature-strain rate domain during the forging stage and relate the results with respect to process windows coming from literature. Considering the values range for both temperature and strain rate, a comparison with a process map for the considered alloys was given using data coming from a study conducted by Seshacharyulu et al. [76] on workability of Ti-6Al-4V. Using the equations proposed in this paper (Eq. 55, Eq. 56), an instability zone, separating the safe region from the instable flow one, was calculated.

$$\eta = \frac{2m}{m+1} \qquad \text{Eq. 55}$$

$$\xi(\dot{\varepsilon}) = \frac{\partial ln\left(\frac{m}{m+1}\right)}{\partial ln\dot{\varepsilon}} + m < 0 \qquad \text{Eq. 56}$$

Where η is the efficiency of power dissipation, ξ is is a dimensionless instability parameter and m is the strain rate sensitivity coefficient which was considered equal to 1.3 (middle value among the strain rate range involved within the process).

Basing on this map, the point tracking of temperature and strain rate were used to locate in which zone of the diagram where the selected points were placed. Investigating the S2S cases, it was found that the temperature-strain rate of the selected points (Figure 111) have almost totally fallen within the safe region in both 950 °C and 1050 °C cases (Figure 151). Most of values are concentrated close to the instability line, which denotes that an increasing in strain rate (or forging speed) may cause instability in material flow.

If experimental forgings are observed (Figure 152), some specimen forged with a billet temperature of 1050 °C suffered of damages in the thinnest zone.

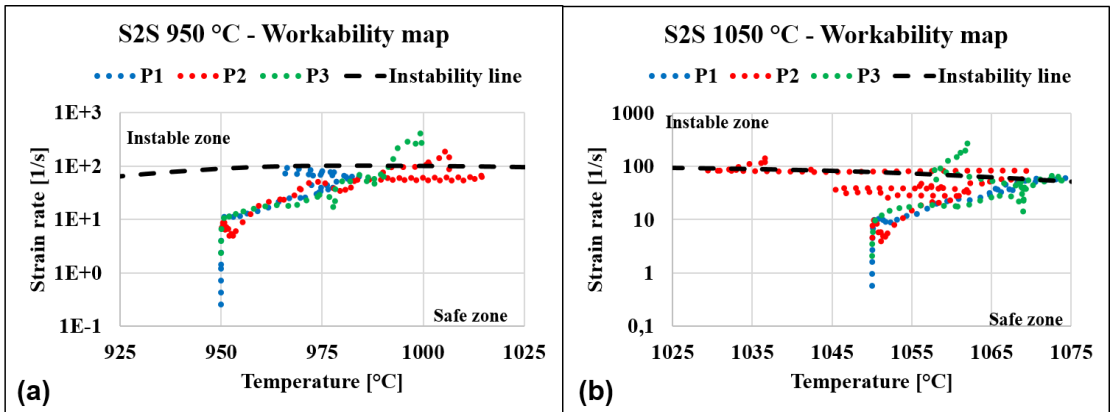

Figure 151: Instability map obtained from numerical temperature-strain rate data for the S2S case forget at (a) 950 °C and (b) 1050 °C; the black line represents the border separating safe and instable zones

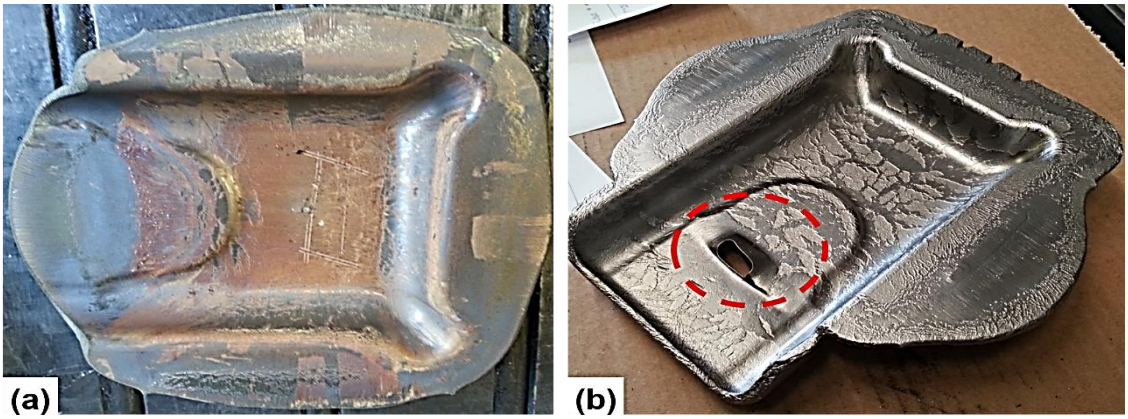

Figure 152: Experimental forgings of S2S workpiece: (a) 950 °C and (b) 1050 °C billet temperature cas

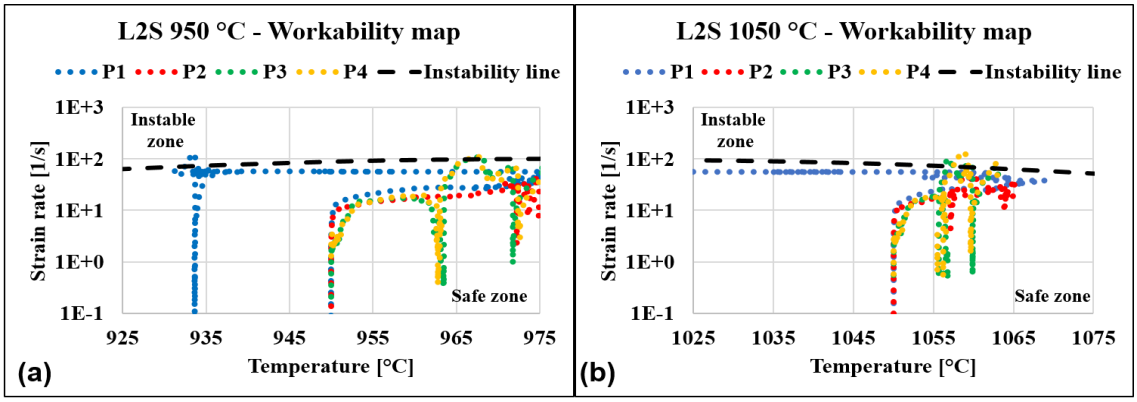

Figure 153: Instability map obtained from numerical temperature-strain rate data for the L2S case forget at (a) 950 °C and (b) 1050 °C; the black line represents the border separating safe and instable zones

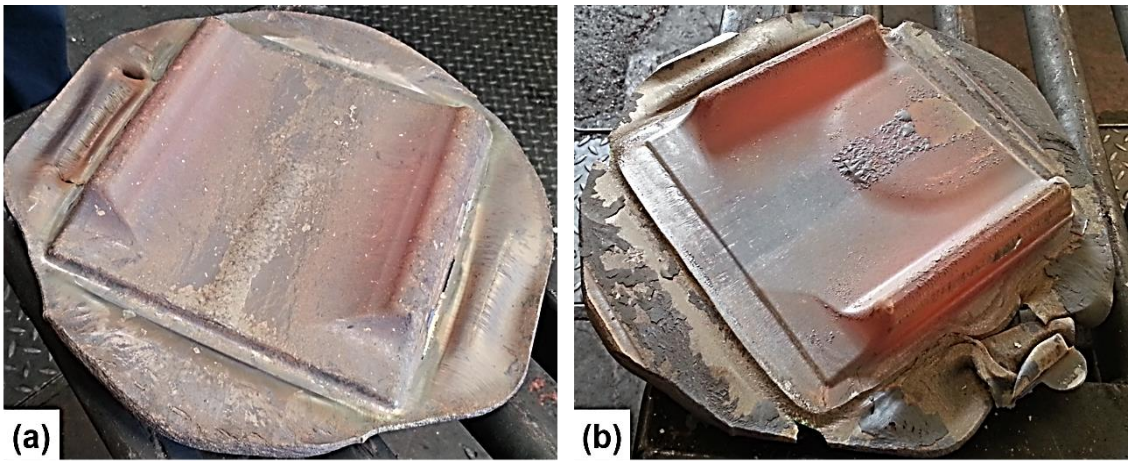

Figure 154: Experimental forgings of L2S workpiece: (a) 950 °C and (b) 1050 °C billet temperature case

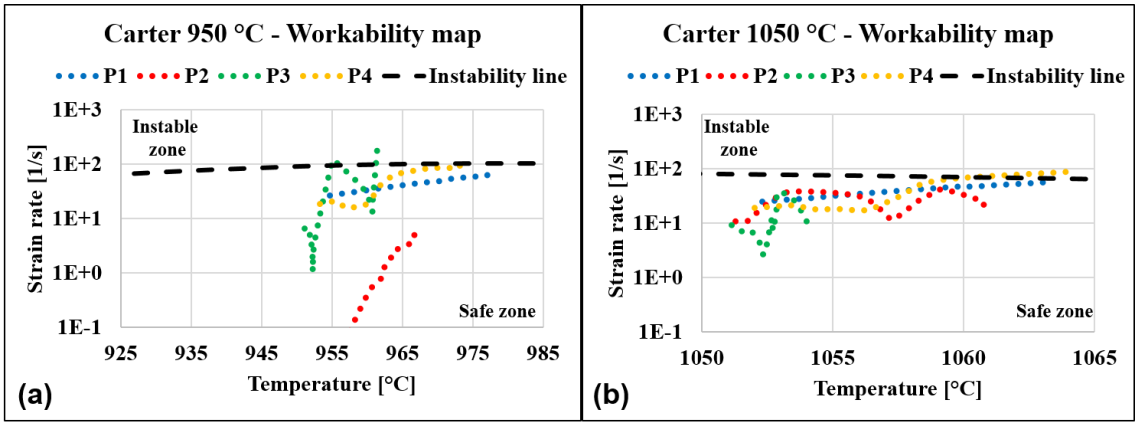

Figure 155: Instability map obtained from numerical temperature-strain rate data for the Carter case forget at (a) 950 °C and (b) 1050 °C; the black line represents the border separating safe and instable zones

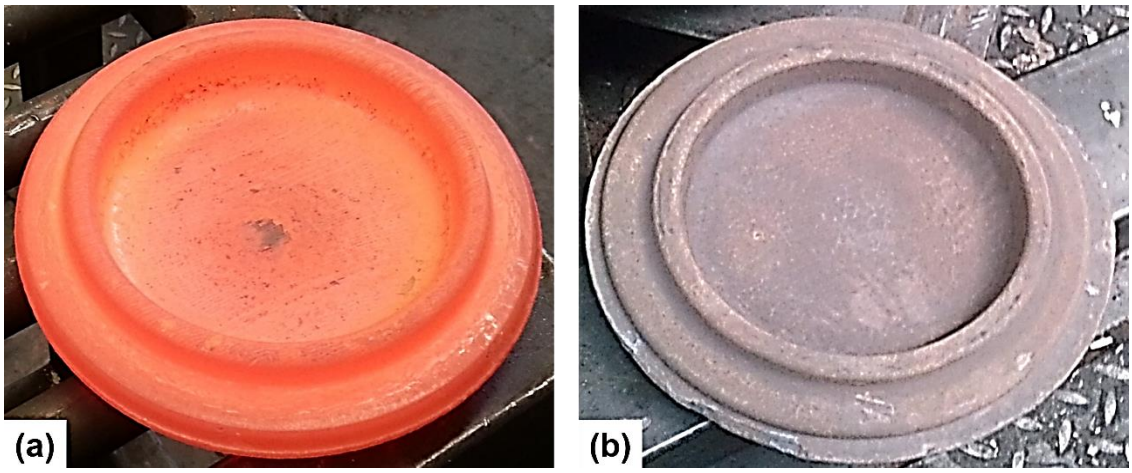

Figure 156: Experimental forgings of Carter workpiece: (a) 950 °C and (b) 1050 °C billet temperature case

Similar consideration can be given for both L2S (Figure 153) and Carter (Figure 155) workpieces which displayed to be totally included into the safe region with very few points over the instability line.

The numerical prediction was confirmed by real forgings, which did not show any flow instability (Figure 154, Figure 156).

6.7.2. Metallographic analysis of forgings and comparison with numerical phase prediction and distribution

The last step in validation procedure of numerical characterization was the comparison with the numerical prediction of final phase distribution within each case study and the micrographic analysis (Figure 157) on the forged workpieces by means of observation of samples extracted in the selected points (Figure 111).

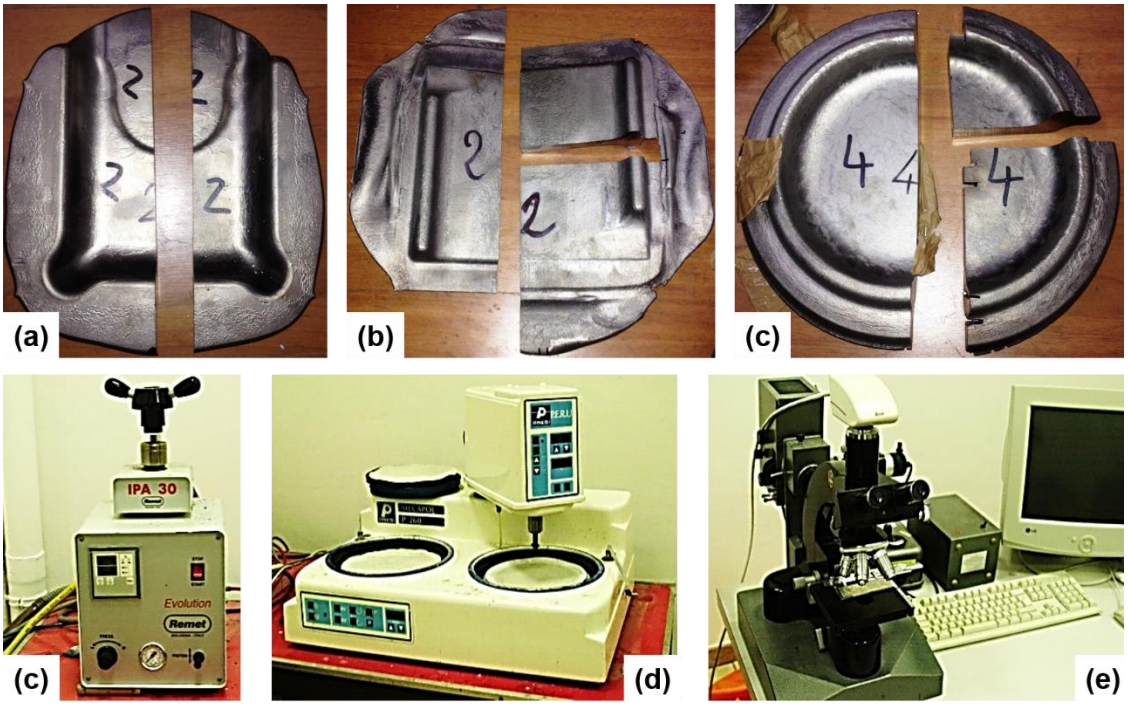

Figure 157: Sectioned forgings: (a) S2S, (b) L2S and (c) Flangia–20718; (c) micrographic mounting press, (d) grinding and polishing machine and (e) digital optical microscope

In order to obtain both qualitative and quantitave measurements of microstructure type and volume fraction of the inspected specimens, a computer automated system to classify the phases of a Ti-6Al-4V was created by means of Matlab™ code [188].

The main goal was to find a compact and functional description of the image information, in order to classify all the areas of the image into the two possible classes: individual Alpha/Beta and Alpha+Beta.

The working scheme of the overall system includes the following steps (Figure 158):

- Images (size M×N) are first decomposed into a grid of (m×n) non-overlapping sub-blocks of size B×B, where m=M/B and n=N/B. The value of B will be further described in the experimental section.
- Features are extracted from each sub-block and concatenated to form a $BxBxN_i$ vector, where N_i is the size of a single block descriptor vector.
- Feature vectors are then used to train a Support Vector Machine used as binary classifier. which is the most used and the simplest solution whenever a binary classification problem has to be solved.

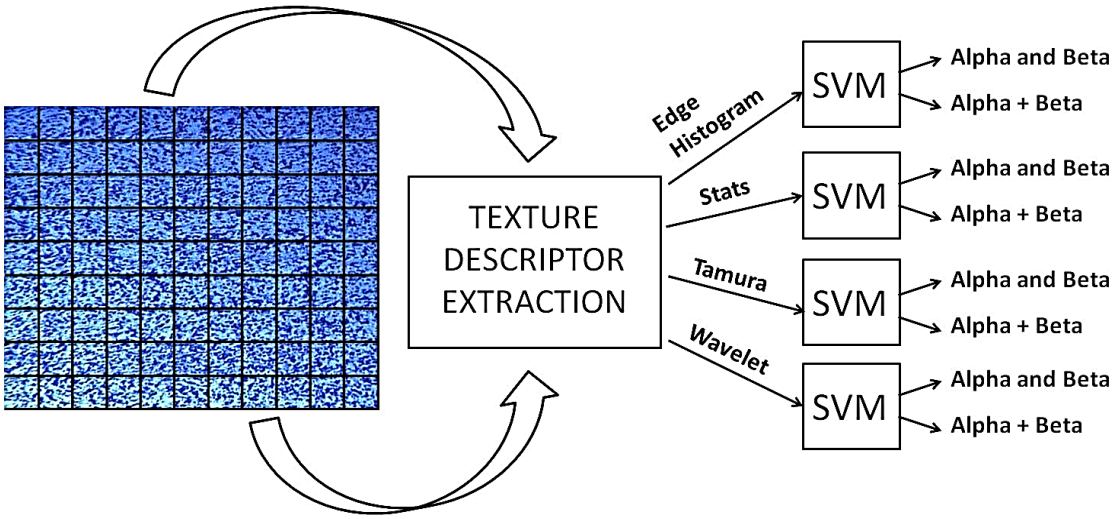

Figure 158: Scheme for automated micrographic analysis system [188]

The Matlab™ subroutine was used to analyze the zones of each forged part corresponding to the significant points (Figure 159) chosen for point tracking data extraction at the end of the simulation campaign.

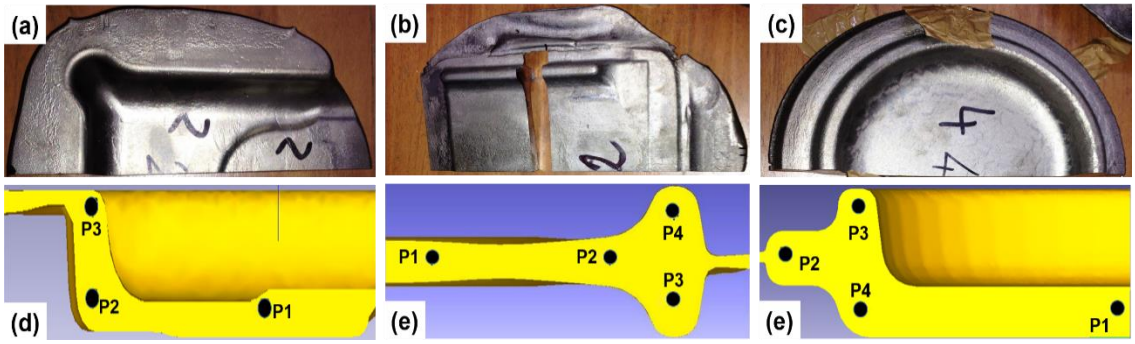

Figure 159: Point tracking positions for microstructure analysis of (a, d) S2S, (b, d) L2S and (c, e) Carter workpieces

The comparison between numerical and experimental data showed a very good agreement in all observed zones of all workpieces. The numerical output demonstrated a fine level of prediction in final phase distribution, and very low differences in percentage of phase amount in the selected points.

The S2S part phase prediction was sufficiently accurate with an error in microstructure prevision between 4 and 15 % for the 950 °C case (Figure 160).

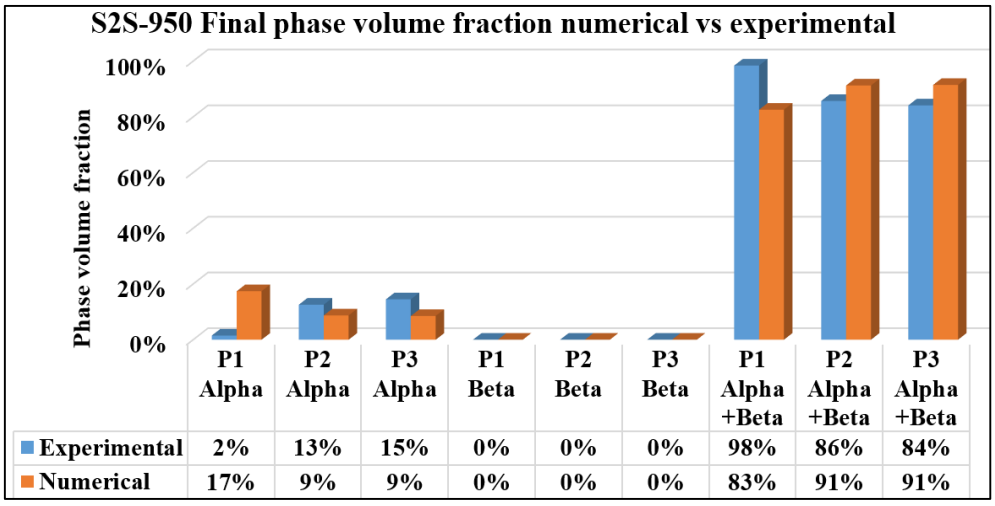

Figure 160: Numerical vs experimental comparison in final phase volume fraction of selected points for the S2S case forged at 950 °C billet temperature

If micrographic images (Figure 161) are analyzed, it was found that the final microstructure includes lamellar Alpha+Beta microstructure inside a matrix of globular Alpha phase. The simulation of S2S case forged at 1050 °C produced a better prediction of final microstructure volume fraction (Figure 162) with no residual Alpha prior phase

and a complete lamellar Alpha+Beta morphology at room temperature. The results are confirmed by micrographic analyses (Figure 163) of the selected points.

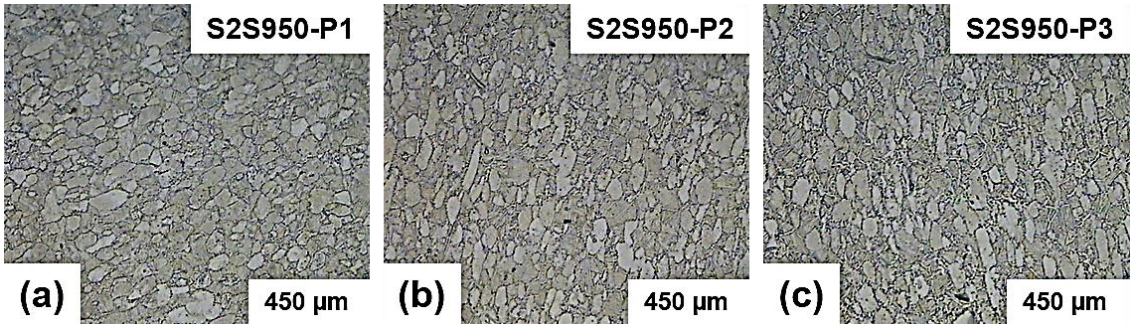

Figure 161: Micrographic images of (a) P1, (b) P2 and (c) P3 points of the S2S case forged at 950 °C billet temperature

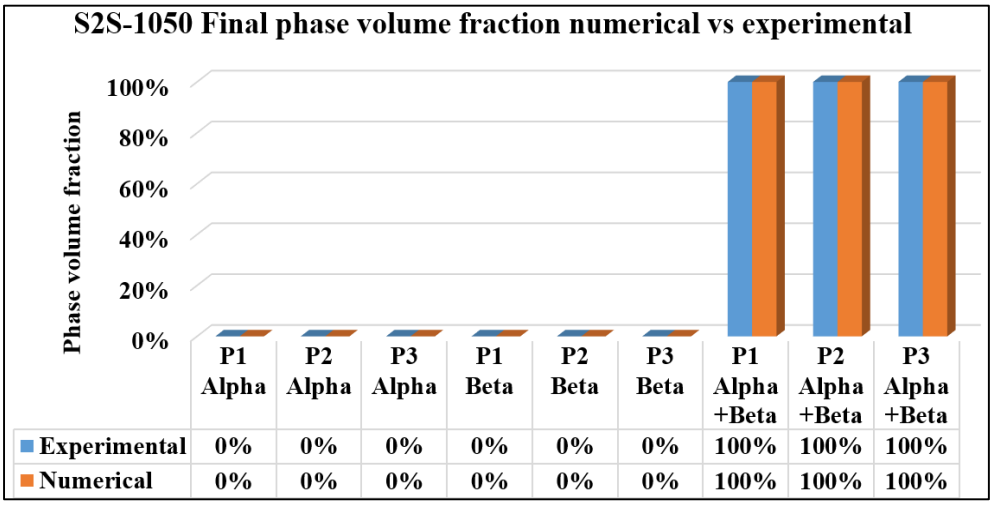

Figure 162: Numerical vs experimental comparison in final phase volume fraction of selected points for the S2S case forged at 1050 °C billet temperature

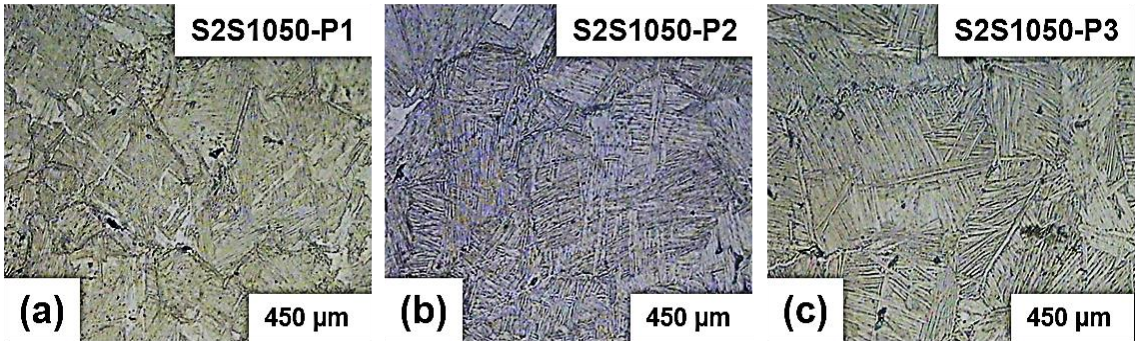

Figure 163: Micrographic images of (a) P1, (b) P2 and (c) P3 points of the S2S case forged at 1050 °C billet temperature

A brief clarification has to be done about the differences in final phase amount between numerical model prediction and experimental observations. The approximations of the numerical model, coming from the use of equations and coefficient values which nearly estimate the real phenomena, is in addiction of the errors of micrographic analysis software. These errors are directly linked to the training operations of the texture descriptors in which an already existing micrographic database produced on different devices was used. The quality of images coming from a different equipment could have influenced the statistical calculation of the software. In this scenario, an increasing in discrepancies between experimental and numerical data may be obtained.

The L2S part phase prediction was much more accurate with an error in microstructure prevision between 1 and 5 % for the 950 °C case (Figure 164).

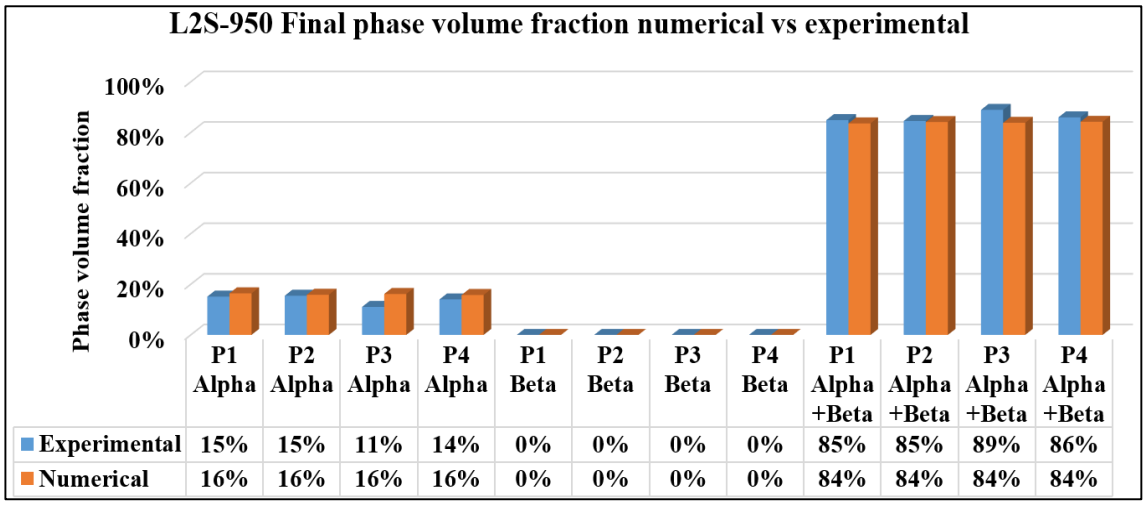

	P1 Alpha	P2 Alpha	P3 Alpha	P4 Alpha	P1 Beta	P2 Beta	P3 Beta	P4 Beta	P1 Alpha +Beta	P2 Alpha +Beta	P3 Alpha +Beta	P4 Alpha +Beta
Experimental	15%	15%	11%	14%	0%	0%	0%	0%	85%	85%	89%	86%
Numerical	16%	16%	16%	16%	0%	0%	0%	0%	84%	84%	84%	84%

Figure 164: Numerical vs experimental comparison in final phase volume fraction of selected points for the L2S case forged at 950 °C billet temperature

The micrographic images (Figure 165) showed that the final microstructure includes lamellar Alpha+Beta microstructure inside a matrix of globular Alpha phase, as well as the previous forged part. Even in this case, the simulation of L2S case forged at 1050 °C produced a better prediction of final microstructure volume fraction (Figure 166) with no residual Alpha prior phase and a complete lamellar Alpha+Beta morphology at room temperature. Same results can be observed on micrographic analyses (Figure 167) of the selected points.

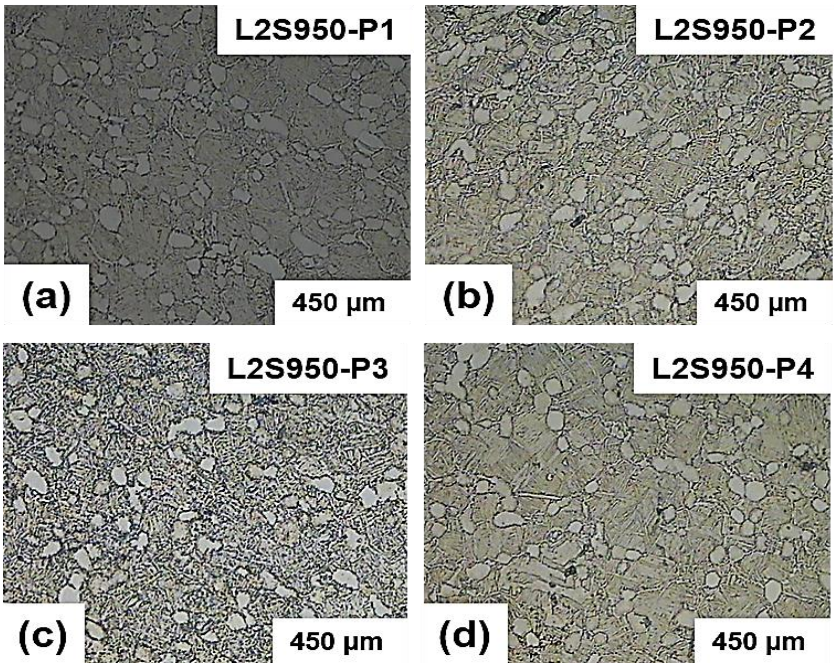

Figure 165: Micrographic images of (a) P1, (b) P2, (c) P3 and (d) P4 points of the L2S case forged at 950 °C billet temperature

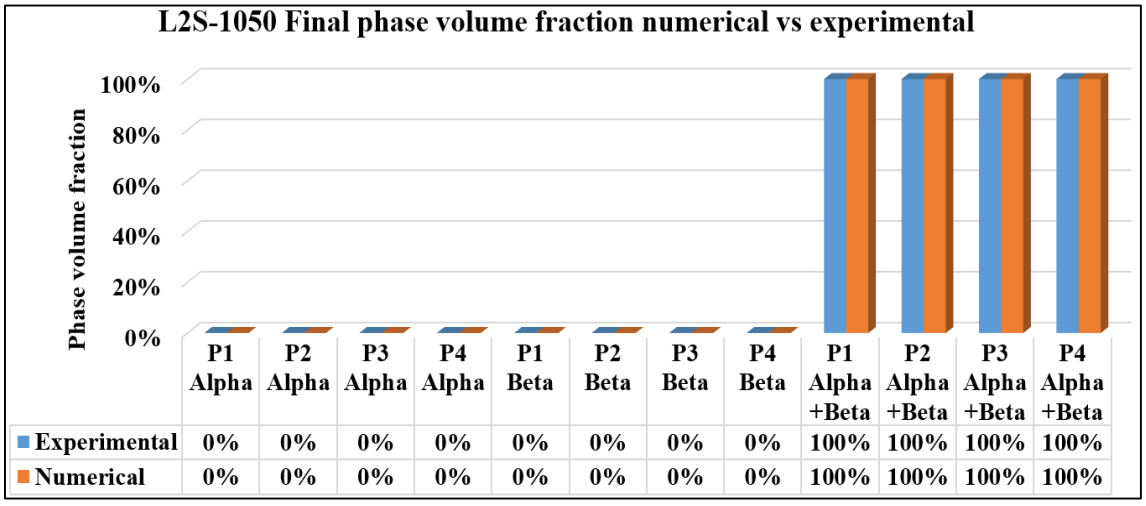

Figure 166: Numerical vs experimental comparison in final phase volume fraction of selected points for the L2S case forged at 1050 °C billet temperature

The Carter case phase prediction was showed a similar accuracy than the S2S workpiece, with an error in microstructure prevision between 1 and 8 % for the 950 °C case (Figure 168). The micrographic images (Figure 169) showed that the final microstructure includes lamellar Alpha+Beta microstructure inside a matrix of globular Alpha phase, with a P1 point exhibiting an almost total amount of lamellar Alpha+Beta microstructure.

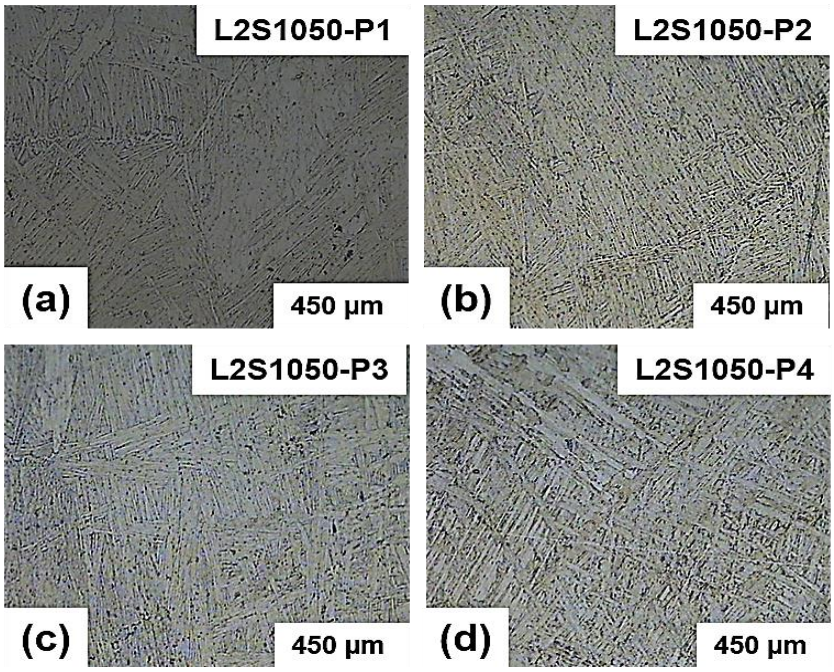

Figure 167: Micrographic images of (a) P1, (b) P2, (c) P3 and (d) P4 points of the L2S case forged at 1050 °C billet temperature

It can be related to the overheating during the forging stage, which produced an extra-transformation of residual Alpha phase to Beta phase.

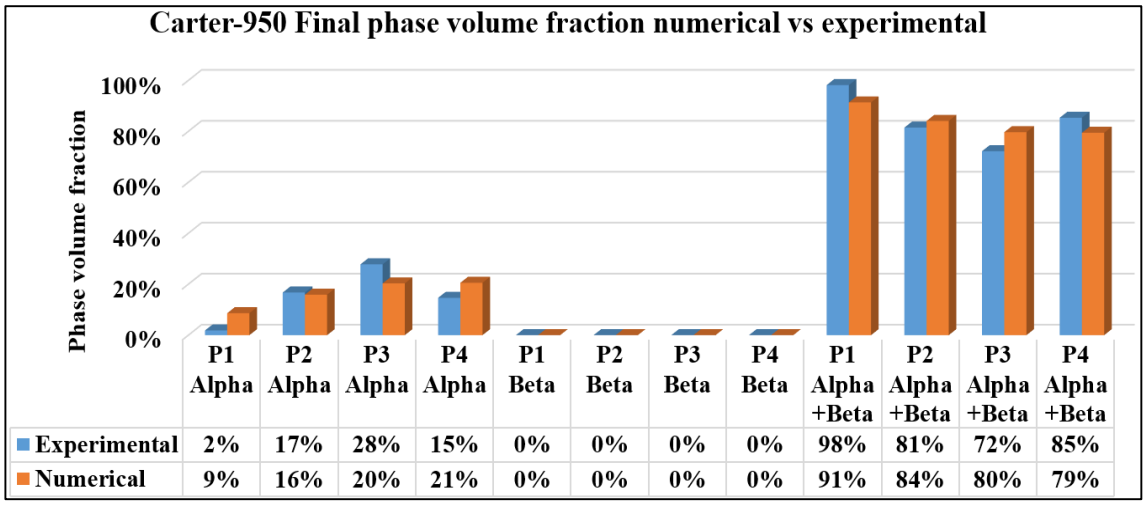

	P1 Alpha	P2 Alpha	P3 Alpha	P4 Alpha	P1 Beta	P2 Beta	P3 Beta	P4 Beta	P1 Alpha +Beta	P2 Alpha +Beta	P3 Alpha +Beta	P4 Alpha +Beta
Experimental	2%	17%	28%	15%	0%	0%	0%	0%	98%	81%	72%	85%
Numerical	9%	16%	20%	21%	0%	0%	0%	0%	91%	84%	80%	79%

Figure 168: Numerical vs experimental comparison in final phase volume fraction of selected points for the Carter case forged at 950 °C billet temperature

Even in this case, the simulation of Carter case forged at 1050 °C produced a final microstructure (Figure 170) with no residual Alpha prior phase and a complete lamellar

Alpha+Beta morphology. Same results can be observed on micrographic analyses (Figure 171) of the selected points with a less refined microstructure than the L2S case.

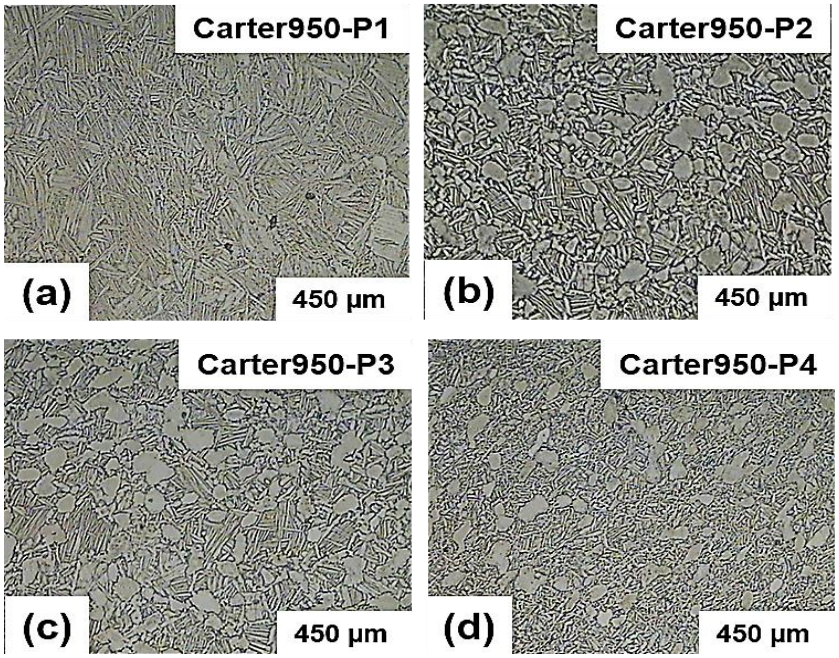

Figure 169: Micrographic images of (a) P1, (b) P2, (c) P3 and (d) P4 points of the Carter case forged at 950 °C billet temperature

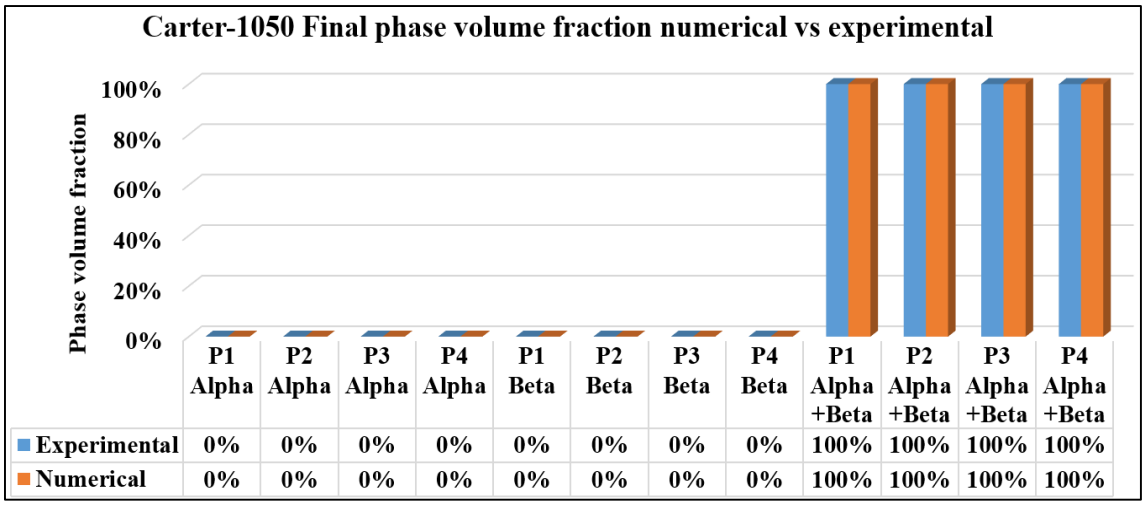

Figure 170: Numerical vs experimental comparison in final phase volume fraction of selected points for the Carter case forged at 1050 °C billet temperature

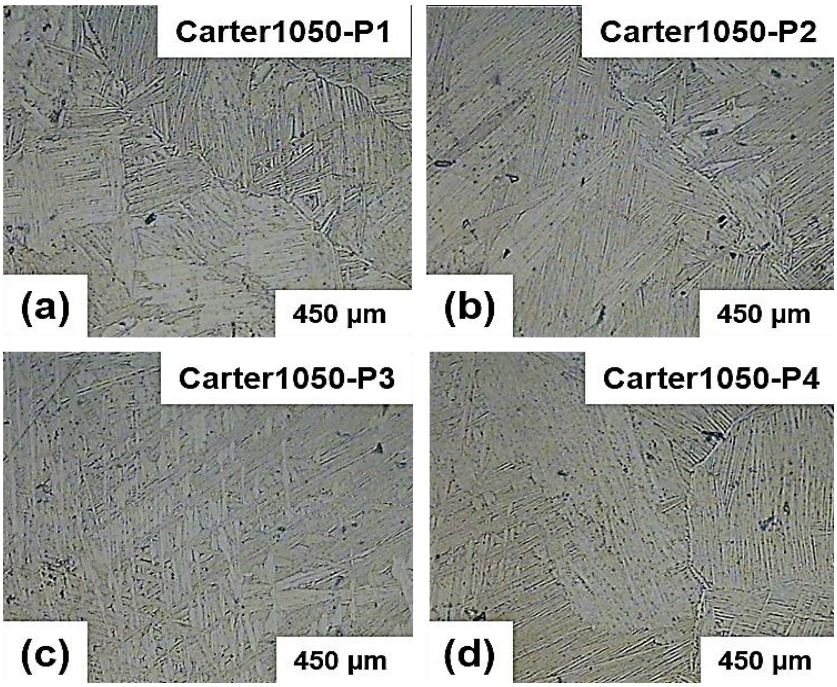

Figure 171: Micrographic images of (a) P1, (b) P2, (c) P3 and (d) P4 points of the Carter case forged at 1050 °C billet temperature

7. Self-consistent modeling

After the numerical characterization has been validated through Titaform project and the experimental data coming from forged part analysis, a study on the modelization of a fully-coupled (Figure 68) constitutive model taking into account both the thermo-mechanical behavior of each allotropic form within the material and the phase transformation kinetics was pursued. The final objective was to use a self-consistent model (SCM) [189, 190] with the aim to find the best solution able to predict the flow stress of biphasic Alpha/Beta Ti-6Al-4V titanium alloy during a hot forging process in both Alpha/Beta and Beta fields with different deformation rates. This approach required to filter the flow stress curve data of the base Ti-6Al-4V to a phasic data set containing the flow stress behavior of each allotropic form. Such a subdivision, in addition to the phase transformation models, could be very useful to predict the correct flow behavior of the mixture material by taking into account the contribution of each phase at varying of temperature and strain rates.

The logic approach in filtering procedure of the phasic flow stress curves was based on previous works developed by Semiatin [64] and Kim [111] about the understanding of the constitutive relations of each microstructural type by means of an estimation of the flow stresses of the individual Alpha and Beta phases in Ti-6Al-4V titanium alloy. These studies are based on measurements of phase compositions and volume fractions in predicting the flow stress of Ti-6Al-4V with an equiaxed Alpha microstructure, considering the stress following the initial strain-hardening transient in constant strain-rate flow curves. Basing on prior studies of Oikawa and Oomori [191-194] about the influence of Aluminum and vanadium content on the strength coefficients of Alpha and Beta phases (Figure 172 - a, b), considering the effects coming from the other alloying elements as negligible. The relations linking the Aluminum content to Alpha phase flow stress (Eq. 57) and Vanadium to Beta phase one (Eq. 58) are shown below.

$$\sigma_{\alpha}^{4.6} = k_{\alpha}(Al)\left[\exp\left(\frac{Q_{\alpha}}{RT}\right)\right]\dot{\varepsilon} \qquad \text{Eq. 57}$$

$$\sigma_{\beta}^{4.2} = k_{\beta}(V)\left[\exp\left(\frac{Q_{\beta}}{RT}\right)\right]\dot{\varepsilon} \qquad \text{Eq. 58}$$

Basing on previous equations and considering the aluminum/vanadium content in each phase of Ti-6Al-4V (Figure 172 – a, b) and their variations with temperature (Figure 172 - c), it was initially found that it is possible to consider the strength of Alpha phase from 2.8 to 3.2 times higher that Beta phase within a temperature range from 800 to 1000 °C [64]. This constant ratio between mechanical properties of both Alpha and Beta phases of the considered material was very useful in defining a constitutive model as function of phase content percentage.

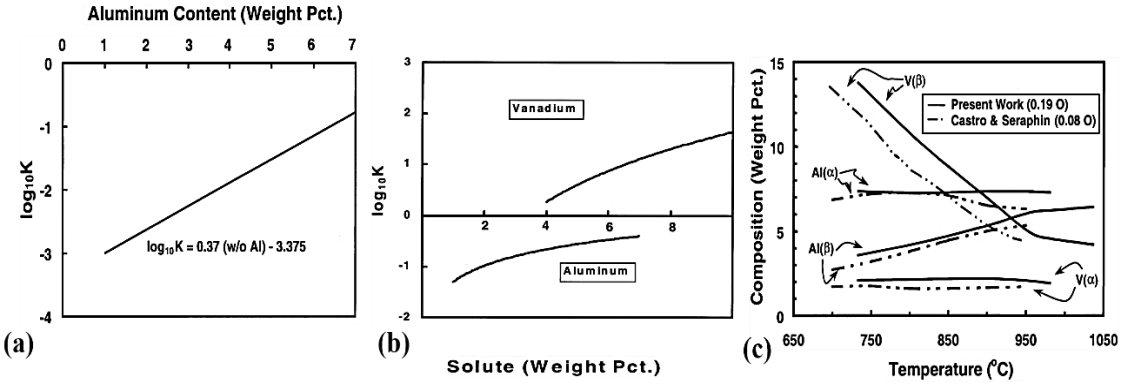

Figure 172: Dependence of the strength coefficient on aluminum or vanadium content for binary Ti-Al alloys hot worked in the Alpha phase field k_α (a) and for binary Ti-X alloys hot worked in the Beta phase field k_β (b) [64]; Electron microprobe analyses of the compositions of the Alpha and Beta phases in Ti-6Al-4V as a function of temperature (c) [64, 195]

Moreover, the previous ratio resulted to be corrected by Kim [111] in 3.5 about in a temperature range from 750 to 950 °C (Figure 173 - b).

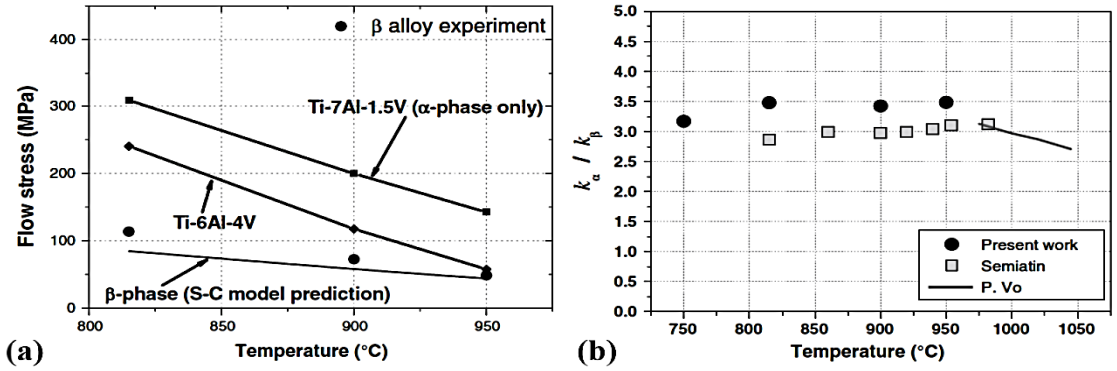

Figure 173: Predicted flow stress of Beta phase obtained from the self-consistent approach (a) [111]; temperature variation of the viscosity-parameter ratio k_α/k_β for the Alpha and Beta phases of Ti-6Al-4V (b) [64, 111]

However, the flow stress prediction is affected by the model itself, which does not take into account the effect of temperature and phase transformations on calculation, confining its use to isothermal conditions only. This approach may be improved by the use of a constitutive model, which, in contrast of equations above (Eq. 57), takes into account both strain rate and temperature effects on phase content on flow behavior of the considered material.

7.1. Phasic flow stress curve SCM determination

Using the previous assumptions, the single phases flow stress curves were filtered by applying the Semiatin's approach, obtaining that each flow stress curve for pure material results from combination of curves of single phases at the same temperature/strain rate conditions, taking into account each phase volume fraction.

As first, the processes specifications and parameters ranges used in forging of titanium alloys were considered, and the initial data set was filtered choosing a temperature range from 800 to 1050 °C while the original strain rate range from 0.001/s to 1000/s was maintained. The grid below (Figure 174) shows the temperature/strain rate range chosen in data filtering and each point represents a flow stress curve.

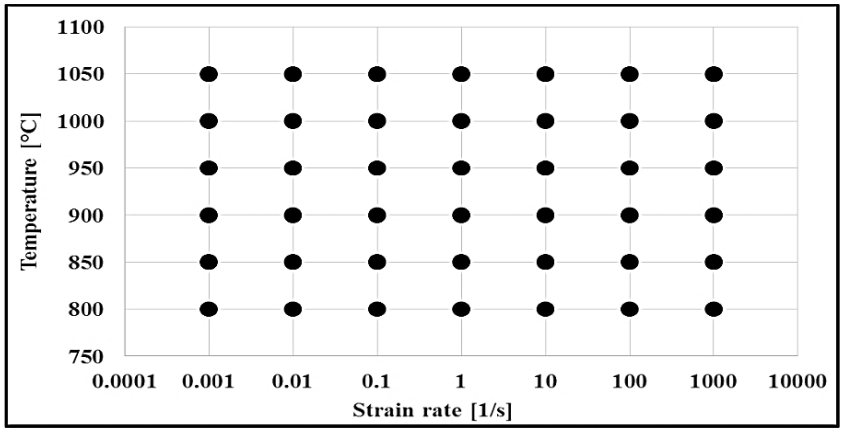

Figure 174: Grid for temperature/strain rate range in flow stress data filtering

Basing on flow stress data for base material, each curve was split considering the contribution of each phase coming from their specific mechanical properties and volume

fraction at the considered temperature. While the flow behavior ratio was defined by Semiatin [64] and Kim [111], the volume fraction determination was referred to the phase kinetics characterization (Section 5.4 - Eq. 51) [196-201] by means of simplified Avrami model [202]. After the improvement in curve fitting for the generalized Avrami model, the initial volume fraction of each phase [134], the Avrami equation (Section 5.4 - Eq. 51) was used to define two different equations in order to calculate the phase amount as function of temperature (Eq. 59, Eq. 60).

$$f_\alpha(T) = \left\{ exp\left[a\left(\frac{T - T_S}{T_E - T_S} \right)^d \right] \right\} - f_{S_\beta} \quad \text{Eq. 59}$$

$$f_\beta(T) = \left\{ 1 - exp\left[a\left(\frac{T - T_S}{T_E - T_S} \right)^d \right] \right\} + f_{S_\beta} \quad \text{Eq. 60}$$

Where T, T_S, T_E, a and d have the same meaning explained in Section 5.4 (Section 5.4 - Eq. 51); $f_\alpha(T)$ represents the Alpha phase volume fraction as function of temperature; $f_\beta(T)$ represents the Beta phase volume fraction as function of temperature; f_{S_β} represents the initial volume fraction of Beta phase.

After that, the definition of phase volume fraction as function of temperature (Eq. 59, Eq. 60) was used, in combination with the Semiatin's approach [64] (Eq. 61) to calculate the flow stress of pure bacterial as sum of contributions of both phases, considering the strength ratio between Alpha and Beta phases constant within the entire temperature range (Eq. 62).

$$\frac{\sigma_\alpha(\varepsilon, \dot{\varepsilon}, T)}{\sigma_\beta(\varepsilon, \dot{\varepsilon}, T)} = \frac{k_\alpha}{k_\beta}(T) \quad \text{Eq. 61}$$

$$\sigma_{Ti-6Al-4V}(\varepsilon, \dot{\varepsilon}, T) = \sigma_\alpha(\varepsilon, \dot{\varepsilon}, T) * f_\alpha(T) + \sigma_\beta(\varepsilon, \dot{\varepsilon}, T) * f_\beta(T) \quad \text{Eq. 62}$$

By making the flow stress of each phase explicit as function of base material and volume fractions, it is possible to obtain the following couple of equations (Eq. 63, Eq. 64).

$$\boldsymbol{\sigma_{\alpha}(\varepsilon,\dot{\varepsilon},T)=\frac{\sigma_{Ti-6Al-4V}(\varepsilon,\dot{\varepsilon},T)}{f_{\alpha}(T)+\frac{f_{\beta}(T)}{\frac{k_{\alpha}}{k_{\beta}}(T)}}}$$ **Eq. 63**

$$\boldsymbol{\sigma_{Ti-6Al-4V}(\varepsilon,\dot{\varepsilon},T)=\sigma_{\alpha}(\varepsilon,\dot{\varepsilon},T)*f_{\alpha}(T)+\sigma_{\beta}(\varepsilon,\dot{\varepsilon},T)*f_{\beta}(T)}$$ **Eq. 64**

The denominator of each one of the previous equations (Eq. 63, Eq. 64) can be assumed as a weight coefficient linking the flow behavior of each microstructure to the base material. In this case, the mechanical properties of each allotropic form and their contributions within the unite volume of base material were considered to carry out the following equations (Eq. 65, Eq. 66), taking into account the phase percentage at the considered temperature.

$$\boldsymbol{w_{\alpha}(T)=\frac{1}{f_{\alpha}(T)+\frac{f_{\beta}(T)}{\frac{k_{\alpha}}{k_{\beta}}(T)}}}$$ **Eq. 65**

$$\boldsymbol{w_{\beta}(T)=\frac{1}{f_{\alpha}(T)*\frac{k_{\alpha}}{k_{\beta}}(T)+f_{\beta}(T)}}$$ **Eq. 66**

Where T, T_S, T_E, A, D, $f_{\alpha}(T)$ and $f_{\beta}(T)$ have the same meaning explained above (Section 5.4 - Eq. 51); $\frac{k_{\alpha}}{k_{\beta}}(T)$ represents the strength ratio between Alpha and Beta phases as function of temperature (assumed equal to 3.5 from 800 to 1050 °C).

Basing on the previous equations (Eq. 65, Eq. 66), the flow stress data for each phase was calculated as the flow stress value at the considered temperature/strain rate value multiplied by the weight coefficients, as shown in the next equations (Eq. 67, Eq. 68).

$$\boldsymbol{\sigma_{\alpha}(\varepsilon,\dot{\varepsilon},T)=\sigma_{Ti-6Al-4V}(\varepsilon,\dot{\varepsilon},T)*w_{\alpha}(T)}$$ **Eq. 67**

$$\boldsymbol{\sigma_{\beta}(\varepsilon,\dot{\varepsilon},T)=\sigma_{Ti-6Al-4V}(\varepsilon,\dot{\varepsilon},T)*w_{\beta}(T)}$$ **Eq. 68**

The equations above (Eq. 67, Eq. 68) were used to reformulate the flow stress curve set of Alpha and Beta phases in the temperature/strain rate range previously described. The graph below (Figure 175) shows the flow behavior of both Ti-6Al-4V alloy and its phases at 800 °C and different strain rates, in which Alpha phase flow stress is slightly higher than pure material while the contribution of Beta phase in flow behavior is more than 3 times lower than Alpha flow stress.

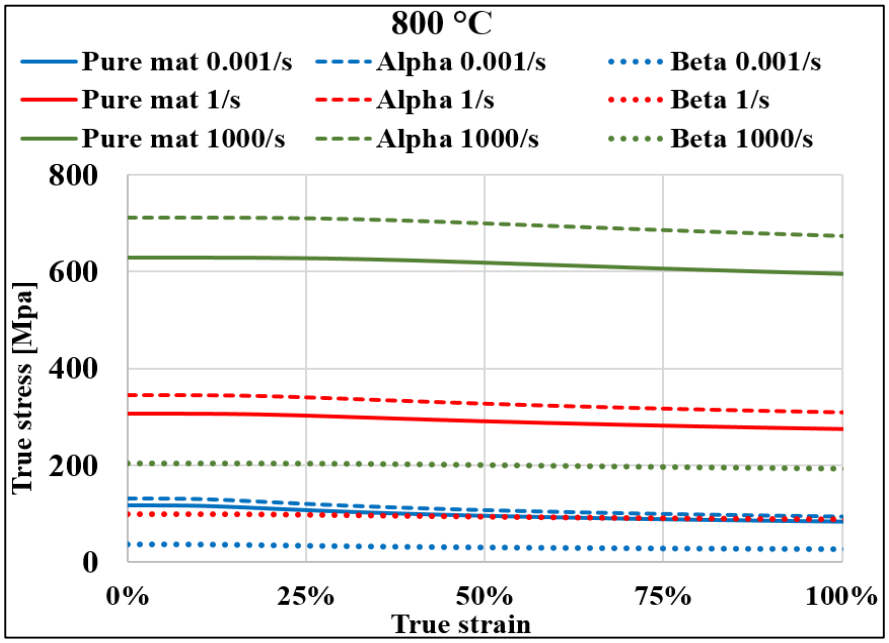

Figure 175: True stress/true strain curves for Ti-6Al-4V pure material, Ti-6Al-4V Alpha phase and Ti-6Al-4V Beta phase at 800 °C and different strain rates

However, it should be considered that the characterization of flow behavior of each phase into a wider temperature range (with respect to its existing field) is possible due to the strength ratio with regard to the base material, and it has to be taken into account in accordance with the phase evolution curve showed below.

It means that as the temperature is close to the Beta-transus value the mechanical properties of base material match the Beta phase ones. This result is shown in the following images (Figure 176, Figure 177, Figure 178) in which the contribution of each phase with respect to the flow behavior of base material is proportional to its volume fraction with respect to temperature.

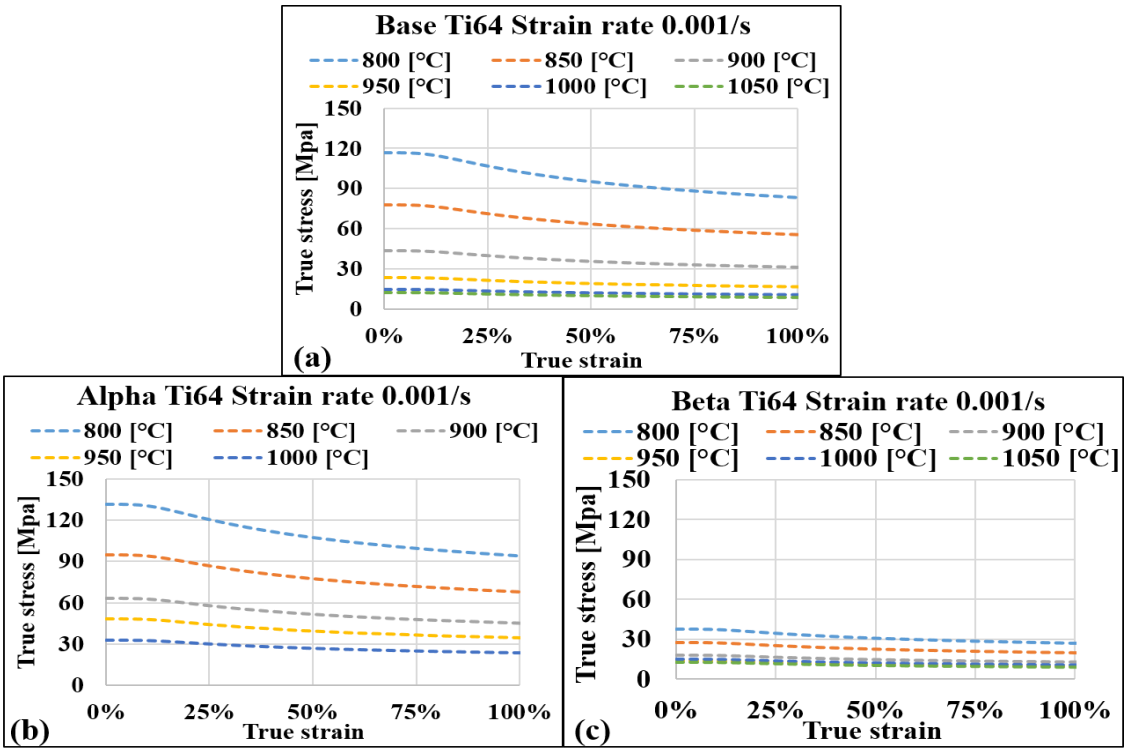

Figure 176: True stress/true strain curves for the (a) base material, (b) Alpha phase and (c) Beta phase of Ti-6Al-4V titanium alloy from 800 to 1050 °C and strain rates of 0.001/s

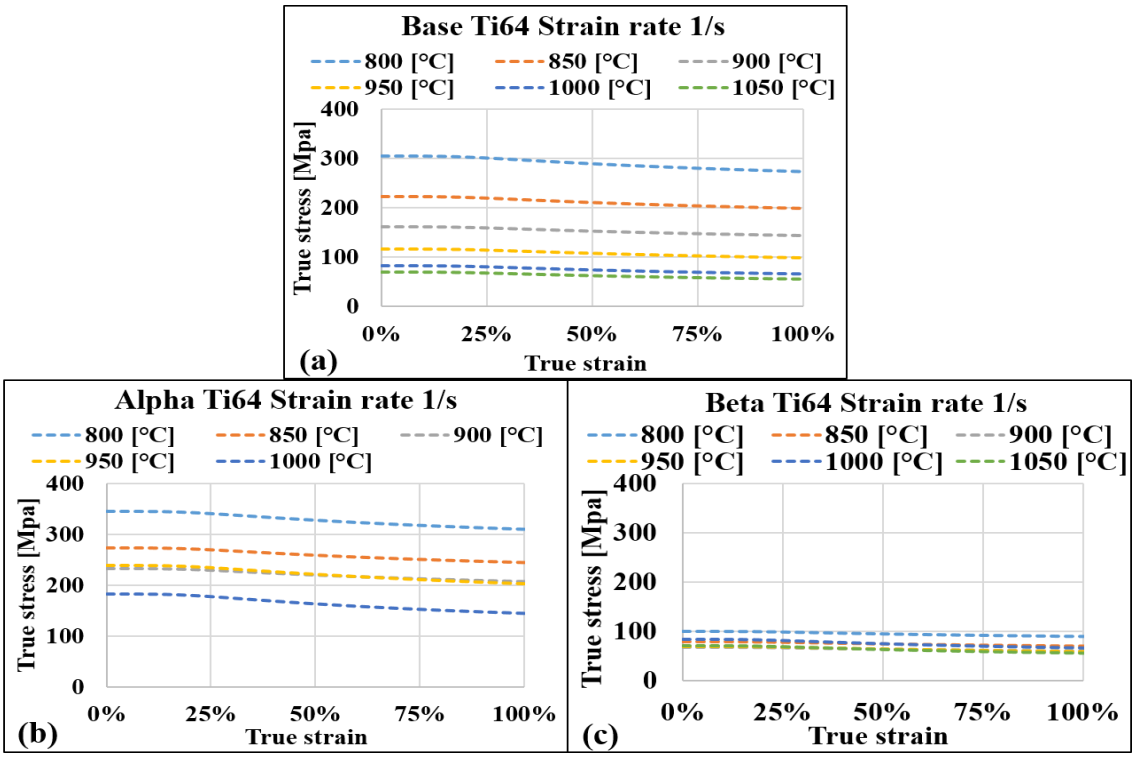

Figure 177: True stress/true strain curves for the (a) base material, (b) Alpha phase and (c) Beta phase of Ti-6Al-4V titanium alloy from 800 to 1050 °C and strain rates of 1/s

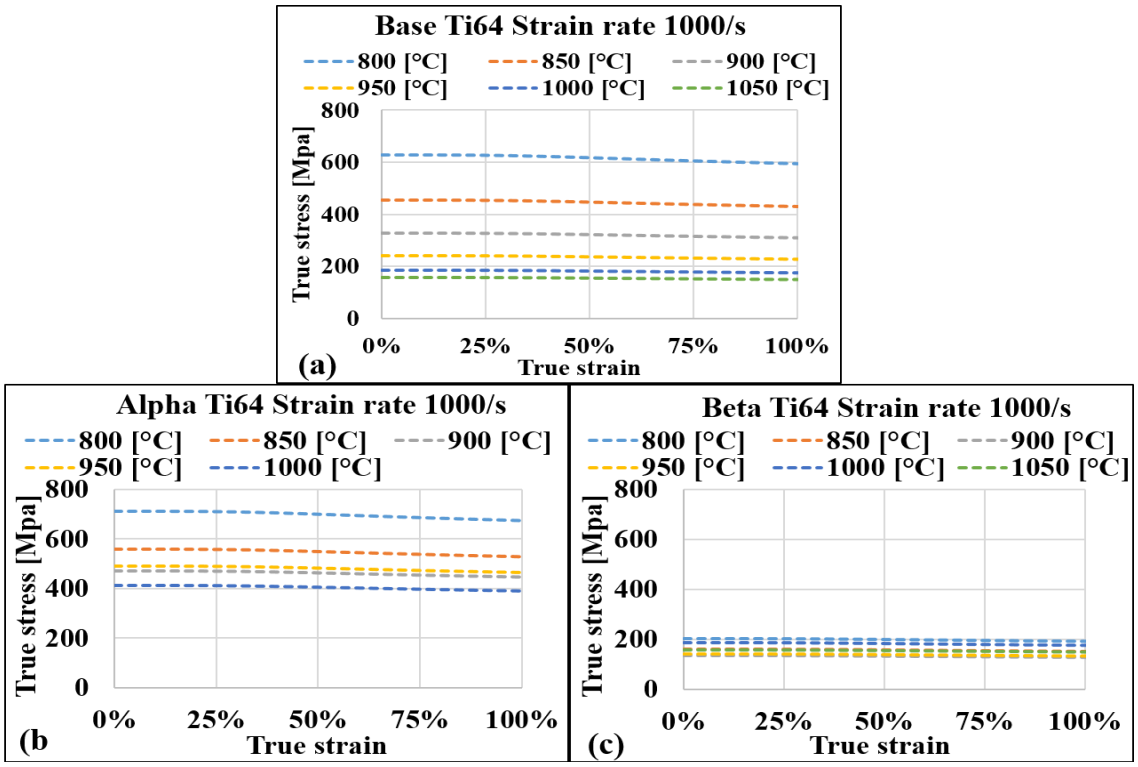

Figure 178: True stress/true strain curves for the (a) base material, (b) Alpha phase and (c) Beta phase of Ti-6Al-4V titanium alloy from 800 to 1050 °C and strain rates of 1000/s

Once the phasic flow stress filtering was obtained a further simulation campaign, based on isothermal hot compression already used in validation if previous flow stress curve set (Section 6.2), was carried out with the aim to test the quality of prediction.

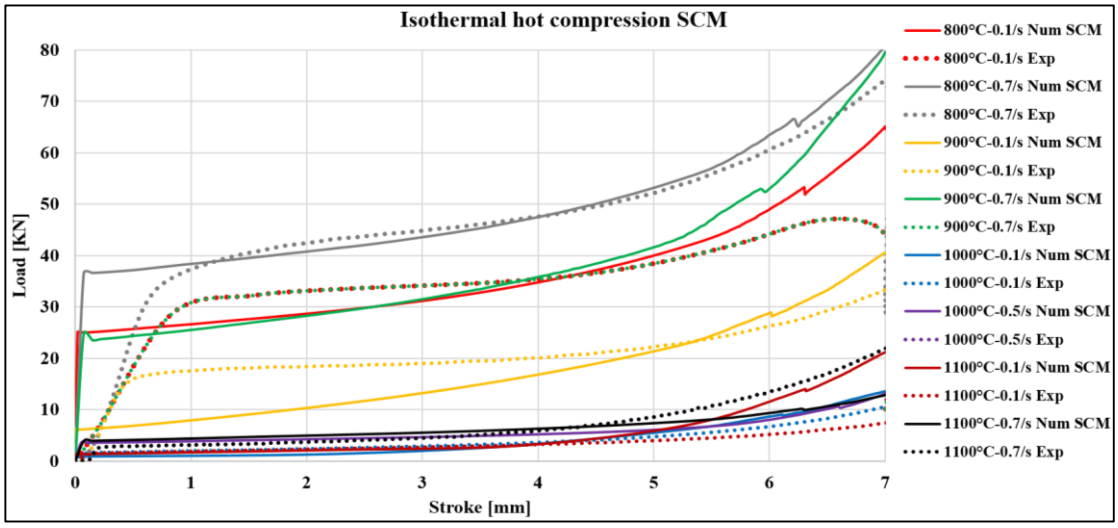

Figure 179: Comparison between experimental and numerical SCM load/stroke data for isothermal hot compression of Ti-6Al-4V cylindrical billets

This new material definition used a fully coupled computation, which connects the mechanical behavior of each phase to the phase transformation kinetics.

Results showed a slight improvement in load/stroke curve prediction with respect to the non-phasic material characterization.

7.2. Johnson-Cook SCM modelization

Starting from the phasic subdivision of the flow stress curves for Ti-6Al-4V alloy previously obtained, the generalized Johnson-Cook equation [85] (Eq. 69) was used to obtain a curve fitting of the true stress/true strain curves in order to define SCM based on two equations defining the flow behavior of each phase.

$$\bar{\sigma} = (A + B\bar{\varepsilon}^{n})\left\{\left[1 + Cln\left(\frac{\dot{\bar{\varepsilon}}}{\dot{\bar{\varepsilon}}_0}\right)\right]\left(\frac{\dot{\bar{\varepsilon}}}{\dot{\bar{\varepsilon}}_0}\right)^{\alpha}\right\}\left\{\left[D_0 exp\left[k(T - T_b)^{\beta}\right]\right] - \left[E\left(\frac{T - T_r}{T_m - T_r}\right)^{m}\right]\right\} \quad \text{Eq. 69}$$

Where A is the yield stress, B is the strain hardening modulus, n is the strain hardening exponent, C is the strain rate sensitivity modulus, $\dot{\bar{\varepsilon}}_0$ is the reference strain rate, α is the strain rate sensitivity exponent, D_0 is the temperature effect modulus, k is the temperature effect exponential modulus, β is the temperature effect exponent, T_b a reference temperature, T_r is the room temperature, T_m is the melting temperature, E is the thermal softening modulus, m is the thermal softening exponent.

The calibration was carried out considering the MSE between the experimental data coming from literature research and the predicted flow stress coming from the use of the two obtained parameters set for JC equation, taking into account the weight of each phase in the base material flow behavior (Eq. 61). The model calibration scheme is showed in the image below (Figure 180). The definition of this equation within a wide range of thermo-mechanical conditions could represents a serious problem due to variability in material behavior with temperature and strain rate, especially in the case of multiphasic materials in which there is a great difference in mechanical properties of each phase.

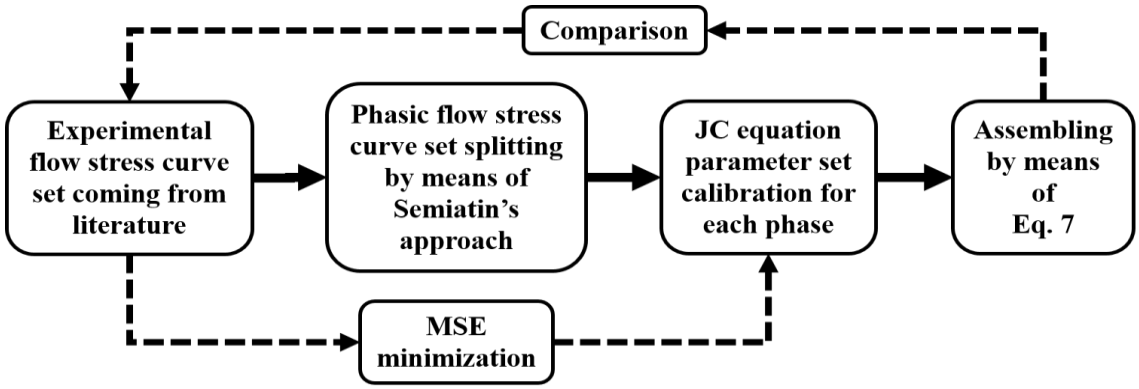

Figure 180: JC self-consistent model calibration scheme

Due to this inconvenience, a further classification of thermo-mechanical conditions in very-slow, slow and high strain rates was carried out in order to obtain a good curve fitting as function of the forging equipment within the conventional temperature range of forging processes for Ti-6Al-4V (Table 10).

Table 10: Process parameters classification in curve fitting for JC SCM

Equipment/ application	JC Self-consistent model process parameters windows	
	Temperature range [°C]	Strain rate range [1/s]
Very slow forming	800 - 1050	0.001 - 0.1
Hydraulic press	800 - 1050	0.1 -10
Mechanical press	800 - 1050	10 - 1000

The model calibration was based on previous studies concerning both the approach in parameters calculation [98] and coefficients measurement [74, 81, 203, 204] in order to find the correct way in assignment of a value without affecting its physical meaning. Considering that each equation has to work on a specific temperature/strain rate range, the regulation needed the use of average values for some parameters while the calculation of some exponent was reached by the use of a specific formula as suggested in literature [98]. In the end, each phase of Ti-6Al-4V was considered as an independent material in assigning the specific values for each JC equation. It means that all comparison in coefficient calibration were done considering the flow stress curve set of each phase.

7.2.1. *A*-parameter determination

The value of *A* parameter is referred to the yield stress of the considered material but its definition cannot be linked to a single value of a single flow stress curve because it could difficult to match a group of experimental curves in the case of process parameters far from the calibration conditions. Due to this inconvenience, the range for yield stress in calibration of *A* parameter for each phase was choses among the entire range of yield stress values of the considered phase within the considered temperature/strain rate range (Table 11).

Table 11: A parameter value range for JC SCM

	JC Self-consistent model A parameter value ranges [MPa]					
	Very slow forming		Hydraulic press		Mechanical press	
	Alpha	Beta	Alpha	Beta	Alpha	Beta
Max	264.58	75.59	448.35	128.10	710.89	203.11
Min	48.09	12.43	151.56	39.31	296.96	84.85

7.2.2. *B*-parameter determination

The determination of *B* parameter was based on minimization of MSE between the calculated flow stress curves previously explained and the predicted JC interpolation on a large strain range, from 0 to 4.

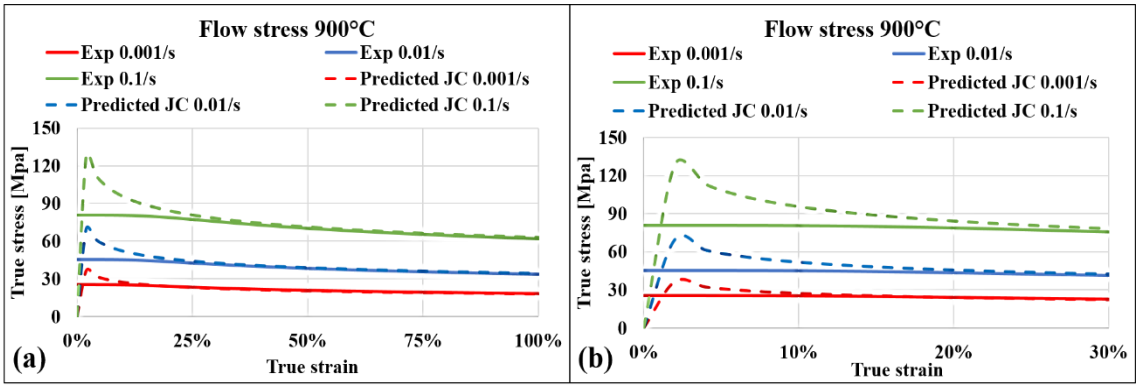

Figure 181: Example of curve fitting for experimental flow stress and JC predicted flow stress obtained at 900 °C and different strain rates (a) and magnification of the same prediction at very low strain (b).

In this case, the measure of the maximum error reached during the curve fitting was not considered due to the large errors obtained at very low strain (Figure 181).

7.2.3. Strain hardening exponent determination

The strain-hardening exponent *n* is considered to be numerically equal to the uniform plastic strain for materials which exhibit a power law true stress/true strain relation resulted from a balance between hardening mechanisms depending mainly on strain and softening mechanisms depending mainly on time [205]. Several researchers conducted the study about the selection of the value for this parameter and it is possible to find many literature data about strain hardening sensitivity for Ti-6Al-4V [81, 99, 100, 206-209] at different strain rates and temperatures considering the influence of strain reached during isothermal compression tests.

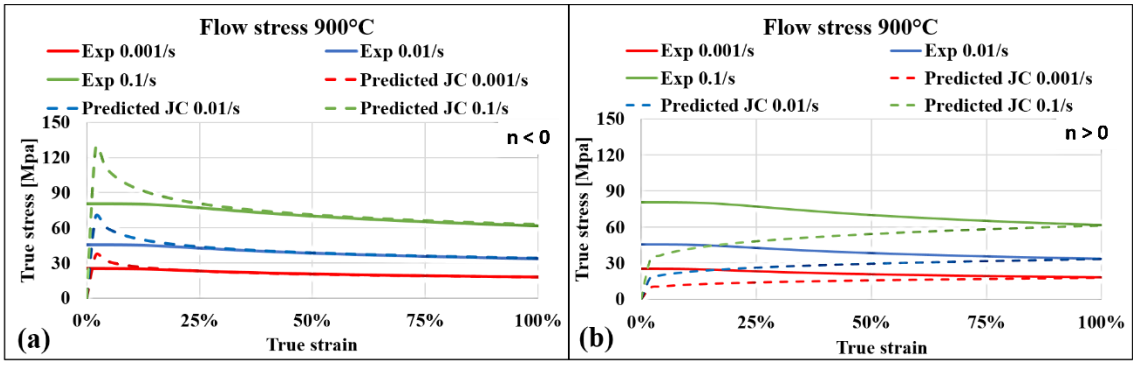

Figure 182: The determination of value for strain hardening exponent was carried out by means of the classical approach [205]. The ratio between the flow stress at selected conditions on the entire strain range and the flow stress at zero strain (Eq. 70), maintaining both temperature and strain rate constant, was used to calculate the ratio between logarithmic stress and strain (Eq. 71)

In this scenario, the study conducted by Luo et al. [81] is particularly useful due to definition in a similar temperature range of hot forging processes of Ti-6Al-4V and propose different value of strain hardening sensitivity for different strain rates, including negative values (Figure 36).

However, keeping in mind the flow softening occurring at high temperature, only negative values for *n* parameter determine a concavity that best fits the experimental curves, especially in the case of a power law with both *A* and *B* positive parameters.

In fact, if positive strain hardening is used, the comparison with experimental flow stress at low strain shows an error greater than 50% (Figure 182). The image below shows the difference in curve fitting using negative and positive value for strain hardening coefficient. The use of negative values (Figure 182 - a) provide a better prediction of experimental data with a big error for very low strain only, while the most of flow stress curves is followed with a good quality. On the other hand, if positive value (having the same modulus of negative case) is used, the prediction results to have a poor quality with a high MSE on the whole strain range (Figure 182 - b).

$$\boldsymbol{R_n(\varepsilon) = \frac{\sigma(\varepsilon)}{\sigma(\varepsilon_0)}\Big|_{\dot{\varepsilon},T}} \qquad \textbf{Eq. 70}$$

$$\boldsymbol{n(\varepsilon) = \frac{log R_n(\varepsilon)}{log \varepsilon}\Big|_{\dot{\varepsilon},T}} \qquad \textbf{Eq. 71}$$

Where $R_n(\varepsilon)$ is the ratio between the stress at selected strain and the stress at 0 strain at fixed temperature and strain rate, $\sigma(\varepsilon)$ is the stress at selected strain, $\sigma(\varepsilon_0)$ is the stress at 0 strain, $n(\varepsilon)$ is the strain hardening exponent as function of strain at fixed temperature and strain rate.

The previous equation allowed calculate the strain-hardening exponent for at varying of strain for each temperature/strain rate condition within the considered range of parameters (Table 10). If the average value at fixed temperature or strain rate is used, the evolution of *n* parameter as function of temperature/strain rate can be obtained (Figure 183). Considering that each phasic flow stress curve set was created as a fixed proportion of base material flow stress data, very small variations between strain hardening of Alpha and Beta were found. The image below (Figure 183) shows that both temperature and strain rate affect the strain hardening exponent, from 3 to – 4 (Figure 183 - b), with positive values at strain lower than 1 and negative ones at higher strain. However, at varying of strain rate (Figure 183 - b), the strain hardening changes significantly with

lower values at high strain rate and vice versa, while in the case of temperature (Figure 183 - a) the difference among the different curves is extremely reduced.

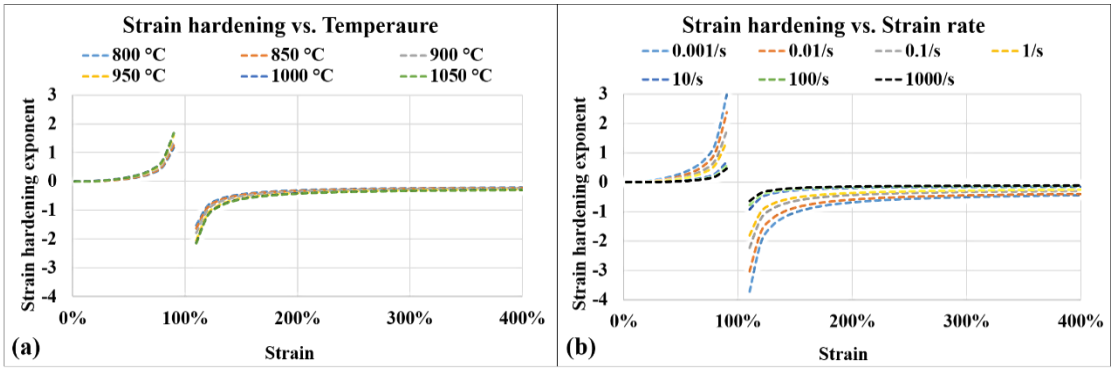

Figure 183: Strain hardening exponent as function of temperature (a) and strain rate (b) for Alpha and Beta phase of Ti-6Al-4V alloy

If the average value of strain hardening at fixed strain rate/temperature is considered, it is observed an almost constant behavior at higher strain rates with values from -0.07 at 800 °C to -0.09 at 1050 °C. While for middle values of strain rate, corresponding to the parameters window of hydraulic press applications, the variability is increased with a range from -0.1 at 800 °C to -0.24 at 1050 °C. For the lowest strain rate value the behavior is constant with a value of -0.27 about (Figure 184).

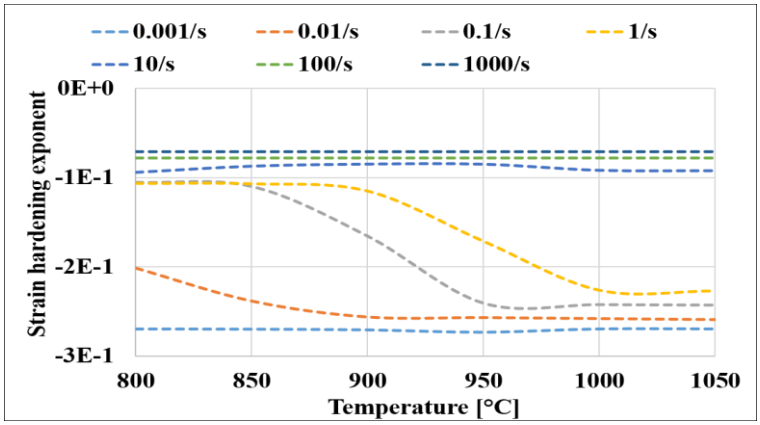

Figure 184: Strain hardening exponent at varying of temperature and strain rate for Alpha and Beta phase of Ti-6Al-4V

In the end, an average value for both Alpha and Beta phases in the temperature/strain rate range of each application case (Table 11) was used in order to have a single JC. The table below (Table 12) shows a summary of the selected values.

Table 12: Strain hardening exponent range for JC SCM

JC Self-consistent model n parameter value ranges					
Very slow forming		Hydraulic press		Mechanical press	
Alpha	Beta	Alpha	Beta	Alpha	Beta
-0.228	-0.233	-0.135	-0.144	-0.078	-0.079

7.2.4. Strain rate sensitivity modulus determination

The choice of strain rate sensitivity modulus should be related to the dynamic stress-strain curves, using for instance a Split Hopkinson Pressure Bar (SHPB), in which the experimental load displacement curve is reduced into a strain-stress curve at room temperature. However, basing on prior results [99, 100, 206-208] about parameterization of Johnson-Cook equation, the estimation for the coefficient C was carried out by best fitting the dynamic experimental true stress/true strain curves for base material to the JC model with the already obtained parameters, considering a range between -1 and 0 in order to obtain that.

7.2.5. Reference strain rate determination

The choice of the reference strain rate is sometimes made as a matter of convenience, or possibly due to a misunderstanding of the role of this parameter. It is often thought this parameter simply plays the role of making the time units in the strain rate term non-dimensional. The important part of selecting this parameter is to note that it must be consistent with the choices of the yield and hardening parameters, like *A* and *B*. However, the value of reference strain rate $\dot{\bar{\varepsilon}}_0$ is often assumed as 1/s, accordingly with the range of validity of the JC model into the quasi-static regime. In fact, is different values of reference strain rate are used, it may be lose the strain rate sensitivity at varying of deformation speed. Due to this assumption, it could be acceptable to use the standard value all cases.

7.2.6. Strain rate sensitivity exponent determination

The strain rate sensitivity exponent depends on different properties like grain size, phase volume fraction and temperature.

Observing its evolution at high temperature, as proposed by Luo et al. [81], tends to increase with the increasing of temperature, with oscillations coming from variation of grain size, while and the maximum value is obtained close to the Beta-transus temperature [210]. This behavior can be related to microstructural properties of the material in which the phase volume fraction is function of temperature so that at higher temperature it corresponds a higher percentage of Beta phase as well as a higher strain rate sensitivity due to the mechanisms of grain boundary sliding temperature. Moreover, the strain rate sensitivity exponent m decreases with the increasing of strain rate at the deformation temperatures (Figure 36).

The determination of value for strain hardening exponent was carried out by means of the same approach used for determination of strain hardening [81, 205]. The ratio between the flow stress at selected conditions on the entire strain range and the flow stress at unit strain rate (Eq. 72), maintaining both temperature and strain constant, was used to calculate the ratio between logarithmic stress and strain rate (Eq. 73).

$$\boldsymbol{R_n(\varepsilon) = \frac{\sigma(\varepsilon)}{\sigma(\varepsilon_0)}\Big|_{\dot{\varepsilon},T}} \qquad \textbf{Eq. 72}$$

$$\boldsymbol{n(\varepsilon) = \frac{logR_n(\varepsilon)}{log\varepsilon}\Big|_{\dot{\varepsilon},T}} \qquad \textbf{Eq. 73}$$

Where $R_\alpha(\dot{\varepsilon})$ is the ratio between the stress at selected strain rate and the stress at reference strain rate at fixed temperature and strain, $\sigma(\dot{\varepsilon})$ is the stress at selected strain rate, $\sigma_{\dot{\varepsilon}_0}$ is the stress at reference strain rate, $\alpha(\dot{\varepsilon})$ is the strain hardening exponent as function of strain at fixed temperature and strain.

If the average value at fixed temperature or strain rate is used, the evolution of strain rate sensitivity as function of temperature/strain rate can be obtained (Figure 185). As it was found for strain hardening, the strain rate sensitivity behavior at varying of temperature and strain rate showed negligible differences between Alpha and Beta

phases. In this case, the image below (Figure 185) shows a similar range in variation of strain rate sensitivity as function of temperature and strain rate, with an increasing value as the temperature increases (Figure 185 - a) and very similar behavior for temperatures above Beta-transus (Figure 185 - b). While, it sensitivity shows a regular increasing of value with decreasing of strain rate (Figure 185 - b).

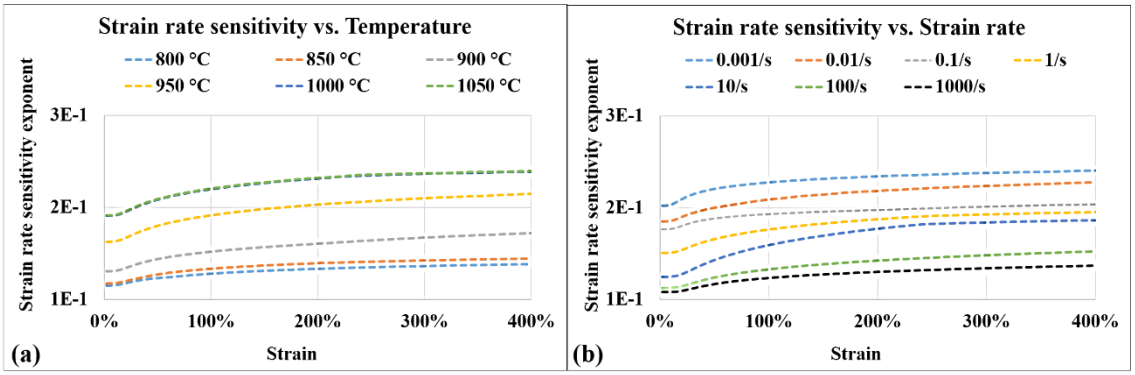

Figure 185: Strain rate sensitivity exponent as function of temperature (a) and strain rate (b) for Alpha and Beta phase of Ti-6Al-4V alloy

Considering the average value of strain rate sensitivity at fixed strain rate/temperature, it is observed a similar behavior for all strain rates above 0.1/s in the temperature range from 800 °C to 850 °C with all values close to 0.11 and an evolution as swift as the strain rate is lower (Figure 186).

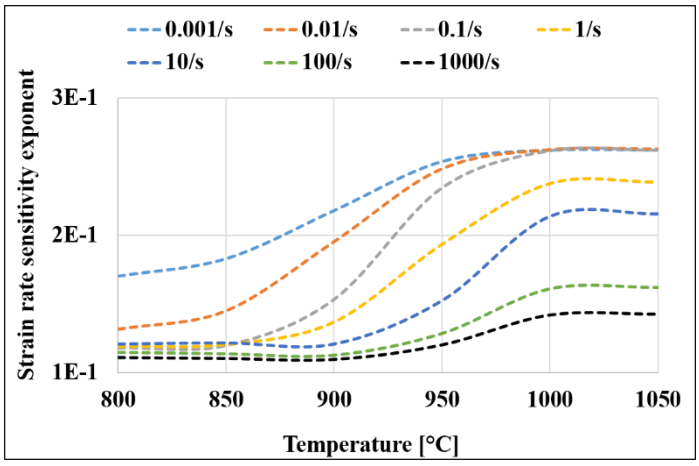

Figure 186: Strain rate sensitivity exponent at varying of temperature and strain rate for Alpha and Beta phase of Ti-6Al-4V

As considered for strain hardening exponent, an average value of strain rate sensitivity for both Alpha and Beta phases in the temperature/strain rate range of each application case (Table 11) was used in order to have a single JC. The table below (Table 13) shows a summary of the selected values.

Table 13: Strain rate sensitivity exponent range for JC SCM

JC Self-consistent model α parameter value ranges					
Very slow forming		Hydraulic press		Mechanical press	
Alpha	Beta	Alpha	Beta	Alpha	Beta
0.197	0.208	0.161	0.174	0.130	0.137

7.2.7. Thermal modulus, exponential modulus and exponent determination

During the literature research, no value or value ranges was found to select properly both D_o, k and β parameters thermal effect law. However, considering that the thermal law is usually set equal to 1, it was decided to extrapolate the value of each single parameter in order to obtain a value of thermal law from 0 to 1 due to the best curve fitting obtained using this logic. Basing on this assumption, the thermal effect modulus D_o and the thermal effect exponential one k were determined using curve fitting on a range of values from 0 to 1, while the thermal effect exponent β was calculated on a range varying from -15 to 0. The same ranges were used for both Alpha and Beta phases.

7.2.8. Thermal softening modulus and reference temperatures determination

As well as the thermal law parameter, the thermal softening modulus E was calculated considering that it is usually set equal to 1 in the general approach of JC equation. However, to improve the quality of curve fitting with respect to experimental curves, I was considered to vary the value from 0 to 1.

While, the choice of reference temperature t_b was based on the phase transformation behavior of Ti-6Al-4V alloy. In fact, considering that the mechanical response of base

material comes from the both phase volume fractions and their flow stress behavior; the change can be related to the Avrami curve for Alpha-to-Beta phase transformation curve (Section 5.4 - Eq. 51). It means that, observing the phase change equations (Eq. 59, Eq. 60), there is a balance up 700 °C about in mechanical properties of material due the invariability of phase, while after that temperature a new degree of freedom is added to the system. Basing on this assumption the reference temperature was chosen equal to 700 °C for both phases.

In the end, the room temperature and the melting temperature were chosen equal to 25 °C and 1660 °C respectively on the base of thermo-physical properties of Ti-6Al-4V alloy.

7.2.9. Thermal softening exponent determination

The thermal softening exponent depends on depends on flow stress behavior at varying of temperature. Usually, it could be negligible when isothermal low temperature applications are considered, while in the case of high strain rates and high temperatures its rule is predominant in order to take into account the reduction in mechanical properties of the selected material. Several studies were conducted on the determination of parameter set and the proper value of thermal softening exponent [99, 207, 211-215] but the most of analysis were based on machining applications and high strain rate cases only.

The classical approach in thermal softening exponent determination is based on the comparison between the flow stress at the considered temperature and the flow stress at room temperature by means of the last of following equations (Eq. 74, Eq. 75, Eq. 76).

$$m(T) = \left. \frac{log[1 - R_m(T)]}{log\, T^*} \right|_{\varepsilon, \dot{\varepsilon}} \quad \text{Eq. 74}$$

$$R_m(T) = \left. \frac{\sigma(T)}{\sigma(T_r)} \right|_{\varepsilon, \dot{\varepsilon}} \quad \text{Eq. 75}$$

$$T^* = \frac{T - T_r}{T_m - T_r} \quad \text{Eq. 76}$$

Where $R_m(T)$ is the ratio between the stress at selected temperature and the stress at room temperature at fixed strain and strain rate, $\sigma(T)$ is the stress at selected temperature, $\sigma(T_0)$ is the stress at room temperature, $m(T)$ is the thermal softening exponent as function of temperature at fixed strain and strain rate, T^* is the normalized temperature, T_r and T_m are the reference temperature and the melting temperature of the selected material respectively.

Using the classical equation (Eq. 74) the average value of thermal softening at fixed temperature or strain rate, the following graphs (Figure 187) were obtained, in order to show the evolution of the calculated parameter. The results show a small range of values at varying of temperature, with a variability form 0.3 and 0.55 (Figure 187 - a), while in the case of thermal softening related to strain rate the range of values is wider with a variability from 0.05 to 0.87 (Figure 187 - b). As occurred for the other calculated parameters, a small the difference in values of Alpha and Beta thermal softening was found.

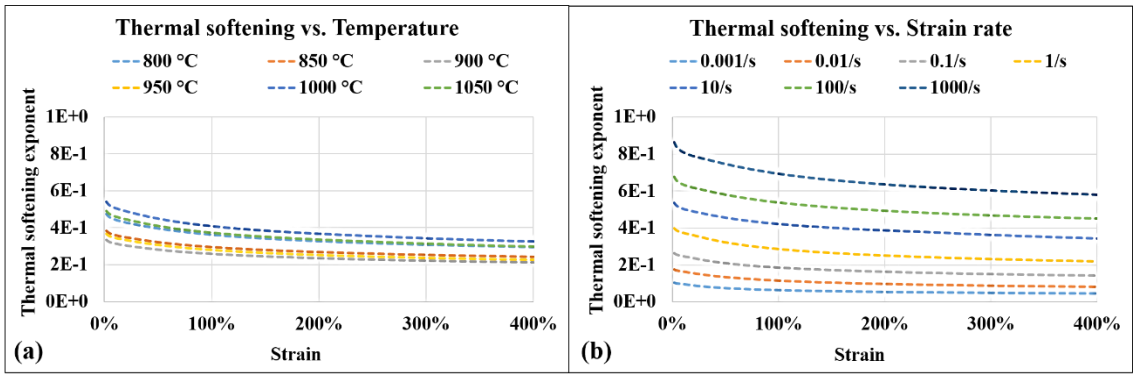

Figure 187: Thermal softening exponent as function of temperature (a) and strain rate (b) for Beta phase of Ti-6Al-4V alloy

In the end, considering the average value of thermal softening exponent at fixed strain rate/temperature, it is observed a similar behavior for all strain rates above 0.1/s in the temperature range from 800 °C to 850 °C with all values close to 0.11 and an evolution as swift as the strain rate is lower (Figure 186).

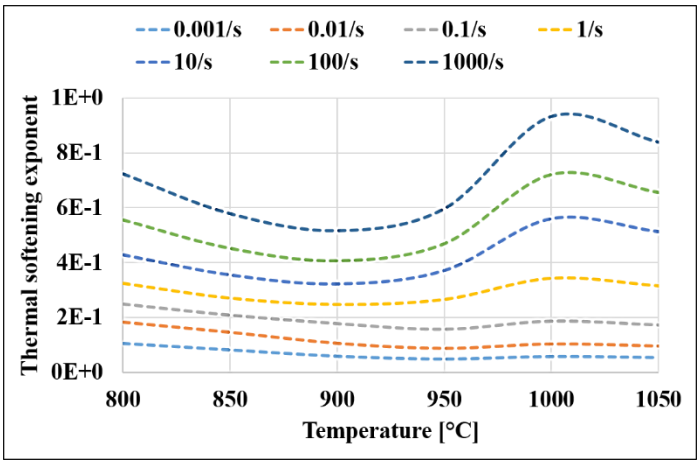

Figure 188: Thermal softening exponent at varying of temperature and strain rate for Beta phase of Ti-6Al-4V

As considered for strain hardening exponent, an average value of strain rate sensitivity for both Alpha and Beta phases in the temperature/strain rate range of each application case (Table 10) was used in order to have a single JC. The table below (Table 14) shows a summary of the selected values.

Table 14: Thermal softening exponent range for JC SCM

JC Self-consistent model m parameter value ranges					
Very slow forming		Hydraulic press		Mechanical press	
Alpha	Beta	Alpha	Beta	Alpha	Beta
0.131	0.130	0.304	0.298	0.533	0.532

After calculating all derivable parameters, an interpolation routine was created using MS-Excel™ in order to calibrate the rest of coefficients of the JC equation and finally obtain a complete set of parameters valid for all selected application cases (Table 10). The calculation of the rest of parameters of the JC equation was carried out considering the initial logic scheme (Figure 180) adopted for the SCM approach, so that the initial set of flow stress curve built from literature data was used to obtain a feedback from comparison between model prediction and experimental data. In this case, the data interpolation was continued until the mean square error between the experimental curves and the JC model was under 15%.

A comprehensive table resuming all calculated and derivative parameters and coefficients for all application cases is show below (Table 15).

Table 15: Parameters summary for generalized JC SCM

Parameter	JC Self-consistent model parameters					
	Very slow forming		Hydraulic press		Mechanical press	
	Alpha	Beta	Alpha	Beta	Alpha	Beta
A - Yield stress [MPa]	48	75	152	40	458	95
B - Strain hardening modulus [MPa]	96	112	1490	183	308	256
n - Strain hardening exponent	-0.228	-0.233	-0.135	-0.144	-0.078	-0.079
C - Strain rate sensitivity modulus	0.04	0.05	0.01	0.06	0.001	0.0012
$\dot{\varepsilon_0}$ - Reference strain rate [1/s]	1					
α - Strain rate sensitivity exponent	0.197	0.208	0.161	0.174	0.130	0.137
D_0 - Temperature effect modulus	0.17	0.18	0.008	0.075	0.01	0.06
k - Temperature effect exponential modulus	0.64	0.60	0.06	0.46	0.24	0.20
β - Temperature effect exponent	-6.78	-7.86	-6.72	-11.75	-8.84	-11.79
T_b - Reference temperature [°C]	700					
T_r - Room temperature [°C]	25					
T_m - Melting temperature [°C]	1660					
E - Thermal softening modulus	-4 E-3	-1 E-6	-7.7 E-4	-2.1 E-3	-3.9 E-3	-2.1 E-3
m - Thermal softening exponent	0.131	0.130	0.304	0.298	0.533	0.532

7.2.10. Model results and discussions

The comparison with experimental data (Figure 189, Figure 190, Figure 191) showed a good agreement in curve matching for most of curves, with very high quality of

interpolation obtained for higher temperatures. The best fitting was obtained for very low strain rates (Figure 189) with the exception of the colder case at 800 °C. In particular, the power law contribution revealed a high peak of stress for very low strain and the negative strain hardening was not sufficient to compensate the rapid decreasing in flow stress.

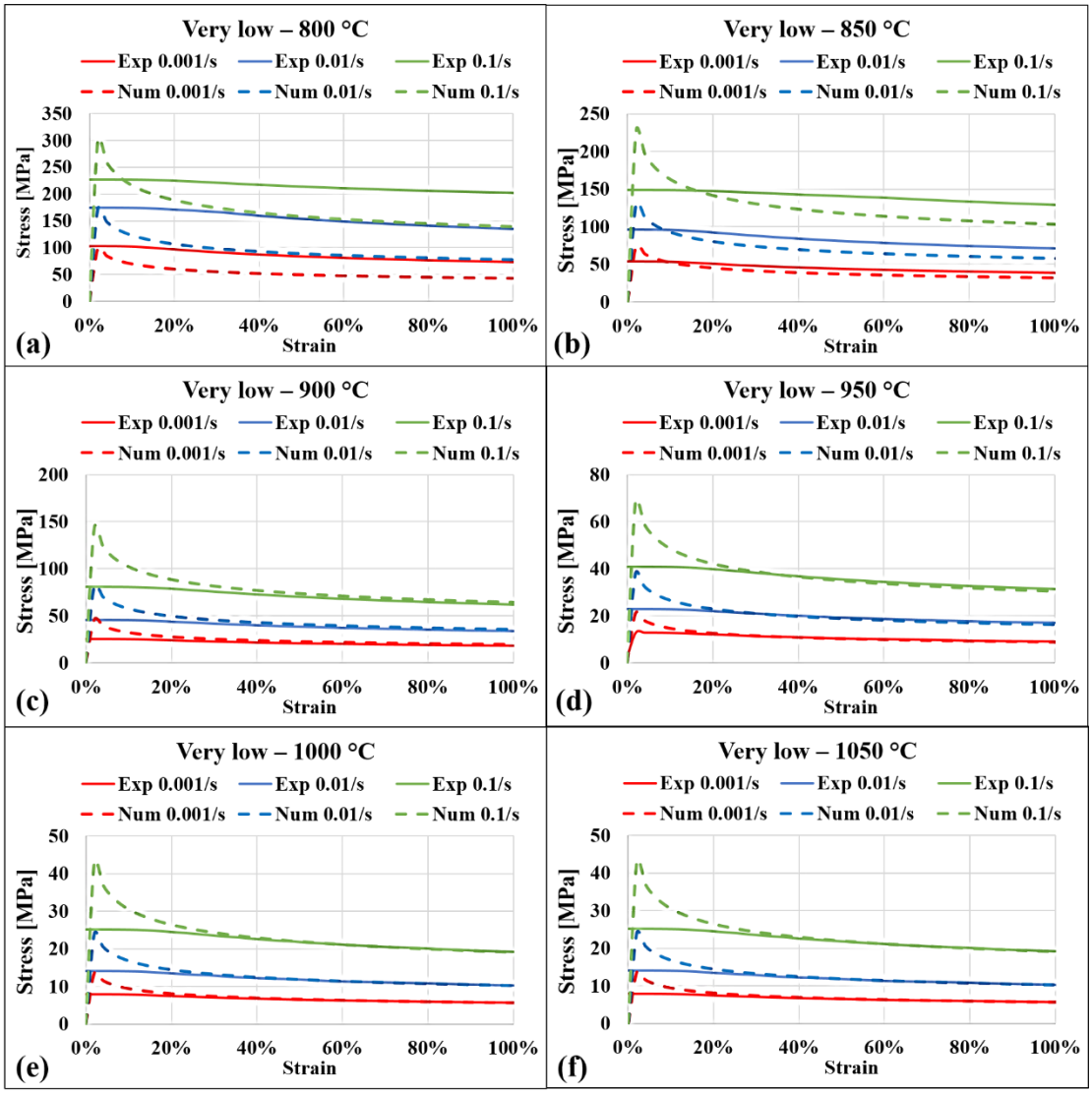

Figure 189: Experimental and predicted flow stress curves using the JC SCM modelization at very low strain rates and (a) 800 °C, (b) 850 °C, (c) 900 °C, (d) 950 °C, (e) 1000 °C and (f) 1050 °C

The hydraulic press case (Figure 190) displayed a similar quality in curve fitting with a mean error at 16% about at 800 and 850 °C while better results were found above 850 °C. In this case, the power law carried out closer values at lower strain with respect to the experimental curves and higher accuracy in predicting the strain effect. However, the

prediction was influenced with temperature variation so that the initial peak of stress was increased at higher temperature, producing a larger error at initial strain.

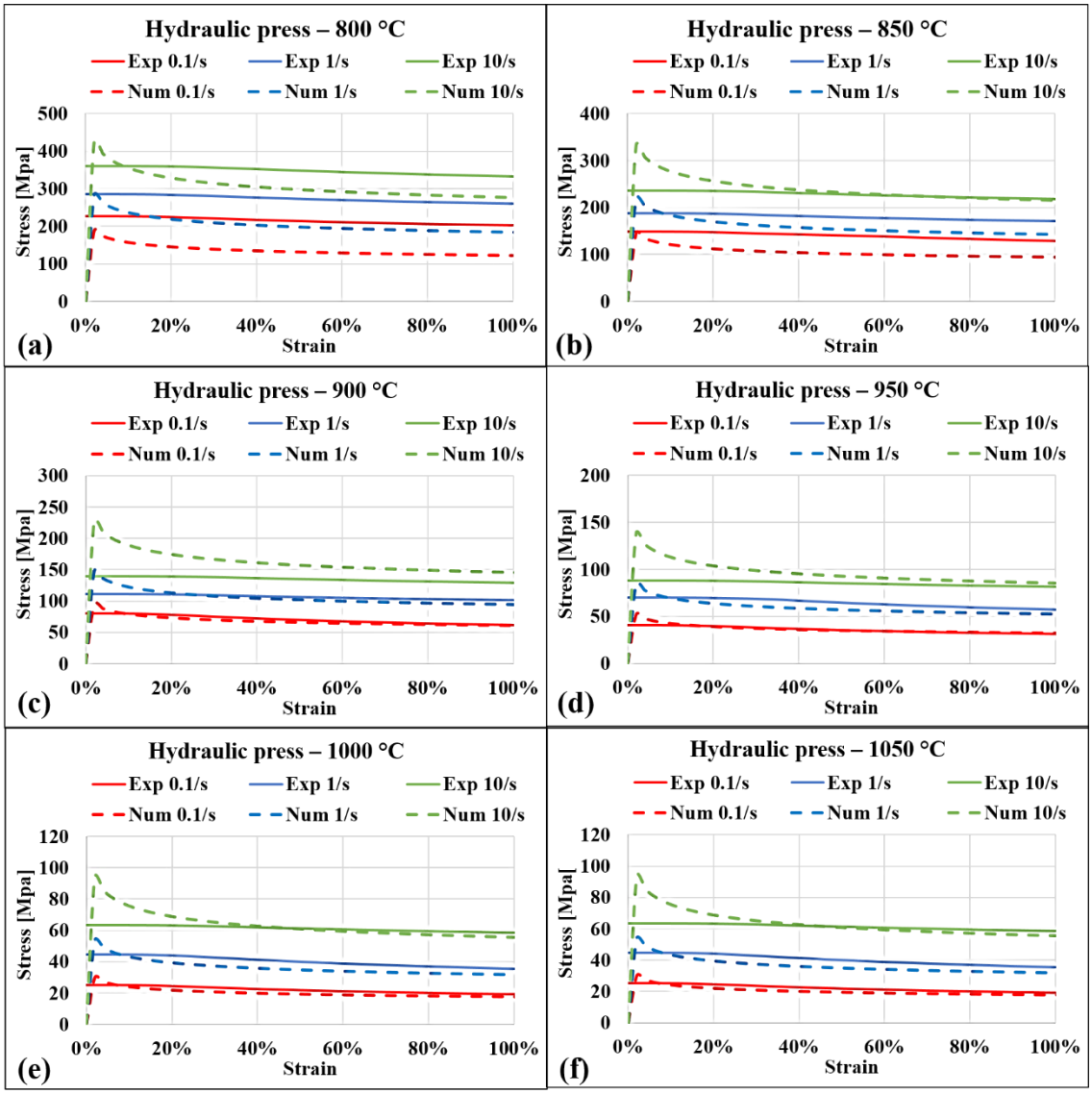

Figure 190: Experimental and predicted flow stress curves using the JC SCM modelization at hydraulic press strain rates and (a) 800 °C, (b) 850 °C, (c) 900 °C, (d) 950 °C, (e) 1000 °C and (f) 1050 °C

In the end, the mechanical press case (Figure 191) displayed the lower quality in curve fitting with a mean error over 20% about at 800 and 850 °C while better results were obtained at higher temperature.

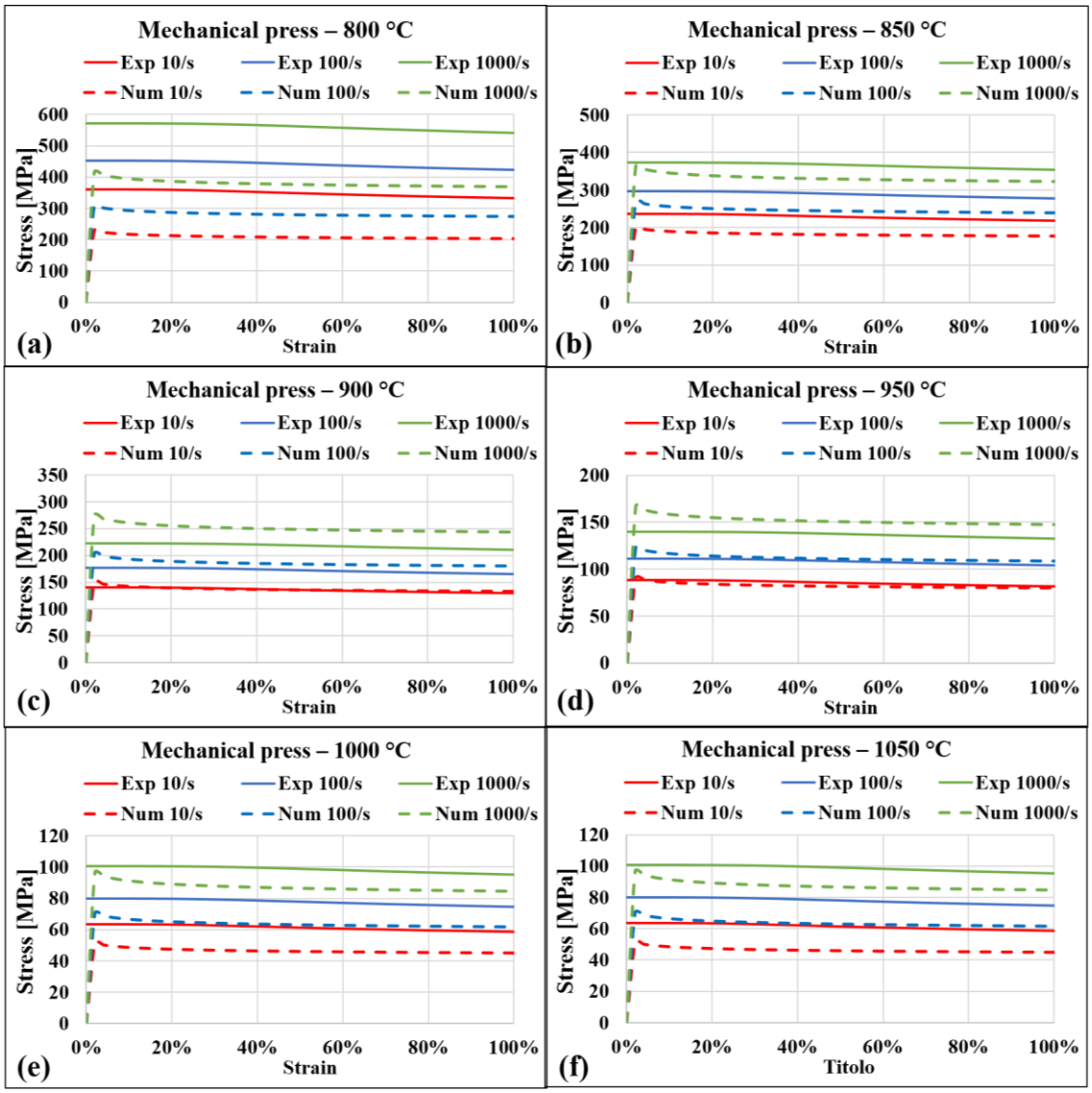

Figure 191: Experimental and predicted flow stress curves using the JC SCM modelization at mechanical press strain rates and (a) 800 °C, (b) 850 °C, (c) 900 °C, (d) 950 °C, (e) 1000 °C and (f) 1050 °C

8. Conclusions and further developments

The aim of this study was to define the thermo-mechanical-metallurgical characterization of Ti-6Al-4V titanium alloy, with the aim of obtaining a good numerical representation of the macroscopic behavior of the selected alloy when undergoing to a complex thermo-mechanical evolution as imposed by a hot forging process.

For this purpose, a meticulous literature research on the hot deformation processes and applications of Ti64 alloy was conducted in order to identify the workability windows within temperature, strain and strain rate ranges have to be defined.

As first, a complete thermo-physical definition of the material including elastic properties, density variation, thermal energy transportation and heat exchange phenomena was focused. Moreover, an exhaustive examination on the flow stress behavior of the alloy at different strain rate and high temperature allowed to collect a large amount of true stress/true strain curves within a T, ε, $\dot{\varepsilon}$ domain, which was easily included into the DEFORM™ implicit-lagrangian software. This initial characterization was validated through a series of numerical/experimental comparisons between compression tests on cylindrical billets at different temperature and deformation rates in both Alpha/Beta and Beta region. The modelization showed a good agreement in prediction of the compression load/stroke curves. The high temperature tests conducted exhibited that the yield strength decreases with increase in temperature and the strain hardening behavior changes with less strain hardening. According with the first results, a strong variation in mechanical properties within the 800 – 1000 °C temperature range was found as the influence of allotropic form of the material matrix on the flow stress characteristics is displayed. Also, the varied strain rate tests showed that Ti-6Al-4V is a strain and strain rate sensitive alloy. In fact, the strain hardening behavior changes with change in strain rate and, at quasi-static strain rates (up to 10^{-2} s^{-1}); more strain hardening as compared to the higher strain rates is found.

After the thermo-mechanical properties definition, the microstructructural behavior were analyzed by means of a further literature screening, taking into account both the phase transformation kinetics as function of thermal history and the morphology produced as function of different cooling conditions. According to the cooling rates from

Beta transus temperature, different microstructures formed which were equilibrium Alpha (Widmanstätten Alpha) and Beta phases for furnace cooling, basket–weave Alpha for air cooling and martensitic α' for water quenching. In addition, aging of martensite at different temperatures resulted in decreasing of vanadium concentration from martensite phase and an increase in the width of martensite plates after 700 °C.

The collected data was used to define the three main phase transformations involved during both generic heating and cooling stages by means of the Avrami model. In particular, the Alpha-to-Beta change during heating was based on the generalized Avrami equation without time-dependency, in which the coefficients were calculated by means of a MSE minimization. The diffusionless Beta-to-Alpha+Beta and Beta-to-martensitic Alpha transformations were modellized using the classical Avrami model calibrated using the collected literature data.

The microstructural characterization was validate by means of experimental comparison based on the TitaForm research project, which was based on the set-up of a near-net-shape forging sequences of aeronautical components made out of Ti-6Al-4V alloy, including both the die design and selection of process conditions. In order to obtain both quantitative and qualitative examinations of micrographic images extracted from the forgings, an in-house Matlab™ subroutine was compiled. The comparison between the output of simulations and the experimental campaign displayed a good correlation between the numerical predictions and the experimental data.

This step of the numerical characterization was still a non-fully coupled solution because both thermo-mechanical and thermo-metallurgical aspects were connected but no link between mechanical and metallurgical calculation was present. Thus, each phase of the Ti64 alloy included the same flow stress curves of the base material.

Once the confirmation on the quality of collected data was obtained, a further evolution in the numerical characterization was pursued with the aim of obtaining a self-consistent definition of the selected material, with the aim to create that lacking link of the previous definition.

The first step of this new characterization was a filtering of phasic flow stress curve set, in which the flow stress curve set of the base material, was filtered for each allotropic form on the basis of the Semiatin's approach found in literature. Once the flow behavior of each phase within the selected temperature/strain rate rage was found, a phasic

constitutive Johnson-Cook equation self-consistent modelling was carried out using the phasic flow stress curve set.

Due to the typical strain rate windows of the forging processes, which depend on the equipment, the JC definition was splitted into three different blocks as function of the strain rate range, in order to define a set of coefficient for both ver low, low and high speed presses.

The determined JC parameters were found to be well agreed with the literature and the interpolation showed a good matching the experimental flow stress curves with some exception of 800 – 850 °C temperature range at all stra rates. Numerical simulations on DEFORM™ software are currently work-in-progress in order to test the code response with respect to the mathematical interpolation.

However, looking at the comparison between experimental and numerical curves, it was evidenced that the JC interpolation offers several opportunities to modelize the flow stress behavior of a material having complex properties coming from allotropic transformations among different kind of phases which strogly differ in mechanical characteristics. Additionally, the power of Johnson-Cook equation, which is usually adopted in analysis of machining operations, can be used for bulk forming processes on condition of perform an appropriate calibration of all coefficients and, eventually, some small changes in the mathematical form of the equation, as demonstrated in some prior studies.

Finally, the characteristic of the SCM approach allow to improve the capabilities of the actual commercial FE codes due to the increasing demand of advanced numerical tools for industrial application on innovative materials.

9. Appendixes

9.1. Figures

9.2. Tables

10. References

[1] Layens C, Peters M. Titanium and titanium alloys: fundamentals and applications. Wiley-VCH; 2003.

[2] Jones DA. Principles and prevention of corrosion: Macmillan; 1992.

[3] Textor M, Sittig C, Frauchiger V, Tosatti S, Brunette DM. Properties and biological significance of natural oxide films on titanium and its alloys. Titanium in medicine: Springer; 2001. p. 171-230.

[4] Lütjering G, Williams J, Gysler A. Microstructure and mechanical properties of titanium alloys. Microstructure and Properties of Materials. 2000;2:1-74.

[5] Donachie MJ. Titanium: a technical guide: ASM international; 2000.

[6] Leyens C, Peters M. Titanium and Titanium Alloys. Fundamentals and Applications. Copyright © 2003 WILEY-VCH Verlag GmbH & Co KGaA, Weinheim. 2003.

[7] Williams J. Titanium: Alloying. Pergamon Press Ltd, Encyclopedia of Materials Science and Engineering. 1986;5.

[8] Davis JR. Properties and selection: nonferrous alloys and special-purpose materials: Asm Intl; 1990.

[9] Lutjering G, Albrecht J, Ivasishin OM. Microstructure and Mechanical Properties of Conventional Titanium Alloys. Microstructure/Property Relationships of Titanium Alloys. 1994:65-74.

[10] Hammond C, Nutting J. The physical metallurgy of superalloys and titanium alloys. Metal Science. 1977;11:474-90.

[11] Malinov S, Sha W, Guo Z, Tang C, Long A. Synchrotron X-ray diffraction study of the phase transformations in titanium alloys. Materials Characterization. 2002;48:279-95.

[12] Lutjering G. Influence of processing on microstructure and mechanical properties of (alpha+beta) titanium alloys. Materials Science and Engineering a-Structural Materials Properties Microstructure and Processing. 1998;243:32-45.

[13] Tiley J, Searles T, Lee E, Kar S, Banerjee R, Russ J, et al. Quantification of microstructural features in α/β titanium alloys. Materials Science and Engineering: A. 2004;372:191-8.

[14] Gil FJ, Ginebra MP, Manero JM, Planell JA. Formation of α-Widmanstätten structure: effects of grain size and cooling rate on the Widmanstätten morphologies and on the mechanical properties in Ti6Al4V alloy. Journal of Alloys and Compounds. 2001;329:142-52.

[15] Lutjering G, Williams JC. Titanium. 2003.

[16] Ding R, Guo Z, Wilson A. Microstructural evolution of a Ti–6Al–4V alloy during thermomechanical processing. Materials Science and Engineering: A. 2002;327:233-45.

[17] Williams J, Chesnutt J. Titanium Alloys: Thermomechanical Treatment. Pergamon Press Ltd, Encyclopedia of Materials Science and Engineering. 1986;5.

[18] Pederson R. Microstructure and phase transformation of Ti-6Al-4V. 2002.

[19] Zeng L, Bieler T. Effects of working, heat treatment, and aging on microstructural evolution and crystallographic texture of α, α′, α ″and β phases in Ti–6Al–4V wire. Materials Science and Engineering: A. 2005;392:403-14.

[20] Ivasishin OM, Teliovich RV. Potential of rapid heat treatment of titanium alloys and steels. Materials Science and Engineering: A. 1999;263:142-54.

[21] Fujii H. Continuous cooling transformation characteristics of alpha+ beta titanium alloys. Nippon Steel Tech Rep(Japan). 1994;62:74-9.

[22] Stanford N, Bate P. Crystallographic variant selection in Ti–6Al–4V. Acta materialia. 2004;52:5215-24.

[23] Semiatin S, Fagin P, Glavicic M, Sukonnik I, Ivasishin O. Influence on texture on beta grain growth during continuous annealing of Ti–6Al–4V. Materials Science and Engineering: A. 2001;299:225-34.

[24] Ivasishin O, Shevchenko S, Semiatin S. Effect of crystallographic texture on the isothermal beta grain-growth kinetics of Ti–6Al–4V. Materials Science and Engineering: A. 2002;332:343-50.

[25] Malinov S, Markovsky P, Sha W, Guo Z. Resistivity study and computer modelling of the isothermal transformation kinetics of Ti–6Al–4V and Ti–6Al–2Sn–4Zr–2Mo–0.08 Si alloys. Journal of Alloys and Compounds. 2001;314:181-92.

[26] Jovanović M, Tadić S, Zec S, Mišković Z, Bobić I. The effect of annealing temperatures and cooling rates on microstructure and mechanical properties of investment cast Ti–6Al–4V alloy. Materials & design. 2006;27:192-9.

[27] Lütjering G. Property optimization through microstructural control in titanium and aluminum alloys. Materials Science and Engineering: A. 1999;263:117-26.
[28] Ahmed T, Rack H. Phase transformations during cooling in< i> α</i>+< i> β</i> titanium alloys. Materials Science and Engineering: A. 1998;243:206-11.
[29] Gil F, Planell J. Behaviour of normal grain growth kinetics in single phase titanium and titanium alloys. Materials Science and Engineering: A. 2000;283:17-24.
[30] Filip R, Kubiak K, Ziaja W, Sieniawski J. The effect of microstructure on the mechanical properties of two-phase titanium alloys. Journal of Materials Processing Technology. 2003;133:84-9.
[31] Sha W, Guo Z. Phase evolution of Ti–6Al–4V during continuous heating. Journal of alloys and compounds. 1999;290:L3-L7.
[32] Filip R, Kubiak K, Ziaja W, Sieniawski J. The effect of microstructure on the mechanical properties of two-phase titanium alloys. Journal of Materials Processing Technology. 2003;133:84-9.
[33] Altan T, Ngaile G, Shen G. Cold and Hot Forging Fundamentals and Applications. 2005:25-49.
[34] Brownrigg A, Prior GK. Hardenability reduction in VN microalloyed eutectoid steels. Scripta Materialia. 2002;46:357-61.
[35] Altan T, Ngaile G, Shen G. Plastic Deformation: Strain and Strain Rate. Cold and Hot Forging Fundamentals and Applications. 2005.
[36] Lange K. International Cold Forging Group (Icfg). Werkstattstechnik Zeitschrift Fur Industrielle Fertigung. 1972;62:298-&.
[37] Kalpakjian S. Manufacturing Processes for Engineering Materials. 1991;2nd Ed.
[38] Lange K. Handbook of metal forming. 1985:293.
[39] Tomov B, Radev R. Shape Complexity Factor for Closed Die Forging. International Journal of Material Forming. 2010;3:319-22.
[40] Hristov DH, Tomov BI, Kolev DK. Stresses and Strains in a Die for Closed-Die Forging of Cylindrical Spur Gears. Journal of Materials Processing Technology. 1990;23:55-63.
[41] Association FI. Design Guide for Forging.

[42] Babu S, Ribeiro D, Shivpuri R. Material and surface engineering for precision forging dies. Precision forging consortium - Ohio aerospace institute and National center for manufacturing sciences. 1999.

[43] Zhang SH, Jin QL, Wang ZT, Li DF, Zhou WL. Development of plasticity processing of magnesium alloys. Thermec'2003, Pts 1-5. 2003;426-4:545-50.

[44] Matsumoto R, Osakada K. Development of warm forging method for magnesium alloy. Materials Transactions. 2004;45:2838-44.

[45] Arif AFM, Sheikh AK, Qamar SZ, Al-Fuhaid KM. Variation of pressure with ram speed and die profile in hot extrusion of aluminum-6063. Materials and Manufacturing Processes. 2001;16:701-16.

[46] Frank JP. Forging the Copper Collar - Byrkit,Jw. American Bar Association Journal. 1982;68:1460-1.

[47] Garza LG, Van Tyne CJ. Surface hot-shortness of 1045 forging steel with residual copper. Journal of Materials Processing Technology. 2005;159:169-80.

[48] Farahat AIZ, Hamed O, El-Sisi A, Hawash M. Effect of hot forging and Mn content on austenitic stainless steel containing high carbon. Materials Science and Engineering a-Structural Materials Properties Microstructure and Processing. 2011;530:98-106.

[49] Sowerby R, Oreilly I, Chandrasekaran N, Dung NL. Materials Testing for Cold Forging. Journal of Engineering Materials and Technology-Transactions of the Asme. 1984;106:101-6.

[50] Nakhaie D, Benhangi PH, Fazeli F, Mazinani M, Karimi EZ, Ferdowsi MRG. Controlled Forging of a Nb Containing Microalloyed Steel for Automotive Applications. Metallurgical and Materials Transactions a-Physical Metallurgy and Materials Science. 2012;43A:5209-17.

[51] Spena PR, Firrao D. Thermomechanical warm forging of Ti-V, Ti-Nb, and Ti-B microalloyed medium carbon steels. Materials Science and Engineering a-Structural Materials Properties Microstructure and Processing. 2013;560:208-15.

[52] Chamanfar A, Sarrat L, Jahazi M, Asadi M, Weck A, Koul AK. Microstructural characteristics of forged and heat treated Inconel-718 disks. Materials & Design. 2013;52:791-800.

[53] Nowotnik A. High temperature deformation of superalloy Inconel 718. Electron Microscopy Xiv. 2012;186:147-50.

[54] Donachie MJ, Donachie SJ. Superalloys - A Technical Guide. 2002.
[55] Kashani H, Amadeh A, Vatanara MR. Improvement of wear resistance of hot working tool steel by hardfacing - Part 2 - Case study. Materials Science and Technology. 2008;24:356-60.
[56] General Aspects of Tool Design and Tool Materials for Cold Forging of Steel. Metal Forming. 1970;37:262-&.
[57] Altan T, Deshpande M, Groseclose A. Selection of die materials and surface treatments for increasing die life in hot and warm forging. ERC for Net Shape Manufacturing - The Ohio State University.
[58] Semiatin SL, Altan T. Isothermal and Hot-Die Forging - Background and Applications. Journal of Metals. 1983;35:88-.
[59] Kini SD, Shivpuri R. Precision and ejection issues in the cold forging of a fuel injector nozzle. Proceedings of the Institution of Mechanical Engineers Part B-Journal of Engineering Manufacture. 2001;215:927-33.
[60] Boyer RR. An overview on the use of titanium in the aerospace industry. Mat Sci Eng a-Struct. 1996;213:103-14.
[61] Baufeld B, Biest OVd, Gault R. Additive manufacturing of Ti–6Al–4V components by shaped metal deposition: Microstructure and mechanical properties. Materials & Design. 2010;31:S106-S11.
[62] Park NK, Yeom JT, Na YS. Characterization of deformation stability in hot forging of conventional Ti-6Al-4V using processing maps. J Mater Process Tech. 2002;130:540-5.
[63] Wang J, Fu P, Liu H, Li D, Li Y. Shrinkage porosity criteria and optimized design of a 100-ton 30Cr 2Ni 4MoV forging ingot. Materials and Design. 2012;35:446-56.
[64] Semiatin S, Montheillet F, Shen G, Jonas J. Self-consistent modeling of the flow behavior of wrought alpha/beta titanium alloys under isothermal and nonisothermal hot-working conditions. Metallurgical and Materials Transactions A. 2002;33:2719-27.
[65] Tiley JS. Modeling of microstructure property relationships in Ti-6Al-4V: The Ohio State University; 2003.
[66] Geijselaers H, Huétink H. Thermo-Mechanical Analysis with Phase Transformations. 2004.

[67] McQueen H, Jonas J. Treatise on materials science and technology. Plastic deformation of materials. 1975;6:393.
[68] Zhang JM, Gao ZY, Zhuang JY, Zhong ZY. Mathematical modeling of the hot-deformation behavior of superalloy IN718. Metallurgical and Materials Transactions A. 1999;30:2701-12.
[69] Laasraoui A, Jonas J. Prediction of steel flow stresses at high temperatures and strain rates. Metallurgical transactions A. 1991;22:1545-58.
[70] Goetz R, Seetharaman V. Static recrystallization kinetics with homogeneous and heterogeneous nucleation using a cellular automata model. Metallurgical and Materials Transactions A. 1998;29:2307-21.
[71] Peczak P. A Monte Carlo study of influence of deformation temperature on dynamic recrystallization. Acta metallurgica et materialia. 1995;43:1279-91.
[72] Vanderhasten M, Rabet L, Verlinden B. Deformation mechanisms of Ti-6Al-4V during tensile behavior at low strain rate. Journal of materials engineering and performance. 2007;16:208-12.
[73] Vanderhasten M, Rabet L, Verlinden B. Ti–6Al–4V: deformation map and modelisation of tensile behaviour. Materials & design. 2008;29:1090-8.
[74] Semiatin S, Seetharaman V, Weiss I. Flow behavior and globularization kinetics during hot working of Ti–6Al–4V with a colony alpha microstructure. Materials Science and Engineering: A. 1999;263:257-71.
[75] Seshacharyulu T, Medeiros S, Morgan J, Malas J, Frazier W, Prasad Y. Hot deformation and microstructural damage mechanisms in extra-low interstitial (ELI) grade Ti–6Al–4V. Materials Science and Engineering: A. 2000;279:289-99.
[76] Seshacharyulu T, Medeiros S, Frazier W, Prasad Y. Hot working of commercial Ti–6Al–4V with an equiaxed α–β microstructure: materials modeling considerations. Materials Science and Engineering: A. 2000;284:184-94.
[77] Guan RG, Je YT, Zhao ZY, Lee CS. Effect of microstructure on deformation behavior of Ti–6Al–4V alloy during compressing process. Materials & Design. 2012;36:796-803.
[78] Cai J, Li F, Liu T, Chen B. Investigation of mechanical behavior of quenched Ti–6Al–4V alloy by microindentation. Materials Characterization. 2011;62:287-93.

[79] Fan Z. On the young's moduli of Ti · 6Al · 4V alloys. Scripta metallurgica et materialia. 1993;29:1427-32.

[80] Majorell A, Srivatsa S, Picu R. Mechanical behavior of Ti–6Al–4V at high and moderate temperatures—Part I: Experimental results. Materials Science and Engineering: A. 2002;326:297-305.

[81] Luo J, Li M, Yu W, Li H. The variation of strain rate sensitivity exponent and strain hardening exponent in isothermal compression of Ti–6Al–4V alloy. Materials & Design. 2010;31:741-8.

[82] Pantalé O, Gueye B. Influence of the constitutive flow law in FEM simulation of the Radial forging process. Journal of Engineering. 2013;2013.

[83] Zerilli FJ, Armstrong RW. Dislocation-mechanics-based constitutive relations for material dynamics calculations. Journal of Applied Physics. 1987;61:1816-25.

[84] Zener C, Hollomon J. Effect of strain rate upon plastic flow of steel. Journal of Applied Physics. 2004;15:22-32.

[85] Johnson GR, Cook WH. A constitutive model and data for metals subjected to large strains, high strain rates and high temperatures. Proceedings of the 7th International Symposium on Ballistics: The Netherlands; 1983. p. 541-7.

[86] Montmitonnet P, Chenot J. Introduction of anisotropy in viscoplastic 2D and 3D finite-element simulations of hot forging. J Mater Process Tech. 1995;53:662-83.

[87] Obikawa T, Usui E. Computational machining of titanium alloy—finite element modeling and a few results. Journal of engineering for industry. 1996;118:208-15.

[88] Duan X, Sheppard T. Computation of substructural strengthening by the integration of metallurgical models into the finite element code. Computational materials science. 2003;27:250-8.

[89] Khan AS, Liang R. Behaviors of three BCC metal over a wide range of strain rates and temperatures: experiments and modeling. International Journal of Plasticity. 1999;15:1089-109.

[90] Khan AS, Sung Suh Y, Kazmi R. Quasi-static and dynamic loading responses and constitutive modeling of titanium alloys. International Journal of Plasticity. 2004;20:2233-48.

[91] Kim JH, Semiatin S, Lee CS. Constitutive analysis of the high-temperature deformation of Ti–6Al–4V with a transformed microstructure. Acta materialia. 2003;51:5613-26.

[92] Kim JH, Semiatin S, Lee CS. Constitutive analysis of the high-temperature deformation mechanisms of Ti–6Al–4V and Ti–6.85 Al–1.6 V alloys. Materials Science and Engineering: A. 2005;394:366-75.

[93] Kim JH, Semiatin S, Lee CS. High-temperature deformation and grain-boundary characteristics of titanium alloys with an equiaxed microstructure. Materials Science and Engineering: A. 2008;485:601-12.

[94] Giuliano G. Constitutive equation for superplastic Ti–6Al–4V alloy. Materials & Design. 2008;29:1330-3.

[95] Cai J, Li F, Liu T, Chen B, He M. Constitutive equations for elevated temperature flow stress of Ti–6Al–4V alloy considering the effect of strain. Materials & Design. 2011;32:1144-51.

[96] Šlais M, Dohnal I, Forejt M. DETERMINATION OF JOHNSON-COOK EQUATION PARAMETERS. Acta Metallurgica Slovaca. 2012;18:125-32.

[97] Kıranlı E. Determination of material constitutive equation of biomedical grade Ti6Al4V alloy for cross edge rolling. Izmir Institute of Technology, Izmir. 2009.

[98] Dorogoy A, Rittel D. Determination of the Johnson–Cook Material Parameters Using the SCS Specimen. Exp Mech. 2009;49:881-5.

[99] Meyer Jr HW, Kleponis DS. Modeling the high strain rate behavior of titanium undergoing ballistic impact and penetration. International Journal of Impact Engineering. 2001;26:509-21.

[100] Seo S, Min O, Yang H. Constitutive equation for Ti–6Al–4V at high temperatures measured using the SHPB technique. International Journal of Impact Engineering. 2005;31:735-54.

[101] Donald R. Experimental Investigations of Material Models for Ti-6Al-4V Titanium and 2024-T3 Aluminum. DOT/FAA/AR-00/25, National Technical Information Service, Springfield, Virginia; 2000.

[102] Guo Z, Saunders N, Schillé J, Miodownik A. Modelling high temperature flow stress curves of titanium alloys. MRS International Materials Research Conference, Chongqing2008. p. 9-12.

[103] Babu B, Lindgren L-E. Dislocation density based model for plastic deformation and globularization of Ti-6Al-4V. International Journal of Plasticity. 2013;50:94-108.
[104] Nemat-Nasser S, Guo W-G, Nesterenko VF, Indrakanti S, Gu Y-B. Dynamic response of conventional and hot isostatically pressed Ti–6Al–4V alloys: experiments and modeling. Mechanics of Materials. 2001;33:425-39.
[105] Bruschi S, Poggio S, Quadrini F, Tata M. Workability of Ti–6Al–4V alloy at high temperatures and strain rates. Materials letters. 2004;58:3622-9.
[106] Calamaz M, Coupard D, Girot F. A new material model for 2D numerical simulation of serrated chip formation when machining titanium alloy Ti–6Al–4V. International Journal of Machine Tools and Manufacture. 2008;48:275-88.
[107] Calamaz M, Coupard D, Nouari M, Girot F. Numerical analysis of chip formation and shear localisation processes in machining the Ti-6Al-4V titanium alloy. The International Journal of Advanced Manufacturing Technology. 2011;52:887-95.
[108] Xiao J, Li D, Li X, Deng T. Constitutive modeling and microstructure change of Ti–6Al–4V during the hot tensile deformation. Journal of Alloys and Compounds. 2012;541:346-52.
[109] Fan X, Yang H. Internal-state-variable based self-consistent constitutive modeling for hot working of two-phase titanium alloys coupling microstructure evolution. International Journal of Plasticity. 2011;27:1833-52.
[110] Bieler TR, Semiatin S. The origins of heterogeneous deformation during primary hot working of Ti–6Al–4V. International Journal of Plasticity. 2002;18:1165-89.
[111] Kim JH, Semiatin SL, Lee YH, Lee CS. A Self-Consistent Approach for Modeling the Flow Behavior of the Alpha and Beta Phases in Ti-6Al-4V. Metallurgical and Materials Transactions a-Physical Metallurgy and Materials Science. 2011;42A:1805-14.
[112] Reddy N, Lee YH, Park CH, Lee CS. Prediction of flow stress in Ti–6Al–4V alloy with an equiaxed α+ β microstructure by artificial neural networks. Materials Science and Engineering: A. 2008;492:276-82.
[113] Ding R, Guo Z. Microstructural evolution of a Ti–6Al–4V alloy during β-phase processing: experimental and simulative investigations. Materials Science and Engineering: A. 2004;365:172-9.

[114] Dąbrowski R. The kinetics of phase transformations during continuous cooling of Ti6Al4V alloy from the diphase α+ β range. Archives of metallurgy and materials. 2011;56:217-21.

[115] Song H-W, Zhang S-H, Cheng M. Dynamic globularization kinetics during hot working of a two phase titanium alloy with a colony alpha microstructure. Journal of Alloys and Compounds. 2009;480:922-7.

[116] Pinke P, Réger M. HEAT TREATMENT OF THE CASTED Ti6Al4V TITANIUM ALLOY TEPELNÉ SPRACOVANIE LIATEJ TITÁNOVEJ ZLIATINY Ti6Al4V.

[117] Elmer J, Palmer T, Babu S, Specht E. In situ observations of lattice expansion and transformation rates of α and β phases in Ti–6Al–4V. Materials Science and Engineering: A. 2005;391:104-13.

[118] Pelcastre L. Microstructural evolution of Ti-6Al-4V alloy. 2008.

[119] Mironov S, Murzinova M, Zherebtsov S, Salishchev G, Semiatin S. Microstructure evolution during warm working of Ti–6Al–4V with a colony-α microstructure. Acta Materialia. 2009;57:2470-81.

[120] Weiss I, Froes F, Eylon D, Welsch G. Modification of alpha morphology in Ti-6Al-4V by thermomechanical processing. Metallurgical Transactions A. 1986;17:1935-47.

[121] Malinov S, Guo Z, Sha W, Wilson A. Differential scanning calorimetry study and computer modeling of β⇒ α phase transformation in a Ti-6Al-4V alloy. Metallurgical and Materials Transactions A. 2001;32:879-87.

[122] Malinov S, Sha W. Modeling thermodynamics, kinetics, and phase transformation morphology while heat treating titanium alloys. JOM. 2005;57:42-5.

[123] Sha W, Malinov S. Titanium alloys: Modelling of microstructure, properties and applications: Elsevier; 2009.

[124] Murgau CC, Pederson R, Lindgren L. A model for Ti–6Al–4V microstructure evolution for arbitrary temperature changes. Modelling and Simulation in Materials Science and Engineering. 2012;20:055006.

[125] Avrami M. Kinetics of phase change. III. Granulation, phase change, and microstructure. J chem Phys. 1941;9:177-84.

[126] Johnson WA, Mehl RF. Reaction kinetics in processes of nucleation and growth. Trans Aime. 1939;135:396-415.

[127] Kolmogorov AN. On the statistical theory of the crystallization of metals. Bull Acad Sci USSR, Math Ser. 1937;1:355-9.

[128] Koistinen D, Marburger R. A general equation prescribing the extent of the austenite-martensite transformation in pure iron-carbon alloys and plain carbon steels. acta metallurgica. 1959;7:59-60.

[129] Neelakantan S, Rivera-Díaz-del-Castillo PE, van der Zwaag S. Design of Titanium Alloys Showing Plasticity Induced Transformation. Advanced Materials Research. 2010;89:405-10.

[130] Ghosh G, Olson G. Kinetics of FCC→ BCC heterogeneous martensitic nucleation—I. The critical driving force for athermal nucleation. Acta metallurgica et materialia. 1994;42:3361-70.

[131] Shah A, Kulkarni G, Gopinathan V, Krishnan R. Determination of activation energy for α+ β⇒ β transformation in Ti-6Al-4V alloy by dilatometry. Scripta metallurgica et materialia. 1995;32:1353-6.

[132] Ouchi K, Iijima Y, Hirano K, Kimura H, Izumi O. Titanium'80 Science and Technology. Proceedings of the 4th International Conference on Titanium, Kyoto, Japan1980. p. 559.

[133] BaTiO AOO. 128 Diffusion and Defect Data Vol. 11. Diffusion and Defect Data: Trans Tech Publ; 1975. p. 4.

[134] Semiatin S, Knisley S, Fagin P, Barker D, Zhang F. Microstructure evolution during alpha-beta heat treatment of Ti-6Al-4V. Metallurgical and Materials Transactions A. 2003;34:2377-86.

[135] Crespo A, Deus A, Vilar R. Modeling of phase transformations and internal stresses in laser powder deposition. XVII International Symposium on Gas Flow and Chemical Lasers and High Power Lasers: International Society for Optics and Photonics; 2008. p. 713120--10.

[136] Denis S, Farias D, Simon A. Mathematical Model Coupling Phase Transformations and Temperature Evolutions in Steels. ISIJ international. 1992;32:316-25.

[137] Elmer J, Palmer T, Babu S, Zhang W, DebRoy T. Phase transformation dynamics during welding of Ti–6Al–4V. Journal of applied physics. 2004;95:8327-39.

[138] Fischer F, Oberaigner E, Tanaka K, Nishimura F. Transformation induced plasticity revised an updated formulation. International Journal of Solids and Structures. 1998;35:2209-27.

[139] Inoue T, Wang Z. Coupling between stress, temperature, and metallic structures during processes involving phase transformations. Materials Science and Technology. 1985;1:845-50.

[140] Coret M, Calloch S, Combescure A. Experimental study of the phase transformation plasticity of 16MND5 low carbon steel under multiaxial loading. International Journal of plasticity. 2002;18:1707-27.

[141] Magee CL, Paxton HW. TRANSFORMATION KINETICS, MICROPLASTICITY AND AGING OF MARTENSITE IN FE-31 NI. DTIC Document; 1966.

[142] Greenwood G, Johnson R. The deformation of metals under small stresses during phase transformations. Proceedings of the Royal Society of London Series A Mathematical and Physical Sciences. 1965;283:403-22.

[143] Gautier E, Zhang X, Simon A. Role of internal stress state on transformation induced plasticity and transformation mechanisms during the progress of stress induced phase transformation. International Conference on Residual Stresses: Springer; 1989. p. 777-83.

[144] Taleb L, Cavallo N, Waeckel F. Experimental analysis of transformation plasticity. International Journal of Plasticity. 2001;17:1-20.

[145] Abrassart F. Influence des transformations martensitiques sur les propriétés mécaniques des alliages du système Fe-Ni-Cr-C 1972.

[146] Desalos Y. Comportement dilatométrique et mécanique de l'austénite métastable d'un acier A 533. IRSID Report. 1981;95349401.

[147] Leblond J, Devaux J, Devaux J. Mathematical modelling of transformation plasticity in steels I: case of ideal-plastic phases. International journal of plasticity. 1989;5:551-72.

[148] Leblond J. Mathematical modelling of transformation plasticity in steels II: coupling with strain hardening phenomena. International journal of plasticity. 1989;5:573-91.

[149] Neelakantan S, San Martin D, Rivera-Díaz-del-Castillo PE, van der Zwaag S. Plasticity induced transformation in a metastable β Ti-1023 alloy by controlled heat treatments. Materials Science and Technology. 2009;25:1351-8.
[150] Duerig T, Albrecht J, Richter D, Fischer P. Formation and reversion of stress induced martensite in Ti-10V-2Fe-3Al. Acta Metallurgica. 1982;30:2161-72.
[151] Grosdidier T, Roubaud C, Philippe M-J, Combres Y. The deformation mechanisms in the β-metastable β-Cez titanium alloy. Scripta materialia. 1997;36:21-8.
[152] Ishiyama S, Hanada S, Izumi O. Effect of Zr, Sn and Al Additions on Deformation Mode and Beta Phase Stability of Metastable Beta Ti Alloys. ISIJ International. 1991;31:807-13.
[153] Bhattacharjee A, Bhargava S, Varma V, Kamat S, Gogia A. Effect of β grain size on stress induced martensitic transformation in β solution treated Ti–10V–2Fe–3Al alloy. Scripta materialia. 2005;53:195-200.
[154] Grosdidier T, Combres Y, Gautier E, Philippe M-J. Effect of microstructure variations on the formation of deformation-induced martensite and associated tensile properties in a β metastable Ti alloy. Metallurgical and Materials Transactions A. 2000;31:1095-106.
[155] Vassel A. Microstructural instabilities in beta titanium alloys. Beta titanium alloys in the 1990's1993.
[156] Schaeffer L, Brito AM, Geier M. Numerical simulation using finite elements to develop and optimize forging processes. Steel research international. 2005;76:199-204.
[157] Altan T, Nichols D, Henning H, Sabroff A. CALCULATION OF GEOMETRICAL PARAMETERS IN DESIGNING THE FORGING PROCESS FOR AXISYMMETRIC SHAPES. DTIC Document; 1969.
[158] Ngaile G, Altan T. Computer aided engineering in forging. Proc 3rd JSTP International Seminar on Precision Forging, Nagoya, Japan: Mar2004. p. 21-30.
[159] Oh S, Wu W, Tang J. Simulations of cold forging processes by the DEFORM system. Journal of materials processing technology. 1992;35:357-70.
[160] Vazquez V, Altan T. New concepts in die design—physical and computer modeling applications. Journal of Materials Processing Technology. 2000;98:212-23.

[161] Castro C, António C, Sousa L. Optimisation of shape and process parameters in metal forging using genetic algorithms. Journal of Materials Processing Technology. 2004;146:356-64.
[162] Kim H, Sweeney K, Altan T. Application of computer aided simulation to investigate metal flow in selected forging operations. Journal of materials processing technology. 1994;46:127-54.
[163] Kim H, Alfan T. Cold forging of steel—practical examples of computerized part and process design. Journal of materials processing technology. 1996;59:122-31.
[164] Song J-H, Im Y-T. Process design for closed-die forging of bevel gear by finite element analyses. Journal of Materials Processing Technology. 2007;192:1-7.
[165] Duggirala R, Shivpuri R, Kini S, Ghosh S, Roy S. Computer aided approach for design and optimization of cold forging sequences for automotive parts. Journal of materials processing technology. 1994;46:185-98.
[166] Im C, Suh S, Lee M, Kim J, Joun M. Computer aided process design in cold-former forging using a forging simulator and a commercial CAD software. Journal of Materials Processing Technology. 1999;95:155-63.
[167] Kim D, Kim B, Choi J. Determination of the initial billet geometry for a forged product using neural networks. Journal of materials processing technology. 1997;72:86-93.
[168] Hsu Q-C, Lee R-S. Cold forging process design based on the induction of analytical knowledge. Journal of materials processing technology. 1997;69:264-72.
[169] Meidert M, Knoerr M, Westphal K, Altan T. Numerical and physical modelling of cold forging of bevel gears. Journal of materials processing technology. 1992;33:75-93.
[170] Badawy AA, Raghupathi P, Kuhlmann DJ, Altan T. Computer-aided design of multistage forging operations for round parts. Journal of mechanical working technology. 1985;11:259-74.
[171] Di Lorenzo R, Micari F. An inverse approach for the design of the optimal preform shape in cold forging. CIRP Annals-Manufacturing Technology. 1998;47:189-92.
[172] Tomov B, Gagov V. Modelling and description of the near-net-shape forging of cylindrical spur gears. Journal of Materials Processing Technology. 1999;92:444-9.

[173] Liou J, Jang D. Forging parameter optimization considering stress distributions in products through FEM analysis and robust design methodology. International Journal of Machine Tools and Manufacture. 1997;37:775-82.
[174] Banaszek G, Dyja H, Mróz S, Berski S. INFLUENCE OF MAIN PARAMETERS OF FORGING PROCESS AND OPTIMAL CHOICE OF SHAPE ANVILS ON THE INTERNAL QUALITY OF FORGING FOR STEEL WCL.
[175] Hu Z, Dean T. Aspects of forging of titanium alloys and the production of blade forms. Journal of Materials Processing Technology. 2001;111:10-9.
[176] Hu Z, Brooks J, Dean T. Experimental and theoretical analysis of deformation and microstructural evolution in the hot-die forging of titanium alloy aerofoil sections. Journal of Materials Processing Technology. 1999;88:251-65.
[177] Parikh H, Mehta B, Gunasekera J, Mayer R. Forging Process Analysis and Preform Design. Current Advances in Mechanical Design and Production. 2000;3:117-23.
[178] GOHIL D. The Simulation and Analysis of the Closed Die Hot Forging Process by A Computer Simulation Method. Journal of Systemics, Cybernetics & Informatics. 2012;10.
[179] Boivineau M, Cagran C, Doytier D, Eyraud V, Nadal M-H, Wilthan B, et al. Thermophysical properties of solid and liquid Ti-6Al-4V (TA6V) alloy. International journal of thermophysics. 2006;27:507-29.
[180] Sente-Software-Ltd. JMatPro. 2014.
[181] Basak D, Overfelt R, Wang D. Measurement of specific heat capacity and electrical resistivity of industrial alloys using pulse heating techniques. International Journal of Thermophysics. 2003;24:1721-33.
[182] Sieniawski J, Filip R, Ziaja W. The effect of microstructure on the mechanical properties of two-phase titanium alloys. Materials & Design. 1997;18:361-3.
[183] Dieter GE. Handbook of workability and process design: ASM international; 2003.
[184] Micari F, Fratini L, Squillace A, Giorleo G, Testani C, Argentero S, et al. TITAFORM-Precision Hot Forming, Development of Innovative Hot-forming Processes of Aeronautical Components in Ti-alloy with Low Buy/Fly Ratio: an Italian Example of Cooperation between Academy and Industry. STEEL RESEARCH INTERNATIONAL. 2012:25-30.

[185] Davis JR, Semiatin SL, ASM. ASM Metals Handbook, Forming and Forging. 1998;14.

[186] George E. Dieter HAKSLS, Dieter GE. Handbook of Workability and Process Design: A S M International; 2003.

[187] Box GEP, Hunter WG, Hunter JS. Statistics for experimenters: an introduction to design, data analysis, and model building: Wiley; 1978.

[188] Ducato A, Fratini L, La Cascia M, Mazzola G. An Automated Visual Inspection System for the Classification of the Phases of Ti-6Al-4V Titanium Alloy. Computer Analysis of Images and Patterns: Springer; 2013. p. 362-9.

[189] Suquet P. Overall potentials and extremal surfaces of power law or ideally plastic composites. Journal of the Mechanics and Physics of Solids. 1993;41:981-1002.

[190] Briottet L, Jonas J, Montheillet F. A mechanical interpretation of the activation energy of high temperature deformation in two phase materials. Acta materialia. 1996;44:1665-72.

[191] Oikawa H, Oomori T. Steady state deformation characteristics of α-Ti ・ Al solid solutions. Materials Science and Engineering: A. 1988;104:125-30.

[192] Oikawa H, Fujishiro S, Eylon D, Kishi T. Metallurgy and technology of practical titanium alloys. TMS, Warrendale. 1994;213:93-100.

[193] Oikawa H, Ishikawa Y, Seki M, Froes F, Caplan I. Titanium'92 Science and Technology. TMS, Warrendale, PA. 1993:1779-86.

[194] Oikawa H, Nishimura K, Cui M. High-temperature deformation of polycrystalline beta titanium. Scripta metallurgica. 1985;19:825-8.

[195] Castro R, Seraphin L. CONTRIBUTION TO METALLOGRAPHIC AND STRUCTURAL STUDY OF TITANIUM ALLOY TA6V. Memoires Scientifiques De La Revue De Metallurgie. 1966;63:1025-&.

[196] Buffa G, Ducato A, Fratini L. FEM based prediction of phase transformations during Friction Stir Welding of Ti6Al4V titanium alloy. Mat Sci Eng a-Struct. 2013;581:56-65.

[197] Ducato A, Fratini L, Micari F. Coupled thermo-mechanical-metallurgical analysis of an hot forging process of titanium alloy. Key Eng Mater. 2013;554-557:638-46.

[198] Ducato A, Fratini L, Micari F. Advanced numerical models for the thermo-mechanical-metallurgical analysis in hot forging processes. Aip Conf Proc. 2013;1532:3-14.

[199] Astarita A, Ducato A, Fratini L, Paradiso V, Scherillo F, Squillace A, et al. Beta Forging of Ti-6Al-4V: microstructure evolution and mechanical properties. Key Eng Mater. 2013;554-557:359-71.

[200] Buffa G, Ducato A, Fratini L. Dissimilar material lap joints by Friction Stir Welding of Steel and Titanium Sheets: Process Modeling. Aip Conf Proc. 2013;1532:491-8.

[201] Buffa G, Ducato A, Fratini L. Numerical procedure for residual stresses prediction in friction stir welding. Finite Elem Anal Des. 2011;47:470-6.

[202] Avrami M. Kinetics of phase change. I General theory. The Journal of Chemical Physics. 2004;7:1103-12.

[203] Seshacharyulu T, Medeiros SC, Frazier WG, Prasad YVRK. Hot working of commercial Ti-6Al-4V with an equiaxed alpha-beta microstructure: materials modeling considerations. Mat Sci Eng a-Struct. 2000;284:184-94.

[204] Bruschi S, Poggio S, Quadrini F, Tata ME. Workability of Ti–6Al–4V alloy at high temperatures and strain rates. Materials Letters. 2004;58:3622–9.

[205] Hollomon JH. Tensile deformation. AIME TRANS. 1945;12:1-22.

[206] Lee W-S, Lin C-F. Plastic deformation and fracture behaviour of Ti–6Al–4V alloy loaded with high strain rate under various temperatures. Materials Science and Engineering: A. 1998;241:48-59.

[207] Lee W-S, Lin C-F. High-temperature deformation behaviour of Ti6Al4V alloy evaluated by high strain-rate compression tests. J Mater Process Tech. 1998;75:127-36.

[208] Kay G. Failure modeling of titanium-61-4 V and 2024-T3 aluminum with the Johnson-Cook material model. Technical Rep, Lawrence Livermore National Laboratory, Livermore. 2002.

[209] Motyka M, Kubiak K, Sieniawski J, Ziaja W. Hot Plasticity of Alpha Beta Alloys. 2012.

[210] Lee D, Backofen W. An experimental determination of the yield locus for titanium and titanium-alloy sheet. AIME MET SOC TRANS. 1966;236:1077-84.

[211] Jaspers S, Dautzenberg J. Material behaviour in conditions similar to metal cutting: flow stress in the primary shear zone. J Mater Process Tech. 2002;122:322-30.

[212] Tounsi N, Vincenti J, Otho A, Elbestawi M. From the basic mechanics of orthogonal metal cutting toward the identification of the constitutive equation. International Journal of Machine Tools and Manufacture. 2002;42:1373-83.

[213] Hamann J, Grolleau V, Le Maitre F. Machinability improvement of steels at high cutting speeds–study of tool/work material interaction. CIRP Annals-Manufacturing Technology. 1996;45:87-92.

[214] Umbrello D. Finite element simulation of conventional and high speed machining of Ti6Al4V alloy. J Mater Process Tech. 2008;196:79-87.

[215] Karpat Y. Temperature dependent flow softening of titanium alloy Ti6Al4V: An investigation using finite element simulation of machining. J Mater Process Tech. 2011;211:737-49.